SHAKE TABLE EXPERIMENTS FOR THE DETERMINATION OF THE SEISMIC RESPONSE OF JUMBO CONTAINER CRANES

Presented to
The Academic Faculty

By

Laura Diane Jacobs

In Partial Fulfillment
of the Requirements for the Degree
Doctor of Philosophy in Civil Engineering

Georgia Institute of Technology

December, 2010

SHAKE TABLE EXPERIMENTS FOR THE DETERMINATION OF THE SEISMIC RESPONSE OF JUMBO CONTAINER CRANES

Approved by:

Dr. Reginald DesRoches, Co-advisor
School of Civil and Environmental Engineering
Georgia Institute of Technology

Dr. Roberto T. Leon, Co-advisor
School of Civil and Environmental Engineering
Georgia Institute of Technology

Dr. Alan Erera
School of Industrial and Systems Engineering
Georgia Institute of Technology

Dr. Glenn Rix
School of Civil and Environmental Engineering
Georgia Institute of Technology

Dr. Barry Goodno
School of Civil and Environmental Engineering
Georgia Institute of Technology

Date Approved: November 10, 2010

I dedicate this thesis to Curtis O'Malley, which represents the beginning of a lifetime of discoveries. I also dedicate this thesis to the women in my family, who helped make this a world in which I can do anything. You are my heroes and source of inspiration.

ACKNOWLEDGEMENTS

This material is based on work supported by the National Science Foundation under Grant Nos. CMS-0530478 and CMS-0402490. Any opinions, findings, and conclusions or recommendations expressed in this material are those of the authors and do not necessarily reflect the views of the National Science Foundation.

John Donne once wrote, "No man is an island, entire of itself". This quote is particularly applicable to the work involved in the completion of this document, because this work would not have been completed without the significant contributions of many.

I want to thank my advisors Dr. Reginald DesRoches and Dr. Roberto Leon, whose guidance made this work possible. Their patience, understanding, insight and support have been invaluable through my entire time at Georgia Tech.

I am grateful to my committee members: Dr. Glenn Rix, Dr. Barry Goodno and Dr. Alan Erera whose insightful questions, unfailing enthusiasm and tireless efforts helped make my research project the best that it could possibly be.

I wish to thank the staff at the Structural Engineering and Earthquake Simulation Laboratory at the University at Buffalo whose extraordinary efforts made my experiments so successful.

I want to thank Liftech, Inc., especially Michael Jordan and Erik Soderberg, for providing the technical information about container cranes.

The graduate students at Georgia Tech have made my time in graduate school successful on both a personal and professional level. I would like to thank all of my fellow students on the Ports Grand Challenge Project: Laura, Lindsay, Rachelle, and

Varun. A special note of thanks goes to Benjamin Kosbab, who exhibited extreme patience while answering my many questions, as well offering advice for modeling and contributing to the design and execution of the first phase of testing, without which this work would not be complete. Thank you to the many occupants of Mason 522a for their camaraderie and support: Karthik, Tim, Abdollah, Kathy, Emily, Matthew, Jeun, Chris, and Bo Yeon. Thank you also to my other friends in the department who have provided me with laughter, inspiration and advice: Masahiro, Jamie, Monique, Niki, Jazalyn, Jonathan, Andrew, Naiyu, Kennan and many others. A special note gratitude goes out to one of my best friends, Parisa Pooyan, who has helped with homework, provided much needed advice, smiles and laughter and introduced me to the man who would become my husband.

I am grateful to my wonderful husband, Curtis O'Malley, who has been a sounding board, supported me, inspired me and kept me going through my graduate career. I wish to thank my mom and dad, Diane and Charles Jacobs, who have always supported and encouraged me in everything I do and have gotten me to where I am today. I want to thank my brother Brian Jacobs who has encouraged me throughout my whole life. I would also like to thank my grandparents for their prayers and support. I wish to thank all my aunts and uncles for their emails and messages that kept me going through the tough times.

TABLE OF CONTENTS

LIST OF TABLES

LIST OF FIGURES

SUMMARY

Container cranes represent one of the most critical components of ports worldwide. Despite their importance to port operations, the seismic behavior of cranes has been largely ignored. Historic data show that the destruction of a port during an earthquake can have a significant impact on business interruption losses, such as at the Port of Kobe in 1995, as well as complicate rescue efforts in affected regions, such as in Port-au-Prince, Haiti in 2010. Since the 1960s, industry experts have recommended allowing cranes to uplift, believing that it would limit the amount of seismic loading. However, modern cranes have become larger and more stable, and the industry experts are now questioning the seismic performance of modern jumbo cranes.

The main goal of this research is to experimentally investigate the seismic behavior of container cranes from the elastic behavior through the inelastic behavior utilizing the 6 degree-of-freedom shake tables at the University at Buffalo. Due to the complexities of modeling uplift, the characterization of uplift and derailment behavior is of particular interest. Additionally, no experimental studies have ever been conducted on container cranes to gather information about buckling, yield and collapse. This research project addresses these issues.

To characterize the seismic behavior of container cranes, the testing was divided into two phases. The first phase of testing was conducted on a $1/20^{th}$ scale model and focused on the uplift and elastic behavior. The data collected, confirmed that a simple tipping analysis is sufficient to predict when derailment will occur. The results from the Phase I test also indicate that torsion has little effect on the overall response of a jumbo container crane, suggesting that 2D finite element models are sufficient for analysis.

Additional results suggested that the top structure has little influence on the critical response quantities, indicating that simplifications could be made to the structure while preserving the dynamic characteristics.

In support of the experiments, finite element models were created to determine what simplifications could be made to the structure to aid in testing. The results of the finite element models indicate that it is possible to remove the top structure and still have a dynamically equivalent model. This result is advantageous to the port community because it suggests that simplified models can be used for analysis and qualification tests, which can save time and money.

The Phase II test was designed to be representative of a modern jumbo crane. It was also designed such that no inelastic action would develop prior to uplift (as is the common design practice). During testing the crane yielded, buckled and reached an unstable state after uplift, which challenges the conventional wisdom that uplift will provide a limit to the seismic forces. Two different boundary conditions were used: pinned and free to uplift, for the validation of finite element models with different boundary conditions. There were cases for which the pinned boundary condition led to higher forces, suggesting that cranes in earthquake zones should not be pinned except when the weather dictates otherwise. The test specimen was subjected to a suite of ground motions with various combinations of components. The data show that there are cases for which the inclusion of a vertical component will result in the most extreme load case. This result suggests that it would be prudent to run models with and without a vertical component to find the worst case. All of the test and analysis results are used as the basis for recommendations to the port community.

Chapter 1

Introduction and Motivation

1.1 Motivation

1.1.1 Vulnerability and Importance of Sea Ports

Earthquakes pose a considerable threat to the largest seaports in the United States, including, Los Angles, Long Beach, Oakland, Seattle, Tacoma, and Savannah, which serve as gateways to international trade (Figure 1.1). The US is economically dependent on container traffic through its ports, and is thus vulnerable to the consequences of damage due to a seismic event.

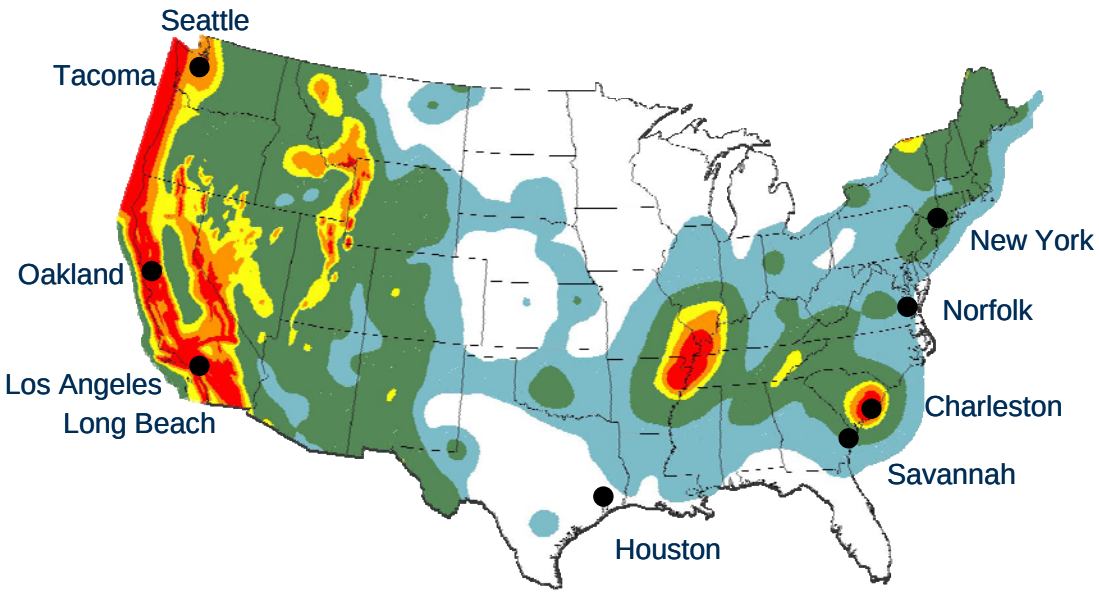

Figure 1.1: Significant U.S. ports and seismic hazard (PGA with 2% PE in 50 years), (Rix, 2007)

Ports have received little attention compared to other infrastructure systems such as: buildings, bridges, water, and power systems. This lack of attention is surprising

considering the importance of uninterrupted operations at ports. For example, a 10-day labor lockout at the ports on the west coast of the US had an estimated daily economic impact of $1 billion (Caltrade, 2008). The 1995 Hoyogken-Nanbu earthquake, which caused severe damage to the Port of Kobe provides an example of the long term effects of heavy port damage. After the earthquake, the port struggled to make extensive repairs, and shipping companies were forced to find other ports to continue shipping operations. With little incentive for the companies to return, the Port of Kobe never returned to its pre-earthquake throughput (Chang, 2000). The city of Kobe, which was also struggling to rebuild, had to do so with a significantly reduced economic base. Therefore, with container traffic in the US expected to continue to grow, protecting the seaports from seismic damage should be a high priority.

The social impacts of a damaged port can be as significant as the economic ones. Heavy damage to ports can inhibit relief efforts and emergency response in many parts of the world. For example, the port in Port-au-Prince, Haiti was destroyed after the earthquake that struck the city on January 12, 2010, leaving much of the city in ruins and thousands of people injured or killed. The relief efforts were hampered by the inability to get the much needed medical supplies and food into the country. Since the port was unusable, the airport was the only major hub for receiving supplies. The airport did not have the capacity to receive the amount of goods required for the massive relief efforts. Over 50% of the port was destroyed, including the only container terminal, and the sole container crane was submerged in water (Figure 1.2).

Figure 1.2: Partially submerged container crane at the port in Port-au-Prince following the January 12, 2010 earthquake (Photo courtesy of Glenn Rix)

1.1.2 Vulnerabilities of Container Cranes

The container crane stock is one of the most vulnerable components of a port (Chang, 2000). In many ports, container cranes are the only means of loading and unloading container ships. However, the seismic performance of container cranes has been largely ignored. In fact, until recently, cranes were built with little to no seismic detailing (Soderberg, 2007). The International Navigation Association (PIANC) published a seismic design guide, in which they acknowledge the container cranes' role in the continuous operation of a port and that they may be vulnerable to different levels of damage. However, little is said about ensuring the adequate performance of the cranes

during seismic events. The ASCE *Seismic Guidelines for Ports* suggest that cranes perform well during earthquakes. It reports that cranes will normally uplift before the structure fails, and this tipping will limit the forces in the structures. These statements are based on observations during the limited number of seismic events in US seaports, rather than a true understanding of the seismic behavior of the structures. The Port of Los Angles uses well-developed performance-based design guidelines for port structures. The guidelines state that an operational level earthquake must not damage the cranes and a contingency level earthquake must not cause collapse. However, no guidelines are in place to ensure that these design targets are met.

The lack of seismic consideration of container cranes is in spite of the fact that container cranes have a significant effect on the post-earthquake downtime in a port. Container cranes are usually built abroad and shipped to ports in which they will be used. Therefore, it can take longer to rebuild a container crane than to rebuild other port components. The neglect of container cranes is also in spite of the damage to container cranes in historic earthquakes. Recent seismic events, such as the Eastern Marmara earthquake in 1999 and the 1995 Hyogoken Nanbu earthquake, have highlighted these vulnerabilities. After these earthquakes, three main damage states have been observed including: derailment, local buckling and collapse (Kanayama et. al. 1998, Yuksel et. al. 2001). Due to the importance of cranes to the functionality of a port and the ever-present threat of earthquakes in most major U.S. ports, an understanding of the seismic performance of container cranes is critical.

1.2 Crane Terminology

Container cranes are structures built for a single purpose: to efficiently load and unload container ships. Initially developed in the 1960's, the general steel-construction A-frame arrangement has proven effective for this purpose, and has become customary (Zrnic 2004, Soderberg and Jordan 2007). Figure 1.3 highlights some important terminology as it relates to a typical A-frame container crane and its components. Two features of this arrangement are critical to the seismic response: the portal frame and the ability to uplift.

The first important feature is the large portal frame (Figure 1.3) made necessary for operational reasons. It is crucial to maintain clearance within the portal frame for the movement of auxiliary equipment and containers on the wharf deck. The portal frame is flexible relative to the rest of the structure. It is located below the center of mass, and it is non-redundant. For these reasons, its behavior is crucial for understanding the seismic response of container cranes.

The second important feature is that container cranes are not attached to the wharves on which they sit. Instead, they have wheels that sit on rails that are imbedded in the wharf deck. The rails are parallel to the waterline (Figure 1.3), allowing for the crane to move along the wharf as needed while servicing a ship. Because this boundary condition does not provide positive vertical restraint, the wheels are free to uplift under sufficient lateral loads.

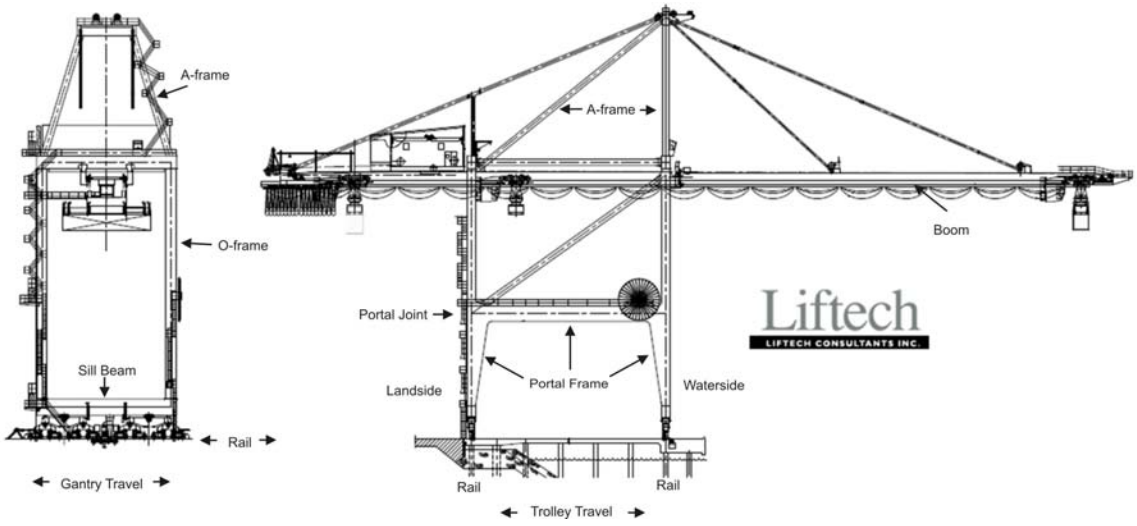

Figure 1.3: Crane terminology

This study considers jumbo container cranes (J100). J100 cranes are representative of cranes ranging from 100ft gauge large Post-Panamax to moderate Super Post-Panamax. Post-Panamax cranes are defined as those having a boom length of 135.01-185.0ft. Super Panamax cranes are defined as those having a boom length of 185.01-200ft. The J100 crane considered in this study is typical of the large cranes built circa 2000.

1.3 Scope

1.3.1 Problem Definition

Damage during historic earthquakes has proven the seismic vulnerability of container cranes. While observations from historic earthquakes and limited experimental testing have led to general ideas of the seismic behavior of container cranes, there have been no efforts to rigorously characterize their responses during seismic events, from

elastic behavior through collapse, as well as when and how uplift occurs and its effects on the structure.

1.3.2 Objectives

To address this problem, several objectives for this research are defined:

- Design shake table experiments that can be used to investigate the behavior of container cranes from general elastic behavior through collapse, including non-linear behavior such as buckling and cross section yielding.
- Characterize the uplift behavior of the crane, including: acceleration levels required to cause uplift, magnitude of uplift, magnitude of horizontal displacements during uplift, and the effect of uplift on the deformations and forces within the structure.
- Characterize the elastic behavior including: the amount of and types of deformations within the structure, and the natural frequencies and mode shapes for the crane.
- Investigate the effects of various components of ground motions on the response of the structure.
- Provide data for the validation of finite element models of container cranes.
- Create fragility curves for the derailment damage state, based on test data.
- Provide guidelines for physical and analytical qualification tests to be performed on existing or future cranes.

1.3.3 Limitations

This study investigated the performance of container cranes, and made the assumption that they can be studied as independent from the wharf system. This assumption was necessary due to the fact that it was impractical to model the wharf system under the crane in the laboratory, and the short duration of the uplift event made the possibility of including the wharf through hybrid testing unrealistic. There are limitations of this study that stem from this assumption:

- In previous earthquakes, differential displacement of the crane rails caused structural deformations far beyond the capacity of the container cranes, leading to collapse. Due to practical constraints with the shake tables, differential displacements at the boundaries could not be applied. From personal communication from Stu Werner (March 31, 2008, Atlanta, GA), the author's understanding that the spreading of the rails is being addressed in the US by retrofits that tie the rails together. These measures should reduce the likelihood of the occurrence of spreading of the crane rails. Therefore, the input motions considered in this study reflect the expected input to the crane in US ports.
- This study assumes that, because the natural period of a typical crane is much higher than that of a typical wharf, that no significant dynamic coupling will take effect. However, Schelcter et al (2000) show that the natural period of the wharf will shift to being close to that of the crane when liquefaction occurs. So, while this study includes the effects of liquefaction on the input to the crane, it does not consider how the dynamic coupling might change.

- Serviceability of a container crane depends on the condition of the crane rails, uninterrupted power, and the functionality of various non-structural components such as machinery, elevators and stairs. This study only considers the structural aspect of the container cranes. Therefore, it is possible that the container crane has no structural damage, but is still inoperable after an earthquake. This possibility is not considered in this study.

1.4 Organization and Outline

This dissertation is composed of 9 chapters, 3 appendices, and a list of references at the end. This chapter has provided the motivation for the research, and defined the scope, objectives and limitations of the research, as well as defining key terms for those unfamiliar with container cranes. The second chapter provides a review of the current state-of-the-art in the research areas that are necessary for the characterization of container cranes. The chapter is divided into four main areas: model analysis in earthquake engineering, behavior of stiffened box sections, previous and concurrent studies on container cranes, and techniques for the development of empirical fragility curves. The third chapter provides the details of the design of the first experiment. The fourth chapter presents and discusses the results of the first test. The fifth chapter presents the finite element modeling necessary for the design of the second test. The sixth chapter provides the details of the design of the second experiment. The seventh chapter presents and discusses the results of the second test. The eighth chapter presents a fragility study based on the results of the second experiment. The ninth and final chapter presents conclusions and recommendations from the work. Appendix A provides

details of the data processing used for this study. Appendix B provides supplementary information on the first test. Appendix C provides supplementary information on the second test.

Chapter 2

Literature Review

The main focus of this research is a series of shake table tests on model container cranes, and as such there have been several relevant studies to this work. Therefore, Section 2.1 describes the development of model analysis and its application to earthquake engineering. The portal structure of container cranes is comprised of stiffened box sections; therefore, Section 2.2 describes research that has been performed to characterize the buckling characteristics and the ductility properties of stiffened box sections. Section 2.3 describes other studies that have been done on container cranes. Section 2.4 describes previous research that has been performed to develop fragility curves. The chapter concludes with Section 2.5, which describes the research needs in the area of seismic response of container cranes.

2.1 Model Analysis in Earthquake Engineering

Physical models to determine the elastic earthquake response have been used since the 1930s (Ruge, 1938). Ruge conducted a detail model study on the earthquake resistance of elevated water tanks. The study included a feasibility study of various model materials and a discussion of feasible model distortions. In the United States, the use of models for the determination of the response in the inelastic material domain became an acceptable alternative in the early 1970s. Many studies involving models were directed towards the verification of analytical models for specific structural systems. The distortions in seismic input or of structural configurations in many studies are

accepted because physical results are compared to analytical results and not prototype behavior. Subsequently, the analytical models are used to predict the prototype behavior.

An extensive four-year study by Moncarz and Krawinkler (1981) evaluated the feasibility of small-scale model studies in earthquake engineering. They studied dynamic modeling theory and evaluated the accuracy of prototype response prediction through several model case studies. The study included both steel and reinforced concrete structures; however, because cranes are made from steel, only the results from the steel structures will be presented below.

The types of models addressed in the study by Moncarz and Krawinkler (1981) are true replica models, in which all physical quantities are properly simulated, and adequate models, in which the violation of specific similitude laws do not appreciably affect the response prediction of the prototype structure. The study determined the adequacy of simulation of prototype response for a series of test models for which test prototype data are available. The study found the correlation between model and test data was good to excellent, depending on the type of structure. They study concluded that model analysis can be used in many cases to obtain quantitative information on the seismic behavior of complex structures. The study also found that structural steel is best suited to material for models of steel structures with artificial mass simulation. The identical shapes of stress-strain diagrams and the ability to closely simulate the prototype connections are major advantages to using structural steel. They also found that the differences in yield due to strain rate effects is 3% for lumped mass models when gravity forces are simulated, without noticeable effects on the elastic and post-elastic stiffness properties.

The purpose of dynamic modeling theory is to predict the dynamic response of prototype structures based on the results of laboratory tests. There are many resources on model development, but all of them describe the use of similitude theory to develop the scaling relationships. Similitude theory is done using dimensional analysis. The following steps are used:

1. Write down the physical quantities on which the responses under study significantly depend.
2. Develop a suitable and complete set of independent dimensionless products from these physical quantities.
3. Establish equality between the prototype and model for each of the independent dimensionless products.

When developing the models, there are three types of models: true replica, adequate and distorted models. Each of the types of models deserves some discussion about their characteristics, limitations and applications to earthquake engineering.

True replica models fulfill all similitude requirements, and as such are the most powerful type of model. However, one, almost insurmountable difficulty exists with this type of model: the selection of a suitable model material. Exact material simulation is more involved than the simulation because it includes all pertinent material properties such as the modulus of elasticity, Poisson's ratio, and strain. No two materials in nature are exactly alike, material simulation always introduces errors in the prediction values. Therefore, true replica models are extremely difficult to realize. It is possible to find acceptable alternatives to true replica modeling which are based on compromises that minimize errors in response prediction.

Physical models that violate any design conditions are distorted models. If the effect of the distortion in the dimensionless product is such that does not require adjustments of other products or the prediction equation, it is called an adequate model. The need for adequate models is based on the desire to use the same materials for a model as can be found in the prototype. One type of distortion that leads to an adequate model is artificial mass simulation. True replica models require the model materials to have a small modulus of elasticity, a large density or both. Such materials are difficult to find in practice. Augmenting the structurally effective material with additional non-structurally effective material can be achieved either using lumped mass or distributed mass systems.

For many types of typical structures, it can be acceptable to represent structurally effective mass by a series of masses concentrated at key locations. In cases such as these, the seismically effective mass can be decoupled from the density of the structurally effective material, meaning that the lumped masses are seismically but not structurally effective.

In some cases, lumped mass distribution is inappropriate. For example, structures consisting of slender, load-carrying members, a scheme should be developed for adding mass which involves attaching suitable amounts of lead or other soft, high-density material arranged in such a way that it contributes negligibly to the strength and stiffness but still augments the weight and inertia of the structure.

Models with artificial mass simulation have been used extensively for static and dynamic model studies. Such model studies have been shown to result in a good prediction of prototype behavior.

2.2 Behavior of Stiffened Box Sections

The portal structure of container cranes is constructed of stiffened box sections. As such, it is important to understand the cyclic and buckling behavior of the box sections, as well as the ultimate strength and ductility behavior. There have been a couple of important studies on the behavior of stiffened box sections under seismic excitation. The first study by MacRae and Kawashima (2001), looked at developing criteria for determining the buckling behavior of stiffened box sections. A study by Usami et al. (2000) sought to characterize the ultimate and ductility behavior of stiffened box sections. A study by Ge et al. (2000) characterized the effects of the stiffeners on the cyclic behavior of stiffened box sections.

The study by MacRae and Kawashima (2001) included 24 tests on large-scale stiffened rectangular steel bridge columns in order to determine their seismic performance and develop methods to assess their performance. The tests included both shake table and reverse cyclic bending tests. The sections were constructed from SS41 and SM50 steel. The columns included both longitudinal and transverse stiffeners. The sections were constructed with welds that were smaller than the recommended weld size.

Based on the results of their experiments, MacRae and Kawashima (2001) proposed a method for deformation capacity of hollow stiffened steel bridge columns subjected to reverse cyclic loading that considers buckling parameters:

$$d_u = (d_y + 2LL_p\varepsilon_{f,des}) / D \tag{2.1}$$

where d_u is the ultimate displacement at the top of the column, and d_y is the displacement at the top of the column at first yield, based on the actual material properties, D is the

member depth, L is the distance from the base of the column to the center of the point of contraflexure, and L_p, the plastic hinge length, and $\varepsilon_{f,des}$ are define as:

$$L_p = \frac{b}{n} \quad \text{when } \frac{\gamma_l}{\gamma_l^*} > 2.0 \tag{2.2}$$

$$L_p = a + \left(\frac{\gamma_l}{\gamma_l^*} - 1.0\right)\left(\frac{b}{n} - a\right) \quad \text{when } 1.0 < \frac{\gamma_l}{\gamma_l^*} < 2.0 \tag{2.3}$$

$$a \quad \text{when } \frac{\gamma_l}{\gamma_l^*} < 1.0 \tag{2.4}$$

$$\varepsilon_{f,des} = \left[4.81\frac{\gamma_l}{\gamma_{l,req}} + 3.36\left(\frac{t}{t_0}\right)^2 - 3.48\right] * 10^{-3} \tag{2.5}$$

where b is the plate width, which is taken as the minimum of the overall section breadth, B, and the overall section depth, D, n is the number of panels divided by vertical stiffeners, a is the height of the base panel, t is plate thickness, t_0 is the minimum allowable plate thickness:

$$t_0 = \frac{b}{kfn} \tag{2.6}$$

where $k = 24$ for grade 50 steel, γ_l is:

$$\gamma_l = I_l / (bt^3 / 11) \tag{2.7}$$

where I_l is the longitudinal stiffener second moment of area about the surface of the main plate, $b_s^3 t_s / 3$, γ_l^* is the critical ratio of longitudinal stiffener stiffness to plate stiffness for wall buckling, given in

$$\gamma_l^* = 4\alpha^2 n(1 + n\delta_l) - \frac{(\alpha^2 + 1)^2}{n}; (\alpha \le \alpha_0) \tag{2.7}$$

$$\gamma_l^* = \frac{1}{n}[\{2n^2(1 + n\delta_l) - 1\}^2 - 1]; (\alpha > \alpha_0) \tag{2.8}$$

where α is defined as the transverse stiffener spacing divided by the plate width; and $\alpha_0 = \sqrt[4]{1+n\gamma_l}$; δ_l is the ratio of the cross-sectional area of the longitudinal stiffener, $A_l = b_s t_s$, to that of the main plate, b_t, where b_s is the longitudinal stiffener width and t_s is the longitudinal stiffener thickness.

A study by Ge et al. (2000) and Usami et al. (2000) characterized the cyclic behavior and the ductility of stiffened steel box columns. The studies utilized both analytical and experimental models. Ge et al. (2000) found that the columns failed by local and overall coupled instability. The analytical models utilized an elastoplastic large deformation finite element method. A two-surface plasticity model developed for structural steels under cyclic loading was utilized to account for material non-linearity. The analytical results were compared with the experimental results. The modified two-surface plasticity model agreed well with the experimental results. Ge et al. (2000) highlighted a few main important parameters for the characterization of steel box columns:

$$R_f = \frac{b}{t}\sqrt{\frac{\sigma_y}{E}\frac{12(1-\nu^2)}{\pi^2 k}} \tag{2.9}$$

$$\bar{\lambda} = \frac{2h}{r}\frac{1}{\pi}\sqrt{\frac{\sigma_y}{E}} \tag{2.10}$$

$$\overline{\lambda_s} = \frac{1}{\sqrt{Q}}\frac{L_d}{r_s}\frac{1}{\pi}\sqrt{\frac{\sigma_y}{E}} \tag{2.11}$$

$$Q = \frac{1}{2R_f}[\beta - \sqrt{\beta^2 - 4R_f}] \tag{2.12}$$

$$\beta = 1.33R_f + 0.868 \tag{2.13}$$

where b is the flange plate width; t is the plate thickness; σ_y is the expected value of the yield stress, assumed at 52.3ksi; E is the Young's Modulus; ν the Poisson's ratio; k the buckling coefficient of a stiffened plate = $4n^2$ (n = the number of subpanels in a stiffened plate), h column height and r the radius of gyration if the cross section, L_d is the distance between two adjacent diaphragms, r_s is the radius of gyration of a T-shape centered on a longitudinal stiffener with a width of b/n, and Q is the local buckling strength of a plate enclosed by two adjacent stiffeners.

The study by Usami et al. (2000) sought to characterize the effect of loading patterns on the cyclic inelastic behavior. This was achieved through a parametric study to investigate the effects of flange plate width-thickness ratio parameter, column slenderness ratio parameter, stiffener's equivalent slenderness parameter, magnitude of the axial load, and the material of the stiffeners on the strength and ductility of the columns. Based on the results of the parametric study, several empirical formulae for the ultimate strength, $H_{\max}/H_y$, and the ductility factors δ_m/δ_y and δ_{95}/δ_y were established. The three ratios are defined as follows:

$$\frac{H_{\max}}{H_y} = \frac{0.10}{(R_f \bar{\lambda} \bar{\lambda}_s')^{0.5}} + 1.06 \tag{2.14}$$

$$\frac{\delta_m}{\delta_y} = \frac{0.22}{R_f \sqrt{\bar{\lambda}} \bar{\lambda}_s'} + 1.20 \tag{2.15}$$

$$\frac{\delta_{95}}{\delta_y} = \frac{0.25}{(1 + P/P_y) R_f \sqrt{\bar{\lambda}} \bar{\lambda}_s'} + 2.31 \tag{2.16}$$

where R_f is defined in equation 2.9, $\bar{\lambda}$ is defined in equation 2.11, $\bar{\lambda}_s'$ defined in equation 2.12.

2.3 Previous and Concurrent Studies on Cranes

There have been few studies on the behavior of container cranes under earthquake loads. Most of the previous studies have been performed in Japan, some of which included shake table testing. Most of the studies have been analytical in nature. The following sections consider each of the studies in detail.

2.3.1 Shake Table Tests

Two main groups performed shake table tests on crane models. The first is a group lead by Kanayama from Ishikawajima-Harima Heavy Industries. The second group is the Japanese Port and Airport Research Institute.

The first study was performed by Kanayama and Kashiwazaki (1998) on a 1/25 scale model of a 30 meter class of crane. The cross sections had to be made so small that problems from insufficient stiffness were anticipated, therefore, only the rigid body motion was examined. The total weight was 79.2 kg and the center of mass was at x = 0.35 m and z = 1.15 m. The crane was made of carbon steel members that were welded together except for the boom. The model had two wheels per leg. The researchers reasoned that because the legs of the cranes act like cantilevers when excited in the direction transverse to the rail, the cranes are supposed to be more susceptible to seismic motion in that direction. Therefore, they only presented input motion transverse to the rail. The input seismic force was derived from the recording taken at the Kobe Port Island during the Southern Hyogo Prefecture Earthquake. The dominant frequency is very low (0.5 Hz) due to liquefaction, and is very severe to container cranes. During the testing, the researchers found the upper structure moves seaward, the landside wheels

uplift, the sea-side legs deform further, and finally the landside wheels land on the ground.

Kanayama et. al. (1998) performed another, larger scale experiment. Due to the limitation of the height of the laboratory, the test was performed on a $1/8^{th}$ scale model. Gravity plays an essential role in the response, so the acceleration scale was selected to be 1. The elastic motion of the crane is dominated by the bending deformation of the members, so axial stiffness does not play an important role. The plastic deformation of the members is not taken into consideration. The bending rigidity was scaled to $1/8^5$ and the mass was scaled to $1/8^3$. Additional masses were applied to compensate for the reduced mass. The axial stiffness does not play an important role in the response, so the reduction in the second order moment is almost equivalent to the reduction of the elastic modulus. Plastic deformation of the members was not considered in the model. The boundary conditions included one wheel per leg, and the wheels were fixed by a bolt to restrain rotation. The crane was excited uniaxially using the N-S component measured at the Kobe Port Island during the Southern Hyogo Prefecture Earthquake. The first eigen mode was bending and occurred at 1.63 Hz. The crane behaved as the previous study indicated.

Sugano et. al. (2003) from the Japanese Port and Airport Research Institute performed a study on a 1/15 scale model of a 30m class of crane. The goal of the experiment was to verify the effectiveness of an isolation system. The moment of inertia was scaled to $1/15^5$ and the mass was scaled to $1/15^3$. The elastic motion of the crane is dominated by the bending deformation of the members, so axial stiffness doesn't play an important role. The plastic deformation of the members is not taken into consideration.

The shake table is capable of biaxial excitation, but does not have the capability of exciting the crane with a vertical component. To investigate the influence of a container hanging from the crane, a load was attached to a rope hanging from the end of the boom. Additionally, to determine the influence of the boom being lowered or stowed, tests were run with the boom in both positions. The researchers used an instrumentation scheme that included accelerometers, strain gauges and a laser displacement gauge. They found that when uplift occurs, the landside leg lifts first and derails. The maximum acceleration measured in the crane when the boom was down was 0.152g and 0.106g when the boom was in the stowed position. Therefore, the boom down represents the most severe loading condition for the crane. Additionally, there is no difference in the dynamic response of the crane when a container is included versus when the container is not included. The study also showed that an isolation system will reduce the maximum acceleration in the crane and will prevent uplift, allowing the crane to remain operational immediately following an earthquake.

Sugano et al (2008) also showed that uplift can be successfully related to peak boom acceleration via a static tipping analysis. A simple system is sketched in Figure 2.1, where H identifies the height to the center of mass, m, of the crane; L_1 the distance between center of mass and waterside leg; L the distance between legs, V_1 and V_2 the vertical reactions at the waterside and landside base, respectively; and a the horizontal threshold acceleration at the center of mass which causes uplift. The sum of moments can be found at the waterside leg, resulting in Equation 2.17.

$$L \cdot V_2 + H \cdot m \cdot a - L_1 \cdot m \cdot g = 0 \tag{2.17}$$

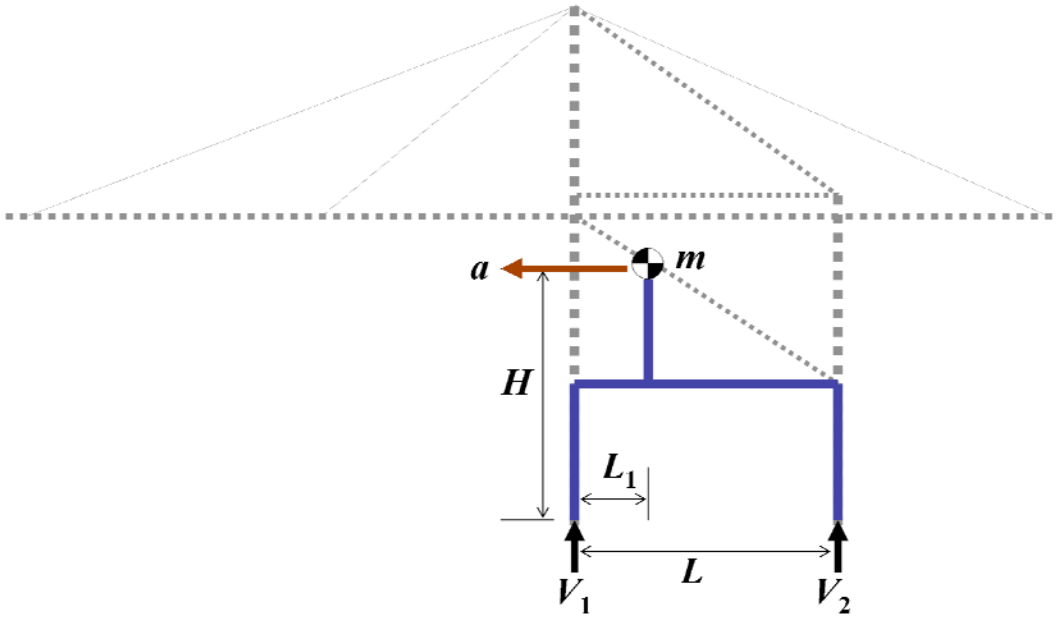

Figure 2.1: Figure for pseudo-static uplift analysis

Because the landside carries a smaller load than the waterside, the landside leg will uplift first, when reaction $V_2 = 0$. Additionally, due to the stiffness of the upper structure of the container crane relative to the portal frame, the acceleration of the center of mass is essentially equal to the acceleration at the boom. The boom acceleration uplift threshold, a_{bu}, can then be evaluated simply by using Equation 2.18:

$$a_{bu} = \left(\frac{L_1}{H}\right) g \tag{2.18}$$

2.3.2 Analytical Studies

There have been a few important analytical studies on container cranes. A study by Murano and Yoshida (2002) at Keio University performed an analysis on container

cranes with a rocking vibration isolation system. Kobayashi et al. (2004) performed an analytical study, which included the nonlinear responses including the contact problem between the wheels and rails. The last study by Kosbab (2010) was performed concurrently with this study, which was an extensive study of the linear and nonlinear response of container cranes.

A study by Murano and Yoshida (2002) performed an analysis on container cranes to evaluate the effectiveness of a rocking vibration isolation system. The study compared the response of a crane with no isolation system to one with a horizontal vibration isolation and one with a rocking vibration isolation system. A rocking vibration isolation system is constructed of a spring and damper that supports the crane vertically. It reduces vibration energy by converting horizontal seismic excitation to rotation and absorbs the rotation through the spring and damper. The study looked at five different ground motions. The researchers found that the rocking vibration isolation system has the best performance for ground motions with a component in the gantry travel direction, which excited the twist vibration motion.

In the study by Kobayashi et al. (2004), the researchers modeled the crane structure and the kinematic relationship between the wheels and rails. The researchers proposed a three-dimensional method for modeling movable, flexible, large container cranes for the purpose of realistically modeling the seismic response. They used a finite segment method to describe the flexibility of the frames. They also developed a contact element to represent the complex contact configuration between wheels and the rails. The method they proposed could model the sliding, uplifting and derailment of the wheel

from the rail. Good agreement was found between their model and the experimental results of Kanayama et al. (1998).

The final study was conducted by Kosbab (2010). In the study, Kosbab developed several crane models to represent the main classes of container cranes found in the US. As part of the study, a contact element is implemented to capture the complex phenomena of uplift and derailment. The study utilized complex, nonlinear finite element models to develop fragility models for the different classes of cranes. The finite element models were validated using the results of the first phase of testing for the current study, described in Chapters 3 and 4. The study also developed a portal uplift theory to predict the sliding, uplift and collapse behavior of container cranes. The study found that the uplift and translation behavior caused an increase in the response of the crane, above what is predicted by a simple pinned condition or a no-tension element that allows for uplift but not translation. The study also found that the twisting of the crane has a negligible effect on the overall response. Therefore, a two-dimensional model is sufficient for the prediction of the response of the structure.

2.4 Probabilistic Seismic Performance Assessment

A key component of seismic performance of structures is the concept of fragility. Fragility describes the probability that a structure will fail to meet a performance objective as a function of the system demand. One of the earliest applications of fragility modeling on civil infrastructure subjected to earthquakes was in ATC-13, (1985). The Federal Emergency Management Agency (FEMA) sponsored the development of a program for loss estimation called HAZUS (FEMA, 2003). Both ATC-13 and HAZUS

are based on expert opinion. In recent years, more rigorous data driven approaches have been developed. Two main types of fragility analyses have been developed: empirical and analytical. Empirical fragility curves use historic or test data. Analytical fragility curves use the results of rigorous finite element analyses. Computational approaches for empirical and analytical fragility curves have been developed (resources), which will be described in further detail in the following sections.

2.4.1 Risk Framework

The concept of risk includes hazards, consequences and context, (Ellingwood et al, 1980). The theorem of total probability (Ang and Tang, 1975) provides the framework to consider the aspects of risk assessment:

$$P\left[Loss > c\right] = \sum_{s}\sum_{LS}\sum_{d} P\left[Loss > c \mid DS = d\right] P\left[DS = d \mid LS\right] P\left[LS \mid SI = s\right] P\left[SI = s\right] \quad (2.19)$$

where $P[SI=s]$ is the probability of a seismic event with $SI=s$, from the standard hazard curve; $P[LS|SI=s]$ is probability of achieving the limit state LS, given the occurrence of a seismic event, $SI=s$; $P[DS=d|LS]$ is the probability of the damage state DS, given the limit state LS; and $P[Loss>c|DS=d]$ (Ellingwood et al, 2007) is the probability that loss exceeds c, given that $DS=d$. The term $P[LS|SI=s]$ is the fragility term, and it describes the conditional probability that a limit state is achieved, given an earthquake intensity.

Many studies have identified interstory drift as an appropriate engineering demand parameter (EDP) for defining limit states, because it can provide insight to the possibility of local or global collapse (Ellingwood, 2007). When interstory drift, or simply drift, is used as the EDP, it is common to assume that the damage states are correlated to limit states.

Historically, it has been customary to use the peak ground acceleration (PGA) as an intensity measure in probabilistic seismic performance assessment. However, it has become more common to use the spectral acceleration at the fundamental period of the structure, because it correlates well to many of the typical engineering demand parameters (EDPs) (Ellingwood, 2001).

When using drift as the EDP and spectral acceleration as the intensity measure, the fragility term can be written as:

$$P[D > \theta \mid S_a = s] \tag{2.20}$$

where D is the EDP of maximum portal drift; θ is a specific value of D; S_a is the seismic intensity measure of spectral acceleration; and s is a specific values of S_a.

2.4.2 Fragility

As previously stated, Equation 2.20 describes structural fragility. It expresses the probability of exceeding a certain drift level when subjected to a given spectral acceleration. Fragility is commonly modeled as a lognormal cumulative distribution function:

$$F_R(x) = \Phi\left[\ln(x / m_R) / \beta\right] \tag{2.21}$$

where m_R represents the median capacity with a logarithmic standard deviation β representing the combination of the inherent randomness and uncertainty; $\Phi[\cdot]$ is the standard normal probability integral; x is a specific value of EDP.

The term β in Equation 2.19 represents the combination of all of the inherent randomness and uncertainty in the fragility formulation. The factor β can be broken down into categories: aleatory randomness, β_{RR}, and epistemic uncertainty β_u. Aleatoric

uncertainty can be further divided into randomness in demand and capacity β_{RD} and β_{RC} respectively. The combination of the effects can be expressed as:

$$\beta = \sqrt{\beta_{RD}^2 + \beta_{RC}^2 + \beta_u^2} \tag{2.22}$$

To use Equation 2.19 to develop fragility curves, it is necessary to develop a relationship between the seismic intensity to limit states in terms of the EDP, to plug in for m_R. These relationships are done in terms of seismic demand models, which is a way to relate spectral acceleration to drift as well as to quantify the uncertainty related to the choice of the demand model. The SAC/FEMA project (Cornell et al, 2002) proposed the following exponential relationship between spectral acceleration and drift.

$$\theta_{\max} = aS_a^b \varepsilon \tag{2.23}$$

where ε is a lognormal random variable with a median of 1 and a log standard normal $\sigma_{ln\varepsilon}$. After performing a number of nonlinear time history analyses or experiments, a liner regression is performed on a $ln\ \theta_{max}$ vs. $ln\ S_a$ to characterized the mean and standard deviation to be used in equations 2.19 and 2.20 respectively.

This methodology for fragility analysis has been successfully applied to steel frames, concrete buildings, unreinforced masonry buildings, bridges, container cranes and other structures.

2.4.3 Uncertainties

There are many factors that influence the seismic response of a structure, and there are uncertainties associated with those factors. The uncertainties in demand come from a lack of knowledge of the characteristics of the earthquake that must be resisted by

the structure and how the structure will behave. The uncertainties in resistance come from a lack of knowledge of how much resistance can be provided when a particular limit state is reached. All of the uncertainties in capacity and demand can be further divided into aleatoric and epistemic uncertainty.

Aleatoric uncertainty comes from physical sources of randomness and cannot be reduced by increased knowledge. For example, the exact characteristics (magnitude, location, frequency content, etc.) of the next earthquake are not, and cannot be known. Additionally, due to the inherent randomness of materials, the precise material properties throughout a structure cannot be known, despite material tests.

The epistemic uncertainty stems from the simplifications, assumptions, lack of knowledge and limitations in supporting data. Epistemic uncertainty can be reduced by additional analysis or additional information, which generally comes at a cost. For example, simplifications (planar vs. 3D models) and approximations (linear vs. nonlinear) made during modeling may not capture the actual behavior of a structure. Additionally, the assumptions made on the attenuation relations, the variation with ground response with depth, etc. can lead to inaccuracy in the definition of he seismic hazard.

2.4.4 Empirical Fragility Curves

Fragility curves can either be made from empirical data or analytical data. Empirical fragility curves are typically developed using observations of damage from past earthquake events. To develop these curves, it is necessary to have damage data

from post-earthquake reports and the data on the spatial distribution of the ground motion. Correlating these two data sets, allows for the creation of fragility curves.

A number of researchers have presented methodologies for creating fragility curves based on empirical data. A study by Basöz and Kiremidjian (1999) investigated how to develop fragility curves based on the data available after the 1994 Northridge Earthquake. The logistic regression model is used for estimating the probability that an event occurs and is used for discrete outcomes for variables that take on two or more possible values. Shinozuka et al (2000, 2003) have presented fragility curves based on data from Calrans for the 1994 Northridge earthquake and the data from the Hanshin Expressway Public Corporation's column damage data after the 1995 Kobe earthquake. This study uses a maximum likelihood method to derive the lognormal distribution for the fragility analysis. Yamazaki et al (1999) also developed empirical fragility curves for expressway bridges in Japan, based on observed damage from the 1995 Kobe earthquake, using the least squares method to derive the lognormal parameters.

2.4.5 HAZUS Curves for Container Cranes

The HAZUS program (FEMA, 2003) was developed to estimate the losses associated with earthquakes. HAZUS defines the damage states of the components as the ratio of repair replacement cost. The program's component restoration curves describe the percent of the components expected to be open or operational as a function of time following an earthquake. The HAZUS program recognizes that a user should consider waterfront structures and cranes of a port when assessing its functionality. In the study, the independence of the components on overall system fragility is not addressed.

The HAZUS program requires specific inputs to estimate the damage to port systems including: the geographic location of the port, the expected peak ground acceleration (PGA) and permanent ground deformation (PGD), and the classification of the structures. The program outputs probability estimates of component functionality and physical damage in terms of the damage ratio.

The damage functions, in the form of fragility curves, are lognormally distributed functions that provide the probability of reaching or exceeding different levels of damage for a given level of ground motion. They are characterized by a median value and an associated dispersion factor. For container cranes, the fragility curves are defined in terms of the PGA and PGD. HAZUS defines four damage states for container cranes, summarized in Table 2.1.

Table 2.1: HAZUS Definitions of Damage States for Container Cranes (FEMA, 2003)

Damage State	*Definition*
Slight/Minor	Minor derailment or misalignment without major structural damage to the rail mount
Moderate	Derailment due to differential displacement of the parallel tracks, rail repair and some repair to structural members necessary
Extensive	Considerable damage to the equipment, toppled or totally derailed cranes, replacement of structural members required.
Complete	Same as Extensive

The probability of reaching or exceeding a damage state D=d is given by (FEMA, 2003):

$$P\left[D \geq d \mid IM\right] = \Phi\left[\frac{1}{\beta}\ln\left(\frac{IM}{IM_D}\right)\right] \tag{2.24}$$

where IM_D is the median value of the intensity measure, IM, at which the threshold of the damage state D is reached, β is the standard deviation of the natural logarithm of IM, and

Φ denotes the standard normal cumulative distribution function. The fragility curve parameters for unanchored/rail mounted container cranes are presented in Table 2.2.

Table 2.2 HAZUS damage parameters for unanchored/rail mounted container cranes (FEMA, 2003)

Damage State	*PGA Median (g)*	*PGD Median (in)*	β
Slight/Minor	0.15	2	0.6
Moderate	0.35	4	0.6
Extensive	0.8	10	0.7
Complete	0.8	10	0.7

2.5 Research Needs

The previous research did not investigate the influence of vertical components of ground motions to the response of container cranes. Also, the models focused solely on the elastic failure mode of uplift and neglected local buckling, cross-section yielding and collapse. The previous studies focused on older generations of container cranes that are expected to exhibit elastic behavior throughout an earthquake. However, modern jumbo cranes are expected to experience cross-section yielding or local buckling prior to uplift. Additionally, all of the previous studies only considered excitation from a single ground motion. In order to make a more general characterization of the seismic response of container cranes, it would be useful to consider a variety of ground motions with different response spectra.

CHAPTER 3

PHASE I TEST OVERVIEW AND SET-UP

The objective of the first experiment was to investigate the response of a 1/20th scale container crane through the measurement of the elastic response and the interaction between flexural behavior and the expected uplift/rocking phenomenon.

There were several expected outcomes for the first phase of testing:

- The data collected was used to validate analytical models and to develop preliminary fragility curves. The data provided insight into the elastic response limits of container cranes.
- The primary focus was on the movement of the legs; therefore, information was gathered on the derailment damage state.
- Information about the forces on the wharf deck and crane rails was collected.
- An instrumentation scheme was tested to ensure that all of the information that is required out of the larger scale test can be collected.

3.1 Specimen Description

3.1.1 Scaling Relationships

In order for a model to accurately reflect the behavior of a prototype structure, special care must be taken in developing the scaling relationships so that similitude is maintained for the most critical quantities. It is not necessary to maintain perfect similitude and still be able to predict the response of the prototype structure. In fact, "adequate" and "distorted" models where some of the laws of similitude have been

relaxed, can still give useful information (Moncarz and Krawinkler, 1981). An understanding of the structure and how the various quantities affect the response are necessary to determine which quantities the similitude laws must be maintained and for which they can be relaxed. In this study, perfect similitude was not maintained, and further explanation of this is provided with the explanations of the model development.

The use of small-scale models for the prediction of the elastic behavior of structures under seismic excitation has become common since it was first reported in the 1930s (Ruge, 1934). In the past few decades, methods have been developed so that scale models can be used when studying inelastic and cyclical structural behavior, while still maintaining similitude with the prototype structure (Harris and Sabnis, 1999). The scaling processes are well understood for experiments in which elastic and rigid body response are the focus, and sufficient similitude can be achieved at small scales (Moncarz and Krawinkler, 1981).

The process of properly scaling values for a model to achieve similitude starts with dimensional analysis. In order to achieve proper scaling so that the response of the model accurately predicts the response of the prototype, three independent, dimensionless quantities were selected, and these established the scale factors for all of the other physical quantities. A length scale of 1:20 was chosen to make the model physically manageable. Gravity is a critical component in the uplift response, so the gravity scale factor was 1:1. Also, the prototype material, steel, was used for the specimen, so the elastic modulus scale factor was 1:1.

In order for the model to be a "true replica" the material must be dense, flexible or both. Because these criteria are not satisfied when using the prototype material, it

becomes necessary to add non-structural or "artificial" mass. Adding non-structural mass results in an "adequate" model, which gives a good estimate of the behavior without perfect scaling (Moncarz and Krawinkler, 1981). Time also must be scaled appropriately, using the derived dimensionless quantity. The important scaling relationships for this experiment are summarized in Table 3.1.

Table 3.1: Scale factors for 1/20th scale model

Quantity	*Symbol*	*Factor*
Geometric Length, l	λ_l	20
Elastic Modulus, E	λ_E	1
Acceleration, a	λ_a	1
Mass, m	λ_m	400

3.1.2 Specimen Design

The relative overall dimensions of a typical jumbo container crane were preserved in the model. The model was 11 feet tall and 22 feet from the end of the trolley girder to the end of the boom. Figure 3.1 illustrates the dimensions of the model with the prototype dimensions in parentheses. The prototype structure was made up of built-up, stiffened box sections and tube sections; the main model sections were constructed of hollow rectangular or circular tube sections that were sized according to scaled moments of inertia. The forestays and backstays were made of multi-strand steel cables and were sized to have an equivalent axial stiffness to the corresponding scaled member. The moments of inertia and cross section area of the members referenced in Figure 3.1 are shown in Table 3.2. Figure 3.2 shows the completed specimen on the shake table.

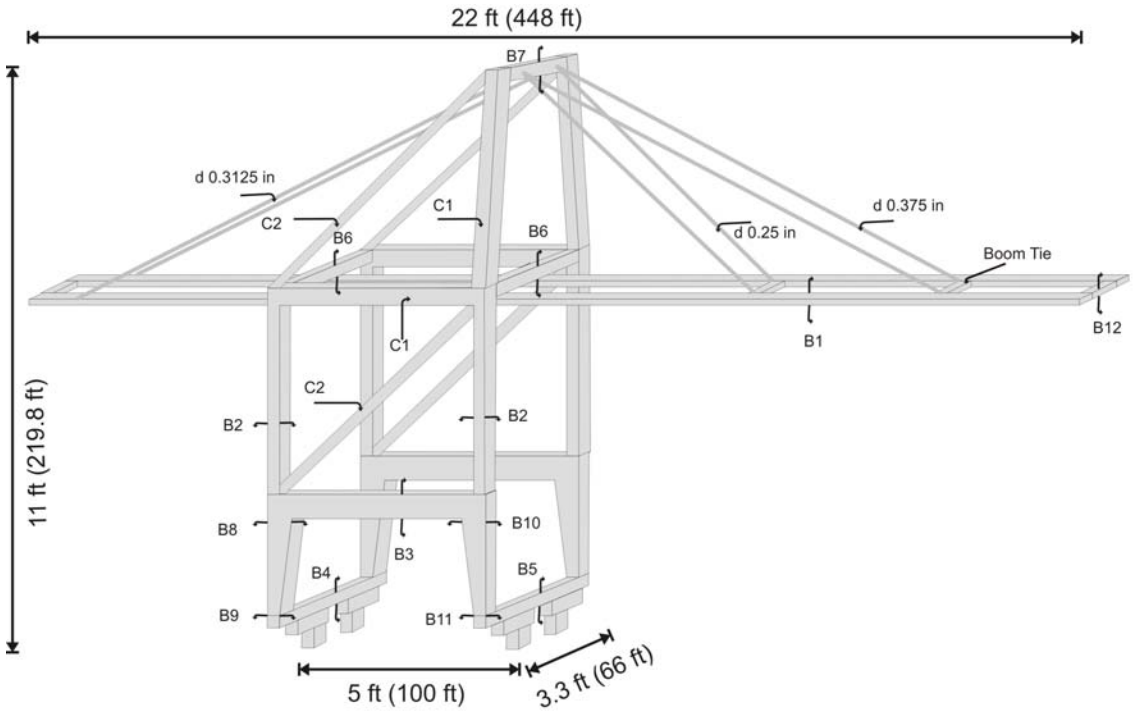

Figure 3.1: 1/20th scale crane model

Figure 3.2: 1/20th scale crane model on shake table

The members of the portal frame were made up of tapered members, and were the most critical to the response of the structure. Therefore, for the model specimen, each portal frame is constructed using built-up, welded plate made from A36 steel to achieve hollow, tapered, rectangular sections with continuity at the portal joints, as shown in Figure 3.3. The structure was constructed at the Georgia Institute of Technology and shipped to the University at Buffalo. In order to ship the structure, it had to be divided into four main sections: the North and South structural frames, the trolley girder and the boom. The structure was then assembled once it reached the University at Buffalo. The tubes that made up the four main sections were welded together. Bolted joints were then employed to connect the North and South frames using the trolley girder support beams and the sill beams, shown in Figure 3.4. The bolted connections were then welded to ensure rigidity. The stays were attached using clips, thimbles, and loops and incorporated a turnbuckle for length adjustments, Figure 3.5.

Table 3.2: Summary of members for 1/20th scale model of a container crane

	Target			***Actual***		
Box Member	***A*** in^2	***Iz*** in^4	***Iy*** in^4	***A*** in^2	***Iz*** in^4	***Iy*** in^4
B1	0.9	0.74	0.33	0.9	0.74	0.33
B2	0.26	0.55	0.31	0.78	0.43	0.27
B3	0.35	2.28	0.84	1.49	1.66	0.93
B4	0.76	2.05	0.63	2	2.07	0.64
B6	0.76	1.51	0.6	1.55	1.68	0.53
B5	0.76	3.45	0.92	2.75	5.31	1.68
B12	0.51	0.28	0.13	0.51	0.28	0.13
B8	0.57	2.65	1.22	1.61	2.7	1.1
B9	0.41	0.7	0.48	1.21	0.65	0.58
B10	0.74	3.31	1.6	1.74	3.21	1.17
B11	0.52	0.93	0.6	1.08	0.58	0.41
B7	0.42	0.86	0.4	1.55	1.68	0.53
Tube Member	***A*** in^2	***I*** in^4		***A*** in^2	***I*** in^4	
C1	0.23	0.16		0.67	0.19	
C2	0.19	0.09		0.49	0.09	

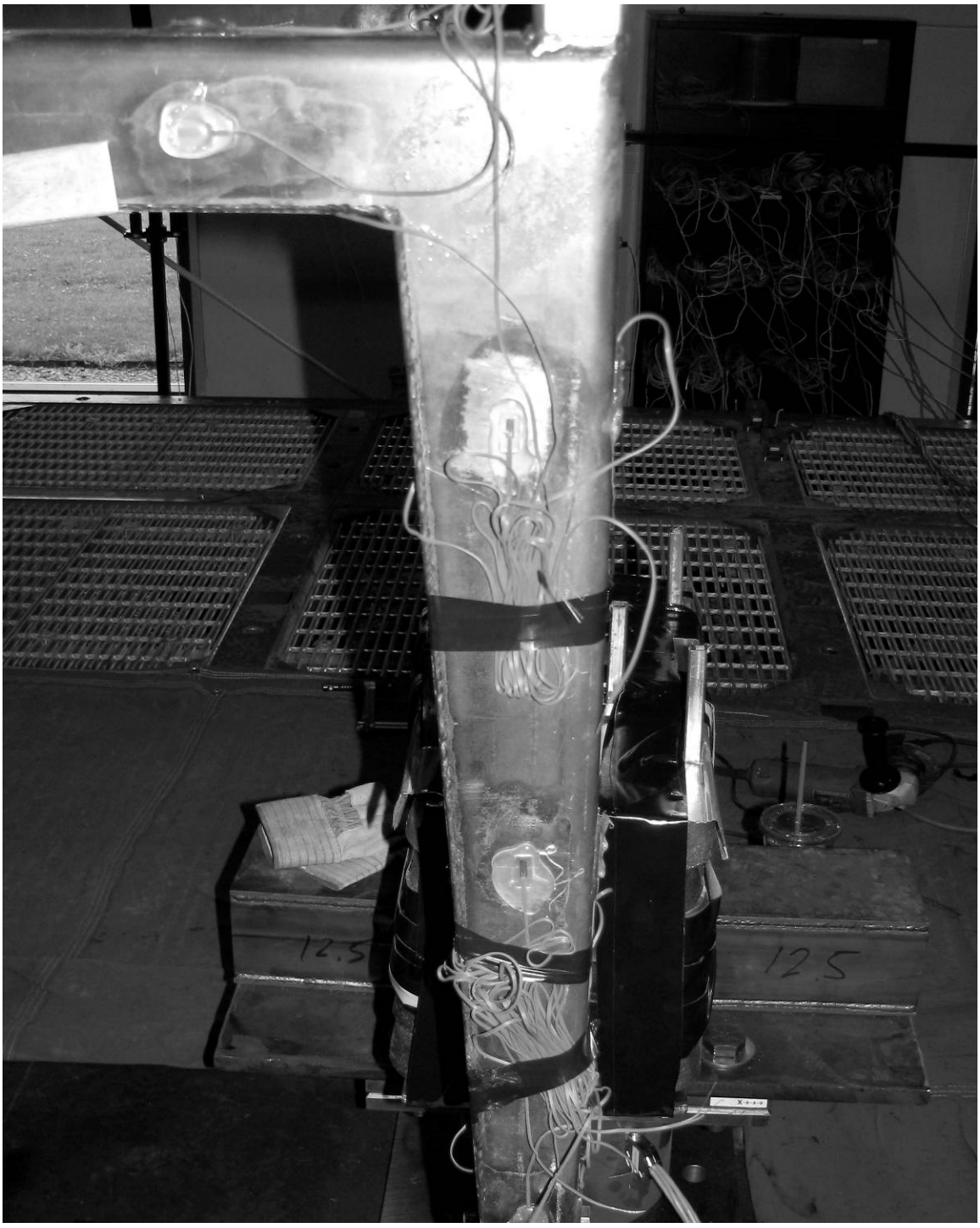

Figure 3.3: Tapered member for 1/20th scale model portal leg

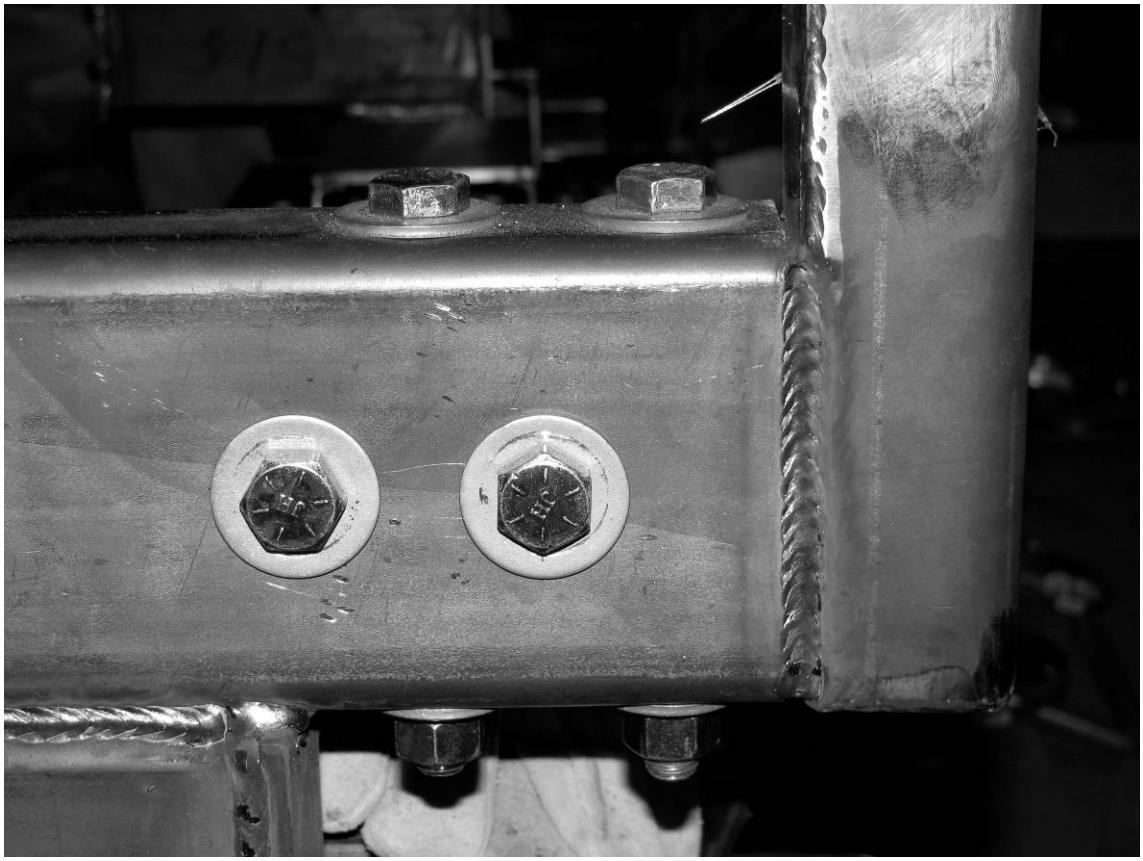

Figure 3.4: Joints connecting the north and south frames for the 1/20th scale model

There are some additional aspects of design that are important to note. First, due to the small size of model sections, it was impractical to include stiffeners. However, their effect on stiffness was accounted for through their inclusion in the calculation of the moment of inertia. Second, a minimum wall thickness of 3.1 mm (0.21in) was imposed on all model sections due to concerns about distortions from the welding process. As a result, even though scaled moments of inertia were preserved, cross-sectional areas of model members were oversized relative to a perfectly scaled prototype structure. This had the effect of increasing the axial stiffness and strength above what is required by similitude. However, because axial properties have a negligible influence on the uplift and elastic response, larger axial capacities are acceptable. In addition, the oversized

sections increase the moment capacities of the sections above what is required by similitude. However, because this experiment targets elastic response, increased moment capacities have the effect of increasing the allowable excitation prior to yielding.

Figure 3.5: Stay connection detail for 1/20th scale model

Further details of the design, such as section dimensions and fabrication drawings, can be found in Appendix B.

3.1.3 Additional Mass

The prototype crane weighs 1250 metric tons. The required weight for the model specimen was 6990 lbs. The specimen itself weighed 600 lbs, requiring an additional 6390 lbs of non-structural mass. The non-structural mass was added in three different ways. First, the sill beams and rigid columns that make up the base were filled with 100 lbs of steel shot. Second, mass was stacked and tack-welded at various locations along the boom to act as concentrated masses. Finally, lead ingots were placed on the portal and O-frames, where lumped masses are inappropriate due to second-order effects related to their large deformations. The use of lead ingots allows for the addition of mass along the members without significantly changing their stiffness. Figure 3.6 shows the distribution of mass on the structure.

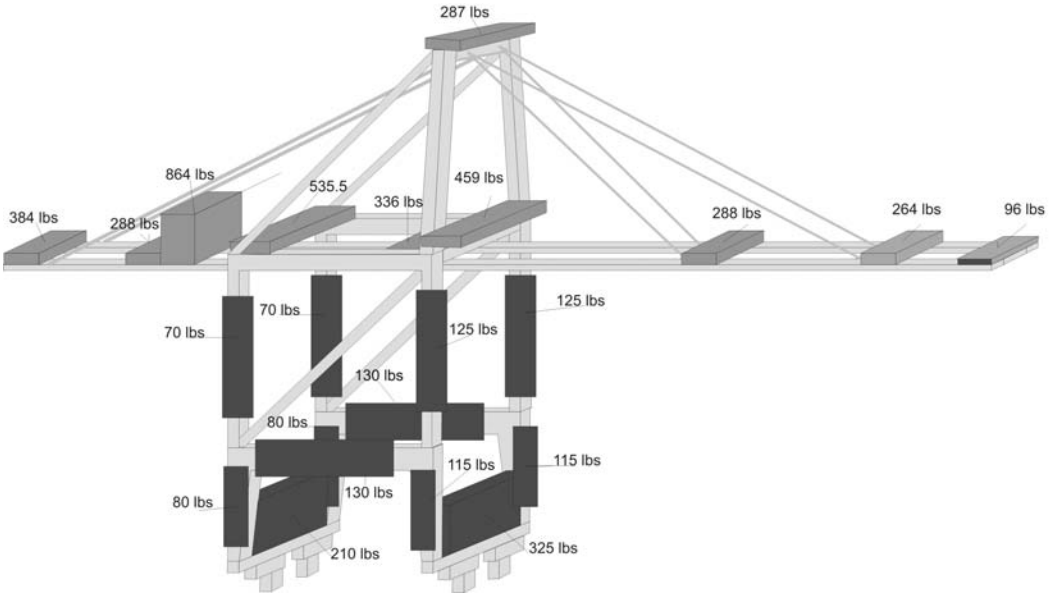

Figure 3.6: Mass distribution on 1/20th scale model of a container crane

3.1.4 Boundary Condition

Modeling the boundary condition was important for being able to ensure that the uplift response of the model was representative of the response of the prototype. Because of the small scale of the model it was not possible to model the system of balance beams, equalizer beams, trucks with wheels and rail (Figure 3.7(a)). This system was represented by a rigid column 2 in by 4 in, as can be seen in Figure 3.7(b) and referred to as a "pseudotruck." An important aspect of the boundary condition was that the crane must have no vertical restraint to uplift, but act essentially pinned prior to uplift. Additionally, the horizontal restraint must be removed when uplift occurs, allowing for large transverse movements of the uplifted legs. Three different boundary conditions between the column and steel plate were used during testing. The first was direct contact between the columns and the steel base plates. For the second, a grinding disk was adhered to the bottom of the column with the rough side resting on the base plate. For the third, two grinding disks were glued together and placed between the columns and the base plates (Figure 3.7(b)). Inclined friction tests indicate that the effective coefficient of friction between the disk and clean steel is between 0.6 and 0.8. The friction approach is effective in causing a leg base to act essentially pinned until uplift, at which point it behaves freely.

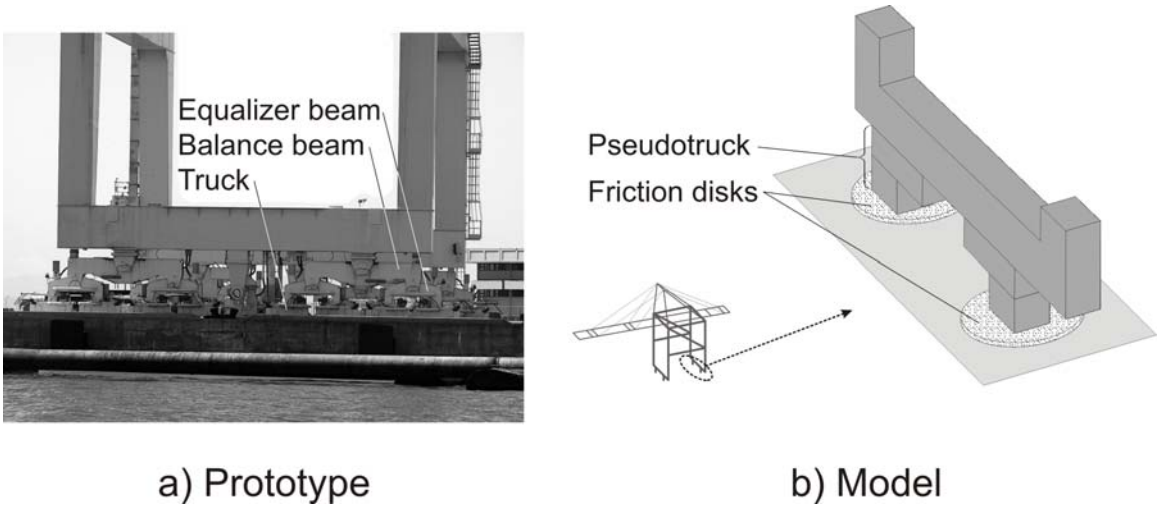

Figure 3.7: Boundary conditions for (a) prototype and (b) model container cranes

3.2 Instrumentation

3.2.1 Response Quantities

There were several important response quantities that were measured in this study, which include: the accelerations and displacements of the boom, vertical and horizontal displacements of the legs, stresses in the portal joints, and distribution of weight. The accelerations and displacements in the boom were important because they help characterize the modes of the dynamic response of the crane. Tracking the displacements of the legs allowed for the characterization of the movement of the crane during seismic loading and the determination of when derailment will occur. Although this study considered only elastic structural response, recording the stresses in the portal joint was important for extrapolating potential damage scenarios to the full-scale structure. Monitoring the distribution of weight of the crane allowed for determining the distribution of forces within the crane as well as to the wharf deck and crane rails. All of these response quantities were important for the validation of finite element models.

3.2.2 Instrumentation Scheme

To measure these response quantities, an instrumentation scheme was developed that uses load cells, accelerometers, string potentiometers, extensometers and strain gages, as summarized in Table 3.3. An advanced Krypton 3D coordinate tracking system was used as a redundant measure of absolute and relative leg base movement. Eight video cameras were placed at various locations. Two high-speed (300 fps) cameras were employed to capture the short-duration uplift events. Close-up views of each leg base were used to further clarify each leg's individual uplift events.

Table 3.3: Instrumentation plan summary for Phase I test

Instrument	*Number of Channels*
Accelerometers	56
String Potentiometers	25
Strain Gages	96
Load Cells	20
TOTAL	197

Fifty-six channels of accelerometers were used. Figure 3.8 shows the details of the accelerometer placements. The locations where three accelerometers are indicated had accelerometers measuring in the three perpendicular directions of the direction along the boom, perpendicular to the boom and vertically. Where only two are indicated, accelerometers were placed perpendicular to the boom and vertically.

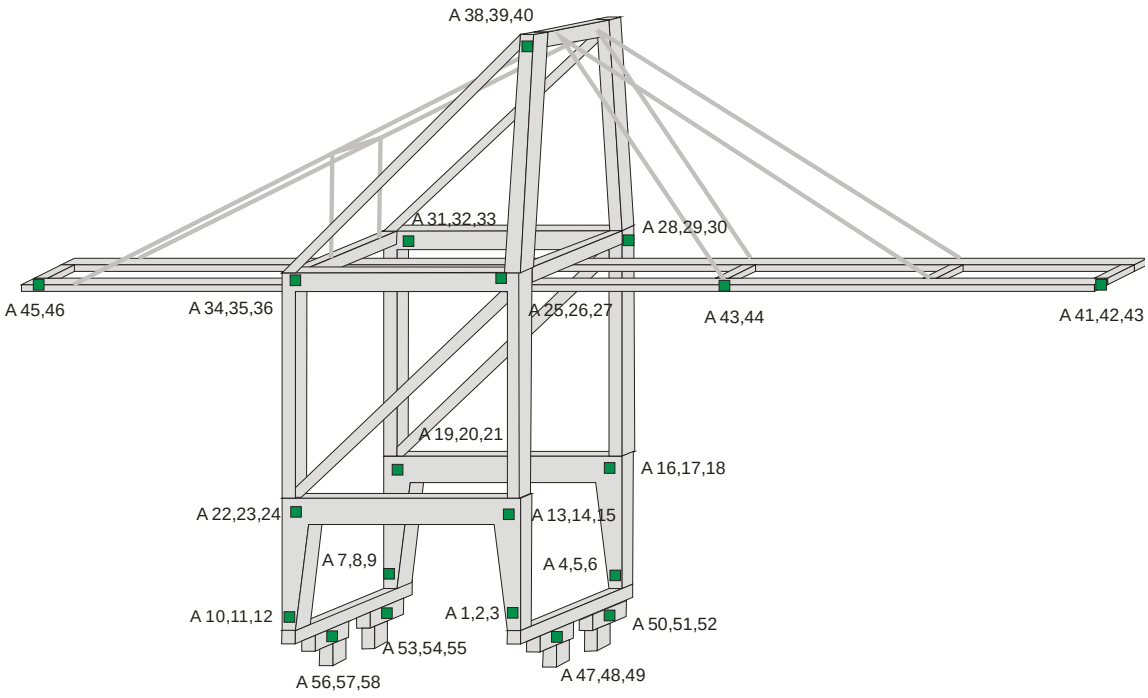

Figure 3.8: Accelerometer plan for 1/20th model container crane

Twenty-five string potentiometers were used to measure important displacement values. Figure 3.9 shows the details of the potentiometer plan. The places where three potentiometers are indicated, the gages were located in the three perpendicular directions of the direction along the boom, perpendicular to the boom and vertically. Where only one is indicated, the displacement was measured in the direction along the boom.

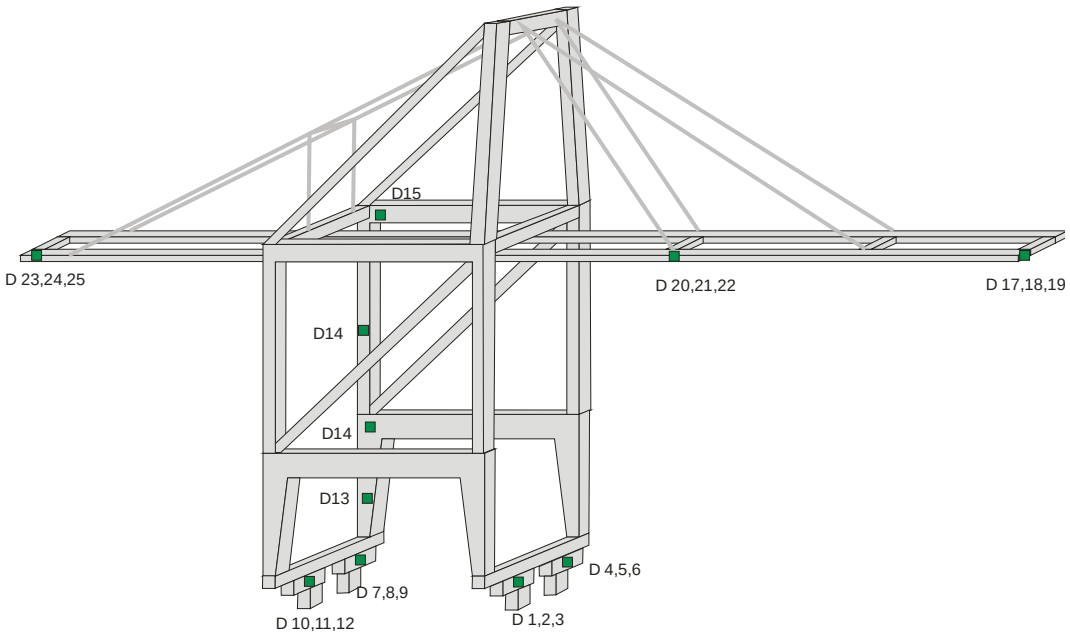

Figure 3.9: Potentiometer plan for 1/20th scale model container crane

Ninety-six channels of strain gages were applied in groups of four at the locations shown in Figure 3.10.

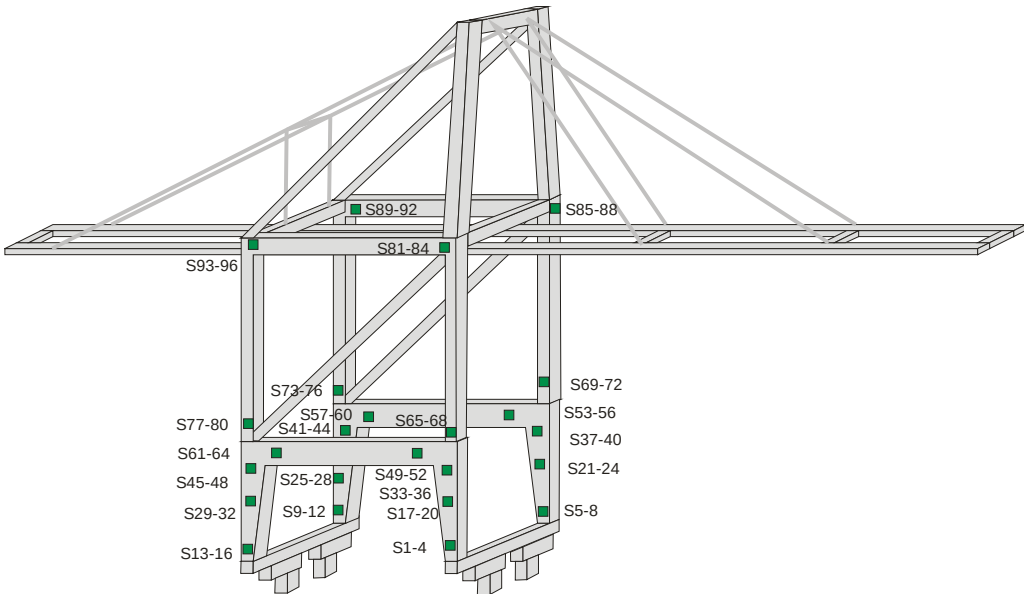

Figure 3.10: Strain gage scheme for the 1/20th scale model

Four load cells were placed where the crane comes into contact with the ground, as shown in Figure 3.11. The load cells have the ability to measure axial loads, shears and moments (SEESL, 2008).

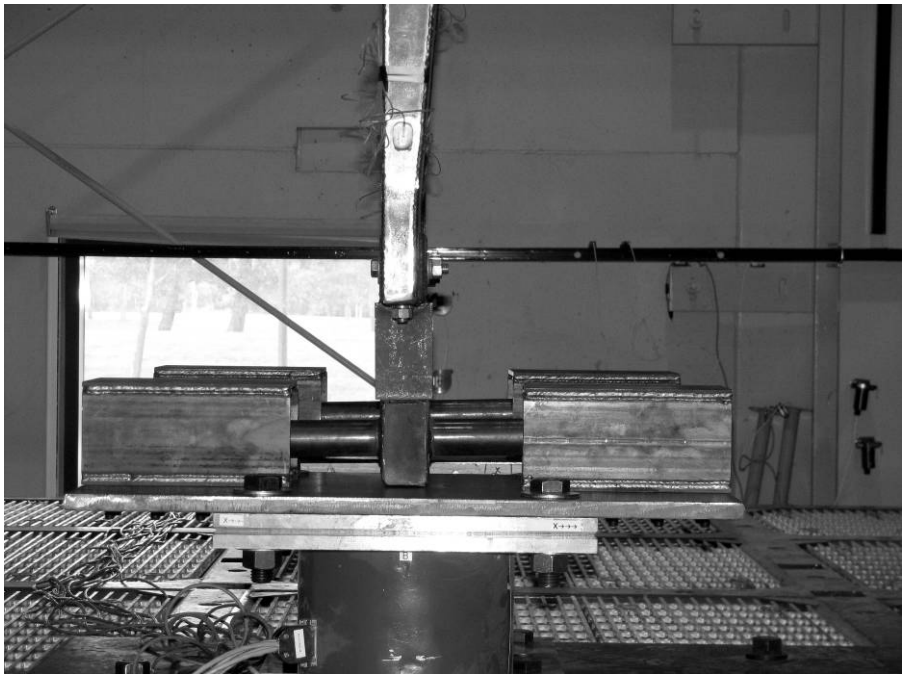

Figure 3.11: Load cell location for 1/20th scale model

3.3 Ground Motions

The selected ground motions used in the testing represent expected port ground motions. One set of relevant ground motions are the acceleration time histories recorded by the California Geologic Survey (CGS) at station 58472 for the 1989 Loma Prieta (LP) earthquake (Shakal et al, 1989). The station, created as part of the California Strong Motion Program, consists of 12 accelerometer channels positioned at various locations on and around Berth 24 at the Port of Oakland, as shown in Figure 3.12. Channels 8 and 9 are located on the wharf deck and represent the gantry travel (H2) and trolley travel (H1)

directions respectively. Channel 11 is located in the backlands, and is the only available vertical motion. Channels 8, 9 and 11 were used as the three orthogonal components of excitation in this test. To the author's knowledge, this is the only significant seismic event to be recorded on a US wharf deck at the time of experiment design.

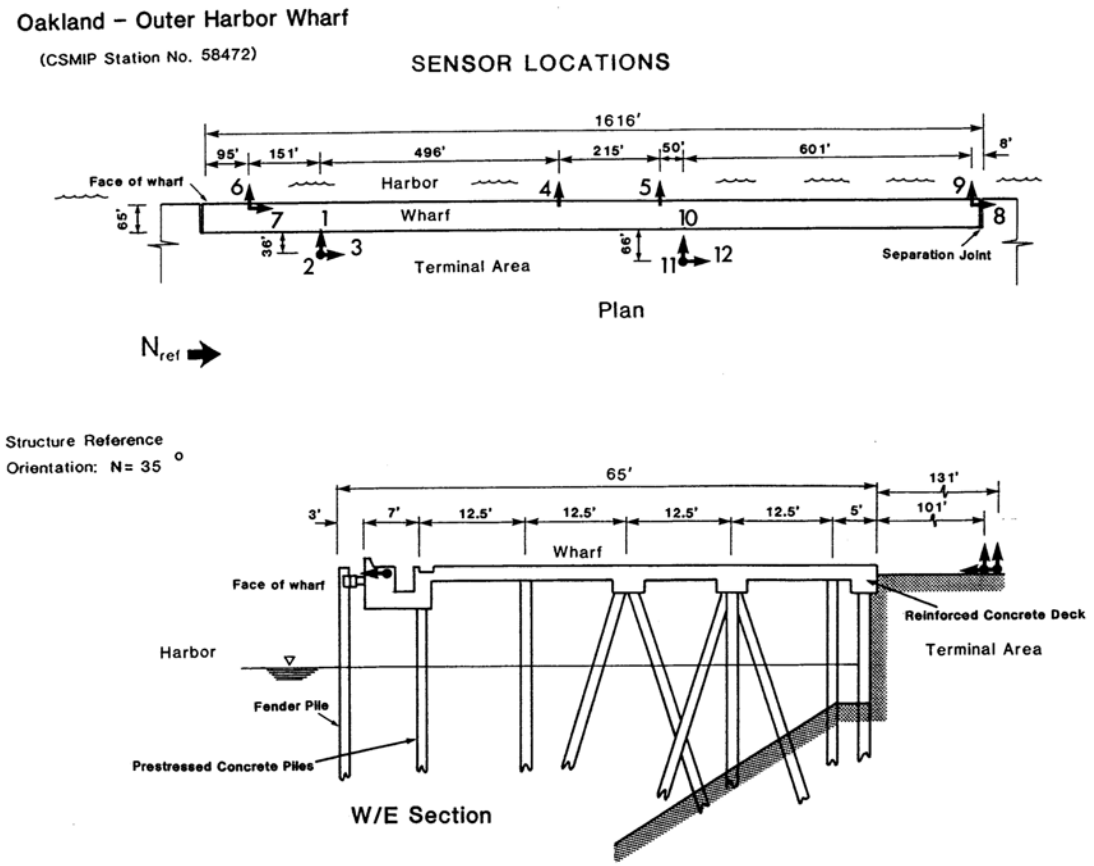

Figure 3.12: Locations of accelerometers at the Port of Oakland (Shakal et al, 1989)

Additional ground motions were chosen to represent the two design level earthquakes defined by the Port of Los Angles and the Port of Long Beach (POLA/LB). The operating-level earthquake (OLE) is an earthquake after which the structure must remain operational, and represents a 72 year return period event. The contingency level earthquake (CLE) represents a 475 year return period event. Time histories for the

POLA/LB study were chosen based on spectrum compatibility based on the overall similarity between the response spectra for the ground motion and their target design spectra for 5% damping adjusted to site-specific soil conditions (EMI, 2006). The time histories were then spectrally matched to that design spectra. For this study, two sets of ground motions at each design level were chosen. The OLE motions contain two components (H1 and H2), while the CLE motions contain three components (H1, H2 and V). Details of all five ground motions, including earthquake, station, magnitude and distance are summarized in Table 3.4.

Table 3.4: Ground motion summary

Set	*Earthquake*	*Station*	*Mag.*	*Dist. (km)*
OLE1	1979 Imperial Valley	EC CO Center FF	6.5	7.6
OLE2	1992 Erzikan	Erizikan	6.9	2.0
CLE1	1999 Duzce	Lamont 1059	7.1	4.0
CLE2	1940 Imperial Valley	El Centro	7.0	6.0
LP	1989 Loma Prieta	CGS 58472	6.9	88

The test structure was subjected to the suite of ground motions in increasing order of acceleration amplification: 1/6, 1/4, 1/2, 3/4 and 1. The time step was reduced by a factor of 4.47, as calculated from the similitude laws. The response spectra for 1.5% damping for the five earthquakes are shown in Figure 3.13. Additionally, low amplitude white noise accelerations were applied at the base of the structure for the identification of the natural frequencies, mode shapes and damping values.

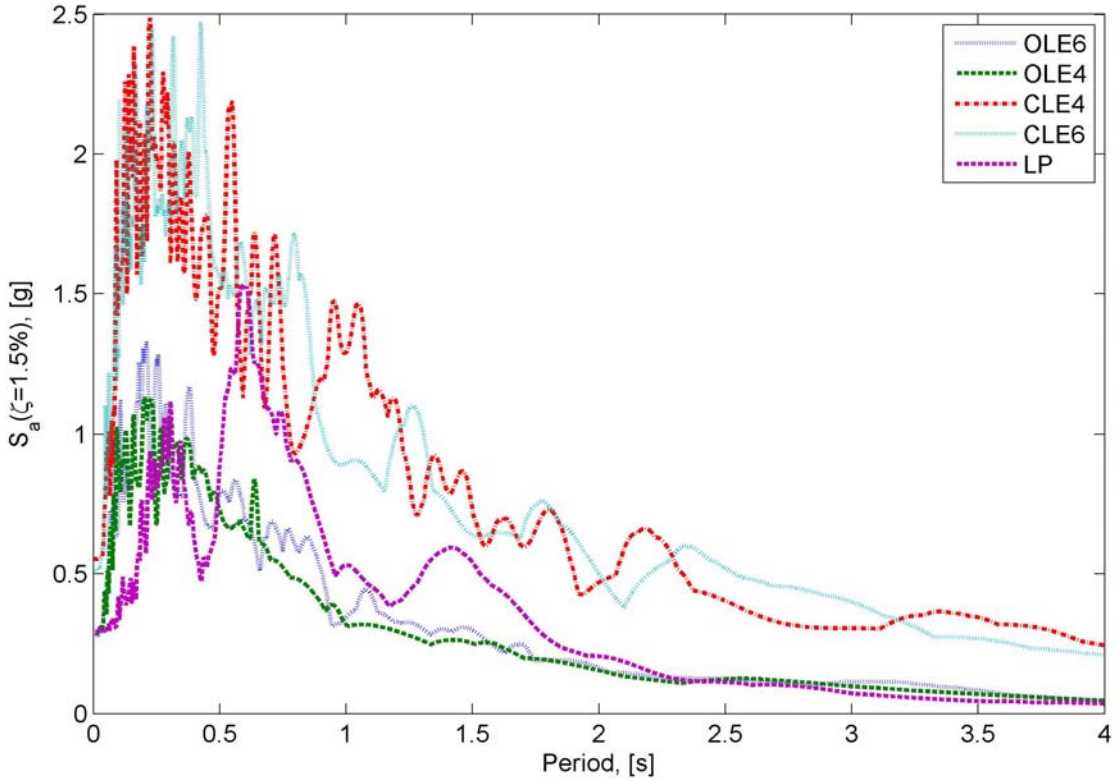

Figure 3.13: Response spectra for selected ground motions

Table 3.5: Ground motion combinations used in the 1/20th scale test

Amplitude Scale	*Earthquake*	*Components*	*PGA (in g)*		
			H1(Long)	*H2(Trnsv)*	*V*
1	White Noise	x			
	White Noise	x,y,z			
1/6	CLE4	H1	0.0922		
		H1+ .3H2	0.0922	0.0270	
		H1+ .3H2+V	0.0922	0.0270	0.0730
1/4	Loma Prieta	H1	0.1091		
		H1+ H2+V	0.1091	0.0734	0.0163
	CLE6	H1	0.1279		
		H1+ .3H2	0.1279	0.0501	
		H1+ .3H2+V	0.1279	0.0501	0.1127
1/2	OLE6	H1+ .3H2	0.1427	0.0478	
	OLE4	H1+ .3H2	0.1394	0.0399	
	Loma Prieta	H1	0.2181		
		H1+ H2+V	0.2181	0.1468	0.0326

Amplitude Scale	*Earthquake*	*Components*	*PGA (in g)*		
			H1(Long)	*H2(Trnsv)*	*V*
1/2	CLE6	H1	0.2559		
		H1+ .3H2	0.2559	0.1001	
		H1+ .3H2+V	0.2559	0.1001	0.2255
	CLE4	H1	0.2766		
		H1+ .3H2	0.2766	0.0809	
		H1+ .3H2+V	0.2766	0.0809	0.2190
		V			0.2190
3/4	OLE6	H1+ .3H2	0.2141	0.0717	
	OLE4	H1+ .3H2	0.2091	0.0598	
	Loma Prieta	H1	0.3271		
		H1+ H2+V	0.3271	0.2202	0.0489
	CLE6	H1	0.3838		
		H1	0.3838		
		H1	0.3838		
		H1+ .3H2	0.3838	0.1502	
		H1+ .3H2+V	0.3838	0.1502	0.3382
	CLE4	H1	0.4148		
		H1+ .3H2	0.4148	0.1213	
		H1+ .3H2+V	0.4148	0.1213	0.3285
		V			0.3285
1	OLE6	H1+ .3H2	0.2854	0.0956	
	OLE4	H1+ .3H2	0.2788	0.0797	
	Loma Prieta	H1	0.4362		
		H1+ H2+V	0.4362	0.2936	0.0652
	CLE6	H1	0.5117		
		H1+ .3H2	0.5117	0.2003	
		H1+ .3H2+V	0.5117	0.2003	0.4509
	CLE4	H1	0.5531		
		H1+ .3H2	0.5531	0.1618	
		H1+ .3H2+V	0.5531	0.1618	0.4380
		V			0.4380
1	CLE4	H1	0.5531		
1.5	CLE4	H1	0.8297		
2	CLE4	H1	1.1062		

CHAPTER 4

PHASE I TEST RESULTS

The goal of the Phase I test was to investigate the response of a $1/20^{th}$ scale jumbo container crane through the measurement of the elastic response and the interaction between flexural behavior and the expected uplift/derailment. Phase I testing was completed at the University at Buffalo August 4-6, 2008. The tests included 47 trials with various earthquake ground motions and low amplitude white noise inputs. The results of the Phase I test that are presented and discussed in this chapter were used to validate finite element models, and to design the Phase II tests. Information was also gathered on the influence of the various components of ground motions. Some observations from testing are also presented.

4.1 White Noise Testing

For system identification, low amplitude, uncorrelated white noise tests were performed. The white noise tests were performed at the beginning of each day of testing and after some of the large amplitude ground motions where one or more of the strain gages indicated nominal yielding of one of the cross sections. White noise was run through the system in all three orthogonal directions. The white noise tests allowed for the determination of the frequencies at which the various modes occur. Figure 4.1 shows a graph of the frequency response of the crane during one of the white noise tests. It can be seen that the primary bending mode occurs at 0.31s (2.9Hz), compared to the target value of 0.34s based on the prototype crane. The primary torsion mode occurs at .61s (1.6Hz), compared to the expected value of 0.89s. The north frame weighed more than

the south frame; which, may account for the difference in the torsion mode. Table 4.1 shows a summary of the four most important vibration modes, illustrated in Figure 4.2. The white noise tests indicated that no softening of the structure occurred throughout testing. Therefore, in none of the sections did a plastic hinge form.

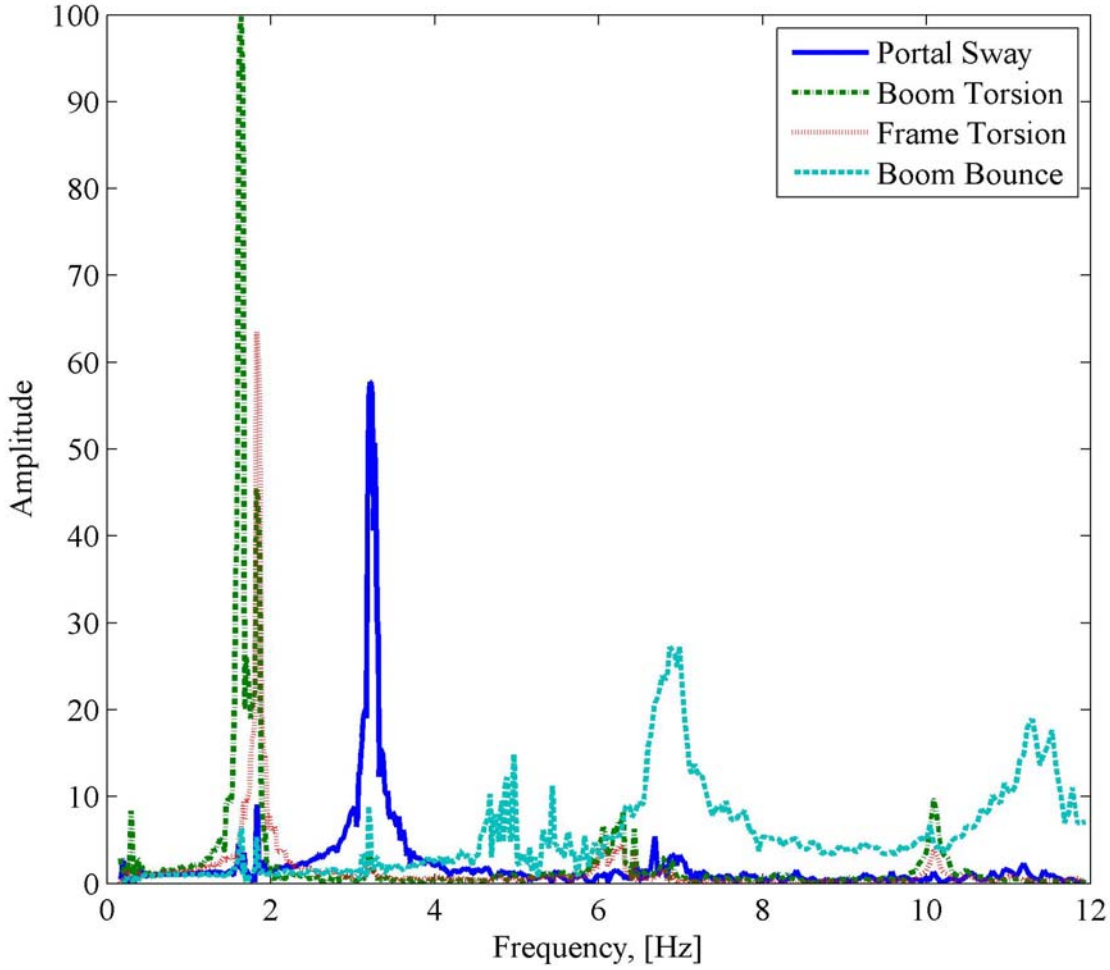

Figure 4.1: Frequency response function for white noise test

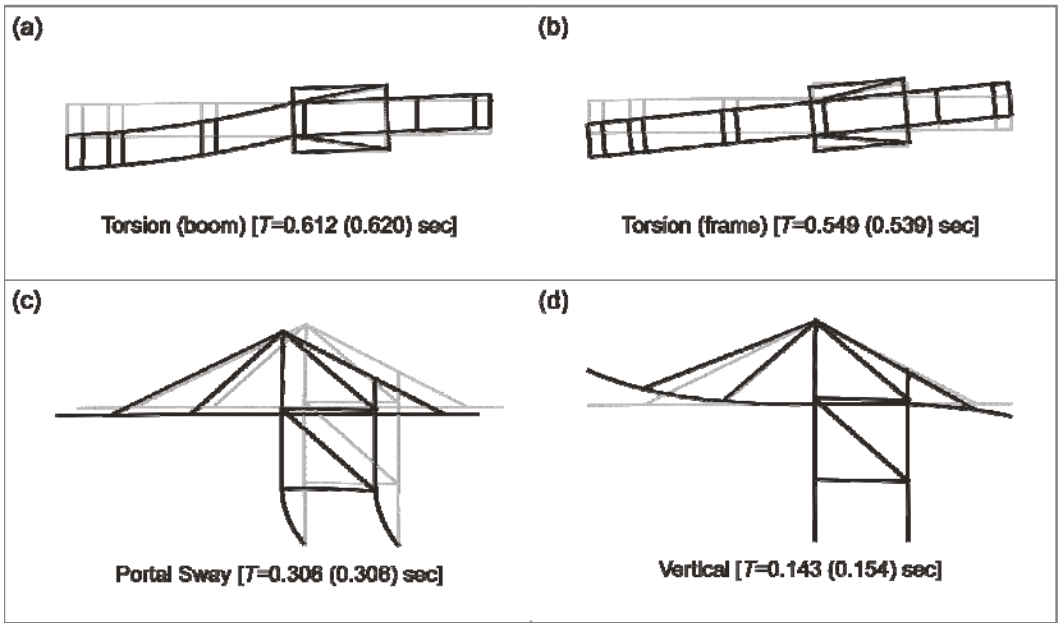

Figure 4.2: Mode shapes for 1/20th scale container crane

Table 4.1: Summary of experimental and theoretical modes

Mode	*T Exp.* [sec]	*ζ Exp.* [%]	*T FEM* [sec]
Portal sway	0.306	0.84	0.306
Torsion (boom)	0.612	2.29	0.620
Torsion (frame)	0.549	1.45	0.539
Vertical boom motion	0.143	2.33	0.154

4.2 Moment and Axial Load Measurements

The array of strain gauges was used to determine the axial loads and bending moments within the crane. The axial loads and moments are calculated from three gauges that define a plane. At each location, four different values for the axial load and bending moment can be determined. Since the values for the axial load and moment are consistent enough in the locations where there is not a clearly broken gauge, it is reasonable to average the measured values. Figure 4.3 shows an example of the force

and bending moments at one of the locations. Because of the consistent results, the remainder of the axial loads and moments that are presented here are the averages of the four values calculated at each point.

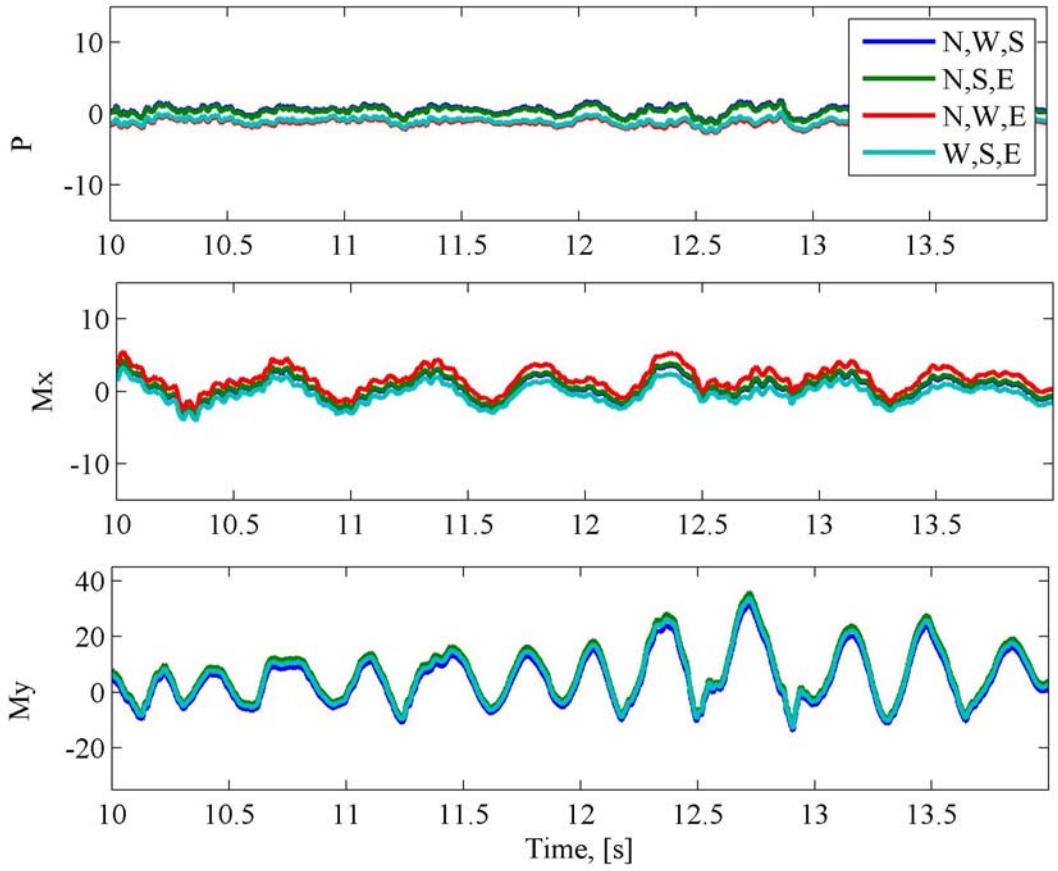

Figure 4.3: Time history for NE top of portal frame for CLE4, triaxial excitation

4.3 Uplift

The videos of the crane's legs clearly showed instances when the legs lifted off the ground. Additionally, the displacement, acceleration, and axial loads indicated uplift occurred.

4.3.1 Observations

Uplift occurred during the larger amplitude ground motions. Adding components to the ground motion had different effects on the uplift. In general, adding a second horizontal component to the ground motion resulted in a smaller maximum uplift. Adding a vertical component led to larger uplift values than both a single horizontal component and two horizontal components. Additionally, more uplift events occurred when a vertical component was added.

4.3.2 Measurements at the Legs

During testing, the displacements of the legs were measured in two different ways. First, string potentiometers were used to measure the absolute horizontal displacements in both the lateral and transverse directions. Additionally, extensometers were used to measure the relative vertical displacements. The second measurement system was the Krypton system, which uses LEDs to measure the relative displacements. The acceleration at the legs was measured using three accelerometers at each location, which allowed for the accelerations to be measured in the three orthogonal directions to fully characterize the accelerations in the structure. Axial loads in the legs were determined from the strain gauges as described in Section 4.2.

In instances when the vertical measurement from the extensometers was greater than 0.01inches, two other phenomena occurred. First, the axial load reached a minimum value and remained constant at that minimum value while the leg remained in the air. This indicates that the axial load was removed when the leg uplifted, which is expected. While the leg was in the air, the axial load increased in the legs that were still on the

ground, indicating a shift in the weight, which is also expected. Second, when the vertical displacement reaches zero again after the leg uplifted, there is an acceleration spike, indicating that an impact occurred. An impact would be expected when the leg hits the ground after uplift. Figure 4.4 shows an example of these phenomena for a full scale CLE4 triaxial excitation. The combination of these phenomena indicates that uplift occurred. In instances when uplift does not occur, there is a change in the vertical measurements. This is a rocking motion that occurs due to the fact that the bottoms of the feet of the crane are not a perfectly flat surface.

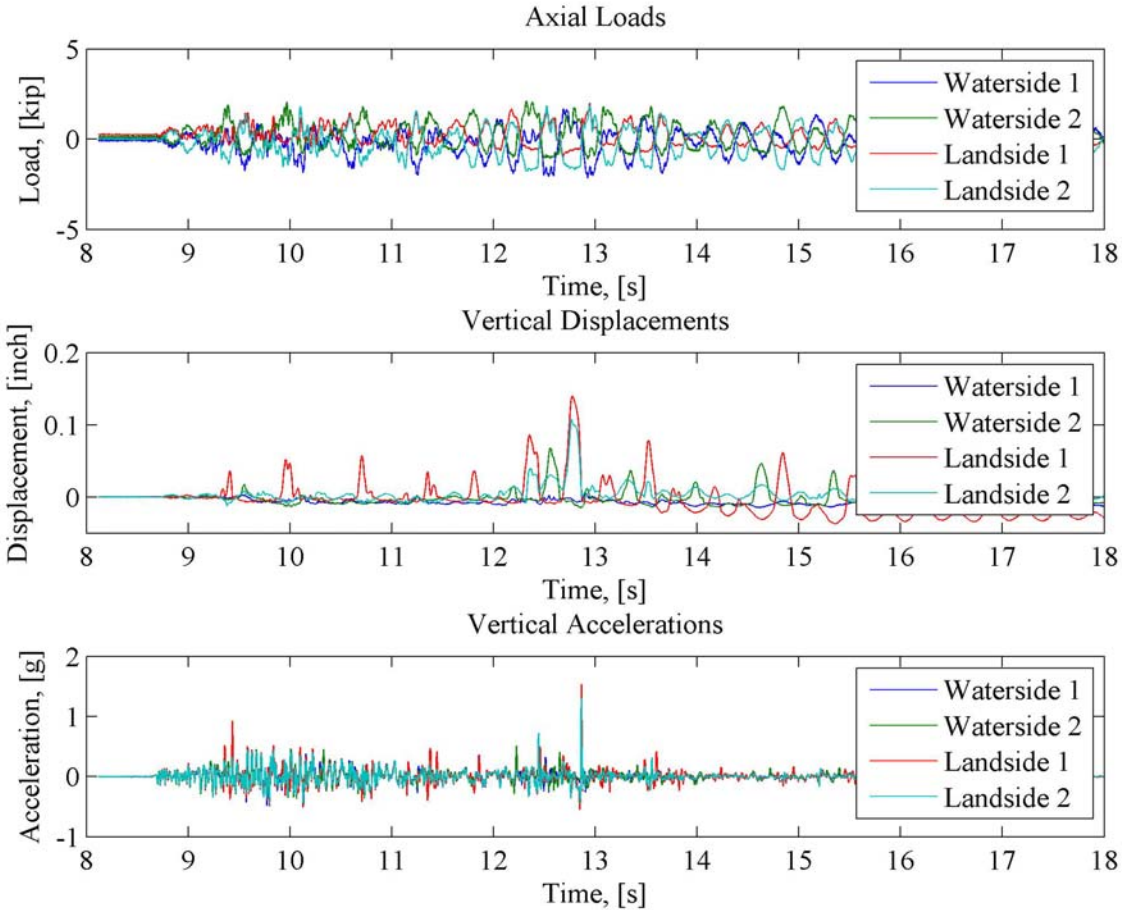

Figure 4.4: Time history of load, displacement and acceleration at the base of the 1/20th scale model under a CLE4 triaxial excitation

4.3.3 Effect of Uplift on Horizontal Displacements

The horizontal displacements of the legs were affected by the amount of load on the legs as well as uplift. When the weight on the legs was reduced, the friction holding the crane legs in place was also reduced, and the legs slid along the plates on which they rested. When the friction was reduced, the legs moved inward in both the x and y directions, resulting in a residual inward bowing of the legs. Additionally, when the legs uplifted, the legs moved without any friction. Therefore, the horizontal movements of the legs were much larger in instances where uplift occurred than instances where uplift did not occur. In all cases, the crane had a residual displacement in the landward direction.

4.3.4 Effect of Acceleration

Figure 4.5 shows a plot of the peak acceleration at the boom vs. the peak base acceleration (PBA) of the table. The individual data points show whether or not uplift occurred. Once the PBA was above 0.35 g, uplift occurred 83% of the time. And, when the PBA reached 0.4 g, uplift occurred 100% of the time. These results indicate a strong correlation between the PBA and uplift. When the acceleration at the boom level was greater than 0.35 g uplift occurred 90% of the time. And, when the acceleration at the boom level was 0.4 g uplift occurred every time. According to a tipping analysis, an acceleration of 0.4 at the center of mass would cause uplift to occur. The measurement of the acceleration at the boom is measurement closest to the center of mass. So, an acceleration of 0.4 g at the boom would be expected to cause an uplift event. In the experiment, an acceleration of 0.35 g caused uplift. This would indicate that the center of mass calculated was slightly different than the actual center of mass.

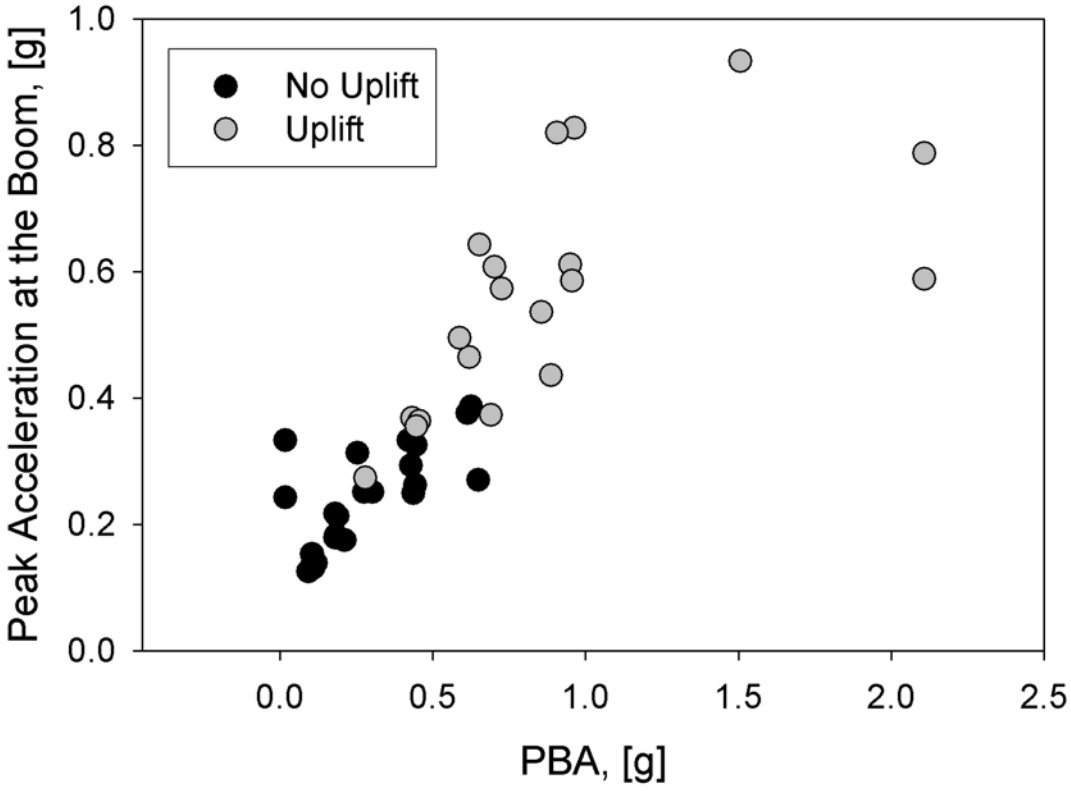

Figure 4.5: Uplift as a function of the peak base acceleration (PBA) and the peak acceleration at the boom

The peak ground acceleration has a significant effect on how high the crane uplifts. Figure 4.6 shows a graph of the maximum uplift versus the PBA. Uplift was defined as when the vertical displacement exceeded 0.01 inches, so only those points were plotted.

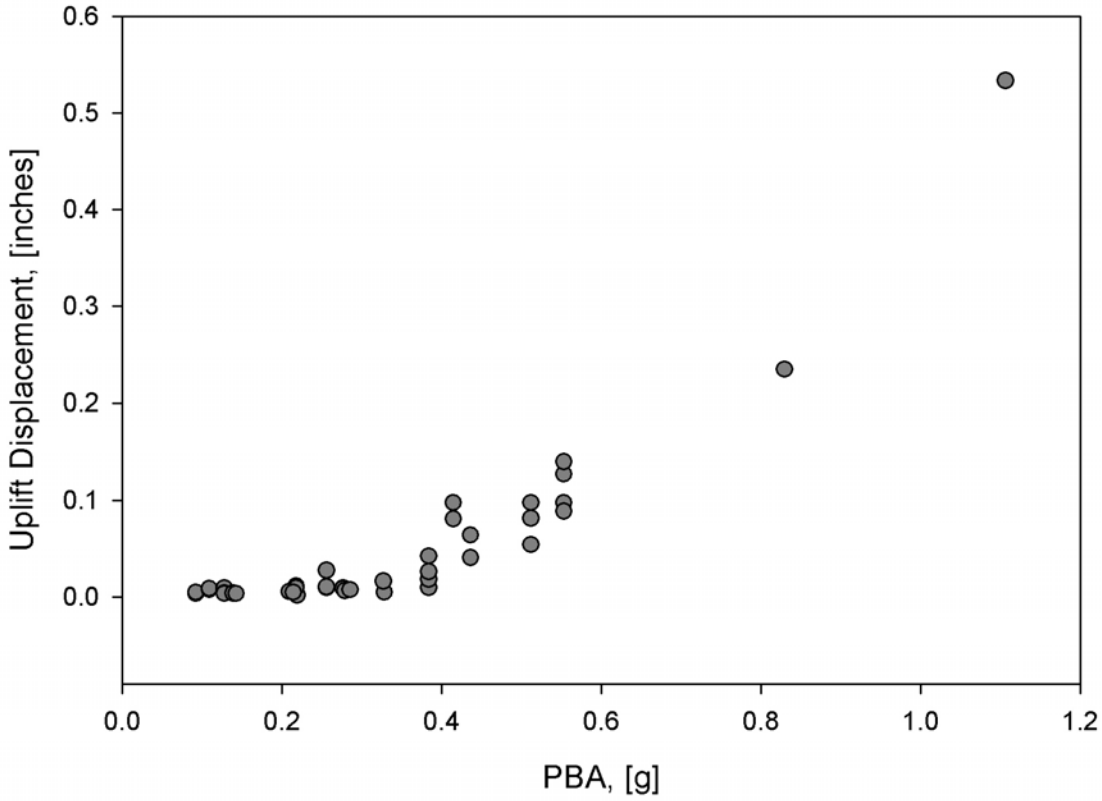

Figure 4.6: Uplift as a function of the peak base acceleration (PBA)

4.4 Drift

The drift in the crane can be measured in two different places, the top of the portal frame and the top of the O-frame. The drift at the top of the portal frame provides information about how much of the deformation in the primary bending mode occurs in the portal frame. The drift at the top of the O-frame provides information about how much deformation occurs in the whole frame structure. The inter-story drift between the top of the portal frame and the O-frame provides information about how much deformation occurs in the portal frame vs. the members above the portal frame.

Figure 4.7 shows the maximum drift in the portal frame vs. the spectral acceleration at 0.31 seconds. The data shows that the maximum drift increases as the spectral acceleration at the portal sway period of the crane increases. From 0 to about 0.5 g, the increase in percent drift is gradual. There is a sharp increase in the percent drift with small increases in acceleration from 0.5 to 1 g. In addition, the trend indicates small increases in percent drift for accelerations greater than 1 g. Overall, the trend indicates that there are larger drift levels as the spectral acceleration at 0.31g increases.

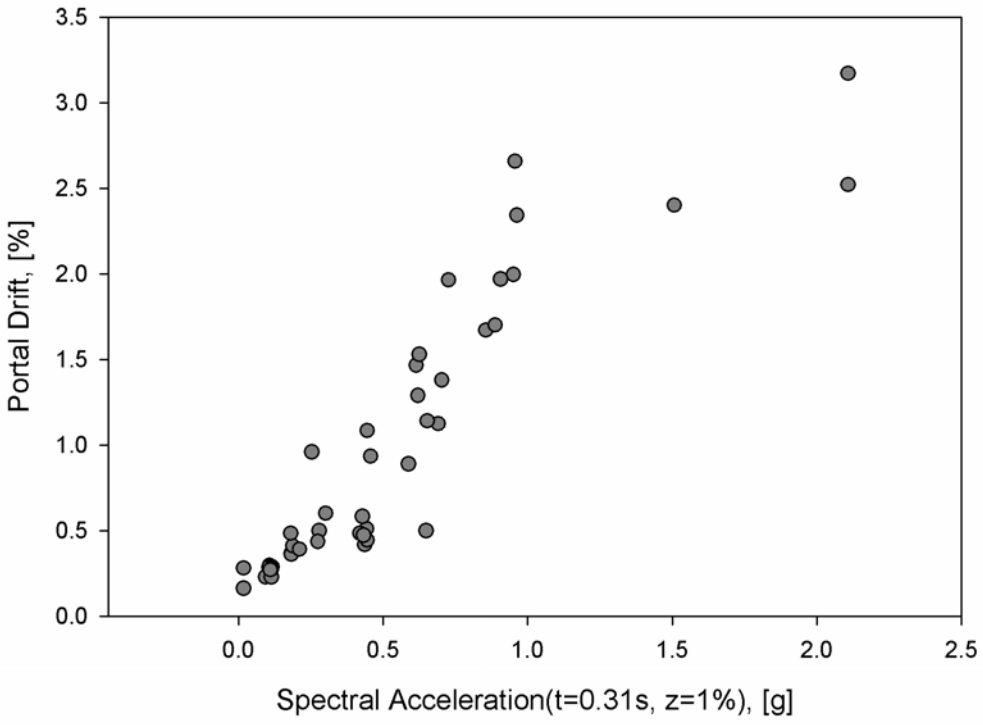

Figure 4.7: Maximum drift in portal frame vs. spectral acceleration at 0.31 seconds

Figure 4.8 shows the residual drift in the portal frame vs. the spectral acceleration at 0.31 seconds. For spectral accelerations above 0.7 g, there are residual drifts of 0.4% and above. Below 0.7g, there is no clear trend to the residual drifts. For the same spectral acceleration, there is a wide range of residual drifts.

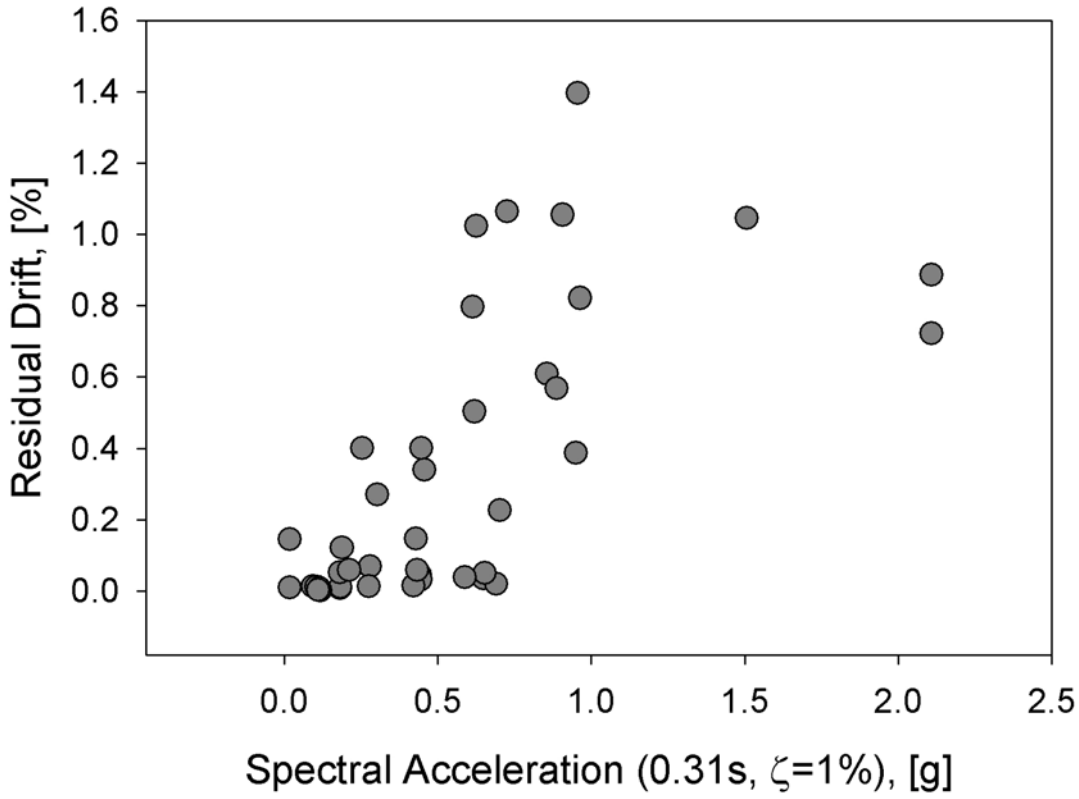

Figure 4.8: Residual drift vs. spectral acceleration at 0.31 seconds

The percent drift in the portal frame is an order of magnitude larger than the percent inter-story drift between the top of the O-frame and the top of the portal frame. Figure 4.9 shows an example of the differences in the time histories between the portal frame and the inter-story drift. These results indicate that the majority of the deformation occurs within the portal frame. These results agree with what the analysis indicated.

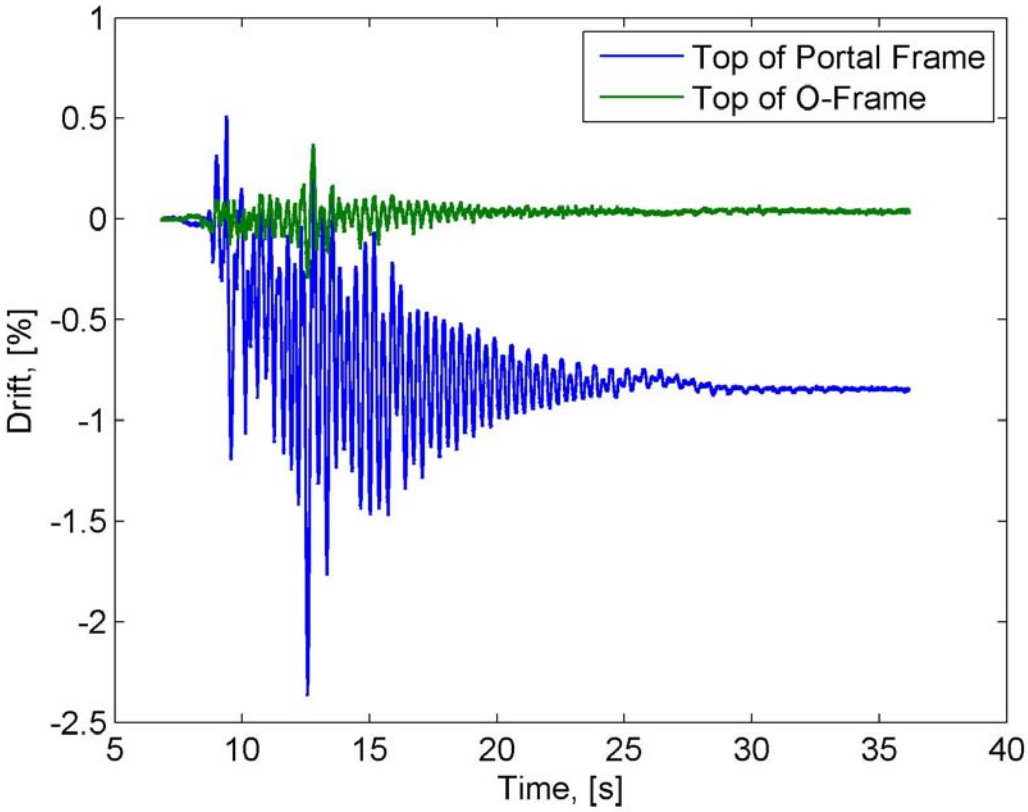

Figure 4.9: Time history of the percent drift at portal level and interstory drift for second story of the 1:20 scale model under a CLE4 triaxial excitation

4.5 Twisting

One of the modes of response of the crane is a torsion mode. One measure of this response is the angle of twist in the boom. Using a small angle assumption, the angle of twist can be calculated by determining the difference between the displacements at two locations on the boom and then dividing by the distance between them. It can be seen in Figure 4.10 that there is a linear relationship between the angle of twist and the PBA. As the PBA increases, so does the angle of twist. The PBA is a good predictor of how much twisting is expected in the crane response.

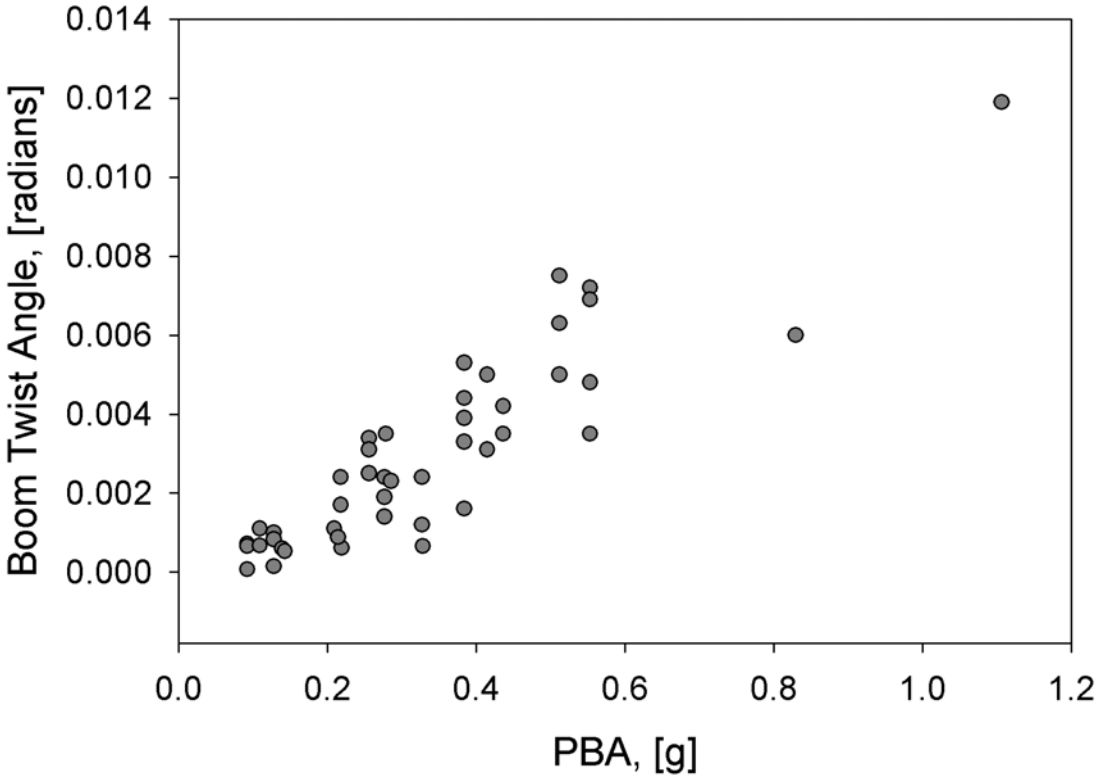

Figure 4.10: Angle of twist of the boom vs. PBA

4.6 Moments

Moments were recorded in several places around the portal frame based on the readings from the strain gauges. There are several trends to notice about the moments in the crane structure, including the value and location of the maximum moment, and the value and location of the member that experienced the highest percentage of its moment capacity. Each of these trends will be further discussed in this section.

All but seven of the runs in the experiment had the top of the waterside leg as having the highest maximum moment. In the other seven runs, the maximum moment was experienced in the top of a landside leg. The cranes are designed such that the waterside leg has a higher moment capacity than the landside legs. The data from the

majority of the tests supports the concept of designing for the highest moments in the waterside legs. However, there are a significant number of cases where the landside legs would experience the highest moments, so it would be prudent to take this into consideration when designing cranes in earthquake prone areas.

There is a clear relationship between the maximum moment and the spectral acceleration at 0.31 seconds, as can be seen in Figure 4.11. The maximum moment increases with increasing spectral acceleration until 1 g. After the spectral acceleration reaches 1 g, the maximum moment stays the same as the spectral acceleration increases. This trend would indicate that the boundary conditions of the crane would only allow for a certain amount of force to be transferred to the crane during an earthquake, thus the maximum moment could not exceed a particular value.

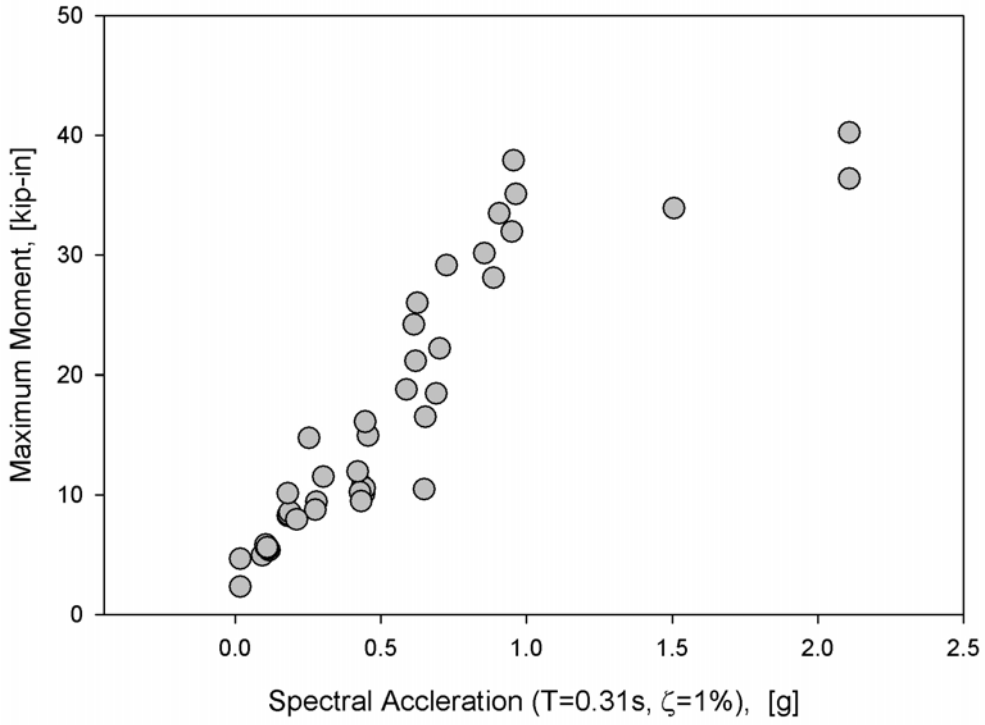

Figure 4.11: Maximum moment versus the spectral acceleration at 0.31 seconds

Another trend to note is the location of the members that experienced the largest moment demand as a percentage of their moment capacity. In all of the tests, the members that had the largest percentage of their moment capacity used were the waterside portal beam or the bottom of the landside leg. When the spectral acceleration exceeded 0.6 g, most of the test data shows that the bottom of the landside leg utilized more of the moment capacity than the other members. For lower values of spectral acceleration, the waterside portal beam had a higher moment demand, as a function of its capacity. These trends can be seen in Figure 4.12.

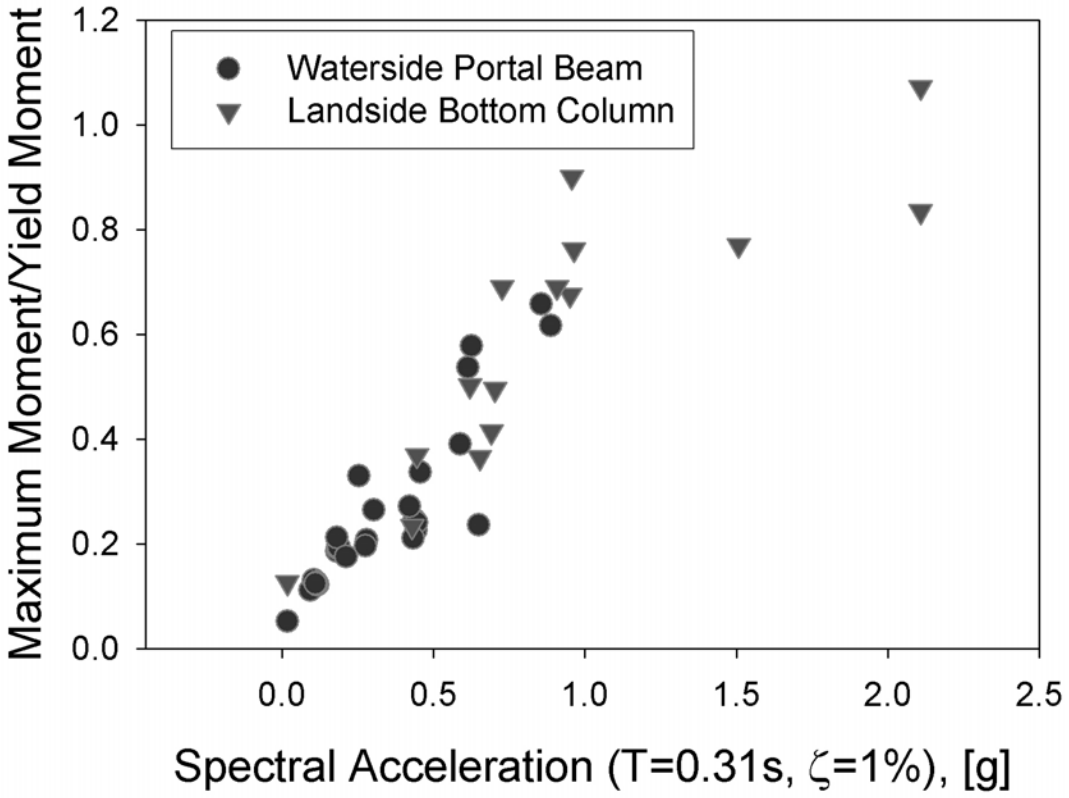

Figure 4.12: Maximum ratio of moment demand to yield moment versus spectral acceleration at 0.31 seconds

There is a clear relationship between the ratio of the maximum moment to the yield moment and the spectral acceleration at 0.31 seconds, as can be seen in Figure 4.12. The ratio increases with increasing spectral acceleration until 1 g. After the spectral acceleration reaches 1 g, the ratio stays the same as the spectral acceleration increases. This trend would indicate that the boundary conditions of the crane would only allow for a certain level of force to be transferred to the crane during an earthquake.

The moments and ratio of moments to yield moments are best predicted using the spectral acceleration at 0.31 seconds, the natural frequency of the primary bending mode. There is less scatter in the data when using this intensity measure instead of the PBA.

4.7 Effects of Boundary Conditions

Three different boundary conditions were used during testing. The first is the use of steel feet on the steel plate. The second is a friction pad adhered to the bottom of the feet on the steel plate. The third is two friction pads glued together between the feet and plates. As expected, the resulting response of the crane varied with the boundary conditions. The CLE6 ground motion with a single horizontal component in the direction along the boom was applied to the specimen with all three boundary conditions. All comparisons between the various boundary conditions were performed utilizing the results for these three runs.

4.7.1 Observations

The steel on steel boundary condition revealed too much sliding and not enough of the uplift response. Therefore, a second boundary condition of a friction disk adhered

to the bottom of the feet was used. There was less sliding and an improvement in the uplift response. However, several tests later, it was observed that the friction disk adhesive had sheared, while the friction disk stayed at rest against the steel base plate. To remedy the problem, two friction disks were adhered together, and allowed to fully cure. The 3/4 amplitude CLE6 was rerun, and the same gravity-settling (bowing in) phenomenon that had occurred in many earlier runs was observed. The next run, 3/4 amplitude CLE4h1, showed a much-improved uplift response. Nearly 0.1 inches uplift of the landside wheels caused nearly 2in. of longitudinal displacement towards landside under longitudinal excitation. Larger shears and moments were visible with the instrumentation, evidence of better transfer from the base to the structure.

4.7.3 Data

Table 4.2 summarizes the results of the various tests. The boundary conditions had a noticeable effect on the response of the crane. The following paragraphs discuss the results in more detail.

The maximum moment in the crane occurred at the top of a waterside leg for all boundary conditions. However, the value of the maximum moment was dependant upon the boundary conditions. The steel-on-steel boundary condition gave the lowest moment of 10.45 kip-inches, and as the number of friction surfaces increase, so did the maximum moment. The maximum moment with one friction surface was 24.19 kip-inches. The maximum moment for two friction surfaces was 26.00 kip-inches. These results suggest that more of the force of the earthquake was transferred into the crane with the addition of a friction surface. However, the difference between two friction pads and one friction

pad was about 13% of the difference between one friction pad and none. The boundary condition consisting of two friction pads was the best for transferring the energy of the earthquake into the crane.

Table 4.2: Comparison of results from different boundary conditions

	Steel on Steel	*Single Friction Pad*	*Two Friction Pads*
Max moment (kip-in)	10.4	24.2	26.0
Location Max Moment	Column top, waterside	Column top, waterside	Column top, waterside
Max Moment/ yield moment	0.24	0.54	0.58
Maximum % drift	0.50	1.47	1.53
Residual % drift	0.04	0.80	1.02
Maximum x base motion	0.52	0.41	0.63
Maximum y base motion	0.04	0.02	0.10
Maximum x boom accel	0.27	0.38	0.39
Maximum y boom accel	0.31	0.27	1.02

The maximum proportion of moment experienced to yield moment occurred in the waterside of the portal beam. As with the maximum moments, the proportion of moment experienced to yield moment increased with the addition of friction surfaces. The maximum proportion of moment to yield moment was 0.2365 for steel on steel, 0.5369 for one friction surface and 0.5782 for two friction surfaces. These results suggest that more of the energy and force of the earthquake was transferred to the crane as the number of friction pads increased. However, the difference between two friction pads and one friction pad was about 14% of the difference between one friction pad and none. The boundary condition consisting of two friction pads was the best for transferring the energy of the earthquake into the crane.

The maximum percent drift increases with each additional friction pad. The amount of drift is three times the steel on steel drift when a single friction pad is added. When the second friction layer is added, the amount of drift is increased by a further

4.3%. These results indicate that adding friction layers helps to transmit more of the energy of the earthquake into the primary bending mode response of the crane. Therefore, the boundary condition with two friction layers was most effective for transferring the energy of the earthquake into the crane.

The residual drift increases with each additional friction pad. The amount of drift is nearly 23 times the steel-on-steel drift when a single friction pad is added. When the second friction layer is added, the amount of drift is increased by 29%. These results indicate that adding friction layers helps to transmit more of the energy of the earthquake into the primary bending mode response of the crane. Therefore, the boundary condition with two friction layers was most effective for transferring the energy of the earthquake into the crane.

The horizontal motions at the base were influenced by the boundary conditions. When a friction disk was added to the crane, the amount of relative motion in both horizontal directions was reduced. This result indicates that the friction disk provided a higher friction and prevented the crane from sliding as much as with the steel-steel boundary condition. When the second friction surface was added, uplift occurred and the amount of motion in the horizontal directions was higher than the previous two tests. Because uplift occurred when two friction surfaces were present, but not with the other two boundary conditions, the two friction boundary condition was the most effective for transferring the input from the earthquake into the crane.

The acceleration at the boom level in the horizontal directions depended on the boundary conditions. The acceleration at the boom level in the direction along the boom is particularly important to the response, because the uplift is best predicted by this

response quantity. There is a 39% increase in the acceleration along the boom at the boom level when there is one friction layer versus none. There is an additional 3% increase in the maximum acceleration at the boom level when a second friction layer is added. These results indicate that uplift is more likely to occur when a friction layer is added than when there is a steel-on-steel boundary condition. Additionally, if an isolation system is added that reduces the acceleration at the boom level, uplift can be prevented. The acceleration in the direction perpendicular to the boom followed a different trend. When one friction layer was used, the maximum acceleration was less than that of the case when the steel-on-steel boundary condition was used. But, when a second friction layer is used, there is a 235% increase over the steel-on-steel case. These results indicate that the two friction layers allowed for the torsion mode of the crane to engage.

All of the measures of the response of the crane indicate that the two friction surface boundary condition was the most effective boundary condition of those utilized at transferring the input of the earthquake into the crane. The boundary conditions influenced the moments the crane experienced. The maximum moment of the crane saturates above an amplitude scale of 1 because the boundary condition cannot transfer any higher force into the crane than it could at an amplitude scale of 1.

4.8 Effects of Amplitude

The CLE4 ground motion with a single horizontal component in the along boom direction was run at six different amplitudes, 1/6, 1/2, 3/4, 1, 1.5 and 2. This section explains the differences in the response due to the changes in the amplitude of excitation.

4.8.1 Observations

The response of the crane to the first two CLE4 ground motions showed little longitudinal and transverse motion and no uplift. At 3/4 scale, the crane response to the CLE4 ground motion exhibited significant uplift/longitudinal motion. As expected, the full scale CLE4 series showed even more significant uplift events. Maximum strains were about 1000 microstrain. Several interspersed white noise tests confirmed that no yielding had occurred. A 1.5 scaled CLE4 was used, with results similar to a full-scale (1) CLE4 in terms of strain readings, although uplift and longitudinal motion was higher with 1.5. Another test was performed with twice the magnitude of CLE4. This time, uplift reached >0.5in, with base displacement of about 4in. Peak portal drift crested at 3%, which caused several landside strain gages, predominantly at the bottom of the lower legs, to show nominal yielding. Residual drift, however, was about 1%, as it has been in many previous tests. The significant base movement caused the crane trucks to move off the friction enhancers.

4.8.2 Data

Table 4.3 summarizes the results of the various tests. The amplitude scaling had a noticeable effect on the response of the crane. The following paragraphs discuss the results in more detail.

Table 4.3: Comparison of results of different amplitude levels

Acceleration Amplitude	1/6	1/2	3/4	1	1.5	2
Max. Moment (kip-in)	4.92	10.1	22.2	36.3	33.9	40.2
Location	TWL	TWL	TWL	TWL	TWL	TWL
Max Moment/Yield	0.11	0.23	0.49	0.83	0.77	1.07
Location	PBW	PBW	BLL	BLL	BLL	BLL
Max % drift	0.23	0.51	1.3581	2.52	2.40	3.17
Uplift Height, inches	0.003	0.009	0.097	0.098	0.24	0.53

The location of the maximum moment in the crane was independent of the amplitude scaling. At every amplitude scale, the location of the maximum moment occurred at the top of the waterside leg. However, the value of the maximum moment depended on the amplitude scale. With the exception of the 1.5 scale run, the value of the maximum moment increases with amplitude. This is expected, because as more force is put into the crane, larger moments will be generated. The moment for the 1.5 scale amplitude was lower than the full (1) scale test. There are several possibilities for why this would be. One explanation is that the uplift occurred at just the right time during the earthquake that it acted like an isolator, reducing the magnitude of the maximum moment. In general, however, the larger the amplitude of the ground motion, the larger the maximum moment the crane experienced.

The location of the maximum ratio of moment to yield moment was dependant upon the amplitude of the ground motion. For the 1/6 and 1/2 amplitudes, the maximum ratio of the moment to yield moment was in the waterside of a portal beam. For amplitudes of 1 and greater, the maximum ratio of moment to yield moment occurred in the bottom of the landside leg. At these amplitudes, uplift of the landside legs occurs, which may have an influence on the location of the most stressed member. With the

exception of the 1.5 scale amplitude, the value of the maximum ratio of moment to yield moment increases with increasing amplitude. This is expected, because the same trend occurred with the maximum moments, and these two quantities should experience identical trends. It should be noted that during the 2 amplitude test, the ratio of moment to yield moment was greater than one, indicating that yielding occurred in the bottom of one of the landside legs.

Ground motion amplitude has an effect on the drift levels experienced by the crane in the portal frame. With the exception of the 1.5 scale test, the maximum drift increased with increasing amplitude of ground motion. This is expected, because as more force and energy is put into the crane, more deformations will occur.

The amplitude of the ground motion has a strong effect on the amount of uplift. At 1/6 and 1/2 amplitudes, the crane does not uplift. However, at 3/4 amplitude and above, uplift does occur. Additionally, the height of uplift increases with increasing amplitude. This is expected, because the force that generates the overturning moment is larger, with larger accelerations. The larger the overturning force, the higher the crane will uplift.

The amplitude of the ground motion influences the maximum moments, the maximum ratio of moment to yield moment, the maximum percent drift experienced in the portal frame, and the amount of uplift. As expected, as the amplitudes increased, these responses increased as well.

4.9 Effects of Components of Excitation

The effects of the different components of ground motions are important to understand in order to determine what is most important for analysis and design. In order to determine which components have the largest effect on the response, the model crane is excited using different components of ground motions. The results are then compared to assess their importance to the overall response.

4.9.1 Effects of transverse excitation

In order to assess the effect of the addition of a transverse excitation, tests were run that have a longitudinal only excitation and a longitudinal plus transverse excitation. The outcomes were then compared to assess the effect of including the transverse excitation. Table 4.4 shows a comparison of the drift levels when a longitudinal only excitation was used and when both the longitudinal and transverse excitations were used. It can be seen for ground motions with a spectral acceleration from 0.42 to 0.44 g, there was a significant decrease in the drift. All of the other ground motions have small increases in drift. Because the addition of a transverse excitation either decreased the response, or only caused a small increase, it would be sufficient to consider only the longitudinal excitation. Considering only the longitudinal excitation reduces the computational effort when doing finite element modeling.

Table 4.4: Effects of transverse ground motion on drift

Ground Motion	*Spectral Acceleration, g*	*H1 Excitation Drift, %*	*H1+H2 Excitation Drift, %*	*% Difference*
CLE4	0.44	0.51	0.42	-18.1
CLE4	0.95	2.52	2.66	5.40
CLE6	0.18	0.37	0.36	-1.12
CLE6	0.42	0.58	0.48	-16.8
CLE6	0.87	1.67	1.70	1.83

4.9.2 Effects of Vertical Excitation

In order to assess the effects of vertical excitation, ground motions were run with a longitudinal, horizontal and vertical ground motions. Table 4.5 shows a comparison of the drift levels between the longitudinal only and the triaxial excitations. There is no consistent trend about what happens when the vertical ground motion is included compared to when it is not. For all of the ground motions, there are larger differences between the ground motions when the vertical component is included versus when it is not; however, there is not a consistent trend about whether the response is increased or decreased. Additionally, uplift does not influence whether the response is increased or decreased. It would be prudent to run analyses with and without vertical excitation in order to capture the most extreme cases for the response of the structure.

Another question to be addressed is if the presence of the vertical excitation influences how much the structure uplifts. Table 4.6 shows a comparison of the amount of uplift between the longitudinal only and the triaxial excitations. For five of the nine ground motions, there was an increase in the vertical displacement. For one of the CLE ground motions, there was not only an increase in the vertical displacement, but the structure went from not uplifting with a longitudinal only excitation to uplifting with a

triaxial excitation. For the two lowest amplitude Loma Prieta excitations, the addition of the vertical component actually decreases the amount of uplift.

Table 4.5: Effects of vertical excitation on drift

Ground Motion	*Spectral Acceleration, g*	*H1 Excitation Drift, %*	*Triaxial Excitation Drift,%*	*% Difference*	*Uplift*
CLE4	0.44	0.51	0.44	-12.8	no
CLE4	0.96	2.52	2.34	-7.09	yes
CLE6	0.19	0.37	0.41	12.5	no
CLE6	0.43	0.58	0.47	-18.9	no
CLE6	0.88	1.67	1.97	17.8	yes
LP	0.12	0.29	0.23	-20.4	no
LP	0.28	0.50	0.44	-12.6	yes
LP	0.45	0.93	1.08	15.9	yes
LP	0.60	1.29	0.89	-31.1	yes

Table 4.6: Effects of vertical excitation on vertical displacement

Ground Motion	*Spectral Acceleration, g*	*H1 Excitation Drift, %*	*Triaxial Excitation Drift,%*	*% Difference*
CLE4	0.44	0.009	0.009	0
CLE4	0.96	0.098	0.14	43.5
CLE6	0.19	0.008	0.01	20.3
CLE6	0.43	0.01	0.03	178.8
CLE6	0.88	0.08	0.10	19.8
LP	0.12	0.004	0.004	-10.3
LP	0.28	0.01	0.009	-19.1
LP	0.45	0.02	0.02	0
LP	0.60	0.04	0.06	57.4

4.10 Conclusions

The most important mode of the crane is the portal sway mode, accounting for as much as 90% of the response. The primary bending mode occurs at 0.31s, which is in good agreement with the theoretical value based on the finite element analysis. The value of damping, calculated using the half power bandwidth, is 0.86%.

The crane model used in the experiment will uplift at a PGA of 0.35g. Uplift occurred at this level 83% of the time. The 0.35g level corresponds well to the theoretical uplift value. The drift levels in the portal frame are at least an order of magnitude larger than the drift levels of the inter-story drift between the O-frame and portal fame. These results indicate that most of the deformation occurs within the portal frame. There is a linear relationship between the PGA and the twist angle of the boom. Indicating that the larger the excitation, the larger the torsion response. However, there is no increase in the torsion response when considering the addition of the second horizontal excitation. The best predictor of the level of drift and moments experienced in the crane is the spectral acceleration at 0.31s, the natural period of the primary bending mode of the structure. This finding is not surprising, considering that 90% of the structural response is in that primary bending mode.

Boundary conditions are very important in any model. The boundary conditions influence the response of the structure. Three different boundary conditions were used in this test, and the boundary condition with two friction surfaces provided the best force transfer between the shake table and the structure. When the two friction surface was used, the crane started to slide and uplift at the accelerations predicted by a simple tipping analysis. There is an important limitation to the boundary condition; the amount of energy transferred to the structure is limited. At excitations above 1g, there is no increase in response, as the excitation increases. This is reasonable for the prototype structure, because once the structure derails, it can slide, as the model can.

CHAPTER 5

SIMPLIFICATION OF THE MODEL

The results of the first phase of testing indicated that it was feasible to simplify the model specimen for ease of construction and testing in the laboratory. In particular, based on preliminary analysis, the top structure, including the A-frame and the boom, do not have much influence on the overall behavior of the structure. Finite element models aimed at determining what simplifications can be made to the specimen while preserving the dynamic response are discussed in this chapter. The objective was to determine if a larger scale model (around 1/8 to 1/10 scale) could be tested within the technical constrains of the equipment and laboratory.

5.1 Finite Element Model Development

A series of finite element models (FEM) were built in parallel with the experimental program, which served as a calibration point. A verified analytical model served as a critical tool to further understand the system dynamics and response characteristics. It was then used to determine what simplifications, if any, can be made to the structure for the second experiment.

5.1.1 Finite Element Models for Simplifications

A set of two-dimensional models was created in OpenSEES to determine if simplifications could be made to the crane test specimen. Results from the first test indicated that the torsional modes have little influence on the dynamic response of the

container cranes. Therefore, a two dimensional model was deemed sufficient for modeling the behavior of the crane.

The first of the two models was one that incorporated all of the main structural components of the crane, as shown in Figure 5.1. The elements that made up the frame and the boom were the available `nonlinearBeamColumn` elements, with 4 integration points. The stays were modeled using OpenSEES' `truss` elements. The elastic section properties were assigned to the members using the `Elastic` section command. To account for the influence of the out-of-plane members, linear and rotational springs with stiffnesses representative of those out of plane members were placed at the joints where they frame in. Mass was applied as nodal masses, shown in Figure 5.2. The gravity load was primarily applied as point loads corresponding to the nodal masses, except for the horizontal members, which had uniformly distributed vertical loads. The geometric nonlinearity was taken into account by the use of the `PDelta` (P-Δ) geometric transformation in OpenSEES.

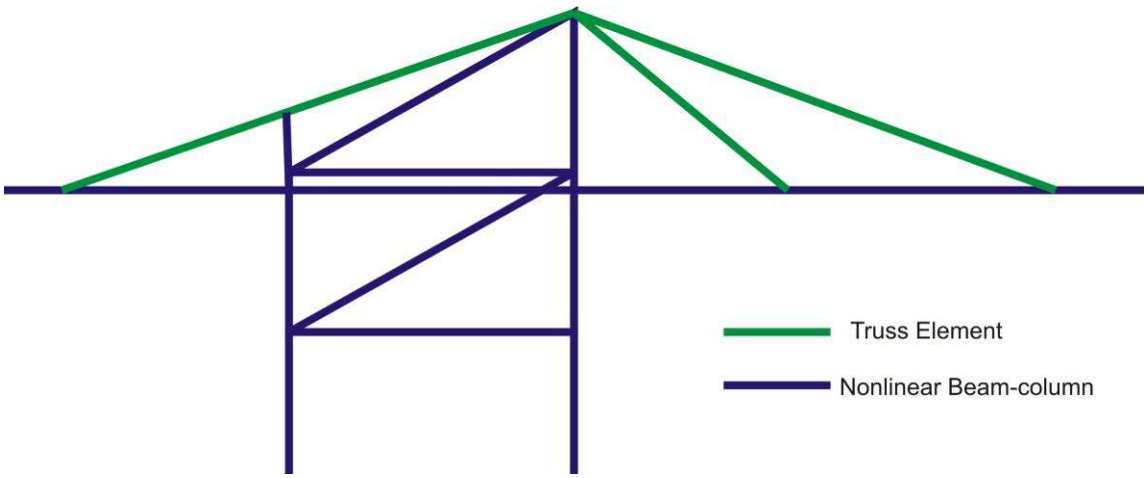

Figure 5.1: Finite element model of a complete crane

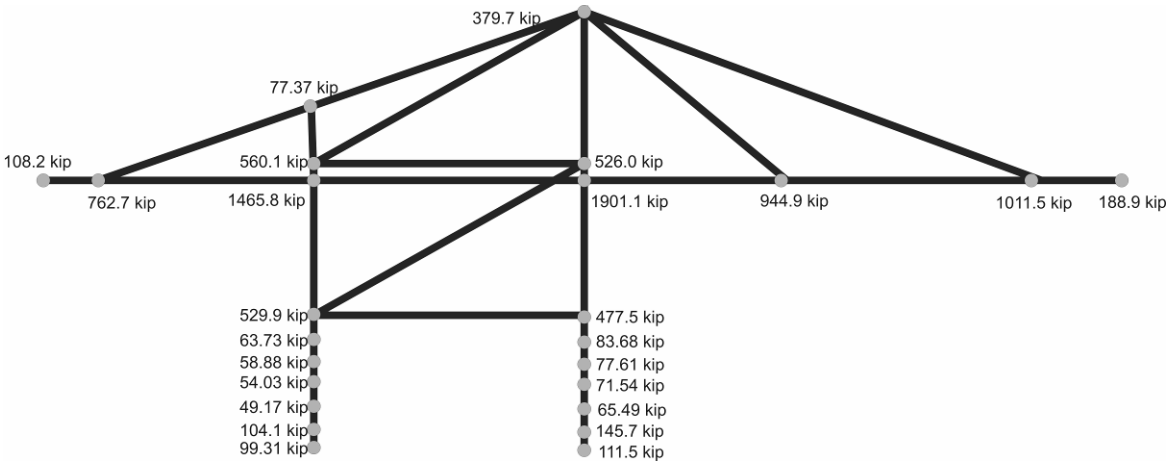

Figure 5.2: Weight distribution for the finite element model of a complete crane

The second of the two models was a simplified model, representative of a structure that could be tested in the laboratory, as shown in Figure 5.3. The elements were all `nonlinearBeamColumn elements`. As in the full crane model, springs were used to account for the influence of the out of plane members. The mass was applied as nodal masses around the portal frame and concentrated at the center of mass of the crane and at the ends of the short boom segments, shown in Figure 5.4. The gravity load was primarily applied as point loads corresponding to nodal masses, except for the horizontal members, which had uniformly distributed vertical loads.

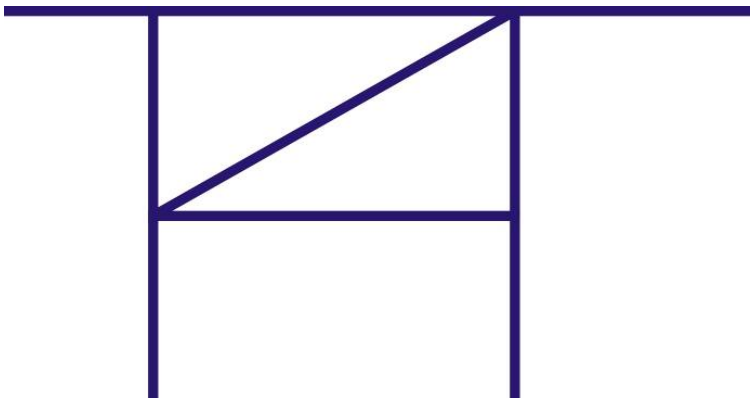

Figure 5.3: Finite element model of a simplified crane

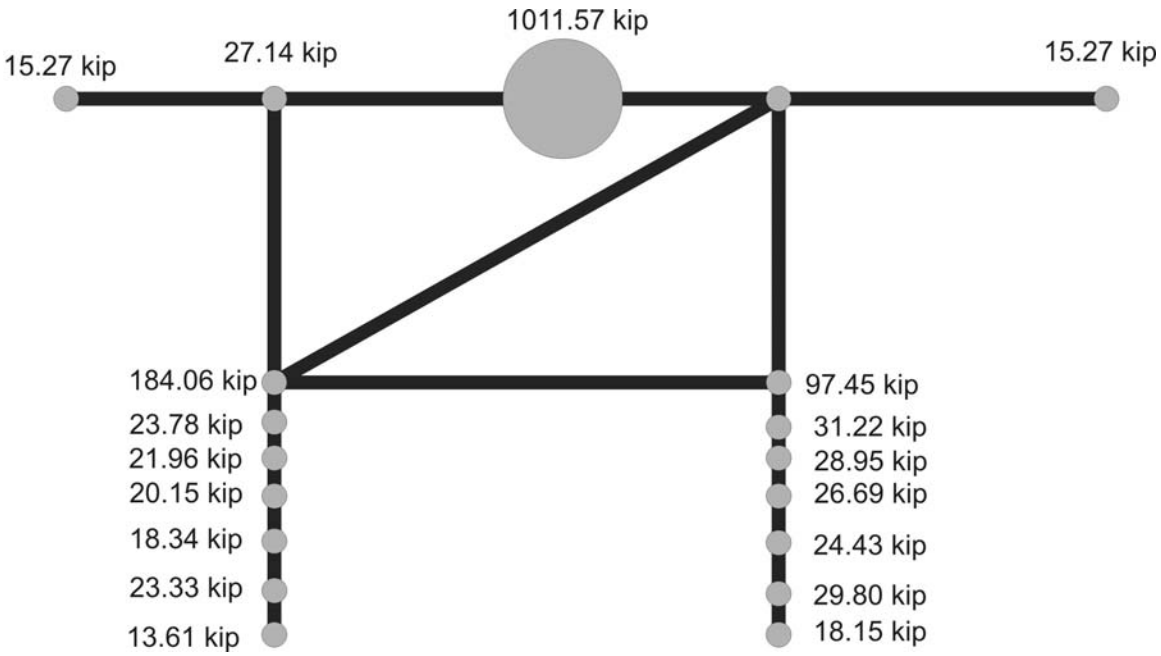

Figure 5.4: Mass distribution for the finite element model of the simplified crane

5.1.2 Finite Element Model for Calibration

The model created for calibration was a 3D model and is based on the scaled physical test structure described in Chapter 3, and thus had the same geometry, section and material properties, mass distribution, and boundary condition as the physical model.

As with the prototype scale models, mass, including the experimental artificial mass due to scaling, was applied as nodal masses. The stiffening effect of the steel plate masses was accounted for by applying rigid diaphragm effects between boom ties. Gravity load was applied as point loads corresponding to the nodal masses, with the exception of horizontal members, which have uniformly distributed vertical loads. Geometric nonlinearity was taken into account by the use of the `PDelta` (P-Δ) geometric transformation in OpenSees.

As with the prototype crane models, all elements are force-based `nonlinearBeamColumn` elements with elastic section properties. The tapered lower legs were discretized into five elements each, with each element having the dimensions as at the midpoint of its length. Rayleigh damping was applied at two modes, based on the experimentally determined half-power bandwidth damping of the portal sway and boom torsion modes.

5.1.3 Boundary Conditions

Two distinct boundary conditions were used as part of this study: pinned and free to uplift. A pinned boundary condition was used to study the elastic response of the crane. Pinning the base allows for the elastic response to be isolated from the uplift response, and is a good first step for checking the response.

Allowing the crane to uplift more realistically models the boundary conditions of a container crane. To model the uplift behavior, a frictional contact element was used. A frictional contact element provides lateral restraint that is equal to the vertical force times the coefficient of friction. This was achieved using the `element zeroLengthContact`. Once the vertical load reaches zero, contact element allows for there to be no horizontal restraint as the crane uplifts.

In order for the impact after uplift to be elastic, it was useful to have a stiff spring between the contact element and the ground. A stiff spring did not appreciably change the overall system dynamics. The stiff spring constant, k_k, was assumed to be 25,000 kip/in as suggested by Muthukumar and DesRoches (2006). A damper in parallel to the

spring allowed for energy dissipation. The damping coefficient, c_k, is calculated based on the coefficient of restitution (e), and can be calculated using the following equation:

$$c_k = 2\zeta\sqrt{k_k m}\ ;\quad \zeta = -\frac{\ln e}{\sqrt{\pi^2 + (\ln e)^2}} \tag{5.1}$$

where m is the structural mass contributing to the vibration of the spring, and ζ is the damping ratio. The coefficient of restitution was assumed to be 0.6, based on the recommendations of Muthukumar and DesRoches (2006).

5.1.4 Analysis

Two types of analyses were performed in this study: an eigen analysis and time history analyses. An eigen analysis was performed to determine the vibration properties of the two cranes. This analysis is important to determine whether both cranes have the same natural frequencies and mode shapes. Four sets of ground motions were used for the time history analysis. They were the same records that are used in the experiment. These time history analyses allow for a comparison of the behavior during an earthquake are essentially predictions of how the model will behave during the experiment. The time histories were run using both the pinned boundary conditions and the contact element.

5.2 Model Calibration

5.2.1 White Noise Comparison

The values of the natural frequencies and damping for the four most significant modes are summarized in Table 5.1 and sketched in Figure 5.6. These modes consist of two torsion modes, boom dominated (Figure 5.5a) and frame dominated (Figure 5.5b),

the portal frame sway (Figure 5.5c), and a vertical boom displacement (Figure 5.5d). The periods of the corresponding modes of the finite element model are listed in Table 5.1 and in parentheses in Figure 5.6. When comparing experiment to FEM periods, only the vertical mode is more than 2% different. The critical portal sway mode of both the experiment and FE models are the same.

Table 5.1 Natural frequencies and damping for four significant modes

Mode	*T Exp.*	*ζ Exp.*	*T FEM*
	[sec]	[%]	[sec]
Portal sway	0.306	0.84	0.306
Torsion (boom)	0.612	2.29	0.620
Torsion (frame)	0.549	1.45	0.539
Vertical boom motion	0.143	2.33	0.154

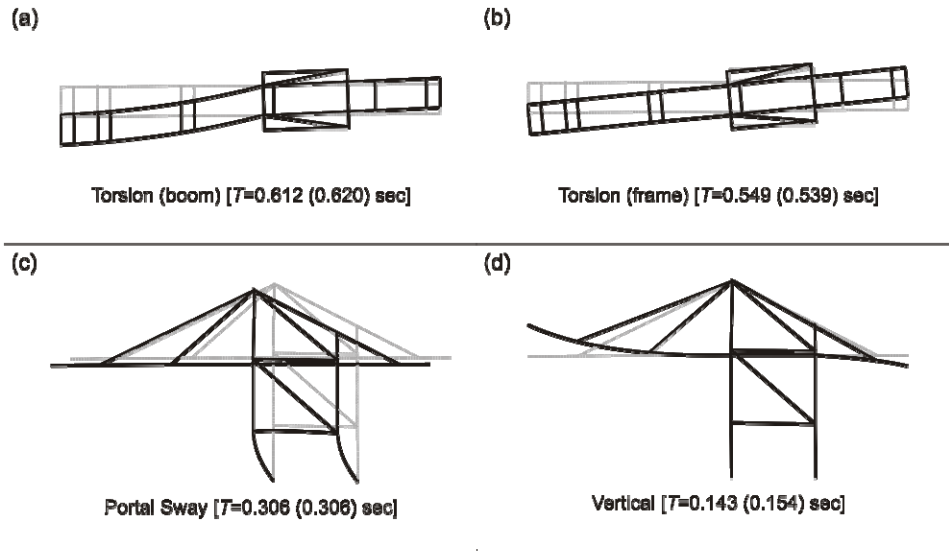

Figure 5.5: Mode shapes for 1/20th scale container crane

5.2.2 Elastic Response Comparison

For comparisons of the elastic response of the experimental and analytical models, the ¼ scale CLE6 excitation, which has a peak base acceleration of 0.11g is

chosen, because it provides an elastic only response without uplift. Since portal sway is deemed the critical response of interest, only input in the trolley-travel direction is considered.

The qualitative responses of the experimental and analytical models are in good agreement, as seen in Figure 5.6, which shows the horizontal displacement of the portal beam as measured at the NW portal joint of the experimental test and analytical models. Both models exhibit similar displacement trends, indicating that the analytical models are capable of capturing the dominant elastic response.

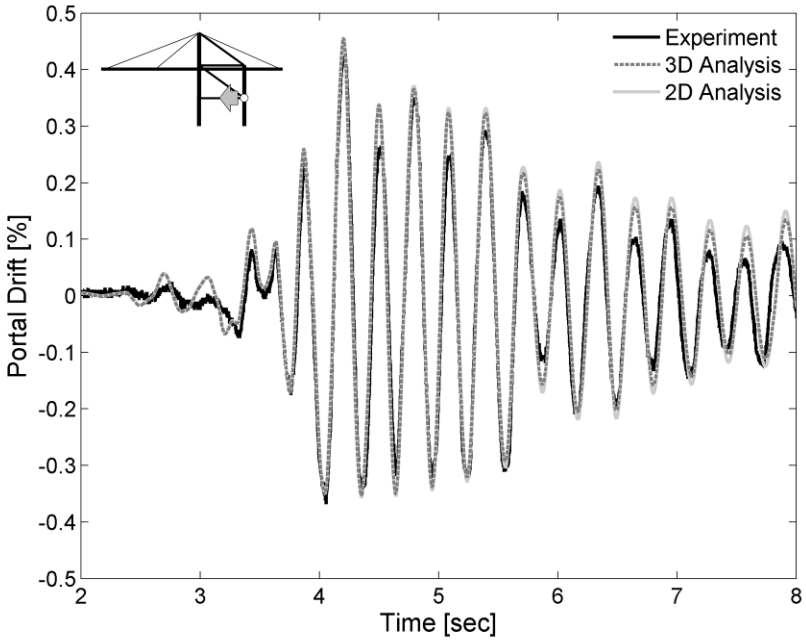

Figure 5.6: Observed portal sway drift of experiment compared with 3D and 2D analytical models for ¼ scale CLE4 excitation

There are some noticeable differences between analytical and experimental response. One reason for these discrepancies is due to a crane leg settling under the gravity load, which caused the crane's trolley-travel axis to be slightly askew of the table excitation direction. The resulting off-axis excitation caused a slight torsion response,

which oscillates at a longer period than the portal sway response. This torsion has some effect on the portal sway, most noticeably at times when the torsion and portal sway responses are out-of-phase, such as at approximately 4.5 and 5.1 seconds. The settling occurred due some legs being slightly longer than others, resulting in an initial gravity distribution different than the assumed values. The difference in gravity distribution also impacted the relative response of each frame. Due to channel limitations, only the North frame is available for response comparisons. In addition, the half-power bandwidth method of estimating damping is an approximation, and could account for the overestimation of response by the analytical models at later times.

It can be seen that the response predicted by the 3D and 2D analytical models are nearly indistinguishable for the jumbo cranes under consideration in this study, demonstrating that the elastic trolley-travel response can be accurately captured using an appropriate 2D analytical idealization. Since the trolley-travel direction has been shown to be the dominant response, an appropriate 2D model is therefore sufficient to analyze the seismic behavior of container cranes not allowed to uplift, or prior to uplift.

5.2.3 Coupled Elastic and Uplift Response

For the comparison of the coupled elastic and uplift response of the experimental and analytical models, the full scale CLE4 excitation having a peak base acceleration of 0.55 g is chosen due to the extent of uplift and derailment response observed. Again, only input in the trolley-travel direction is considered.

The observed responses of the experimental and analytical models are in good agreement. Figure 5.7 shows the recorded horizontal and vertical displacements of the

waterside and landside leg bases. Both the 3D and 2D analytical models predict the timing and duration of uplift events and associated translational motion well. It should be noted that the experimental response of the two parallel frames deviates from the analytical models at times. Early in the excitation, this deviation is caused by the settling described in Section 5.2.2. The large discrepancies of the experimental recorded landside vertical displacements after the primary uplift event are a result of the displacement gauges shifting upon impact; one transducer rotated while another was pushed upwards, leading to readings with artificial residuals.

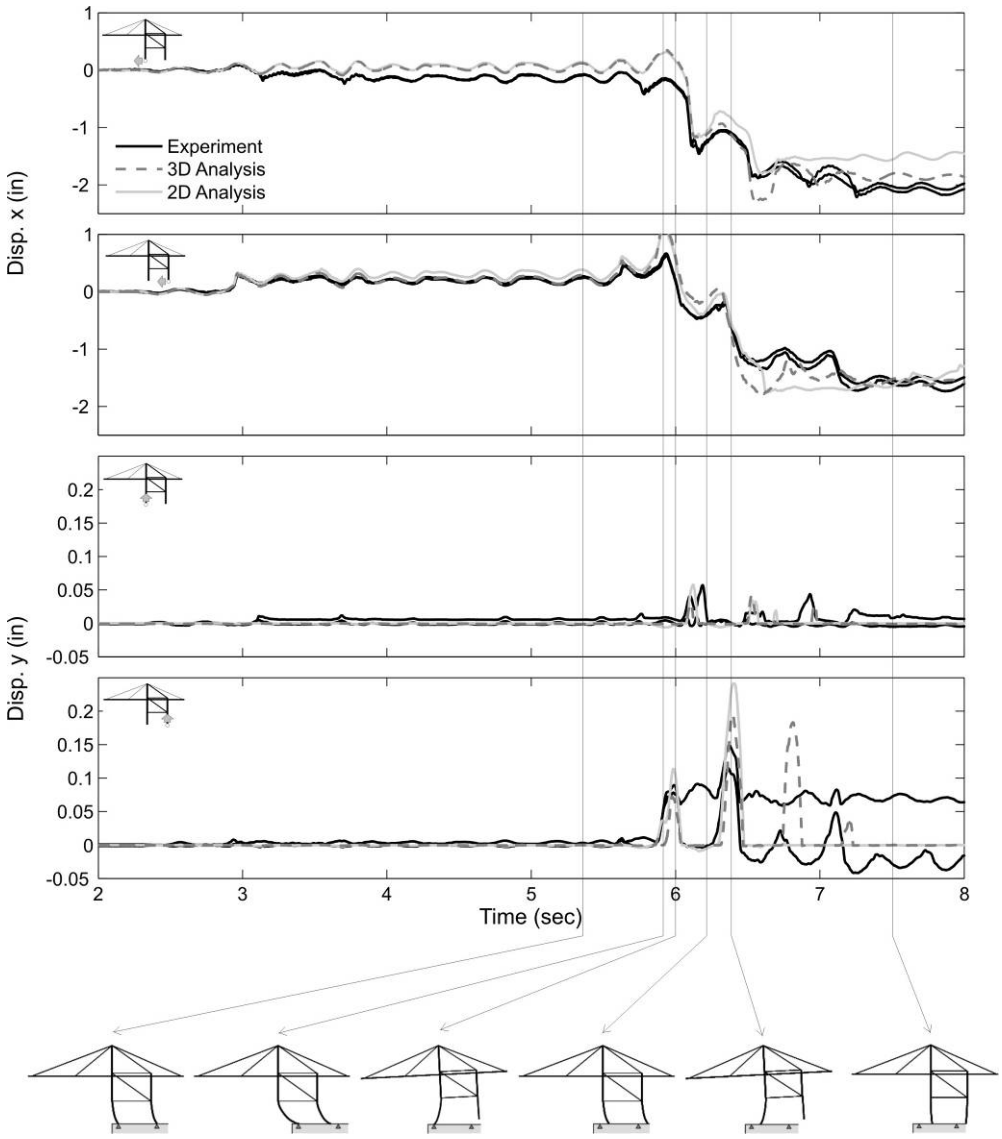

Figure 5.7: Observed portal sway and vertical and trolley-travel horizontal displacements of waterside and landside leg bases for unscaled CLE4 excitation

The critical trolley-travel seismic response is sensitive to the characteristics of uplift and the dominant portal sway component of the elastic structural response, both of which are captured well by the analytical models. Overall, both finite element models proved capable of predicting and capturing the critical response of the elastic crane and its coupling with the uplift/derailment behavior.

5.3 Results of the Finite Element Analysis

There are three main results from the finite element analysis: eigen analysis results, comparison of the elastic response, and comparison of the combined elastic/uplift response. The following sections present and discuss the results.

5.3.1 Eigen Analysis

The first mode is the most critical, because it accounts for 90% of the response. Table 5.2 shows a comparison of the first three modes for the two models. There is excellent agreement between the modes of the complete crane and the simplified model. The portal sway modes are equal for both models. And the two vertical modes differ by 0.01s. The mode shapes for the first three modes are shown in Figure 5.8. The first mode is the portal sway mode (Figure 5.8a). The second and third modes are vertical boom modes (Figure 5.8b and 5.8c). It can be seen, that there is good agreement in the mode shapes between the two models.

Table 5.2: Natural frequencies for complete model and simplified models

Mode	*Complete Model*	*Simplified Model*
Portal Sway	1.36 s	1.36 s
Vertical 1	0.68 s	0.69 s
Vertical 2	0.44 s	0.43 s

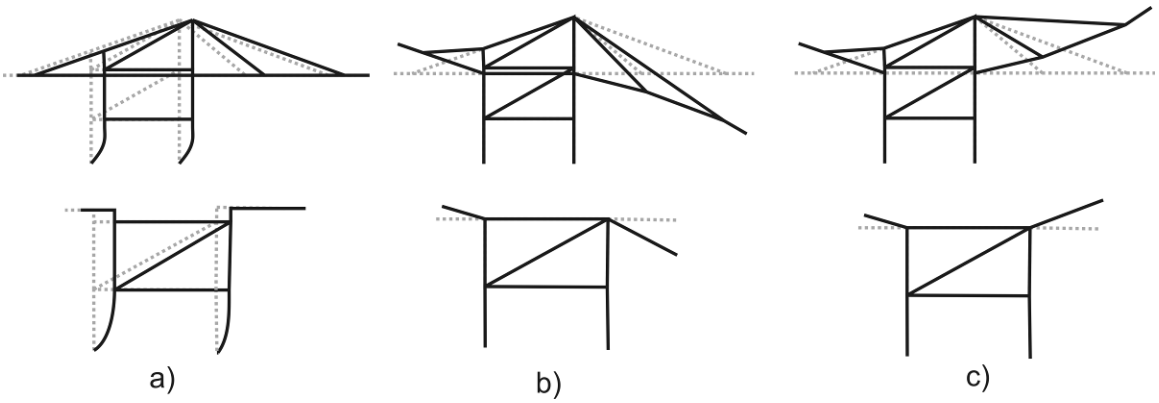

Figure 5.8: Mode shape comparison for complete and simplified crane models

5.3.2 Elastic Time History Response

The pinned boundary condition allows for the isolation of the elastic response, which is dominated by the portal sway. Utilizing a pinned boundary condition allows for a comparison of the elastic responses of the complete and simplified crane models. The two most important indicators of the elastic response are the portal drift and the moments in the portal frame. Table 5.3 summarizes the important results for each ground motion. It can be seen that the maximum portal drifts for each ground motion are within 2.7%. The maximum landside moments are within 1% for each ground motion. The maximum waterside moments are all within 1.4%.

Table 5.3: Maximum responses for FEM with a pinned boundary condition

Ground Motion	*Full Model Portal Drift*	*Modified Model Portal Drift*	*Full Model Landside Moment*	*Modified Model Landside Moment*	*Full Model Waterside Moment*	*Modified Model Waterside Moment*
OLE4	5.18 in	5.04 in	105000 kip	105000 kip	138000 kip	136000 kip
OLE6	4.44 in	4.37 in	95800 kip	95800 kip	118000 kip	117000 kip
CLE4	16.5 in	16.1 in	345000 kip	343000 kip	439000 kip	433000 kip
CLE6	14.1 in	13.8 in	294000 kip	294000 kip	374000 kip	371000 kip

The time history responses to the OLE4 excitation are shown in Figures 5.9-5.11. There is excellent agreement between the full and simplified models for all three response quantities. Figures 5.12-5.14 show the response to the OLE6 excitation. There is good agreement between the full and simplified models. The responses to the CLE4 excitation are shown in Figures 5.15-5.17. There is excellent agreement between the two models. Figures 5.18-5.20 show the response to the CLE6 excitation. There is good agreement between the two models. The results from the models with a pinned boundary

condition suggest that removing the top structure and shortening the boom, and redistributing the weight do not change the critical portal sway response of the crane.

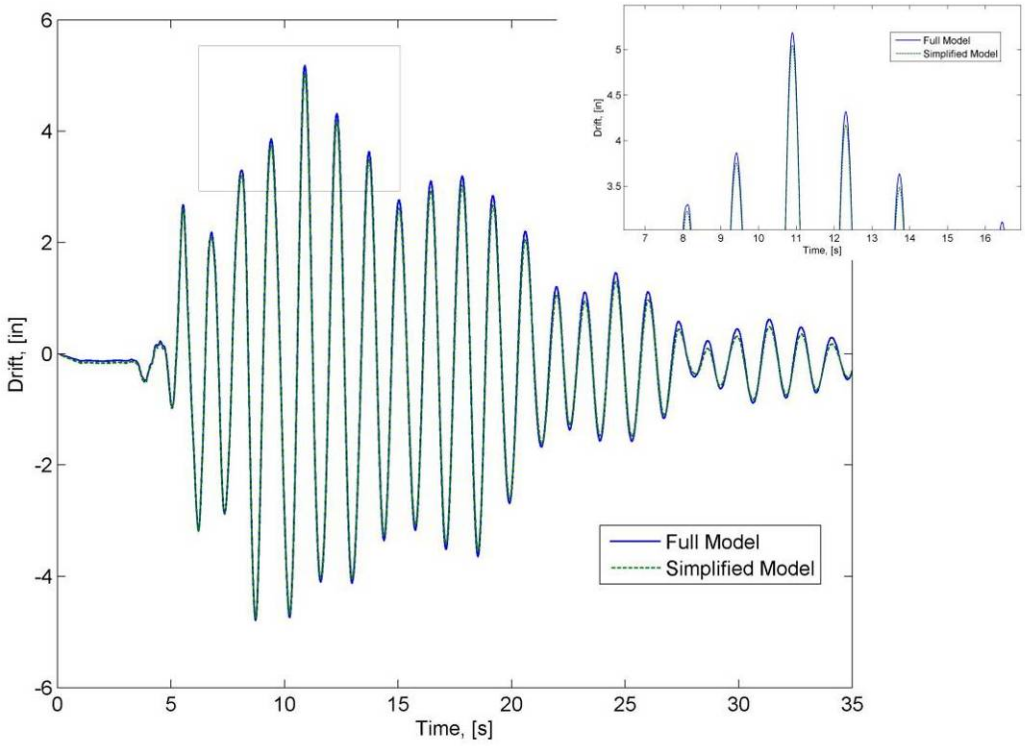

Figure 5.9: Drift response to OLE4 excitation with pinned boundary condition

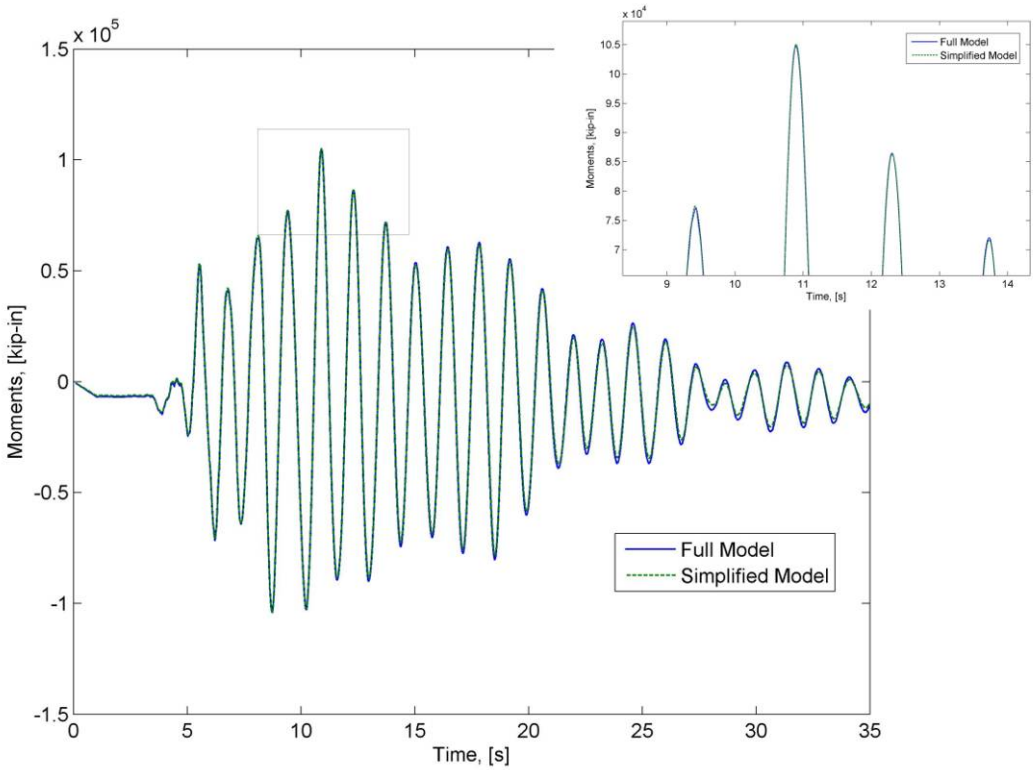

Figure 5.10: Landside moment response to OLE4 excitation with pinned boundary condition

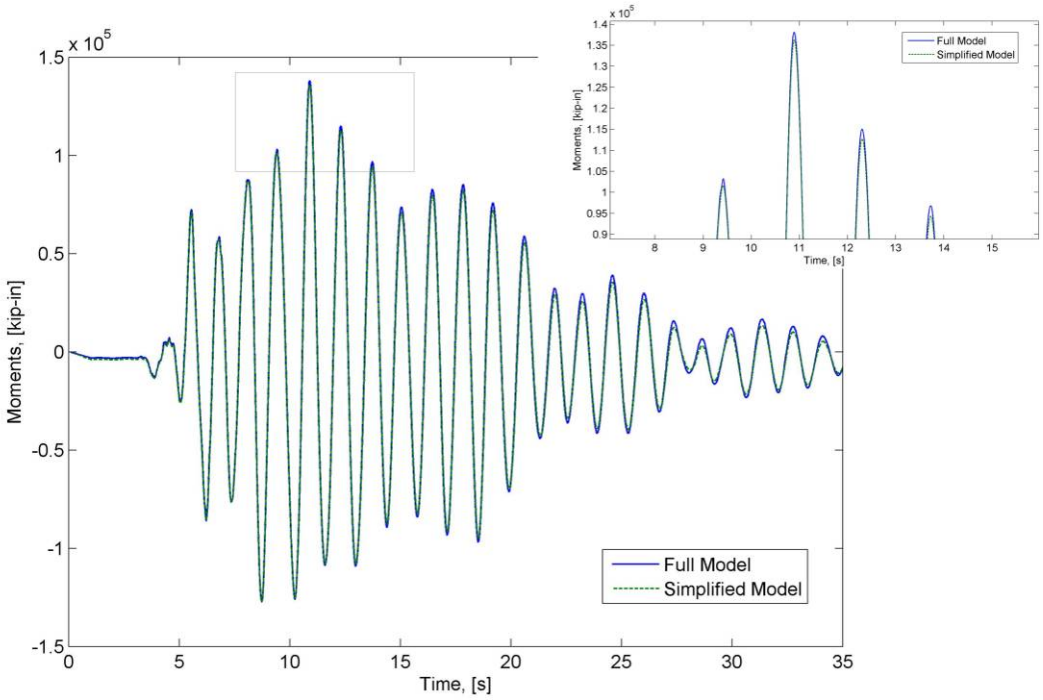

Figure 5.11: Waterside moment response to OLE4 excitation with pinned boundary condition

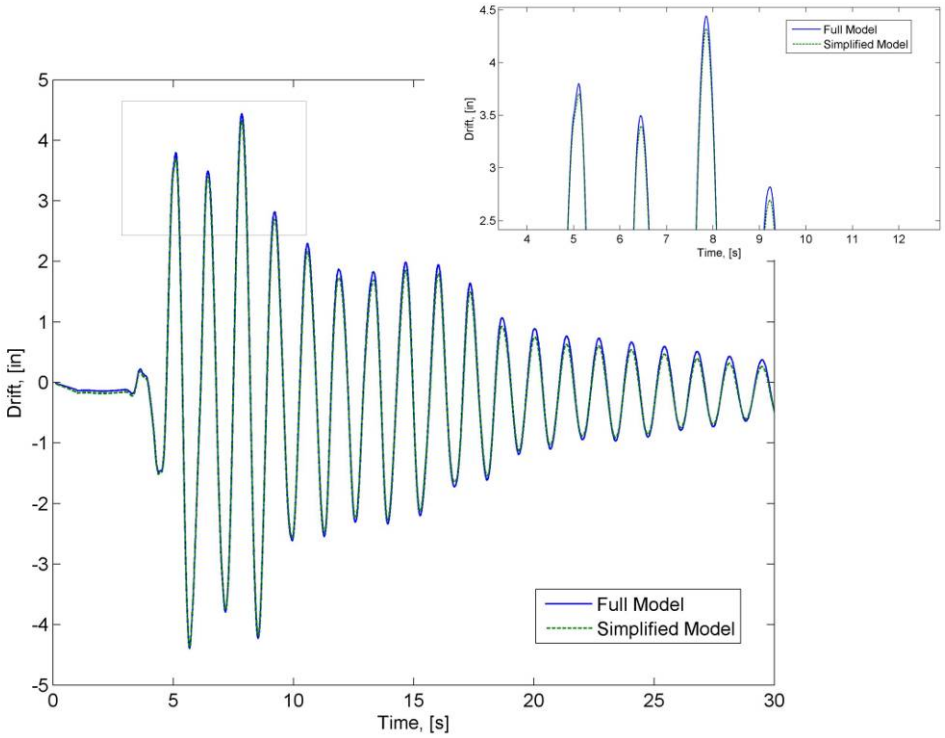

Figure 5.12: Drift response to OLE6 excitation with pinned boundary condition

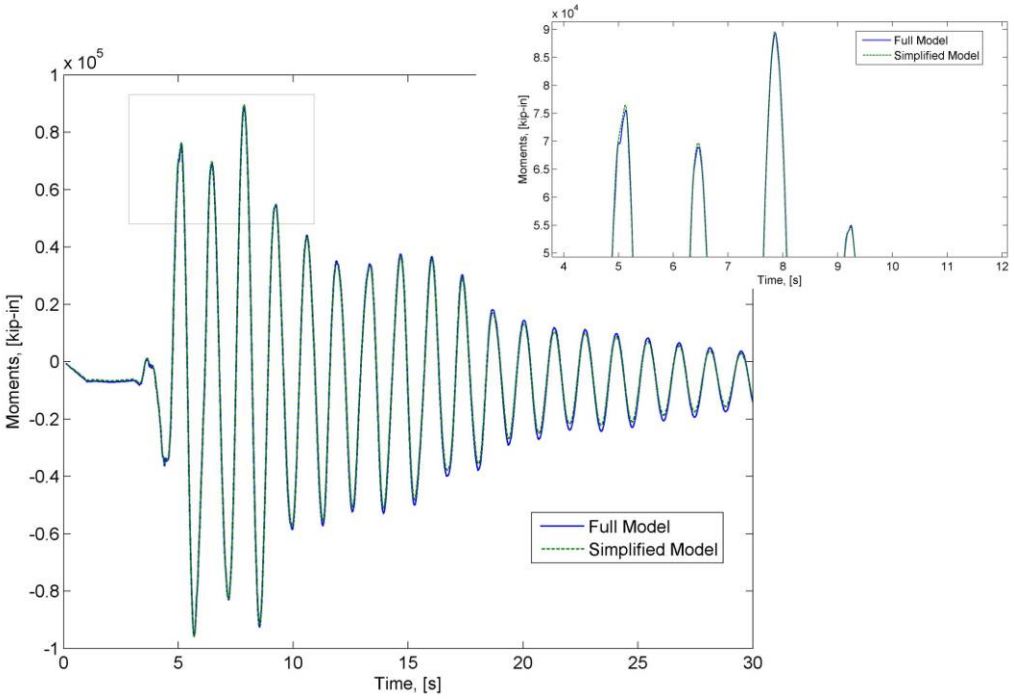

Figure 5.13: Landside moment response to OLE6 excitation with pinned boundary condition

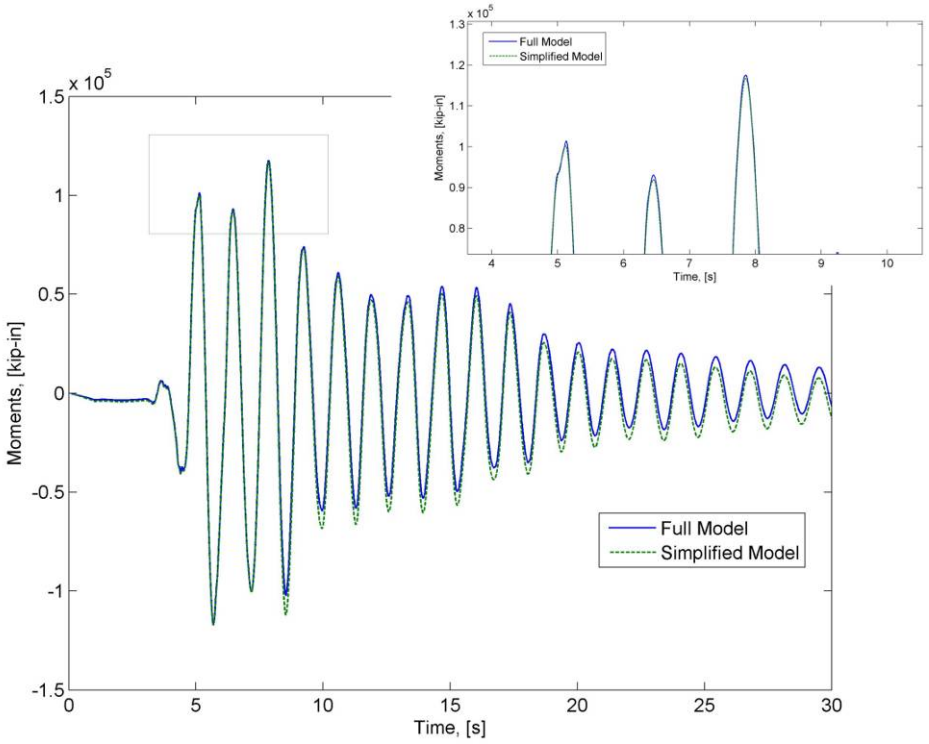

Figure 5.14: Waterside moment response to OLE6 excitation with pinned boundary condition

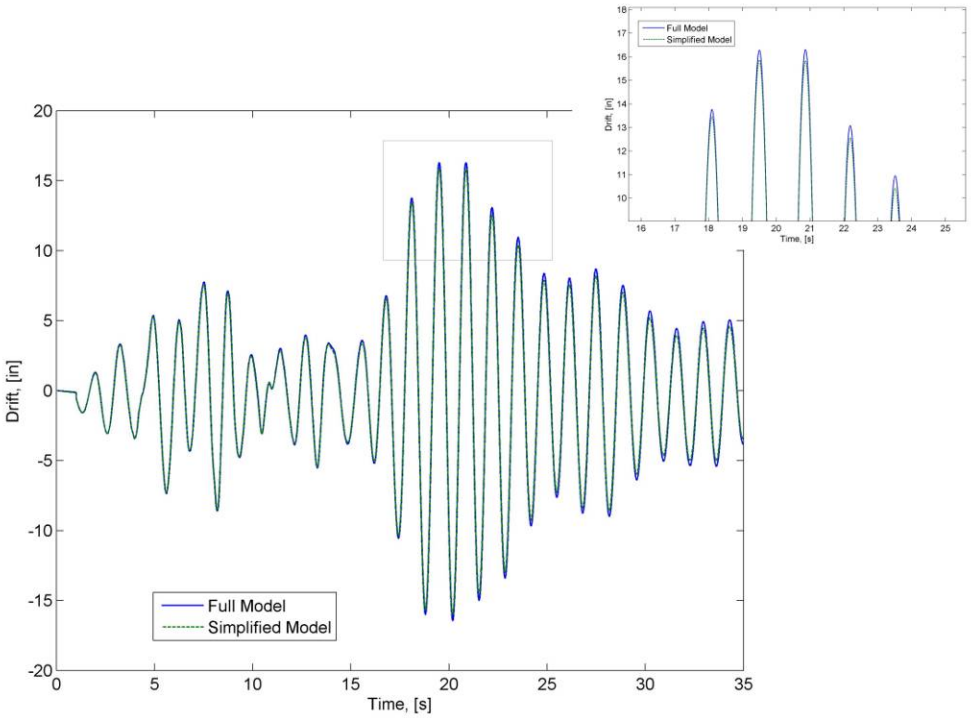

Figure 5.15: Drift response to CLE4 excitation with pinned boundary condition

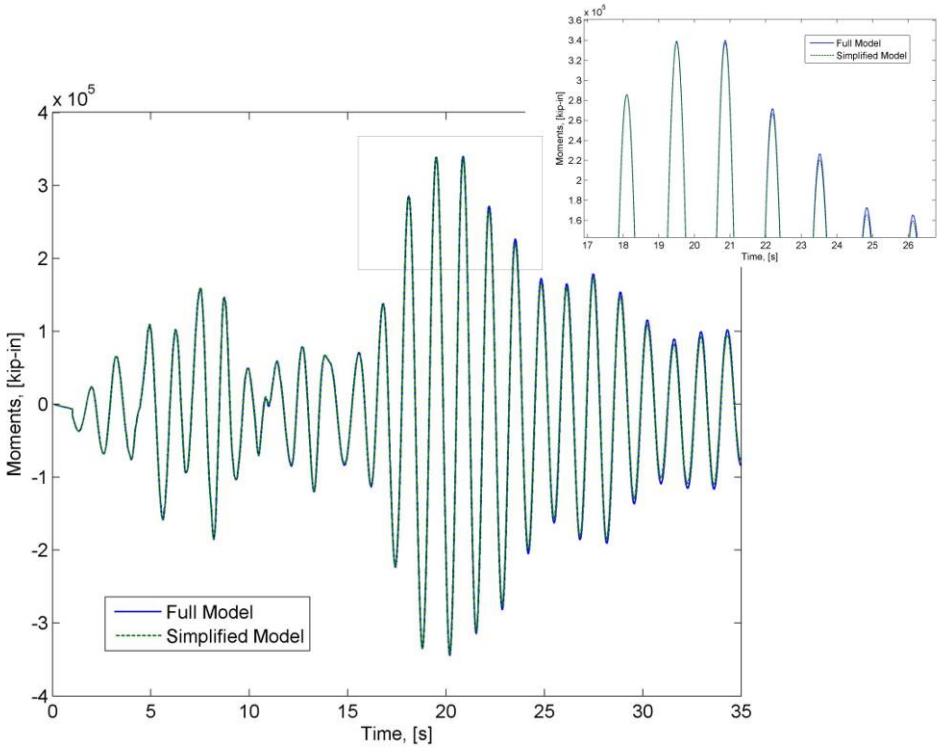

Figure 5.16: Landside moment response to CLE4 excitation with pinned boundary condition

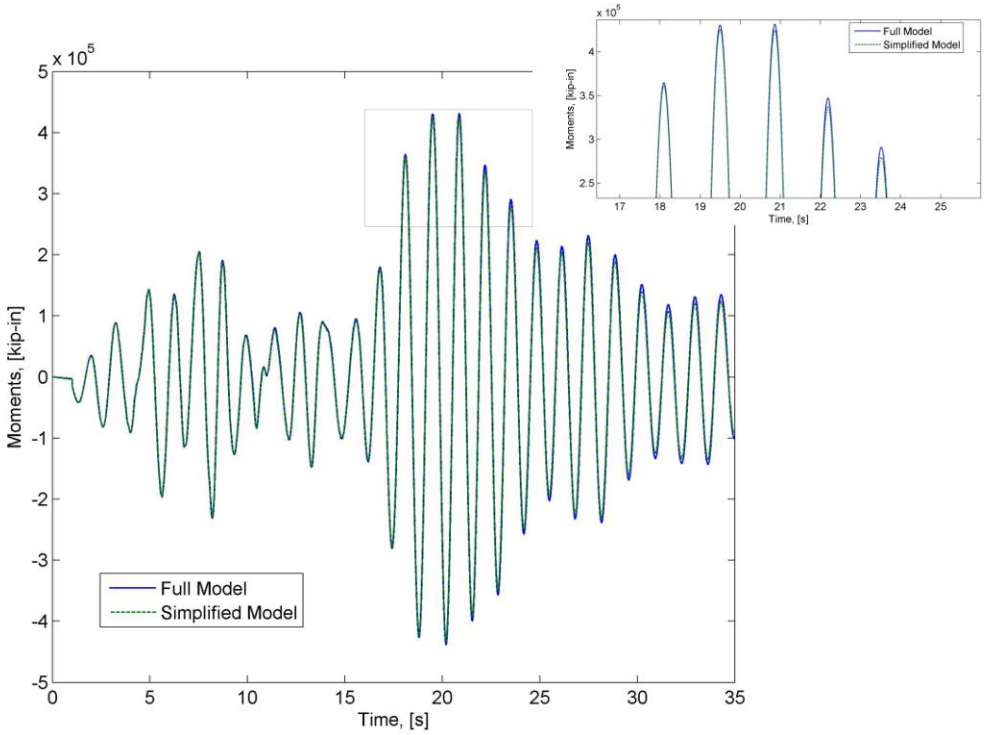

Figure 5.17: Waterside moment response to CLE4 excitation with pinned boundary condition

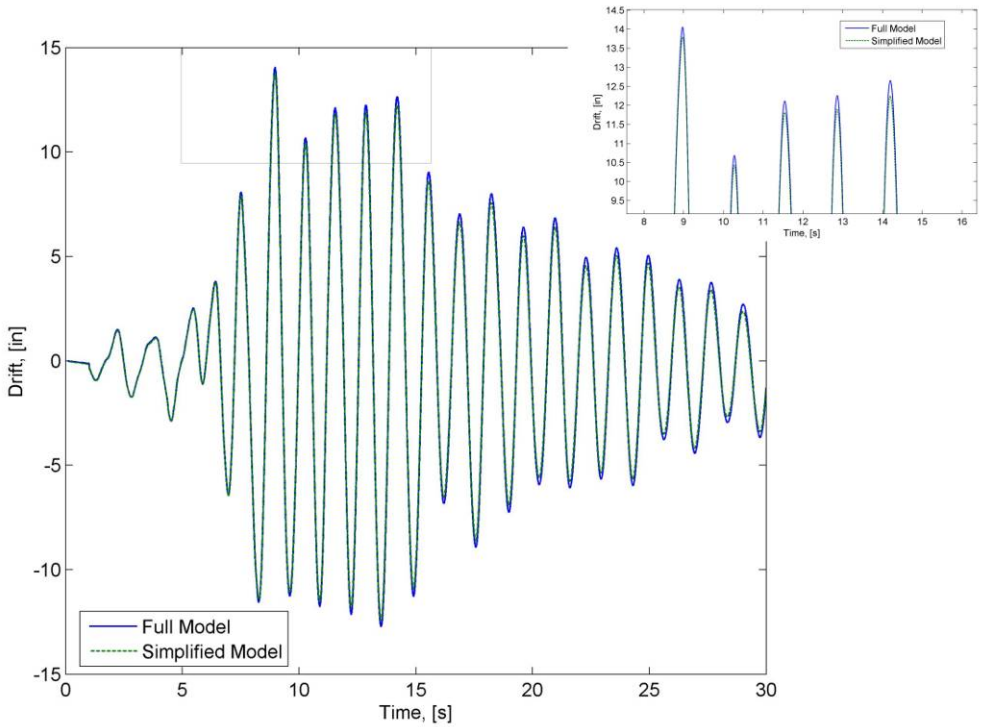

Figure 5.18: Drift response to CLE6 excitation with pinned boundary condition

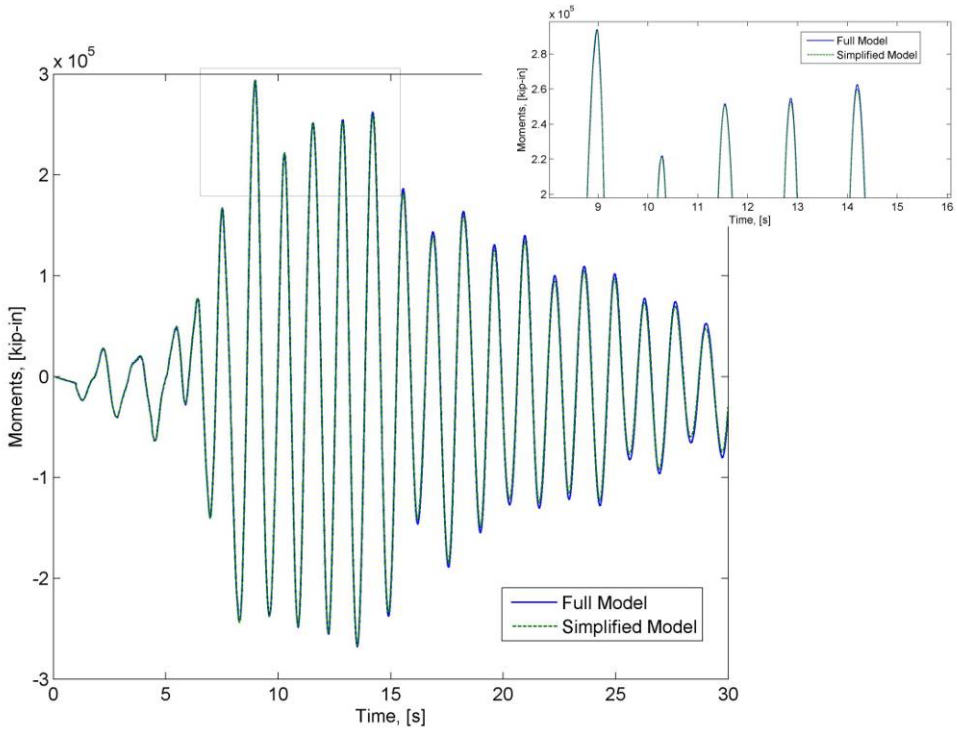

Figure 5.19: Landside moment response to CLE6 excitation with pinned boundary condition

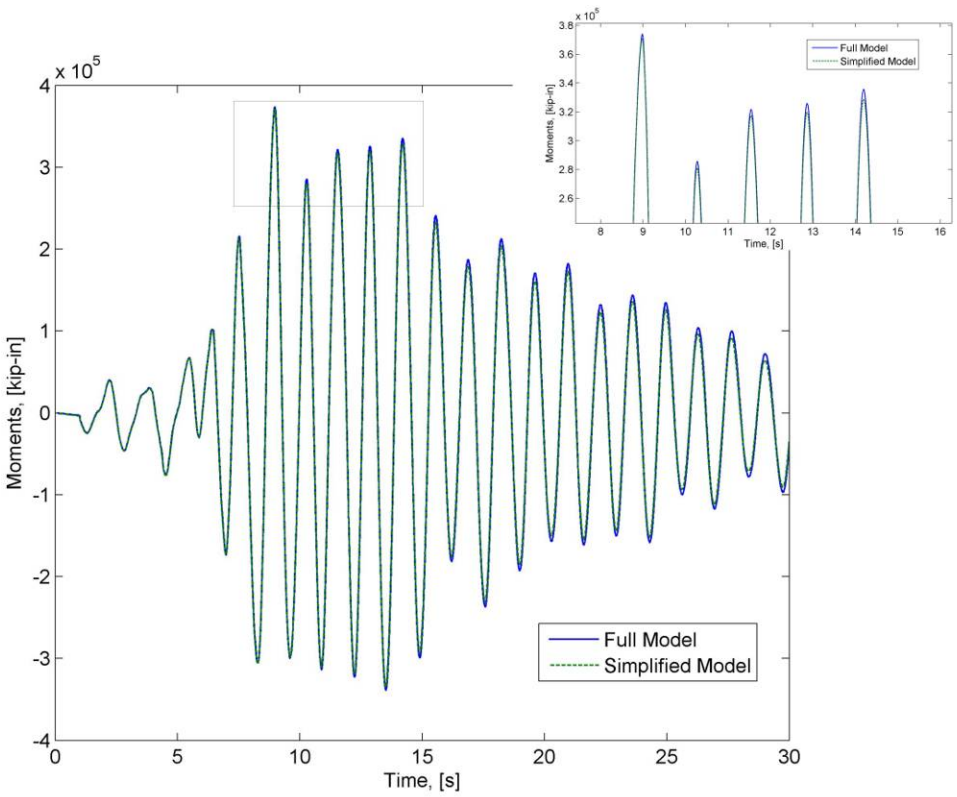

Figure 5.20: Waterside moment response to CLE6 excitation with pinned boundary condition

5.3.3 Uplift Time History Response

The second boundary condition used in the modeling is a frictional contact element, which allows the legs to uplift without a horizontal restraint. Table 5.4 the maximum response values from both models for each ground motion.

Table 5.4: Maximum responses for FEM with a frictional contact element

Ground Motion	*Full Model Portal Drift*	*Modified Model Portal Drift*	*Full Model Landside Moment*	*Modified Model Landside Moment*	*Full Model Waterside Moment*	*Modified Model Waterside Moment*
OLE4	4.88 in	4.84 in	104000 kip	104000 kip	135000 kip	135000 kip
OLE6	4.40 in	4.37 in	95900 kip	95800 kip	118000 kip	117000 kip
CLE4	15.6 in	16.5 in	290000 kip	323000 kip	369000 kip	401000 kip
CLE6	14.5 in	13.7 in	265000 kip	272000 kip	344000 kip	390000 kip

The time history responses for the OLE4 excitation are shown in Figures 5.21-5.23. Up until 12 seconds, there is excellent agreement between the models. After 12 seconds there is a shift in the full model response and the responses are offset, but they match well. Figures 5.24-5.26 show the response to the OLE6 excitation. There is good agreement between the models. After 9 seconds, there is a slight shift in the full model response, but it is much less pronounced than in the OLE4 response. Figures 5.27-5.30 show the responses to the CLE4 excitation. There is good agreement until 8 seconds, after which the full model experiences the same shift as previously noted. At 17 seconds, larger deviations occur. It can be seen in Figure 5.30 that the timing and duration of the first two uplift events are in good agreement. These are the largest and longest duration uplift events, so the most important to match. The responses to the CLE6 excitation are shown in Figures 5.31-5.34. There is good agreement for the drift and landside moments. There are larger deviations for the waterside moment. It is shown in Figure 5.34 that the timing and duration of the large uplift event was captured in both models. The simplified model has similar drift and moment responses to the full model, and the timing and duration of the uplift events can be captured by the simplified model. These results indicate that a simplified model is sufficient for modeling a jumbo container crane.

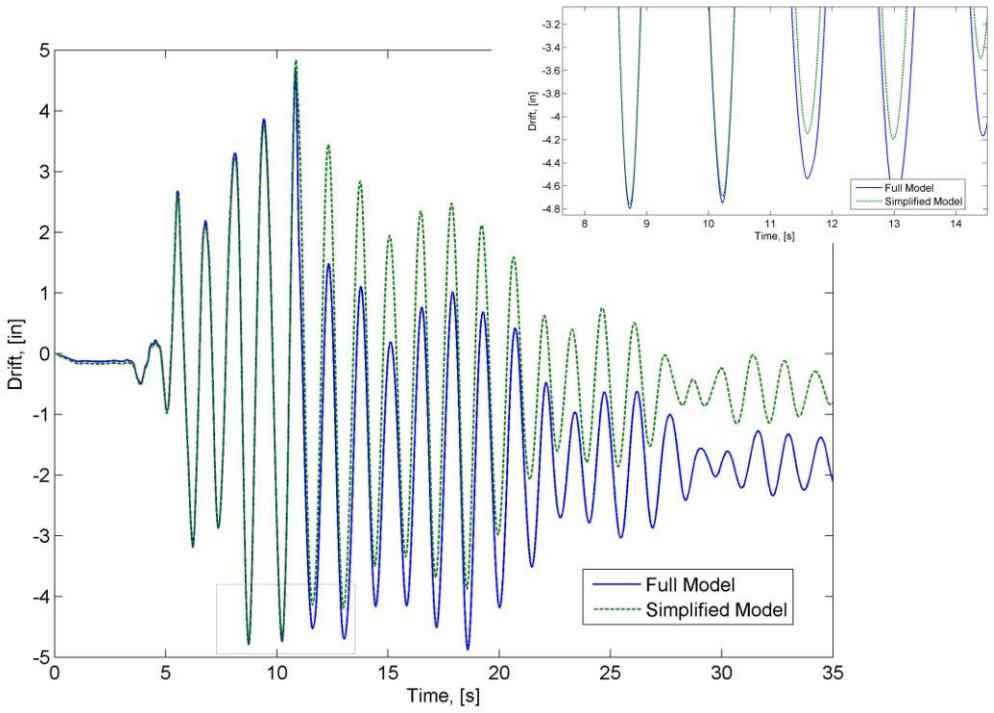

Figure 5.21: Drift response to OLE4 excitation with contact element

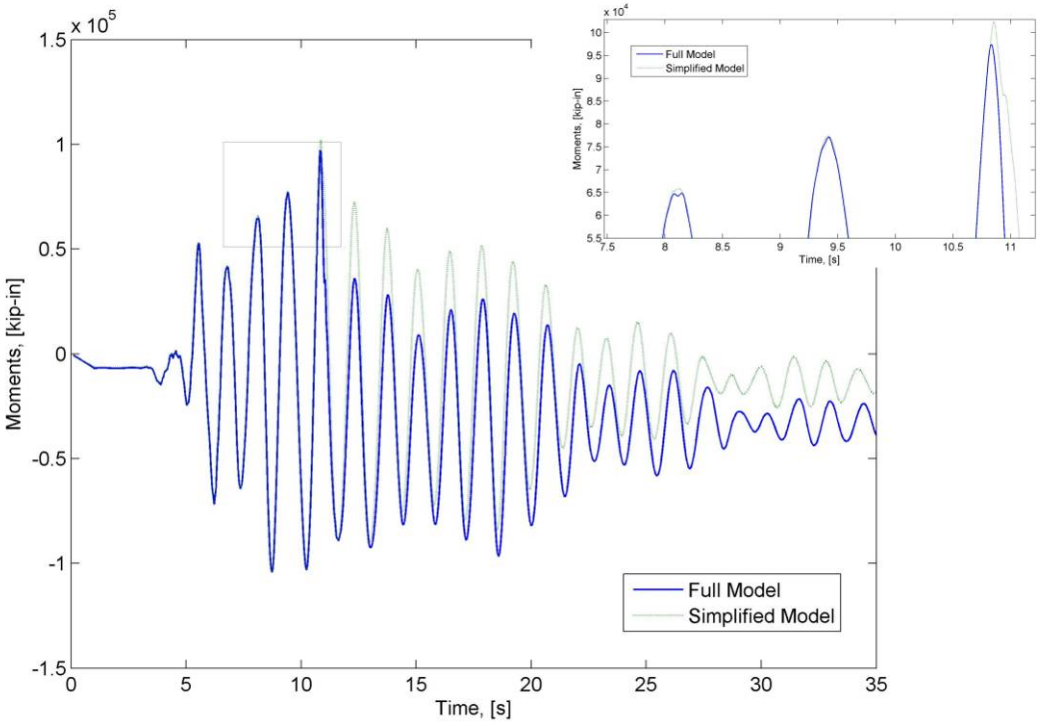

Figure 5.22: Landside moment response to OLE4 excitation with contact element

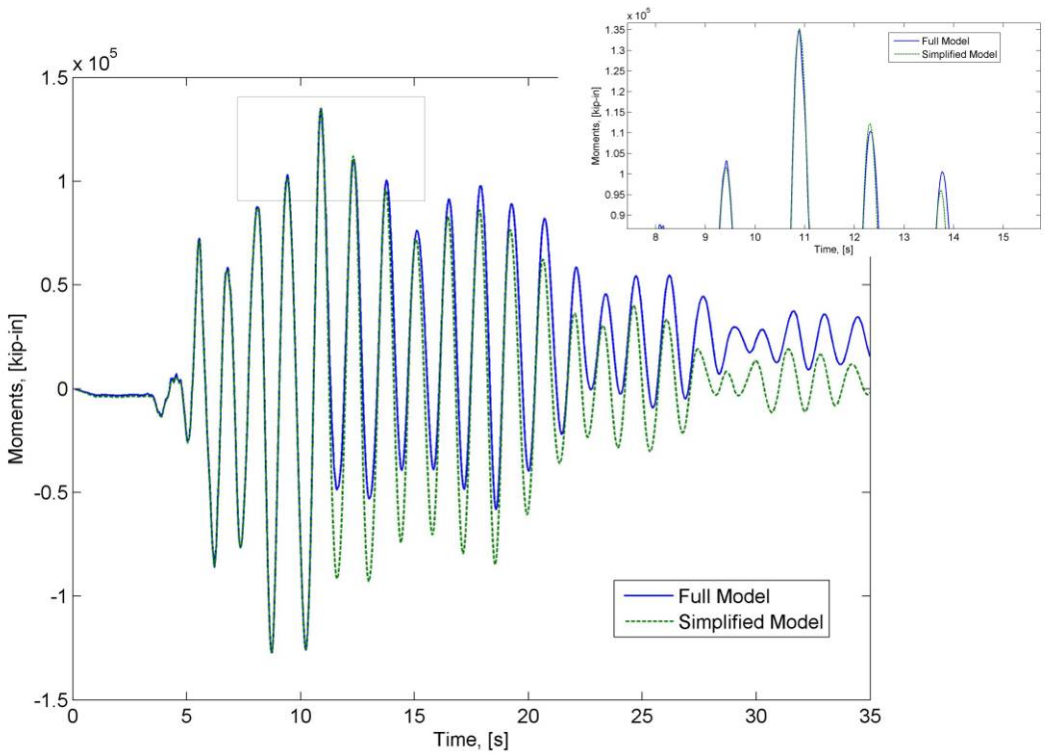

Figure 5.23: Waterside moment response to OLE4 excitation with contact element

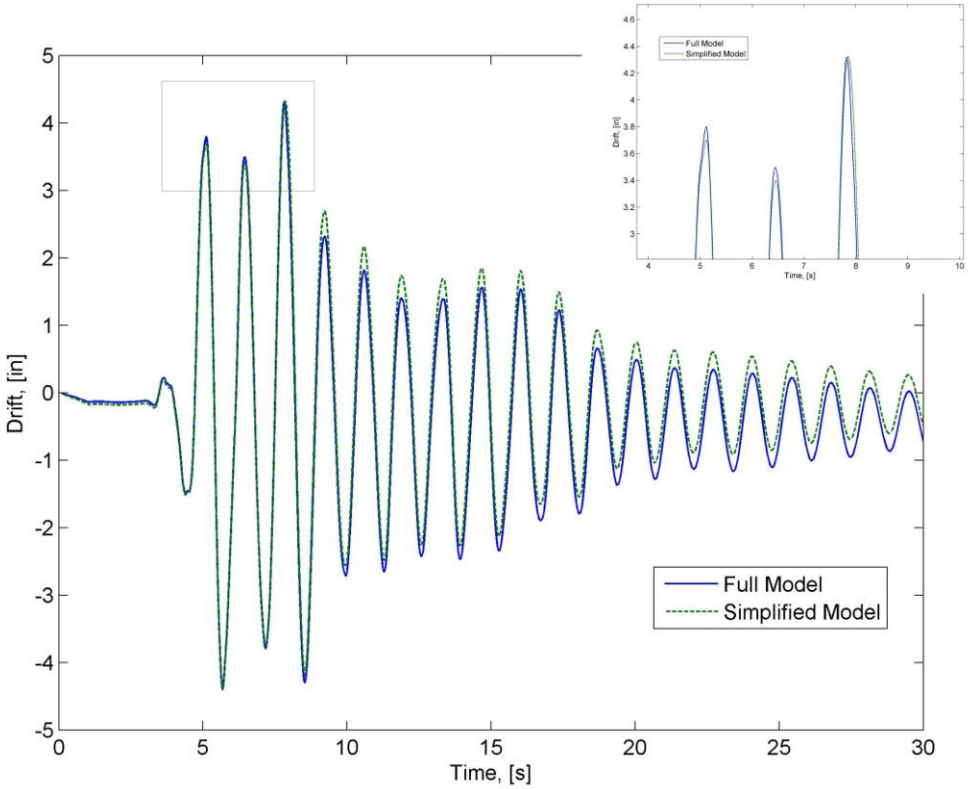

Figure 5.24: Drift response to OLE6 excitation with contact element

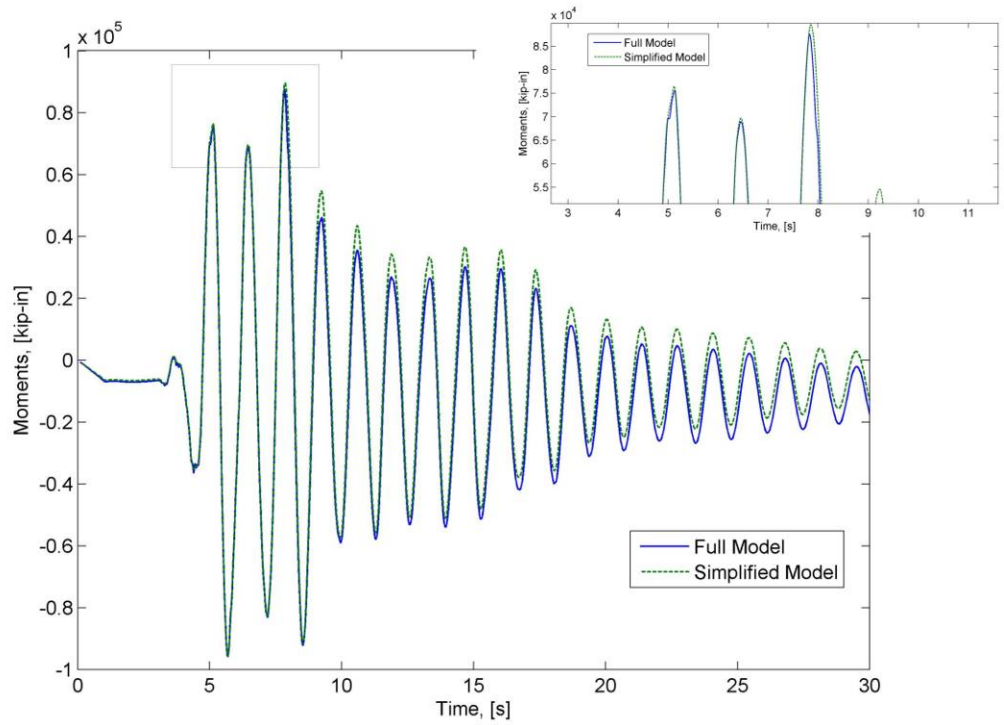

Figure 5.25: Landside moment response to OLE6 excitation with contact element

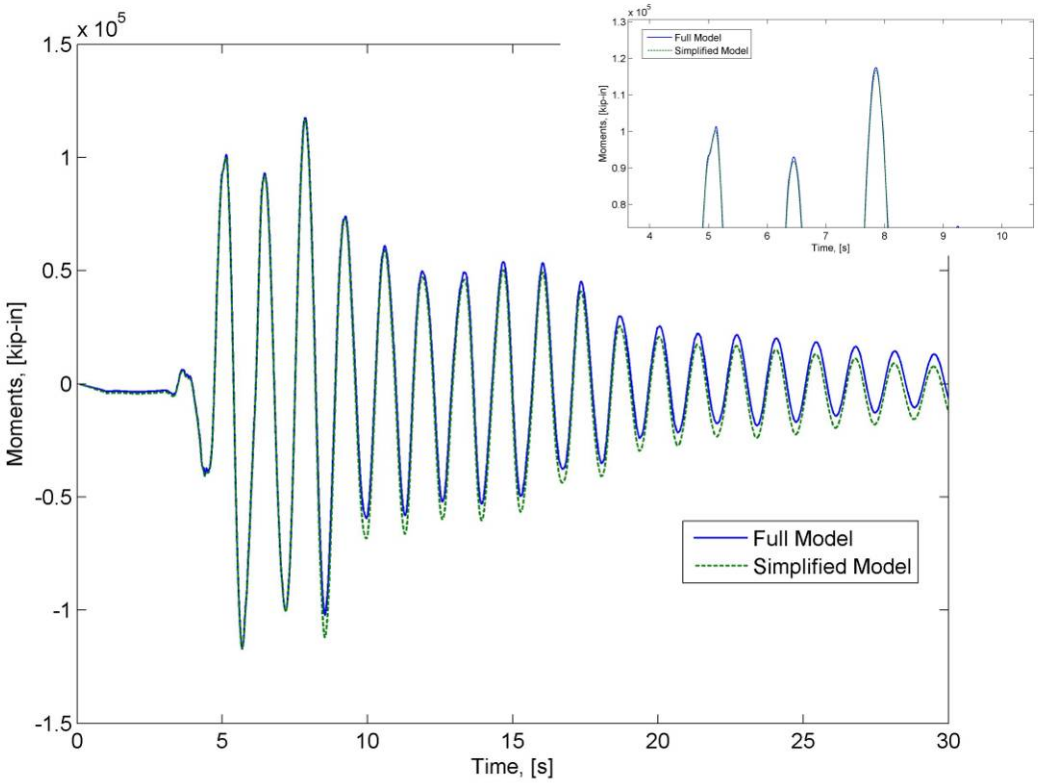

Figure 5.26: Waterside moment response to OLE6 excitation with contact element

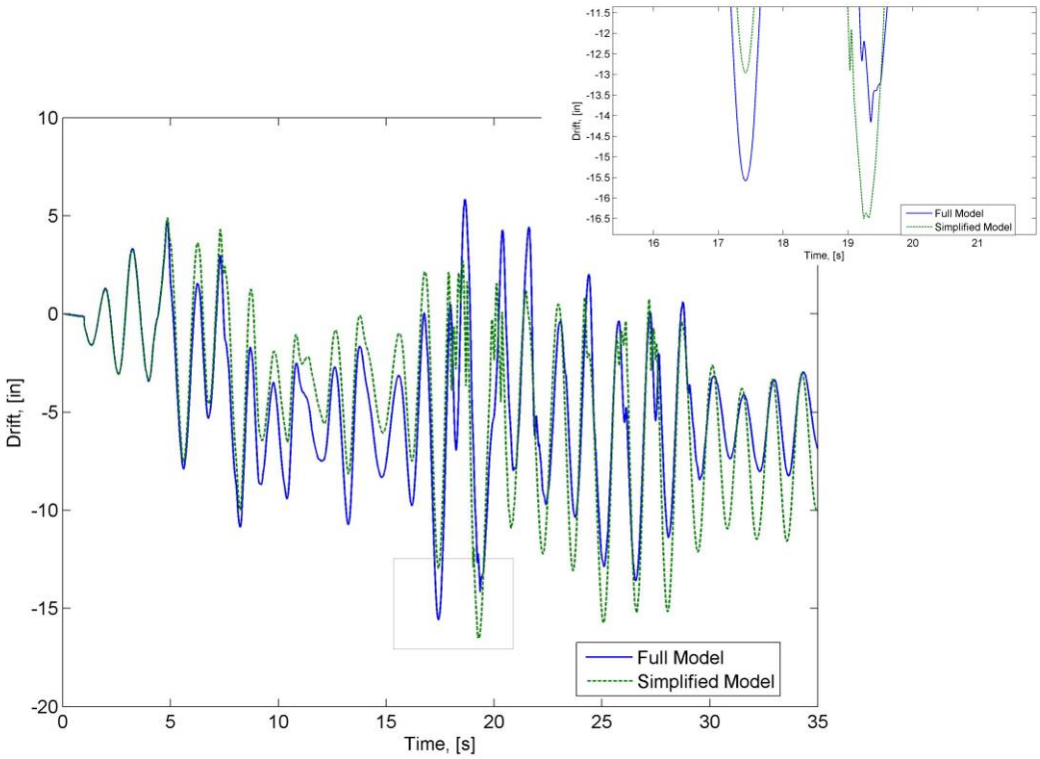

Figure 5.27: Drift response to CLE4 excitation with contact element

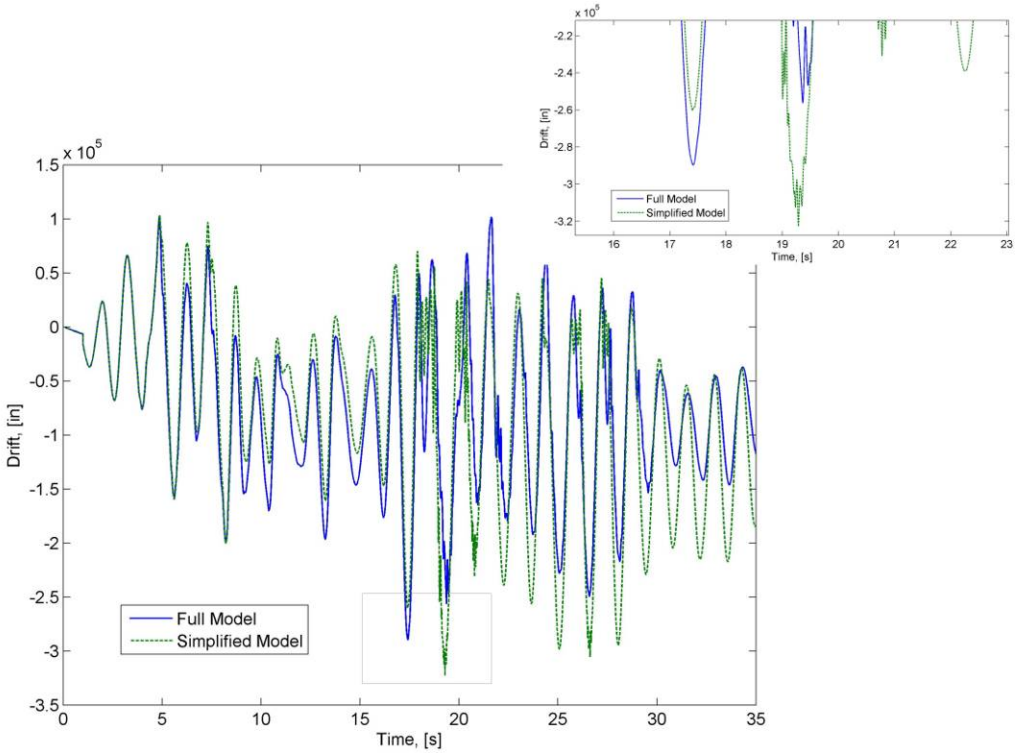

Figure 5.28: Landside moment response to CLE4 excitation with contact element

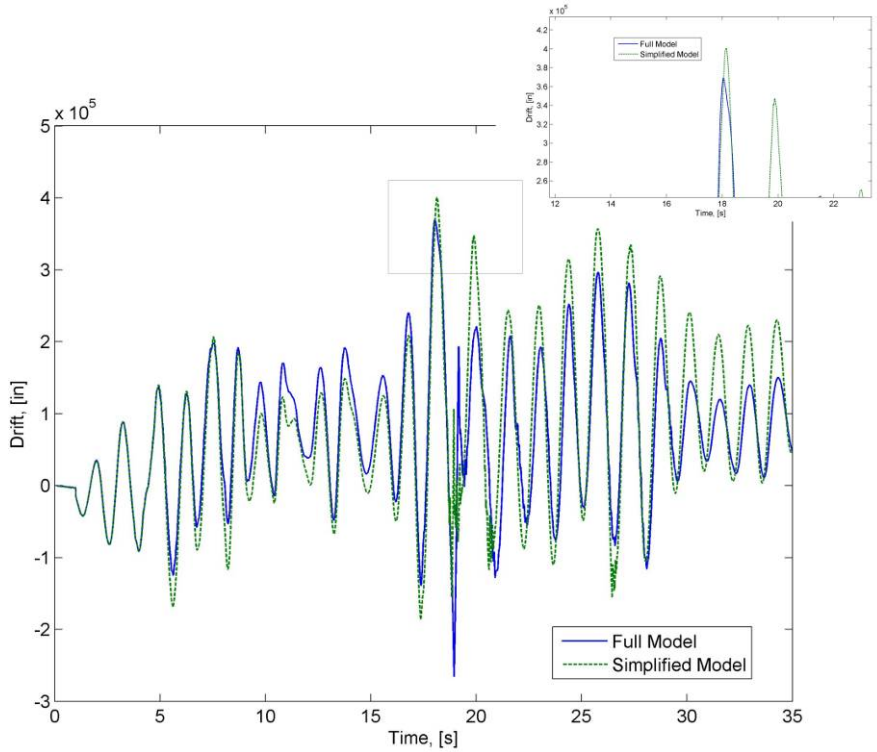

Figure 5.29: Waterside moment response to CLE4 excitation with contact element

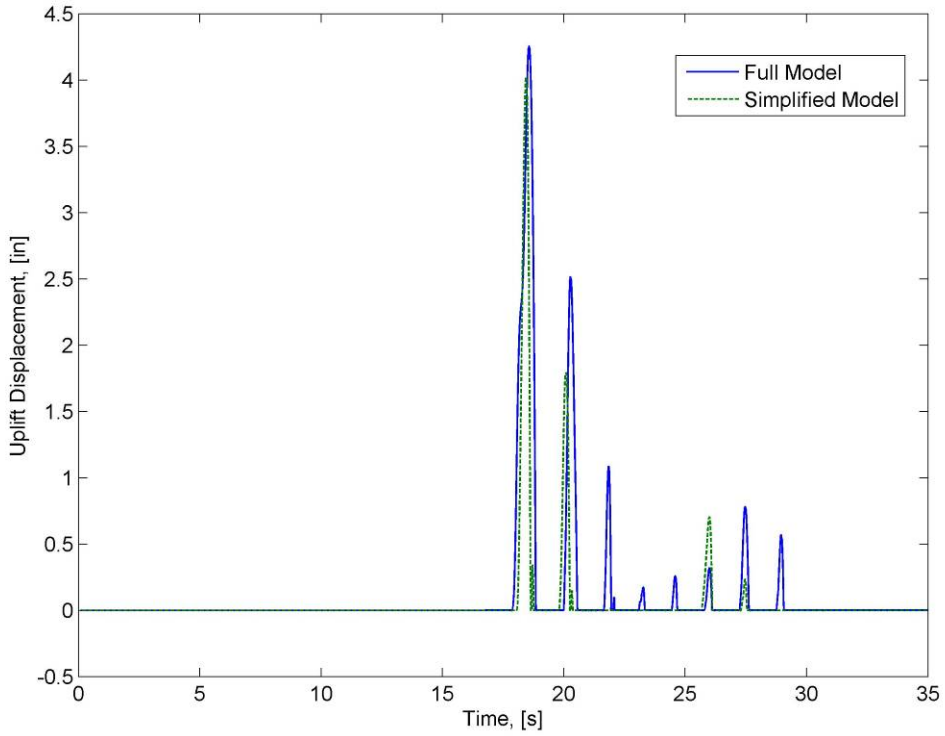

Figure 5.30: Uplift response to CLE4 excitation with contact element

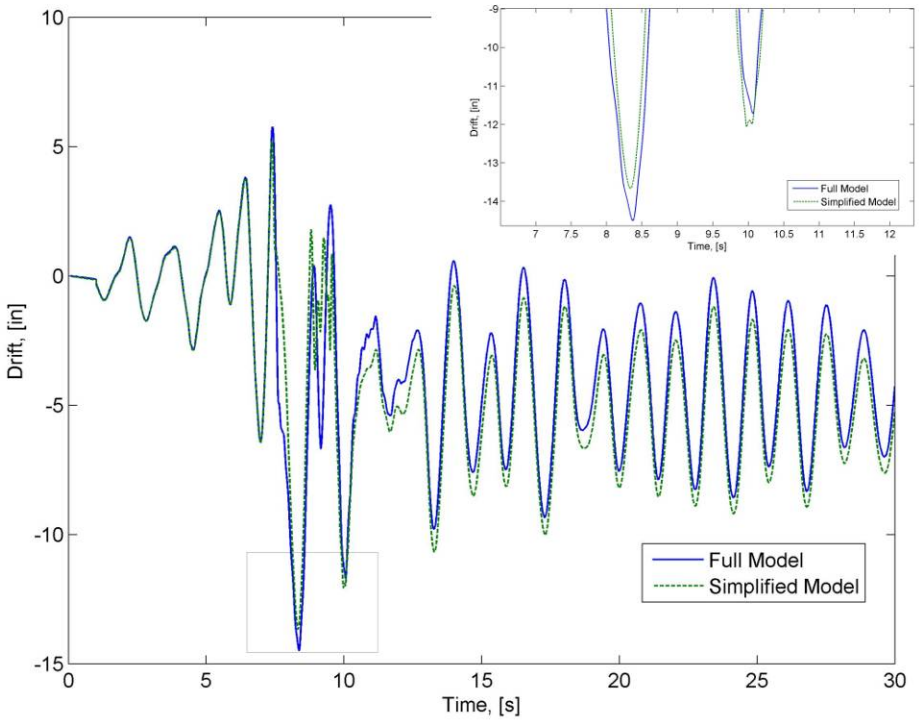

Figure 5.31: Drift response to CLE6 excitation with contact element

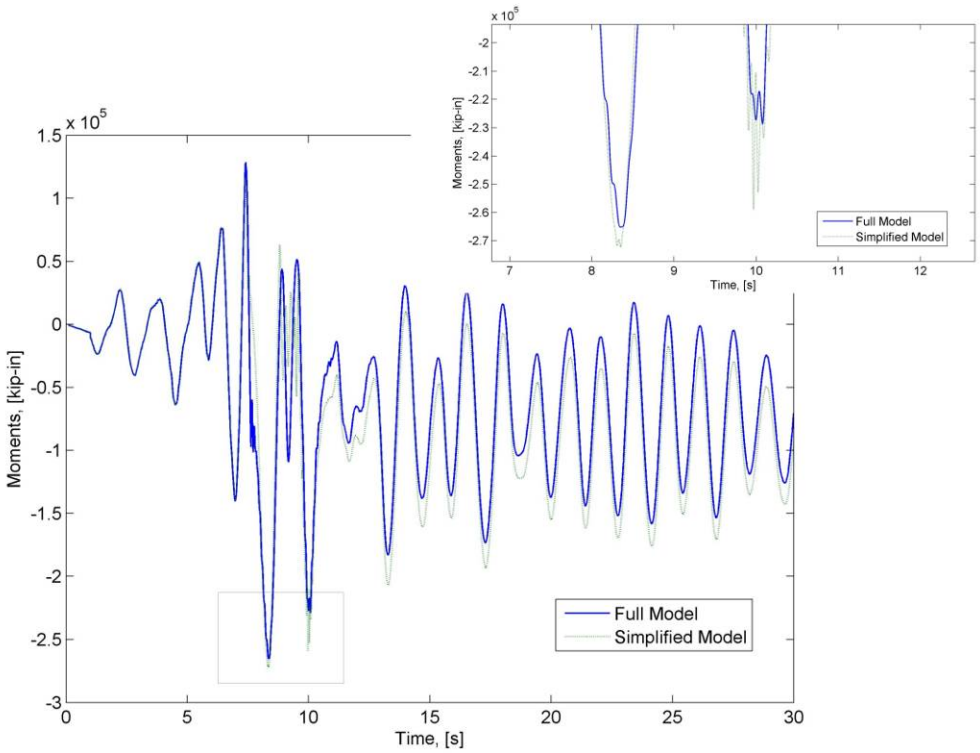

Figure 5.32: Landside moment response to CLE6 excitation with contact element

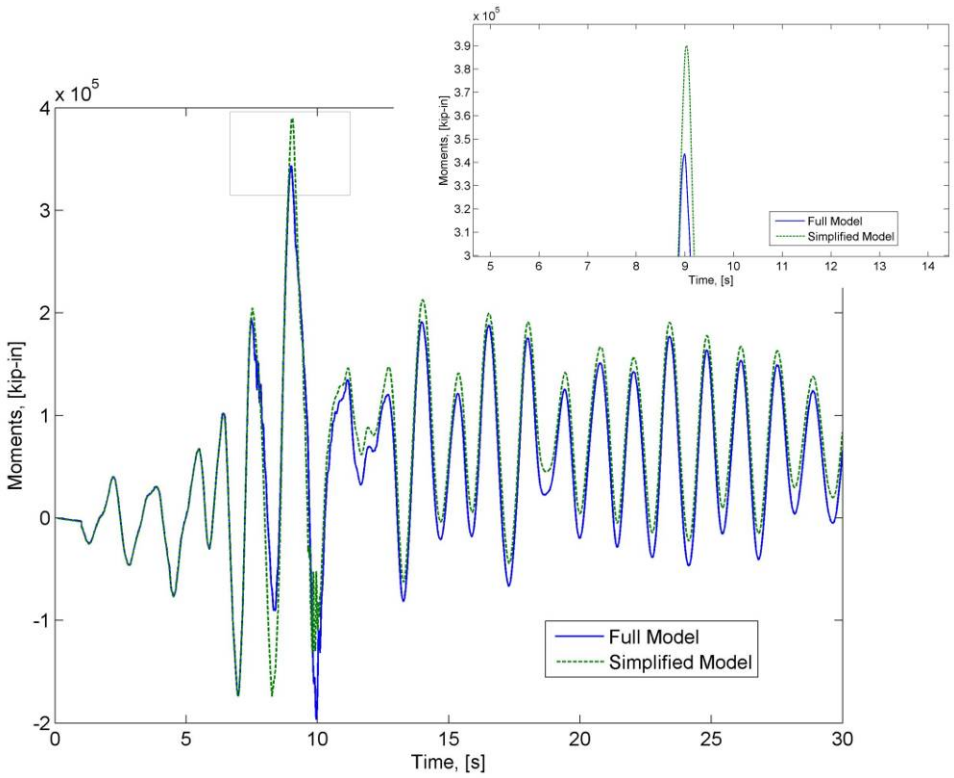

Figure 5.33: Waterside moment response to CLE6 excitation with contact element

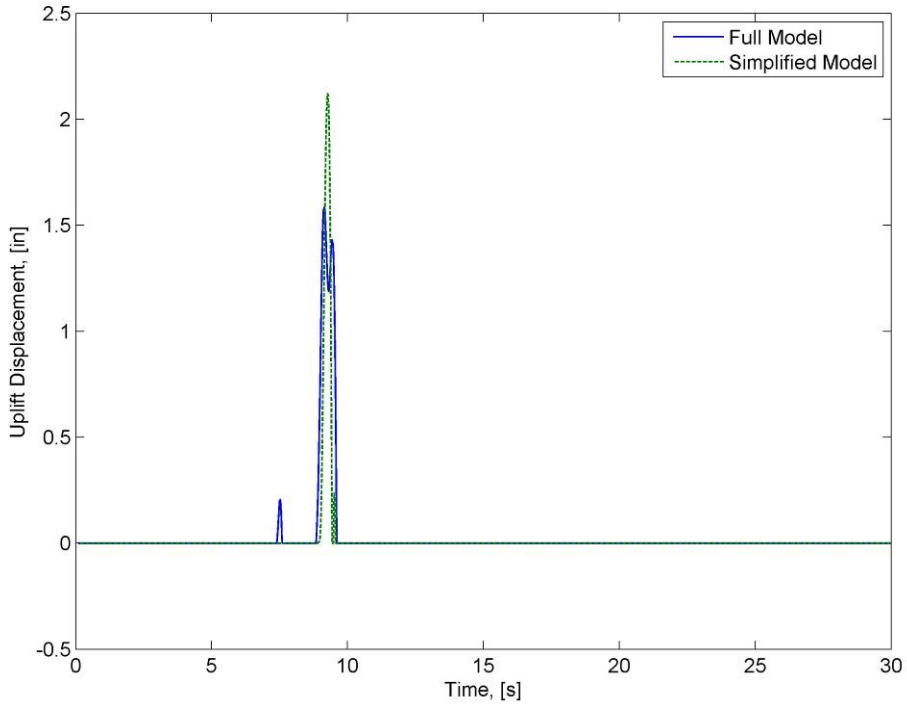

Figure 5.34: Uplift response to CLE6 excitation with contact element

5.4 Conclusions

A finite element model of the test specimen described in Chapter 3 is created and calibrated using the test data from Chapter 4. A 2D finite element model of the test specimen was able to capture the response of the crane observed in the experiments. Two additional 2D finite element models are created, a complete crane model and a simplified crane model. The two models have similar natural frequencies for the first three modes. They also have similar elastic responses. The portal drift levels and moments were in good agreement between the two models for all four ground motions. The simplified model captures the primary uplift responses of the complete crane, as well as the coupled uplift and elastic behavior. The simplifications made to the crane model capture the dynamic properties of the full crane, and can be used to make a model for the laboratory testing.

CHAPTER 6

DESIGN OF 1:10 SCALE EXPERIMENT

The objective of the Phase II test was to investigate the response of a large-scale container crane through the measurement of the elastic and inelastic responses as well as the uplift phenomenon.

The data collected in this phase of testing provided:

- additional data for validating analytical models and refining fragility curves.
- information on the elastic and inelastic responses of container cranes. Information will be gathered on the derailment, local buckling and collapse damage states.
- information on the sequence of damage, including the determination of when and whether plastic hinges will occur, and their rotation capacity.
- original data to characterize the uplift, including if the wheels peel off the ground and partially derail.

6.1 Design Constraints

For the purposes of this experiment, a jumbo crane, found at a large US port was used as the basis for the prototype crane. However, due to the fact that a model of the jumbo crane would not yield within the overturning moment capacity of the shake table certain modifications were made to the model to make it a "typical" container crane. There are several factors that influence the design of the second phase test specimen. Space limitations, constructability and desired data have the largest influence.

6.1.1 Space and Weight Limitations

One of the largest constraints on the design is the limitation on size. There are several factors that influence the size, including:

- *The overturning moment capacity of the table:* The most influential constraint was the overturning moment of the table, which was rated at 333 kip-ft (46 ton-m). Exceeding this limit would lead to severe control problems, and thus this criterion became the controlling parameter for the specimen design. Removing the existing shake table extensions lowered the center of mass of the structure by 3 feet (nearly 1 m), reducing the overturning moment.
- *The geometric constraints of the table*: Removing the shake table extensions reduces the size of the table to 12 ft x 12 ft (~4m x 4m). For practical reasons, the size of the specimen has to be somewhat smaller; thus a 10 ft. maximum gauge was used, leading to a geometric length scale of 1:10 for the specimen.
- *The available masses*: The mass of the structure must be less than 30 kips for the overturning moment to be less 333 kip-ft for the selected ground motions. The masses available at the facility were in the form of large plates that could not be cut apart. Therefore the mass had to be placed as large concentrated masses.

6.1.2 Desired Data and Response

Previous studies have only considered the elastic and uplift responses of container cranes. However, modern jumbo cranes are expected to experience yielding of the cross-sections and local buckling of the legs. Therefore, it was critical to investigate these non-

linear effects. Whatever similitude laws were chosen had to allow for a model that can exhibit these behaviors. The scaling relationships used in the studies by Kanayama and Kashawasaki (1998), Kanayama et al (2008) and Sugano et al (2006) involved scaling moments by l^5 and the mass by l^3. Using these scale factors, the resulting sections often have larger moment capacities than the similitude laws require. In the Phase I test from this study, a minimum thickness of the members was imposed, leading to moment capacities that were larger than the laws of similitude required. A set of scaling relationships that allowed for members with proper moment capacities were used in Phase II.

The current design philosophy is that if a crane is designed to remain elastic until uplift, it will not be damaged during a seismic event. Therefore, the crane should be designed such that it remains elastic until uplift. In order to gather any information on the inelastic damage states, the crane must yield, buckle and collapse within the limits of the overturning moment of the shake table. The jumbo crane yields at accelerations nearly twice what it takes to cause uplift, which is not achievable within the limits of the shake table. Therefore, it was decided to design the crane to yield at 10% higher acceleration than the uplift acceleration, and reach the ultimate limit state at 25% higher acceleration than the uplift acceleration. This allowed for the study of the inelastic behavior of the structure, while illustrating the inadequacy of the current design philosophy.

The most significant deformation mode is the portal sway mode. The torsional modes have little influence on the ultimate behavior of the crane. Removing the boom will remove the torsional mode, but does not have a significant influence on the behavior

of the crane. Additionally, based on the simulations described in Chapter 5, the A-frame has no influence on the portal sway mode. Thus the removal of the boom and a simplified design of the A-frame were used in Phase II to allow the specimen to reach the inelastic range within the constraints of the shake table.

6.2 Scaling Relationships

The objectives of the Phase II test included characterizing the non-linear behavior of the members. Therefore, as large a length scale as possible was chosen. A length scale of 1:10 fits the geometric constraints of the laboratory, and yields a needed mass that could be accommodated by the masses available. The crane was modeled using the laws of similitude, so three independent quantities for the properties were selected, and the rest of the quantities are determined from these. As with the previous test, the gravity and elastic modulus factors were both 1:1, because of the importance of gravity and using steel in the model. All of the other scale factors were calculated based on the previously mentioned scale factors, and are summarized in Table 6.1.

Table 6.1: Summary of scaling properties for 1/10th scale specimen

Quantity	*Symbol*	*Factor*
Geometric Length, l	λ_l	10
Elastic Modulus, E	λ_E	1
Acceleration, a	λ_a	1
Mass, m	λ_m	100

6.3 Simplified Crane Model

6.3.1 Basic Geometry

Figures 6.1 and 6.2 shows a simplified steel moment frame with very similar stiffness and mass properties as a jumbo container crane. The typical gage width for a jumbo container crane in the US is 100 ft (Schleiffarth, 2008). Based on available table width and this typical gage, a 10 ft wide model was selected. The range of typical portal heights is 45 ft to 65 ft (Schleiffarth, 2008). A prototype height of 55 ft, or 5.5 ft in the model scale was chosen to fit in that range.

The moments of inertia for the members of the portal frame were selected based on the prototype crane. The members were then adjusted to ensure that the period of the crane would be within the range of typical periods for container cranes. The typical range of periods for container cranes on the west coast of the US is 1.5 to 1.8s (Schleiffarth, 2008), corresponding to 0.47 and 0.57 in the model scale.

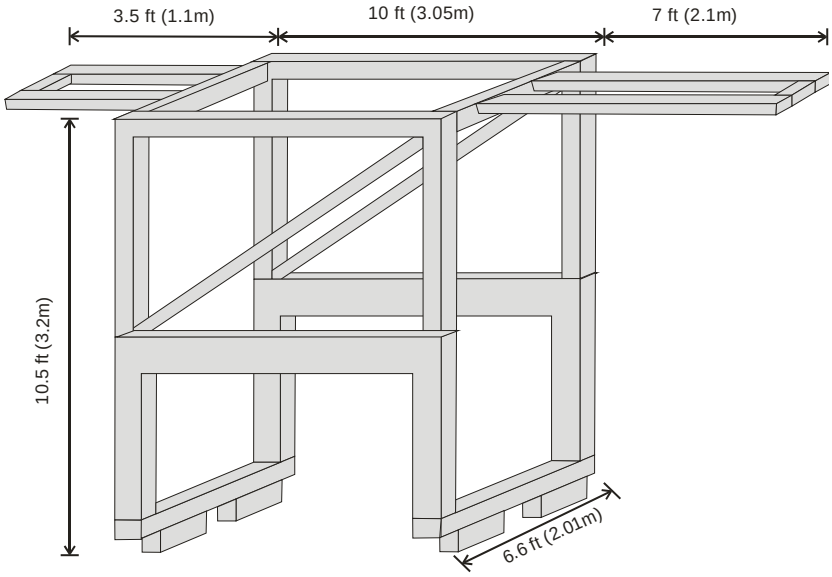

Figure 6.1: 1/10th scale crane model

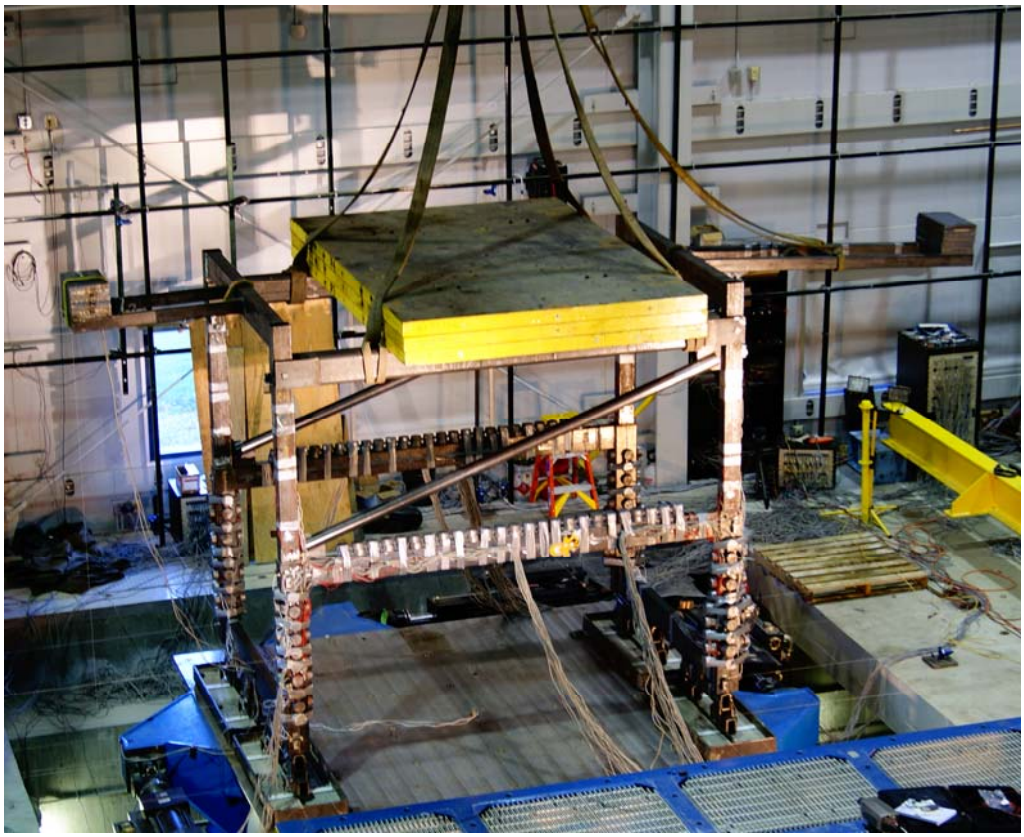

Figure 6.2: 1/10th scale crane model on shake table

6.3.2 Additional Mass

Similitude required the crane model to have a mass of approximately 29.5 kips. To enforce the mass scaling, a very large ballast mass was required, as the specimen itself only weighed 3.5 kips. To save on material cost and to simplify the mass attachment, the required ballast mass was attached in three ways. First, 1570 lbs of lead ingots were distributed around the portal frame. These distributed masses around the portal frame were important for maintaining similitude under the large second order effects expected for this flexible portal frame. Second, the University at Buffalo had 3 large steel plates that totaled 25,500 lbs. These were attached at the center of mass of the crane, as shown

in Figure 6.3. Third, stacks of 40 lb steel plates, totaling 360 lbs, were attached at the end of the boom segments.

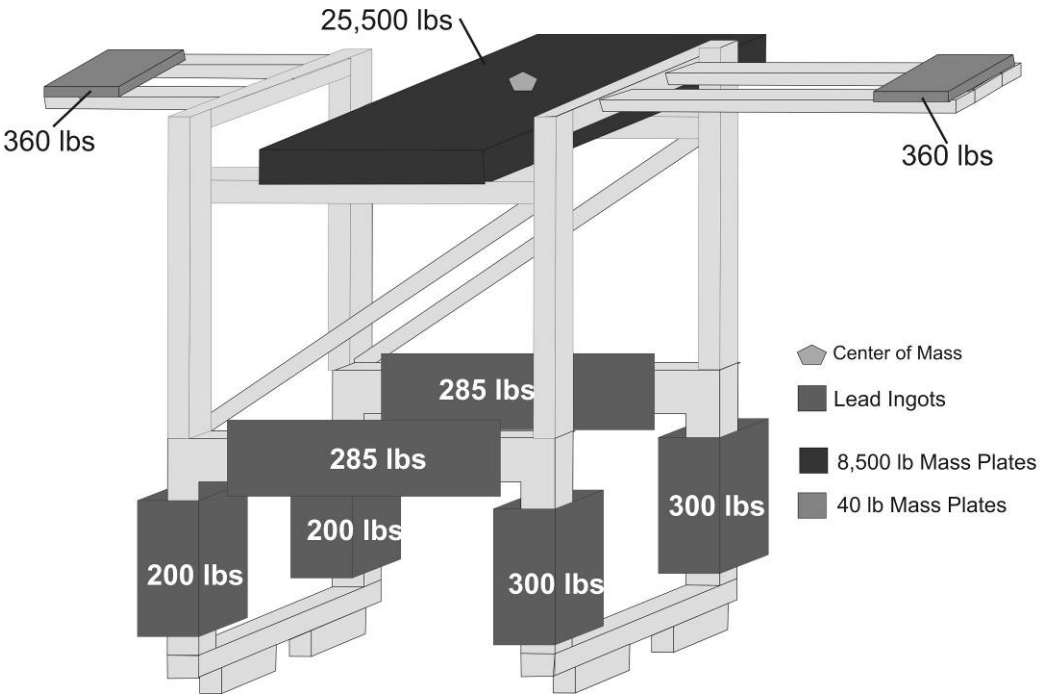

Figure 6.3: Location of applied mass on 1/10th scale model

6.3.3 Boundary Conditions

The boundary conditions play an important role in the response of the structure to earthquake loading. A container crane in the field has a complex system of balance beams and trucks, which sit on a rail. The 1:10 scale model had similar boundary conditions to the prototype structure (Figures 6.4 and 6.5), allowing for an accurate representation of uplift. The model rails were 7/16-inch wide cold rolled steel plate embedded in concrete to simulate a rail embedded in a wharf deck (Figures 6.6 and 6.7). The trucks were connected to a balance beam using pins, as in the prototype structure.

The wheels were constructed of 3-inch circular bar. They were 3/4 inch wide with a 1/2 inch groove. The flanges on the wheels were 1/16 inch, meaning that the wheels must lift 1/16 inch prior to any horizontal movement. The wheels were then cut in half and welded in place to simulate a braked condition. Additionally, the balance beam could be connected to a threaded rod that screws into the concrete pad, so that they could be pinned to the table, allowing for data to be gathered for validation of finite element models with various boundary conditions.

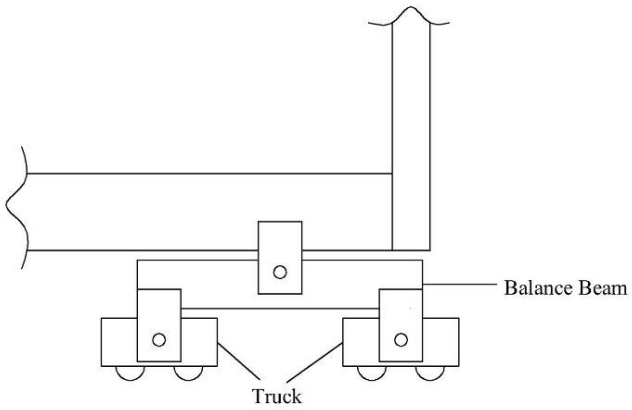

Figure 6.4: Sketch of boundary conditions for the 1/10th scale model crane

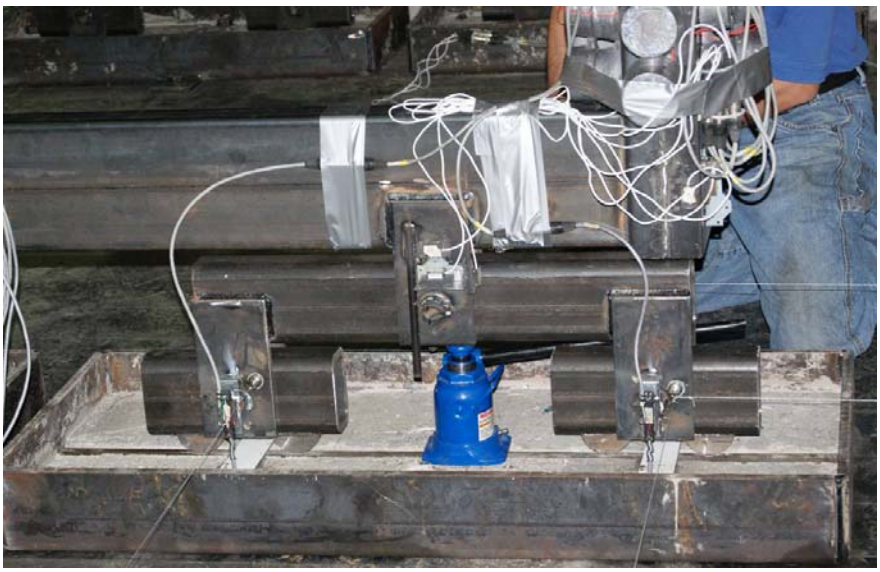

Figure 6.5: Photograph of boundary conditions for the 1/10th scale model crane

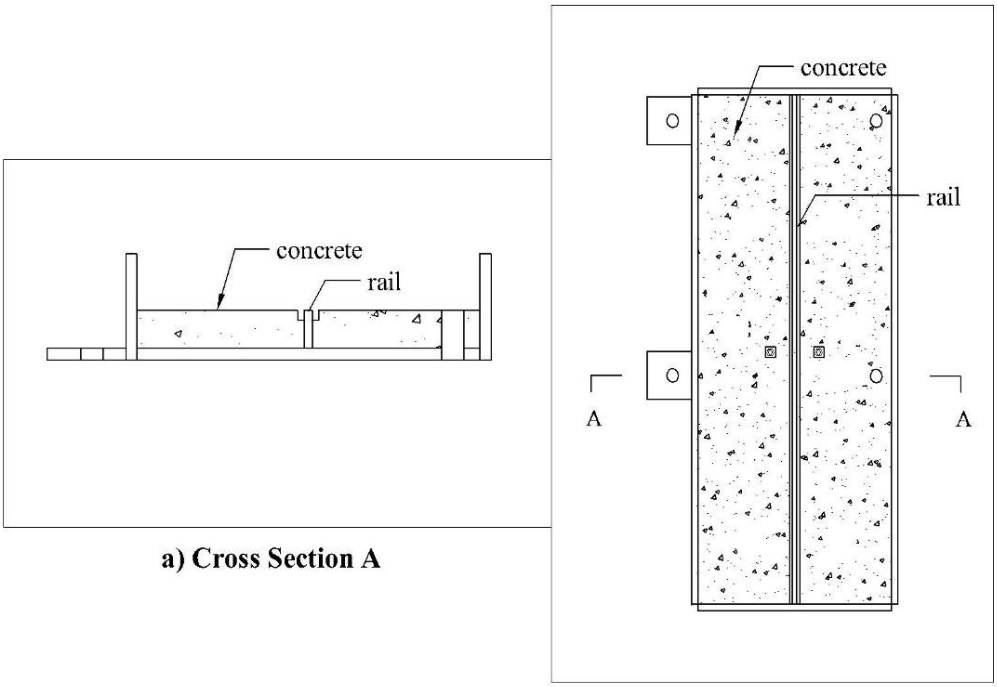

Figure 6.6: Boundary boxes: a) cross section, b) plan view

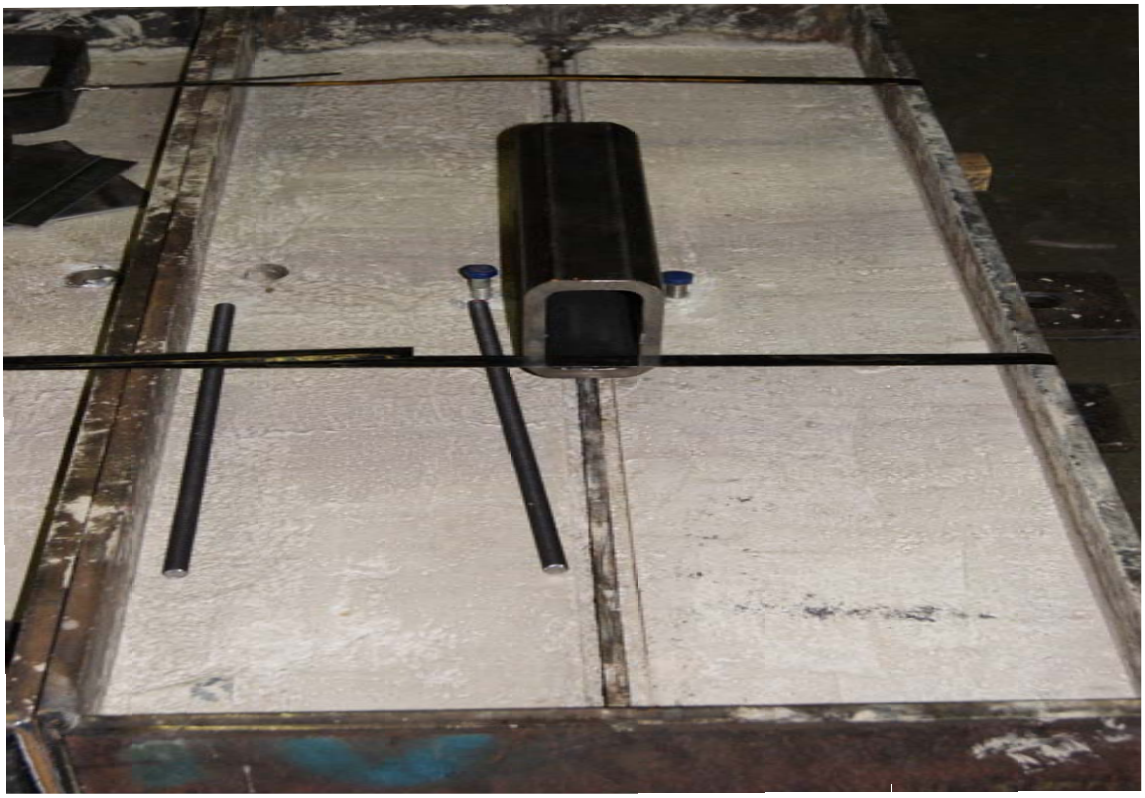

Figure 6.7: Rail boxes for the 1/10th scale model test

6.3.4 Member Design

To design the members of the model crane, the scaled versions of the prototype crane were used as a starting point. Then a simulation was run to ensure that the period of the structure was between 0.47s and 0.57s. Perfectly recreating the members from the jumbo crane would lead to yield moments that were too large to be achieved within the limits of the table. Therefore, the members were resized such that the yield moments for the legs of the portal frame are 1.1 times the tipping force so that the crane would tip before it yields, as typical cranes are designed to do, but the yield moments for the structure were achievable within the capabilities of the shake table. Table 6.2 summarizes the yield moments for the members in the portal frame. Simulation of the model crane on a shake table was run using each of the ground motions to be used during the test to ensure that the structure would yield without exceeding the overturning moment of the shake table.

Table 6.2: Yield moments for 1/10th scale model

Section	*Yield Moment (kip-in)*
Landside Leg	199
Waterside Leg	250
Portal Beam	205

There was a limit to how thin the plates that built-up specimens can be and not suffer from severer distortions and heat effects from the welding process. Therefore, the sections were limited to a minimum 1/8 inch thick. The welds were all designed according to AISC specifications for minimum weld sizes. The width to thickness ratios of the panels on the built up box sections influence when local buckling will occur. Typical cranes have stiffeners on the inside of the sections to limit the width to thickness

ratio of the subpanels. To maintain the same width to thickness ratios in the model, stiffeners were added to the sections. The small size of the sections made it difficult to add the stiffeners without warping the cross-sections. Therefore, a design was developed that allowed for a minimal amount of welding, shown in Figure 6.8.

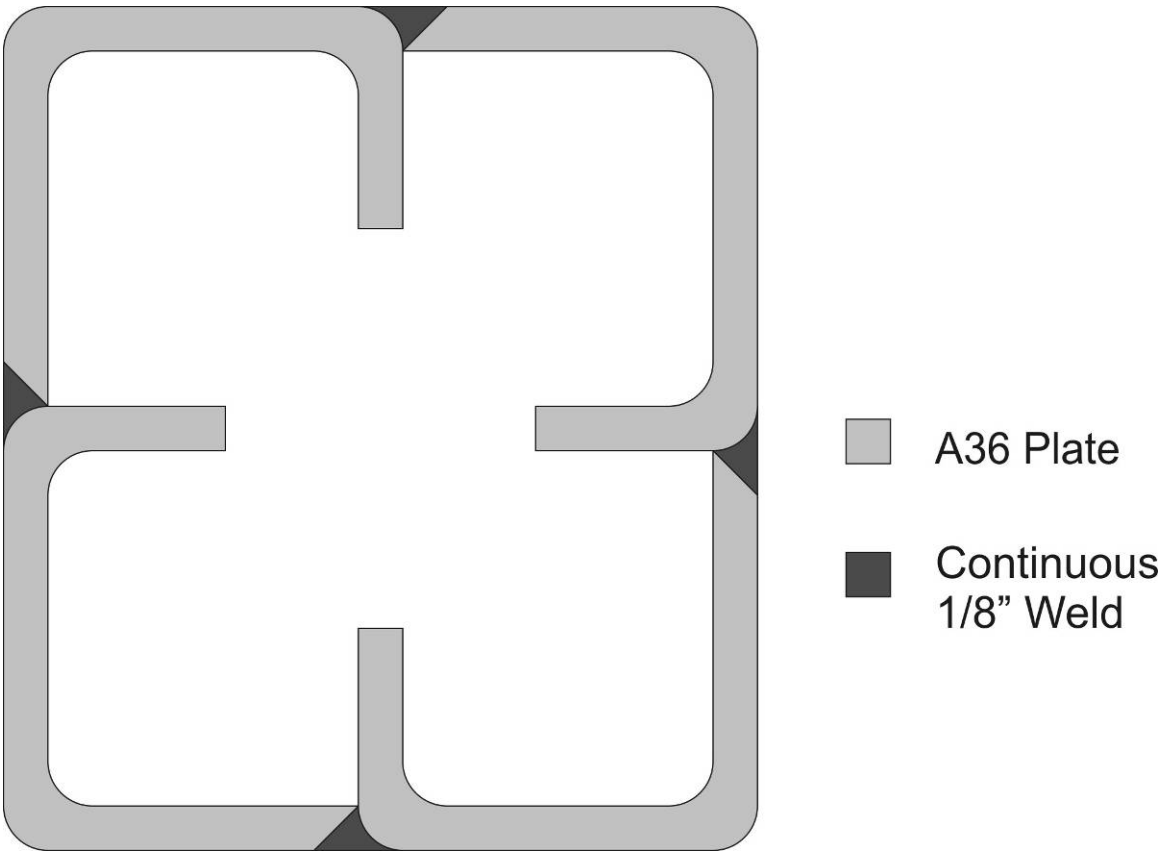

Figure 6.8: Sample cross-section for 1/10th scale model

To design the stiffener pattern, certain parameters of the prototype crane had to be evaluated. For the purposes of this experiment, a jumbo crane, found at a large US port was used for the prototype crane. These parameters give indications of whether the crane will experience wall buckling or panel buckling. In order for elastic panel buckling not to occur, MacRae and Kawashima (2001) indicate the following limits must be satisfied:

$$\frac{t}{t_0} \geq 1.0 \tag{6.1}$$

where t is the plate thickness and t_0 is minimum allowable plate thickness given by:

$$t_0 = \frac{b}{kfn} \tag{6.2}$$

where k = 24 for grade 50 steel; b = plate width, taken as the minimum of the overall section breadth (B) and the overall section depth (D). The parameter f is related to the stress gradient and is conservatively taken as 1. The number of panels divided by vertical stiffeners is n.

The ratio of the longitudinal stiffener stiffness to the plate stiffness is represented by the parameter γ_l, defined as:

$$\gamma_l = I_l / (bt^3 / 11) \tag{6.3}$$

where I_l is the longitudinal stiffener second moment of area about the surface of the main plate ($b_s^3 t_s / 3$). To determine the mode of buckling deformation (panel vs. wall buckling) the ratio of γ_l / γ_l^* must be computed (Japan 1987), where γ_l^* is the critical ratio of longitudinal stiffener stiffness to plate stiffness for wall buckling, given by:

$$\gamma_l^* = 4\alpha^2 n(1 + n\delta_l) - \frac{(\alpha^2 + 1)^2}{n}; (\alpha \leq \alpha_0) \tag{6.4}$$

$$\gamma_l^* = \frac{1}{n}[\{2n^2(1 + n\delta_l) - 1\}^2 - 1]; (\alpha > \alpha_0) \tag{6.5}$$

where α is defined as the transverse stiffener spacing divided by the plate width; and $\alpha_0 = \sqrt[4]{1 + n\gamma_l}$; δ_l is the ratio of the cross-sectional area of the longitudinal stiffener, $A_l = b_s t_s$, to that of the main plate, b_t, where b_s is the longitudinal stiffener width and t_s is the longitudinal stiffener thickness. If γ_l / γ_l^* is greater than one, then panel buckling is expected, and if it is greater than one, then wall buckling is expected.

All the parameters are computed for the prototype crane and then the model crane is designed to have similar parameters, so that the same manner of buckling will occur. Table 6.3 summarizes the results of the calculations. It can be seen that all of the members of the portal frame will fail in panel buckling in both the prototype and model cranes.

Table 6.3: Summary of buckling calculations

Quantity	*Landside Prototype*	*Waterside Prototype*	*Beam Prototype*	*Landside Model*	*Waterside Model*	*Beam Prototype*
b (in)	77.37	77.37	118.1	6.0	6.5	2.5
t (in)	0.630	0.787	0.315	0.125	0.125	0.125
t_0 (in)	0.929	0.929	0.558	0.068	0.094	0.052
b_s (in)	3.94	3.94	3.94	1.25	1.25	1.25
t_s (in)	0.315	0.315	0.315	0.125	0.125	0.125
I_l (in^4)	18.55	18.55	18.55	0.0814	0.0814	0.0814
γ_l	14.63	14.63	66.27	169.1	122.1	219.8
α	1.01	1.01	1.06	N/A	N/A	N/A
n	3	3	5	2	2	2
γ_l^*	12.64	12.64	27.67	86.01	64.99	112.0
γ_l / γ_l^*	1.16	1.16	2.39	1.97	1.88	1.96

Some other parameters that are important to the nonlinear response of the stiffened box sections are the computed maximum strength, $H_{\max}/H_y$, and the ductility factors δ_m/δ_y and δ_{95}/δ_y. A study by Usami et al. (2000b) defines the three ratios as follows:

$$\frac{H_{\max}}{H_y} = \frac{0.10}{(R_f \bar{\lambda} \bar{\lambda}_s')^{0.5}} + 1.06 \tag{6.6}$$

$$\frac{\delta_m}{\delta_y} = \frac{0.22}{R_f \sqrt{\bar{\lambda}} \bar{\lambda}_s'} + 1.20 \tag{6.7}$$

$$\frac{\delta_{95}}{\delta_y} = \frac{0.25}{(1 + P/P_y) R_f \sqrt{\bar{\lambda}} \bar{\lambda}_s'} + 2.31 \tag{6.8}$$

where R_f is flange width-thickness ratio, λ is the column slenderness ratio, λ_s' is the stiffener's equivalent slenderness ratio. These parameters are defined by Ge et al. (2000) as:

$$R_f = \frac{b}{t}\sqrt{\frac{\sigma_y}{E}\frac{12(1-\nu^2)}{\pi^2 k}} \tag{6.9}$$

$$\bar{\lambda} = \frac{2h}{r}\frac{1}{\pi}\sqrt{\frac{\sigma_y}{E}} \tag{6.10}$$

$$\bar{\lambda_s} = \frac{1}{\sqrt{Q}}\frac{L_d}{r_s}\frac{1}{\pi}\sqrt{\frac{\sigma_y}{E}} \tag{6.11}$$

$$Q = \frac{1}{2R_f}[\beta - \sqrt{\beta^2 - 4R_f}] \tag{6.12}$$

$$\beta = 1.33R_f + 0.868 \tag{6.13}$$

where b is the flange plate width; t is the plate thickness; σ_y is the expected value of the yield stress, assumed at 52.3; E is the Young's Modulus, 29,000 ksi; ν the Poisson's ratio, 0.3; k the buckling coefficient of a stiffened plate = $4n^2$ (n = the number of subpanels in a stiffened plate), h column height and r the radius of gyration if the cross section, L_d is the distance between two adjacent diaphragms, r_s is the radius of gyration of a T-shape centered on a longitudinal stiffener with a width of b/n, and Q is the local buckling strength of a plate enclosed by two adjacent stiffeners. The ultimate strength and ductility parameters for the prototype and model crane are summarized in Table 6.4.

Table 6.4: Ultimate strength and ductility parameters

Parameter	*Landside Prototype*	*Waterside Prototype*	*Beam Prototype*	*Landside Model*	*Waterside Model*	*Beam Prototype*
H_{max}/H_y	1.18	1.15	1.10	1.17	1.15	1.13
δ_m/δ_y	1.50	1.41	1.25	1.59	1.45	1.41
δ_{95}/δ_y	2.61	2.52	2.36	2.70	2.56	2.52

Based on the calculated parameters from the prototype crane, rectangular stiffeners that are 1.25 inches wide and 0.125 inches thick are selected. One stiffener per side of the rectangular tube is used, dividing the cross-section into two subpanels. It can be seen in Table 6.3 that the resulting cross-sections will experience panel buckling, as in the prototype crane. It can also be seen in Table 6.4 that the resulting cross sections yield the similar parameters for ultimate strength and ductility parameters. This stiffener design will ensure that the model has similar buckling and post yield behavior to the prototype crane.

Another member that has to be designed with care is the beam that supports the large mass plates. In order to get the proper behavior of the structure, excessive deformations of the structure need to be avoided. Therefore, the member is designed with a limit of 0.25 inch deflection under gravity load. The resulting member has 8x6x5/8 cross section. Additionally, to avoid putting excessive moments in the columns to which they are attached, the beams are attached using pins, Figure 6.9. The pins are designed to carry the entire weight of the mass plates.

Figure 6.10 shows a schematic of the model crane, and highlights the various members of the structure. Additionally, Table 6.5 gives details of the moments of inertia and cross-section area of members in the structure. Further details of the design such as, section dimensions and fabrication drawings can be found in Appendix C.

Figure 6.9: Pin connection for mass plate support beams for 1/10th scale model

Table 6.5: Member details for 1/10th scale model

Member	I_x (in^4)	I_y (in^4)	A (in^2)
A	30.17	13.55	4.51
B	14.04	10.25	3.38
C	7.34	13.51	2.44
D	8.09	17.81	2.63
E	34.95	8.50	4.14
F	132.6	193.1	17.5
G	4.18	16.67	2.44
L	2.86	4.53	2.25

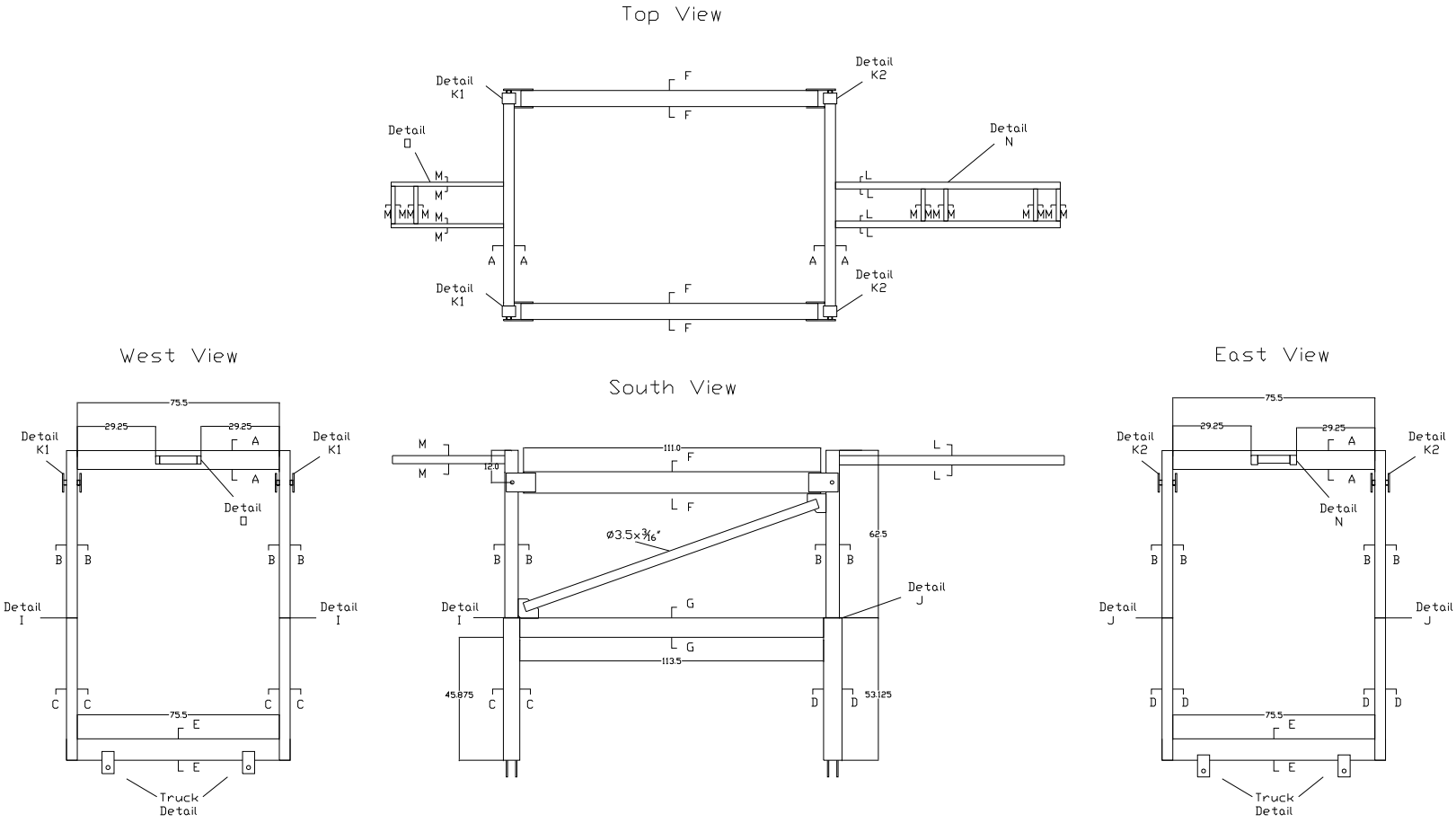

Figure 6.10: Schematic of 1/10th scale model

6.4 Instrumentation

6.4.1 Response Quantities

There were several important response quantities to be measured in this study, including: vertical and horizontal displacements of the legs, stresses in the portal joints, accelerations of the frame and distribution of weight. Tracking the displacements of the legs allows for the characterization of the movement of the crane during seismic loading and to determine when derailment will occur. Part of the goal of the second phase of testing was to determine the nonlinear response of the crane. Monitoring the stresses in the portal joint will allow for determining the sequence of damage and when yielding occurs. Monitoring the distribution of weight of the crane allows for determining the distribution of forces within the crane as well as to the wharf deck and crane rails. All of these response quantities are important to know when designing structures in a port.

6.4.2 Instrumentation Scheme

To measure the response quantities mentioned in the previous section, an instrumentation scheme was developed that uses strain gages, accelerometers and displacement gages. Table 6.6 summarizes the instrumentation plan.

Table 6.6: Instrumentation plan summary for 1/10th scale test

Instrument	*Number of Channels*
Accelerometers	54
Displacement Gages	38
Strain Gages	96
TOTAL	188

Fifty-four channels of accelerometers were used. Figure 6.11 illustrates the details of the accelerometer plan. The accelerometers were in groups of three, oriented in three orthogonal directions.

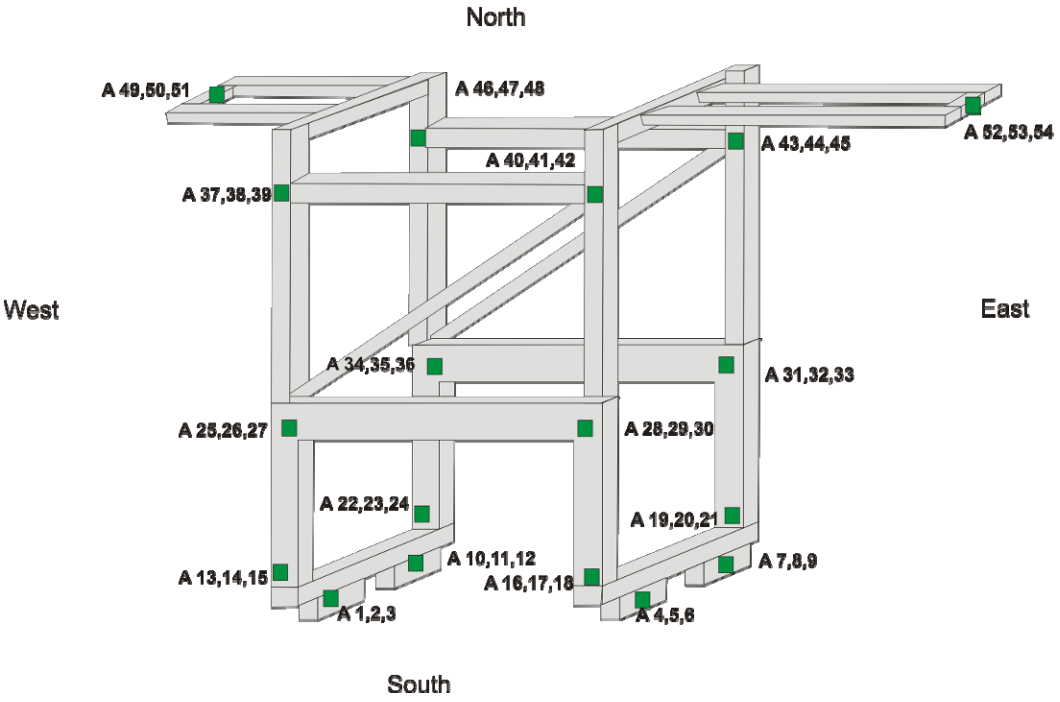

Figure 6.11: Acceleration plan for 1/10th scale experiment

Thirty-eight potentiometers were used to measure important displacement values. Figure 6.12 shows the details of the potentiometer plan. For the vertical displacement at the base, linear variable potentiometers were used. All of the other displacement gages were string potentiometers. The places where three potentiometers are indicated, the gages were oriented in the three perpendicular directions of West-East, North-South and vertical. Where only one is indicated, the displacement was measured in the West-East direction. Where two are located, the gages are oriented in the two horizontal directions.

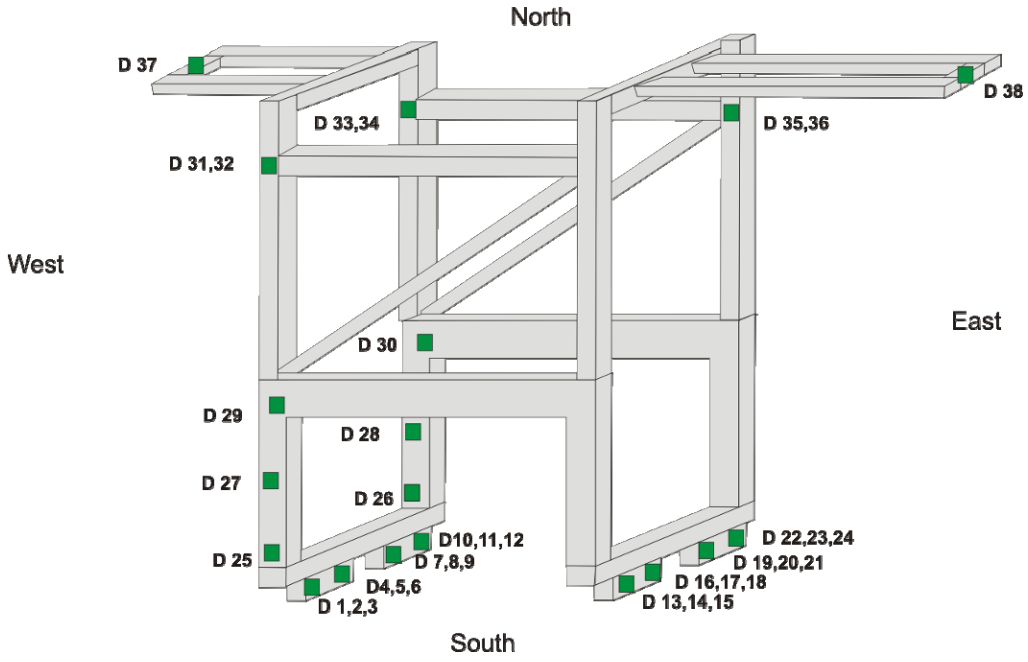

Figure 6.12: Displacement gage scheme for 1/10th scale model

Ninety-six channels of strain gages were applied in groups of four in the locations shown in Figure 6.13.

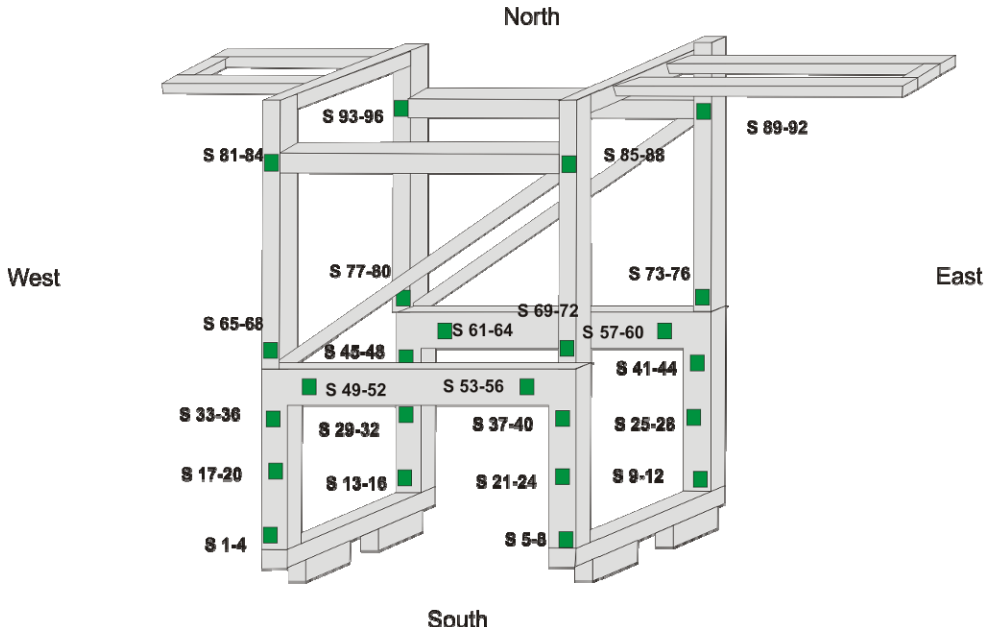

Figure 6.13: Strain gage placement scheme for 1/10th scale model

6.5 Ground Motions

For the Phase II test, six ground motions were chosen that represent expected motions at a port. Five of the six ground motions were the same as in Phase I, and are described in section 3.3. The sixth ground motion is from the results of a centrifuge test performed by Schlecter et al. (2000). The purpose of that study was to examine the seismic performance of pile-supported wharf structures. The configuration of the wharves for the test was chosen so that they are generalized representations of typical pile-supported wharf structures from ports in the western United States. Schlecter et al. did several models using various scaling techniques. The test of most interest to this study was the NMJ02 model, which was a model that was scaled in a manner that the piles did not reach the bottom of the centrifuge box, thus creating a realistic boundary condition for the wharf. The wharf model was constructed in soils that are representative of those found in ports in the western United States. Schelchter et al. (2000) used many gauges, but the accelerometers of most interest to this study were placed on the model wharf deck in three orthogonal directions that correspond to the cranes' trolley travel, gantry travel and vertical directions. The researchers ran several tests utilizing various ground motions. The ground motion input selected for is study is the Northridge Rinaldi with an average peak-to-peak acceleration of 0.806g. This motion was selected because the soil liquefied, and the response of the crane when the soil liquefies is of interest. The response spectra for the ground motions at 1.5% damping are shown in Figure 6.14. The test protocol used in Phase II is shown in Table 6.7.

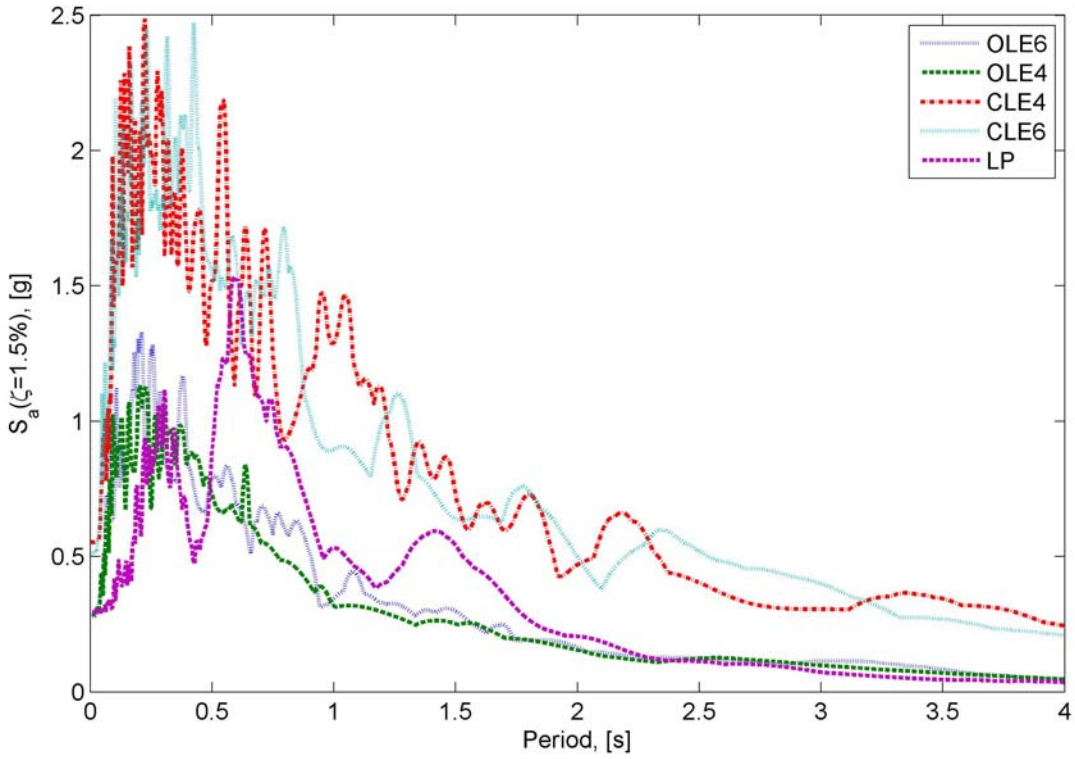

Figure 6.14: Response spectra for ground motions in prototype scale

Table 6.7: Phase II test protocol

Run #	*Boundary Condition*	*Earthquake*	*Components*	*PGA (in g)*		
				H1(Long)	*H2(Trnsv)*	*V*
wn1		white noise	x,y,z	0.08	0.08	0.08
wn2		white noise	x,y,z	0.08	0.08	0.08
1	Tied down	OLE6	H1	0.2141		
2	Tied down		.3H2		0.0717	
3	Tied down		H1+.3H2	0.2141	0.0717	
4	Tied down	OLE4	H1	0.2091		
5	Tied down		.3H2		0.0598	
6	Tied down		H1+.3H2	0.2091	0.0598	
7	Tied down	LP	H1	0.1309		
8	Tied down		.3H2		0.0881	
9	Tied down		H1+.3H2	0.1309	0.0881	
10	Tied down		H1+V	0.1309		0.0196
11	Tied down		H1+.3H2+V	0.1309	0.0881	0.0196

Run #	*Boundary Condition*	*Earthquake*	*Components*	*PGA (in g)*		
				H1(Long)	*H2(Trnsv)*	*V*
12	Tied down	CLE6	H1	0.1535		
13	Tied down		.3H2		0.0601	
14	Tied down		H1+.3H2	0.1535	0.0601	
15	Tied down		H1+V	0.1535		0.1353
16	Tied down		H1+.3H2+V	0.1535	0.0601	0.1353
17	Tied down	CLE4	H1	0.1659		
18	Tied down		.3H2		0.0485	
19	Tied down		H1+.3H2	0.1659	0.0485	
20	Tied down		H1+V	0.1659		0.1314
21	Tied down		H1+.3H2+V	0.1659	0.0485	0.1314
22	Tied down	OLE6	H1	0.2854		
23	Tied down		.3H2		0.0965	
24	Tied down		H1+.3H2	0.2854	0.0956	
25	Tied down	OLE4	H1	0.2788		
26	Tied down		.3H2		0.0797	
27	Tied down		H1+.3H2	0.2788	0.0797	
28	Tied down	LP	H1	0.1745		
29	Tied down		H2		0.1174	
30	Tied down		H1+H2	0.1745	0.1174	
31	Tied down		H1+V	0.1745		0.0261
32	Tied down		H1+H2+V	0.1745	0.1174	0.0261
33	Tied down	CLE6	H1	0.2047		
34	Tied down		.3H2		0.08012	
35	Tied down		H1+.3H2	0.2047	0.08012	
36	Tied down		H1+V	0.2047		0.1804
37	Tied down		H1+.3H2+V	0.2047	0.0801	0.1804
38	Tied down	CLE4	H1	0.2212		
39	Tied down		.3H2		0.0647	
40	Tied down		H1+.3H2	0.2212	0.0647	
41	Tied down		H1+V	0.2212		0.1752
42	Tied down		H1+ .3H2+V	0.2212	0.0647	0.1752
43	Tied down	njm_02_49	H1	0.0789		
44	Tied down		H2		0.0189	
45	Tied down		H1+H2	0.0789	0.0189	
46	Tied down		H1+V	0.0789		0.0081
47	Tied down		H1+ H2+V	0.0789	0.0189	0.0081
wn3	free	white noise	x,y,z	0.08	0.08	0.08

Run #	*Boundary Condition*	*Earthquake*	*Components*	*PGA (in g)*		
				H1(Long)	*H2(Trnsv)*	*V*
wn4	free	white noise	x,y,z	0.08	0.08	0.08
wn5	free	white noise	x,y,z	0.08	0.08	0.08
48	free	OLE6	H1	0.2141		
49	free		.3H2		0.0717	
50	free		H1+.3H2	0.2141	0.0717	
51	free	OLE4	H1	0.2091		
52	free		.3H2		0.0598	
53	free		H1+.3H2	0.2091	0.0598	
54	free	LP	H1	0.1309		
55	free		.3H2		0.0881	
56	free		H1+.3H2	0.1309	0.0881	
57	free		H1+V	0.1309		0.0196
58	free		H1+ .3H2+V	0.1309	0.0881	0.0196
59	free	CLE6	H1	0.1535		
60	free		.3H2		0.0601	
61	free		H1+.3H2	0.1535	0.0601	
62	free		H1+V	0.1535		0.1353
63	free		H1+ .3H2+V	0.1535	0.0601	0.1353
64	free	CLE4	H1	0.1659		
65	free		.3H2		0.0485	
66	free		H1+.3H2	0.1659	0.0485	
67	free		H1+V	0.1659		0.1314
68	free		H1+ .3H2+V	0.1659	0.0485	0.1314
69	free	OLE6	H1	0.2854		
70	free		.3H2		0.0965	
71	free		H1+.3H2	0.2854	0.0956	
72	free	OLE4	H1	0.2788		
73	free		.3H2		0.0797	
74	free		H1+.3H2	0.2788	0.0797	
75	free	LP	H1	0.1745		
76	free		.3H2		0.1174	
77	free		H1+.3H2	0.1745	0.1174	
78	free		H1+V	0.1745		0.0261
79	free		H1+ .3H2+V	0.1745	0.1174	0.0261
80	free	CLE6	H1	0.2047		
81	free		.3H2		0.0801	

Run #	*Boundary Condition*	*Earthquake*	*Components*	*PGA (in g)*		
				H1(Long)	*H2(Trnsv)*	*V*
82	free	CLE6	H1+.3H2	0.2047	0.08012	
83	free		H1+V	0.2047		0.1804
84	free		H1+ .3H2+V	0.2047	0.0801	0.1804
85	free	CLE4	H1	0.2212		
85b	free		H1	0.2212		
86	free		.3H2		0.0647	
87	free		H1+.3H2	0.2212	0.0647	
88	free		H1+V	0.2212		0.1752
89	free		H1+ .3H2+V	0.2212	0.0647	0.1752
90	free	njm_02_49	H1	0.0789		
91	free		.3H2		0.0189	
92	free		H1+.3H2	0.0789	0.0189	
93	free		H1+V	0.0789		0.0081
94	free		H1+ .3H2+V	0.0789	0.0189	0.0081
95	free	CLE6	H1	0.1791		
96	free		.3H2		0.0701	
97	free		H1+.3H2	0.1791	0.0701	
98	free		H1+V	0.1791		0.1578
99	free		H1+ .3H2+V	0.1791	0.0701	0.1578
100	free	CLE4	H1	0.1936		
101	free		.3H2		0.0566	
102	free		H1+.3H2	0.1936	0.0566	
103	free		H1+V	0.1936		0.1533
104	free		H1+ .3H2+V	0.1936	0.0566	0.1533
105	free		H1	0.2489		
106	free		H1	0.2766		
107	free		H1	0.3042		
108	free		H1	0.3319		
109	free		H1	0.3595		
110	free		H1	0.1936		
111	free		H1	0.2489		
112	free		H1	0.2766		
113	free		H1	0.3042		
114	free		H1	0.3319		
115	free		H1	0.3595		
116	free		H1	0.3872		
117	free	LP	H1	0.2835		

Run #	*Boundary Condition*	*Earthquake*	*Components*	*PGA (in g)*		
				H1(Long)	*H2(Trnsv)*	*V*
118	free	LP	.3H2		0.1908	
119	free		H1+.3H2	0.2835	0.1908	
120	free		H1+V	0.2835		0.0424
121	free		H1+ .3H2+V	0.2835	0.1908	0.0424
122	free	CLE6	H1	0.3326		
123	free		H1	0.3070		
124	free		.3H2		0.1202	
125	free		H1+.3H2	0.3070	0.1202	
126	free		H1+V	0.3070		
127	free		H1+ .3H2+V	0.3070	0.1202	
128	free	cle4	H1	0.3595		
wn6	free	white noise	x,y,z	0.08	0.08	0.08
129	free	cle4	H1	0.3042		
130	free		H1	0.3042		
131	free		.3H2		0.1052	
132	free		H1+.3H2	0.3042	0.1052	
133	free		H1+V	0.3042		0.2847
134	free		H1+ .3H2+V	0.3042	0.1052	0.2847
135	free	njm_02_49	H1	0.1577		
136	free		.3H2		0.0378	
137	free		H1+.3H2	0.1577	0.0378	
138	free		H1+V	0.1577		0.0161
139	free		H1+ .3H2+V	0.1577	0.0378	0.0161
wn7	free	white noise	x,y,z	0.08	0.08	0.08
140	free	CLE6	H1+.3H2	0.3070	0.1202	
141	free	LP	H1	0.3053		
142	free		.3H2		0.2055	
143	free		H1+.3H2	0.3053	0.1908	
144	free		H1+V	0.3053		0.0456
145	free		H1+ .3H2+V	0.3053	0.2055	0.0456
146	free	CLE6	.3H2		0.1302	
147	free		H1+.3H2	0.3326	0.1302	
wn8	free	white noise	x,y,z	0.08	0.08	0.08
148	free	CLE6	H1+V	0.3326		0.2931
wn9	free	white noise	x,y,z	0.08	0.08	0.08
149	free	CLE6	H1+.3H2+V	0.3326	0.1302	0.2931
150	free	CLE4	H1	0.3595		

Run #	*Boundary Condition*	*Earthquake*	*Components*	*PGA (in g)*		
				H1(Long)	*H2(Trnsv)*	*V*
151	free	CLE4	.3H2		0.1052	
152	free		H1+.3H2	0.3595	0.1052	
153	free		H1+V	0.3595		0.2847
154	free		H1+ .3H2+V	0.3595	0.1052	0.2847
155	free	njm_02_49	H1	0.1341		
156	free		H1	0.1419		
157	free		H1	0.1498		
158	free		H1	0.1656		
wn10	free	white noise	x,y,z	0.08	0.08	0.08
159	free	njm_02_49	H2		0.0321	
160	free		H1+H2	0.1577	0.0378	
161	free		H1+V	0.1577		0.0161
162	free		H1+.3H2+v	0.1577	0.0378	0.0161
wn11	free	white noise	x,y,z	0.08	0.08	0.08
163	free	CLE4	H1	0.3319		
164	free		H1	0.3872		
165	free		H1	0.4148		
166	free		H1	0.4425		
167	free		H1	0.4701		
168	free		H1	0.4978		
169	free		H1	0.5254		
170	free		H1	0.5531		
171	free		H1+.3H2+V	0.5531	0.1618	0.4380
172	free		H1+.3H2+V	0.6637	0.1942	0.5256
wn12	free	white noise	x,y,z	0.08	0.08	0.08
173	free	njm_02_49	H1+H2+V	0.2366	0.0567	0.0242
174	free		H1+H2+V	0.3154	0.0756	0.0322
175	free		H1+H2+V	0.0789	0.0189	0.0081
176	free		H1+H2+V	0.1183	0.0284	0.0121
177	free		H1+H2+V	0.1577	0.0378	0.0161
178	free		H1+H2+V	0.1972	0.0473	0.0201
179	free		H1+H2+V	0.2366	0.0567	0.0242
180	free		H1+H2+V	0.2760	0.0662	0.0282
181	free		H1+H2+V	0.3154	0.0756	0.0322
182	free	CLE6	H1	0.3582		
183	free		H1	0.4094		
184	free		H1	0.4605		

Run #	*Boundary Condition*	*Earthquake*	*Components*	*PGA (in g)*		
				H1(Long)	*H2(Trnsv)*	*V*
185	free	CLE6	H1	0.5117		
186	free		H1+.3H2+V	0.5117	0.2003	0.4509
187	free		H1+V	0.5117		0.4509
188	free	CLE4	H1	0.5531		
189	free		H1+V	0.5531		0.4380
190	free		H1+.3H2+V	0.5531	0.1618	0.4380
191	free	njm_02_49	H1+H2+V	0.3943	0.0945	0.0403
192	free		H1+H2+V	0.4337	0.1040	0.0443
193	free		H1+H2+V	0.4732	0.1134	0.0483

CHAPTER 7

PHASE II TEST RESULTS AND DISCUSSION

The goal of the Phase II test was to investigate the response of a 1/10-scale container crane through the measurement of the elastic and inelastic responses and the interaction between flexural behavior and the expected uplift/derailment. Additionally, information of the sequence of damage was collected. Phase II testing was completed at the University at Buffalo between November 9 and December 1, 2009. The test included 193 trials with various earthquake ground motions and low amplitude white noise inputs. Information was also gathered on the influence of the various components of ground motions. The results of the Phase II test are presented and discussed in this chapter.

7.1 White Noise Testing

Uncorrelated, low amplitude white noise tests were performed for system identification purposes throughout the testing. The white noise tests were performed at the beginning of each day of testing and after some of the large amplitude ground motions. White noise was run through the system in all three orthogonal directions. The white noise tests allowed for the determination of the frequencies at which the various modes occur. Figure 7.1 shows a graph of the frequency response of the crane during one of the white noise tests. It can be seen that the primary bending mode (via portal sway) occurs at a period of 0.74s (1.35 Hz), compared to the target period of .5s. Table 7.1 shows a summary of the two most important vibration modes for the two boundary conditions. The mode shapes are illustrated in Figure 7.2. Figure 7.3 shows the portal sway mode for each of the white noise tests. The pinned base tests have a shorter period

than the tests where the structure was free to uplift. This is due to the pins themselves adding some rigidity and constraint to the structure. White noise tests 12 and 13 occurred after yielding of the structure occurred, and have longer periods than the previous tests. The model structure is more flexible than predicted from the analytical model due to the flexibility of the truck system, which had been modeled as a rigid system.

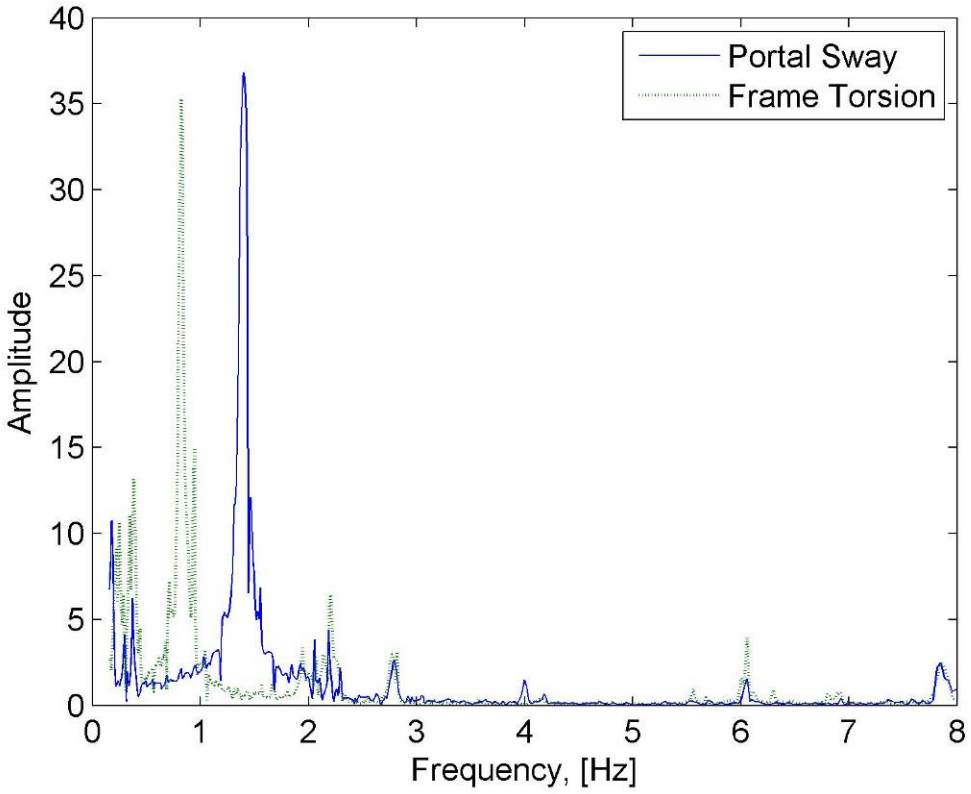

Figure 7.1: Frequency response function for a white noise test

Table 7.1: Summary of experimental modes

Mode	*Boundary Condition*	*T.* [sec]	*ζ.* [%]
Portal sway	Free	0.74	1.87
Frame Torsion	Free	1.22	1.94
Portal sway	Pinned	0.65	1.61
Frame Torsion	Pinned	0.82	1.51

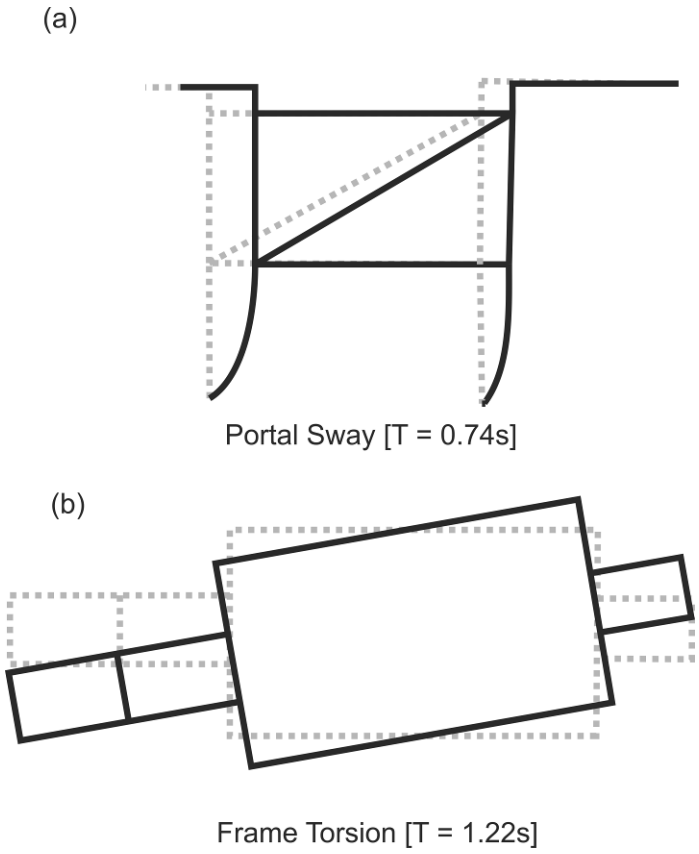

Figure 7.2: Mode shapes for 1/10th scale container crane

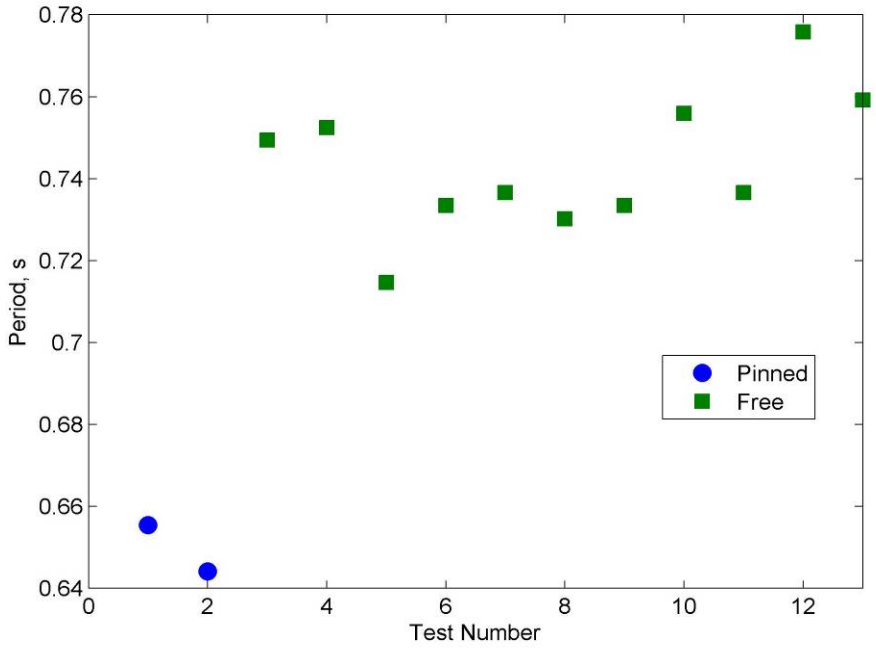

Figure 7.3: Portal sway mode for tests

7.2 Uplift and Derailment

In order for the crane to derail, the axial load in the leg must go to zero, the crane must lift straight up the distance of the flange on the wheel; only at this point can it freely move horizontally. Figure 7.4 illustrates the typical H1 and V movement for the structure. It can be seen that the wheels in the landside leg move almost perfectly vertically for a distance of approximately 1/16 of an inch in the vertical direction, and then the leg begins to experience some horizontal movement. The experiences large horizontal motions on its decent until the vertical displacement returns to zero, indicating that the crane has landed on the wharf. Once landed, the crane slides for some distance on the concrete.

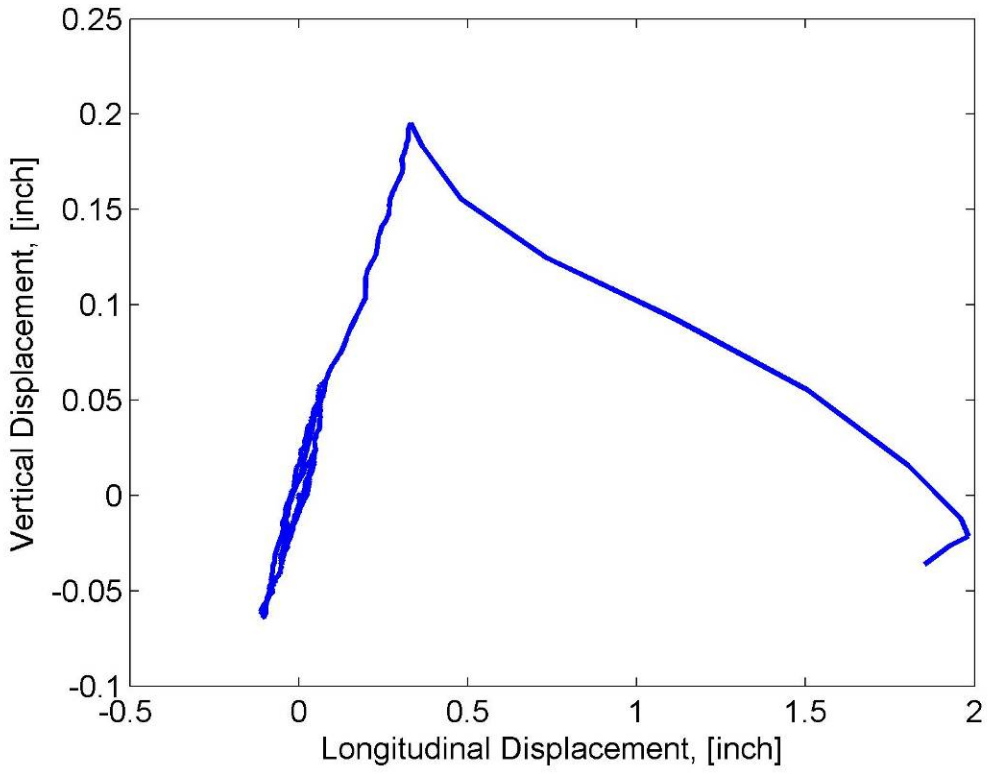

Figure 7.4: Typical H1 and V motion for the landside leg

During the testing, derailment was reported when there were residual displacements measured in the gauges at the base after a loading run. The runs that had the residual displacements at the base also had large maximum displacements of the legs. Figure 7.5 shows the maximum portal drift vs. the maximum horizontal displacement of the legs. It is clear that derailment occurs after exceeding some spectral accelerations and displacement limits.

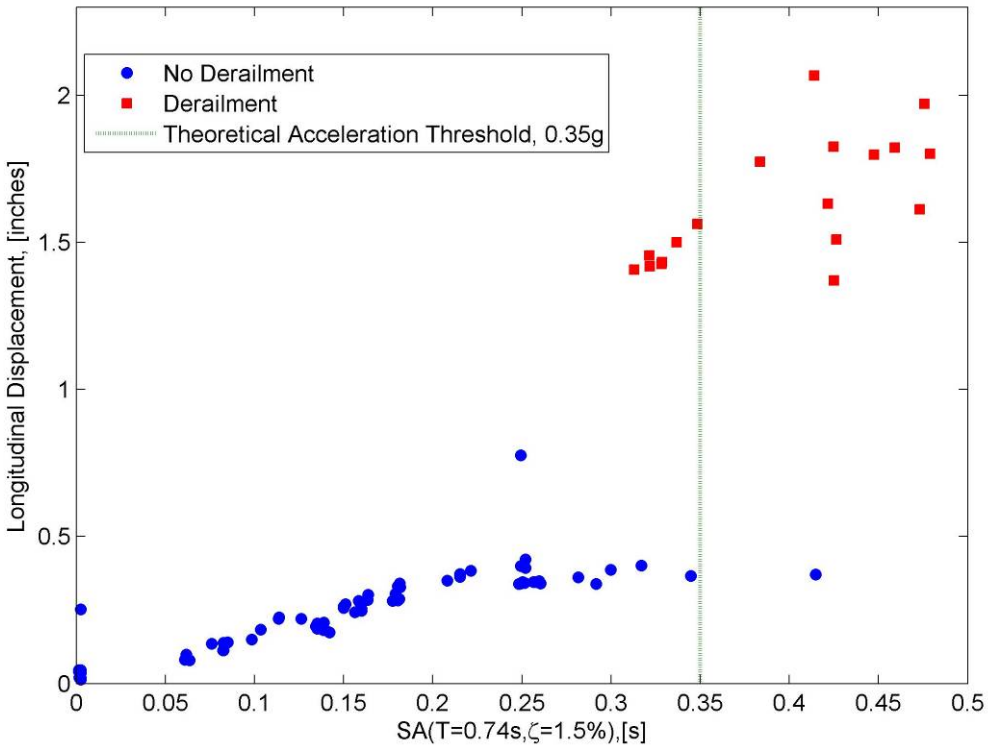

Figure 7.5: Maximum horizontal displacement vs. spectral acceleration at 0.74s

Based on the location of the center of mass, the theoretical acceleration required for uplift and derailment for a rigid structure, from Equation 2.18, is 0.35g. The portal drift that is required to get uplift and derailment is 1.8% drift. Figure 7.6 shows a plot of the maximum spectral acceleration vs. the portal drift for a total of 58 runs. The

theoretical uplift threshold and theoretical portal drift threshold are also shown on the graph. The experimental data agrees well with the theoretical thresholds.

The first item to note is that the experimental data covers a wide range of spectral accelerations with a significant number of data points in the "transition range" where the structure goes from no derailment to derailment. The good representation of a wide range of values is important, because it allows one to make conclusions about the response of the crane under a variety of excitations. The second item to note is that there is a clear trend between the portal drift and the spectral acceleration at the natural frequency of the crane. This would indicate that spectral acceleration is a good intensity measure to pair with portal drift as an engineering demand parameter.

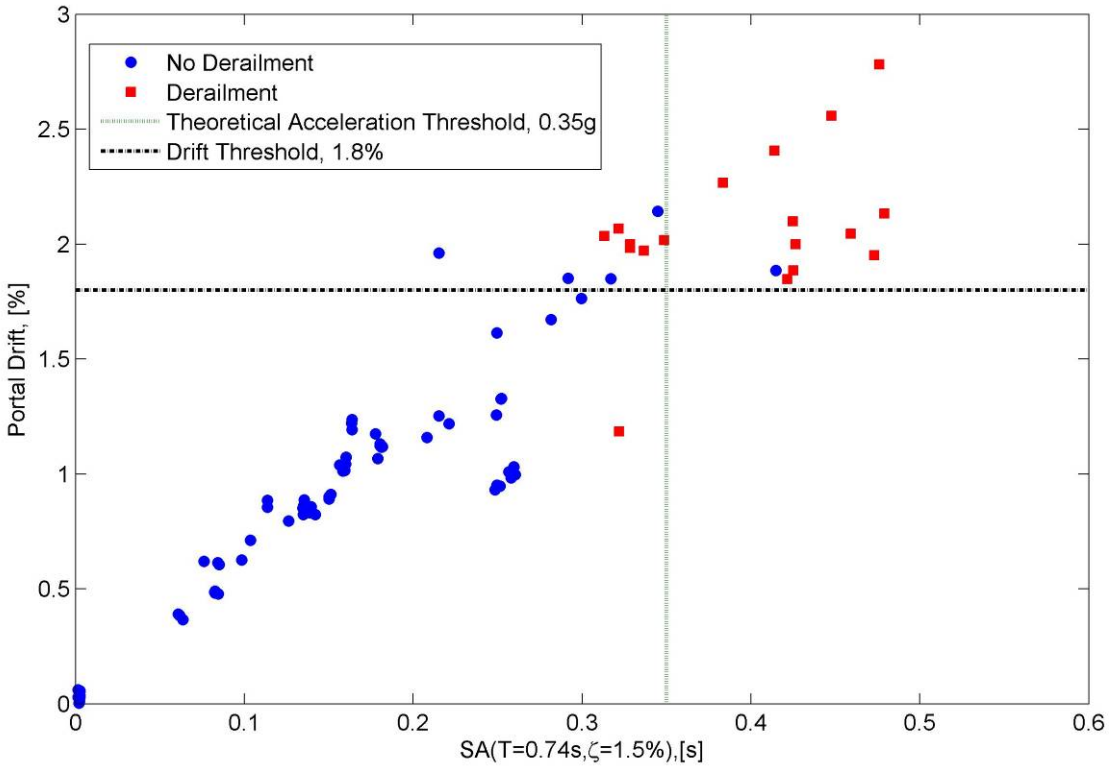

Figure 7.6: Maximum portal drift vs. spectral acceleration at 0.74s

7.3 Moments

The moments in the structure are calculated from the data collected from the strain gages in the legs (see Figure 6.13). At each location, there are four strain gauges. Three gauges are required to calculate the biaxial moments as well as the axial loads. The axial load and moments are calculated for each combination of three gauges at each location, resulting in four different values for the time history of the forces. The four time histories for each force are then averaged to get the best estimate for the actual value of the forces.

The largest moments are found in the top of the legs of the portal frame. Figure 7.7 shows the relationship between the spectral acceleration at the natural frequency of the crane versus the moment in the portal leg. For accelerations less than 0.6g, the relationship between the acceleration and the moment is fairly linear, as would be expected when the structure is responding elastically. Once the excitations exceed 0.6g, the relationship is no longer linear. At 0.6g, the moments in the structure reach 160 to 180 kip-in, which is close to the expected yield moment of 200 kip-in. The maximum moments that the structure experiences are between 190 and 200 kip-in, which the structure experiences over a range of excitations from 0.6g to 1.2g, indicating that the yield moment has been achieved, and that it is acting in an elasto-plastic manner.

Figure 7.8 shows the maximum moment in the portal leg versus the drift levels. There is a linear relationship between the drift and the moments in the portal leg until about 3.1% drift. After 3.1% drift, the moments stay fairly constant, while the drift levels continue to increase. This indicates that the structure has yielded and is acting in an

elasto- plastic manner. The test structure reached its ultimate limit at 5.7% drift, which means that the ductility of the test structure is 1.8.

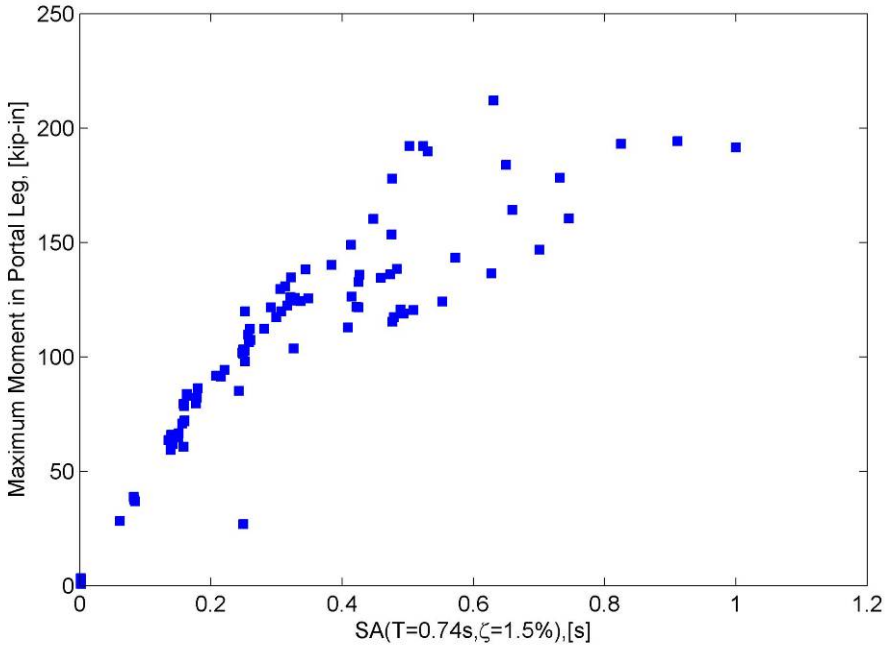

Figure 7.7: Maximum moment in portal leg vs. spectral acceleration at 0.74s

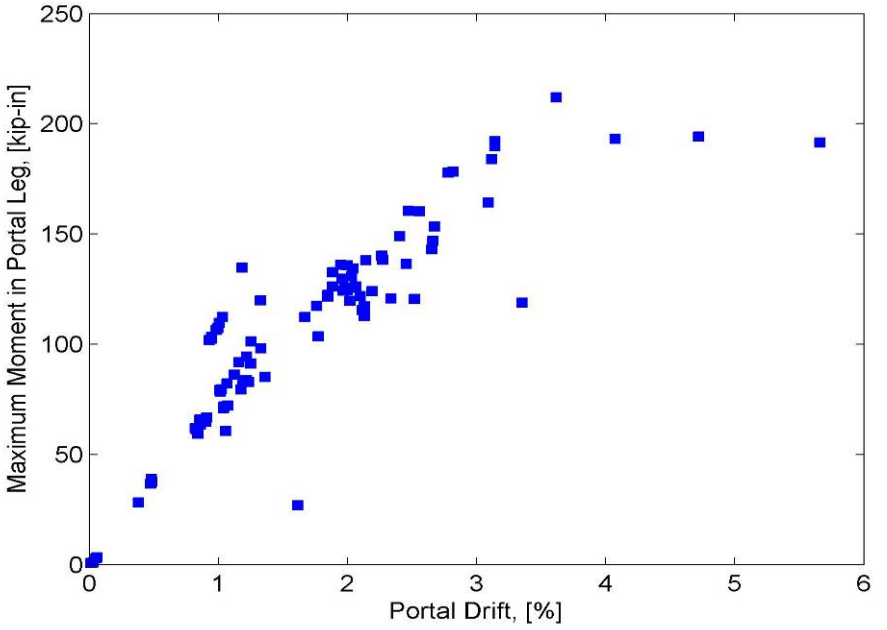

Figure 7.8: Maximum moment in portal leg vs. percent drift of portal frame

There are large moments in the portal beam, near the beam column joint. Figure 7.9 shows the maximum moment in the portal beam versus the spectral acceleration at 0.74s. As with the portal leg, for accelerations less than 0.6g, the relationship between the acceleration and the moment is fairly linear, as would be expected when the structure is responding elastically. Once the excitations exceed 0.6g, the relationship is no longer linear. At 0.6g, the moments in the portal beam reach 95 to 107 kip-in. Figure 7.8 shows the maximum moment in the portal beam versus the drift levels. As with the portal leg, there is a linear relationship between the drift and the moments in the portal leg until of approximately 3.1% drift. After 3.1% drift, the moments stay fairly constant while the drift levels continue to increase.

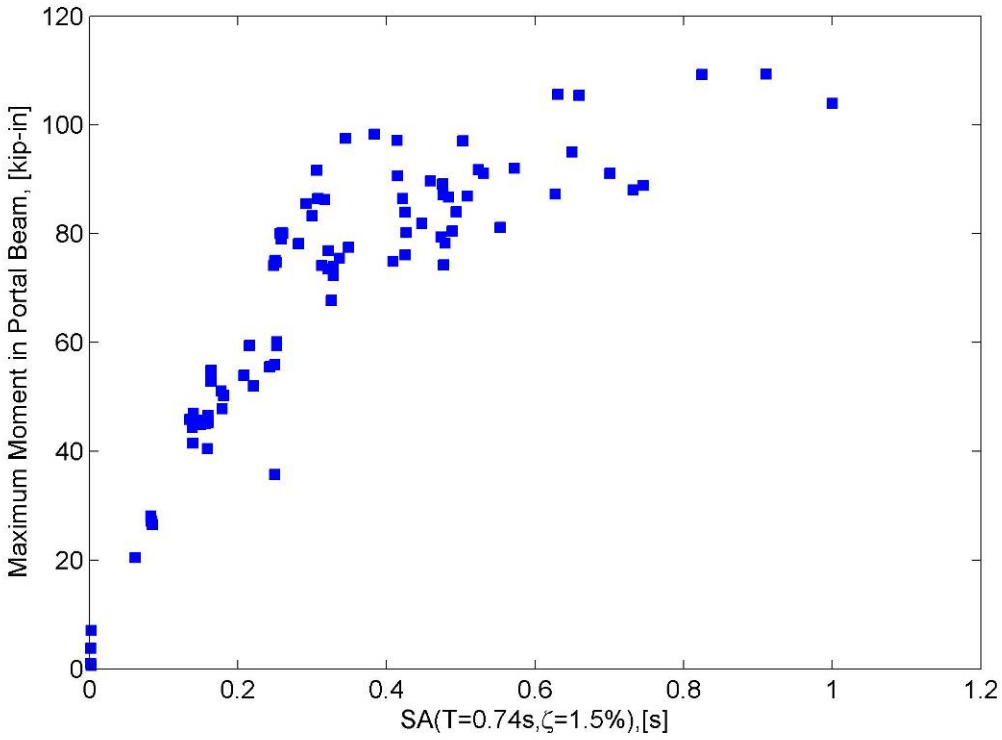

Figure 7.9: Maximum moment in portal beam vs. spectral acceleration at 0.74s

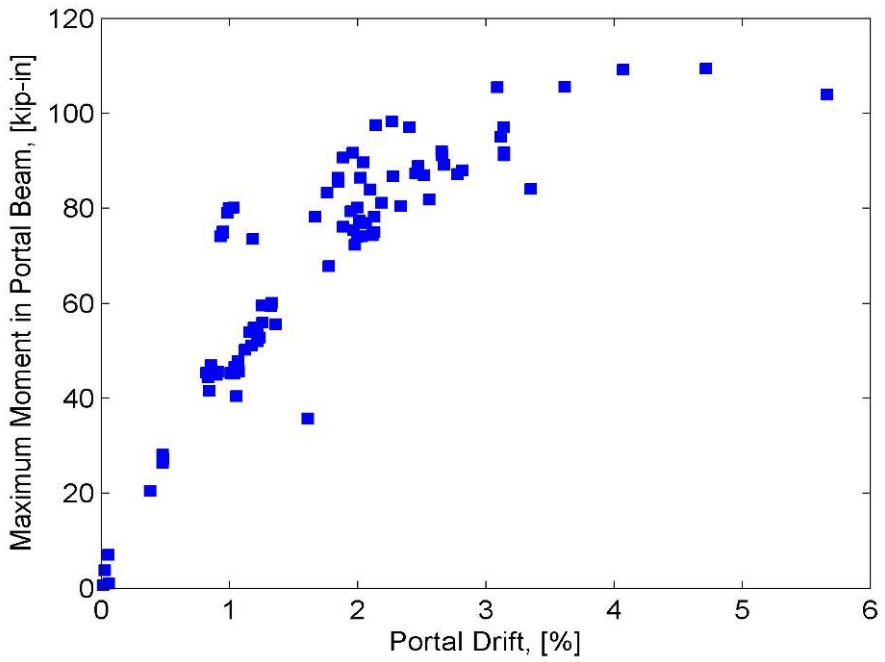

Figure 7.10: Maximum moment in portal beam vs. percent drift of portal frame

7.4 Effects of Ground Motion Components

The effects of the different components of ground motions are important to understand in order to determine what types of load histories should be used for analysis and design. In order to determine which components have the largest effect on the response, the model crane was excited using different components of ground motions. The results are then compared to assess their importance to the overall response.

7.4.1 Effects of transverse horizontal excitation

In order to assess the effect of the transverse (perpendicular to the boom) horizontal component, two different tests were run: transverse only excitation and longitudinal plus transverse excitation. Figure 7.11 shows the maximum drift levels versus the spectral acceleration at 0.74s when the transverse only excitation is used when

the crane is free to uplift (runs 48 and later, Table 6.7). It can be seen that the maximum drift for all of the transverse excitations of the ground motions tested is 0.07%. Table 7.2 shows the drift levels for the H1 only excitation and the H2 only excitation for each level of the test protocol when the crane is free to uplift (Table 6.7). Each run number in the table corresponds to the runs in Table 6.7. It can be seen that the portal drift when there is only an H2 excitation is typically 1-3.5% of the portal drift when an H1 only excitation is used. The maximum drift when there is only an H2 excitation is 9.0% of the portal drift when an H1 only excitation is used. From this data, it can be concluded that the drift from the transverse excitation is not a large portion of the portal drift when there is a longitudinal excitation for the load histories used in this test. Therefore, the transverse excitation does not have a significant effect on the overall response for the load histories imposed on this particular structure.

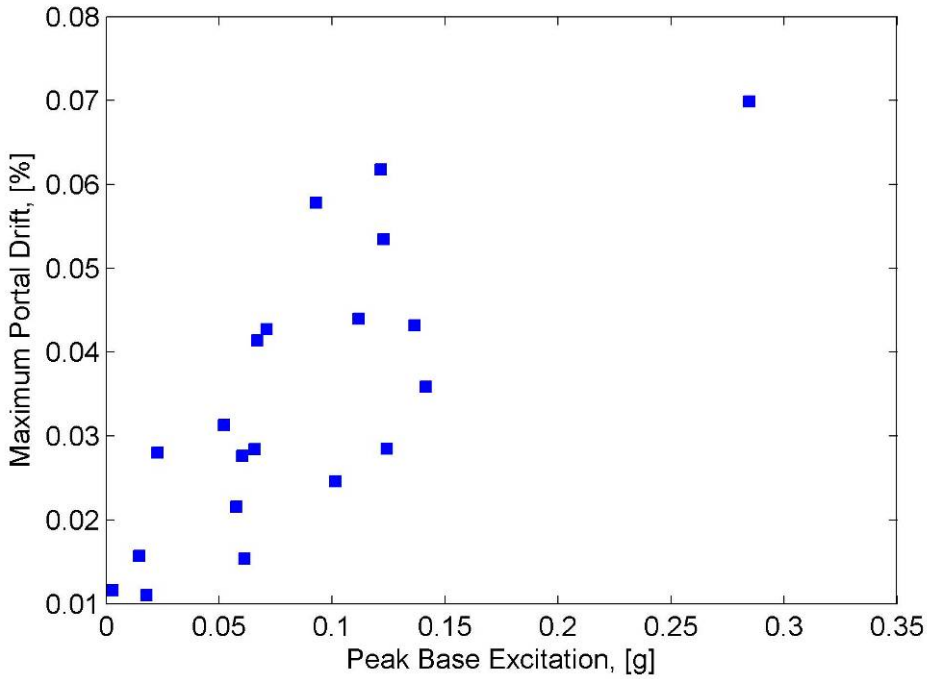

Figure 7.11: Maximum portal drift vs. peak base excitation for transverse only excitation

Table 7.2: Comparison of Drift Response between H1 and H2 excitation

Ground Motion	*Run Numbers*	*H1 Excitation Drift, %*	*H2 Excitation Drift, %*	*H2 Drift Percent of H1 Drift*
OLE6	48, 49	0.61	0.01	1.9
OLE4	51, 52	0.63	0.03	4.5
LP	54, 55	0.49	0.04	7.4
CLE6	59, 60	1.12	0.03	2.8
CLE4	64, 65	0.86	0.03	3.2
OLE6	69, 70	0.85	0.03	3.4
OLE4	72, 73	0.80	0.06	7.3
LP	75, 76	0.48	0.04	9.0
CLE6	80, 81	1.26	0.04	3.3
CLE4	85, 86	1.17	0.04	3.6
NJM	90, 91	1.02	0.01	1.1
CLE6	95, 96	1.16	0.02	1.9
CLE4	100, 101	1.04	0.02	1.5
CLE6	123, 124	1.89	0.04	2.3
CLE4	130, 131	1.03	0.02	2.4
NJM	135, 136	0.93	0.02	1.7
LP	141, 142	1.25	0.07	5.6
CLE4	150, 151	1.96	0.05	2.7
NMJ	158, 159	2.02	0.03	1.4

Table 7.3 shows a comparison of the drift levels versus the spectral acceleration at 0.74s between the longitudinal only and the longitudinal plus transverse ground motions for which the difference between the achieved spectral accelerations at 0.74s is less than 2% for the two ground motions (Table 6.7). Each run number in the table corresponds to the runs in Table 6.7. It can be seen that there is no discernable trend between the drift levels when the transverse ground motions are included compared to when they are not for the CLE4, LP and NJM ground motions. However, for the CLE6 ground motion, there is a large increase (11.3% and 28.4%) in response of the structure. There is no clear reason why there is a large increase in the response for those particular ground motions. As in the first test, the effects of the transverse ground motions are negligible for most of

the ground motions, and need not be considered in analysis. This indicates that a two-dimensional model is sufficient in most cases for the analysis of a J100 container crane.

Table 7.3: Effects of transverse ground motion

Ground Motion	*Run Numbers*	*Spectral Acceleration, g*	*H1 Excitation Drift, %*	*H1+H2 Excitation Drift, %*	*% Difference*
CLE4	64, 66	0.14	0.863	0.823	-4.6
CLE4	130, 132	0.26	1.03	1.01	-2.2
CLE4	150, 152	0.31	1.96	2.02	3.1
CLE6	59, 61	0.18	1.12	1.13	0.9
CLE6	80, 82	0.25	1.26	1.61	28.4
CLE6	123, 125	0.42	1.89	2.10	11.3
LP	117, 119	0.14	0.857	0.861	0.5
NJM	90, 92	0.16	1.02	1.02	-0.1
NJM	134, 135	0.25	0.932	0.948	1.8
NJM	158, 159	0.34	2.02	1.97	-2.3

7.4.2 Effects of vertical excitation

In order to assess the effects of the vertical component, ground motions are run with a longitudinal plus vertical ground motions. Table 7.4 shows a comparison of the drift levels versus the spectral acceleration at 0.74s between the longitudinal only and the longitudinal plus vertical ground motions for which the difference between the achieved spectral accelerations at 0.74s is less than 6% for the two ground motions (Table 6.7). Each run number in the table corresponds to the runs in Table 6.7. It can be seen, that as with the first test, there are no consistent trends when the vertical component is included versus when it is not. The test specimen was subjected to large vertical excitations, and the largest increase in response was 7.23%. From this data, it can be concluded that the vertical accelerations are not important to the primary portal sway response of the crane for the load histories imposed on this particular structure.

Table 7.4: Comparison of longitudinal and longitudinal plus vertical excitation

Ground Motion	*Run Number*	*Spectral Acceleration, g*	*H1 Excitation Drift, %*	*H1+V Excitation Drift, %*	*% Difference*
CLE4	64, 67	0.14	0.863	0.888	2.9
CLE4	85d, 103	0.16	1.03	1.07	3.3
CLE4	130, 133	0.26	1.03	0.984	-4.6
CLE4	150, 153	0.31	1.96	2.03	3.7
CLE6	59, 62	0.16	1.120	1.117	-0.3
CLE6	80, 83	0.25	1.26	1.33	5.8
CLE6	123, 126	0.42	1.886	1.886	0.0
LP	55, 57	0.082	0.486	0.489	0.8
LP	75, 78	0.083	0.482	0.484	0.4
LP	117, 120	0.14	0.857	0.823	-4.0
NJM	90, 93	0.16	1.016	1.024	0.8
NJM	135, 138	0.25	0.932	0.951	2.1
NJM	157, 160	0.32	1.85	1.98	7.2

7.4.3 Triaxial excitation

In order to assess the effects of triaxial excitation, ground motions are run with a longitudinal, horizontal and vertical ground motions. Table 7.5 shows a comparison of the drift levels versus the spectral acceleration at 0.74s between the longitudinal only and the triaxial excitations, for which the difference between the achieved spectral accelerations at 0.74s is less than 3% for the two ground motions. Each run number in the table corresponds to the runs in Table 6.7. It can be seen that for the CLE4 and LP ground motions, there is no discernable trend between when a single component of excitation versus when all three are used. For the CLE6 ground motion, there is an increase in the response for three of the four ground motions. This is not surprising as the addition of a transverse excitation caused an increase in response for the CLE6 motion. For the NJM excitations lower than 0.35g, there is little to no effect of adding the other components; however, there was an increase in response for the excitation larger than

0.35g. This increased response is expected because the addition of the vertical component for the largest NJM excitation also caused an increase in the response. The largest increase in the response when considering triaxial excitation was 8.1%. Therefore, it can be concluded that triaxial excitation does not have a significant effect on the overall response for the load histories imposed on this particular structure.

Table 7.5: Comparison of longitudinal and triaxial excitation

Ground Motion	*Run Numbers*	*Spectral Acceleration, g*	*H1 Excitation Drift, %*	*Triaxial Excitation Drift, %*	*% Difference*
CLE4	64, 68	0.13	0.86	0.85	-1.37
CLE4	85d, 104	0.16	1.04	1.04	0.43
CLE4	130, 134	0.26	1.03	1.00	-3.36
CLE6	59, 63	0.18	1.12	1.12	-0.17
CLE6	80, 84	0.25	1.26	1.33	5.51
CLE6	95, 99	0.21	1.16	1.22	5.27
CLE6	123, 127	0.42	1.89	2.00	6.05
LP	75, 79	0.083	0.48	0.48	-0.68
LP	117, 121	0.14	0.86	0.83	-2.89
NJM	90, 94	0.16	1.02	1.01	-0.41
NJM	135, 139	0.25	0.93	0.95	1.87
NJM	157, 161	0.32	1.85	2.00	8.13

7.5 Effects of Boundary Conditions

Boundary conditions are important to the response in any analytical model. In order to validate models with various boundary conditions, two boundary conditions were used in this experiment: legs pinned and legs free to uplift and displace laterally. For all of the tests where the crane was pinned, tests were also run while the crane was in the free boundary condition. This section compares the responses of the crane for both boundary conditions.

For comparison purposes, the transverse only excitation was ignored, because the response was very small so it was not an informative comparison. For each of the 32 ground motions that were compared, the time histories for the drift for both the north and south frames were compared. The drift was used for comparison, because it is a good indicator of structural response as noted earlier. Table 7.6 summarizes the results.

The data show several interesting trends. First, the damping for the free structure is higher than that of the pinned structure (Table 7.1). For the CLE6 and OLE6 ground motion, the peak drifts were consistently higher in the free structure than the pinned one. At the lower amplitude excitations, the LP and OLE4 ground motions resulted in higher drifts in the free structure than the pinned one, with the exception of the triaxial LP ground motion. At the lower amplitude excitations, the CLE4 motions resulted in significantly lower drift levels in the pinned case than the free one. At the higher amplitude, the LP ground motions generally led to lower drift levels for the pinned case than the free case. Also, the higher amplitude CLE4 ground motion showed no significant difference in the drifts between the pinned and free cases. In general, the pinned case experienced lower drift levels than the free case, which is likely due to the increased flexibility when the restraints were removed.

Table 7.6: Drift comparison between pinned and free boundary conditions

Run Numbers	*Ground Motion*	*Maximum Drift Pinned*	*Maximum Drift Free*	*% Difference*
1 & 48	OLE6	0.54%	0.61%	12.96%
3 & 50	OLE6	0.56%	0.61%	8.93%
4 & 51	OLE4	0.62%	0.63%	1.61%
6 & 53	OLE4	0.43%	0.62%	44.19%
7 & 54	LP	0.38%	0.49%	28.95%
9 & 56	LP	0.38%	0.39%	2.63%
10 & 57	LP	0.39%	0.49%	25.64%
11 & 58	LP	0.39%	0.37%	-5.13%
12 & 59	CLE6	0.69%	1.12%	62.32%
14 & 61	CLE6	0.69%	1.13%	63.77%
15 & 62	CLE6	0.68%	1.12%	64.71%
16 & 63	CLE6	0.68%	1.12%	64.71%
17 & 64	CLE4	1.05%	0.86%	-18.10%
19 & 66	CLE4	1.06%	0.82%	-22.64%
20 & 67	CLE4	1.10%	0.89%	-19.09%
21 & 68	CLE4	1.10%	0.85%	-22.73%
22 & 69	OLE6	0.76%	0.86%	13.16%
24 & 71	OLE6	0.74%	0.89%	20.27%
25 & 72	OLE4	0.80%	0.80%	0.00%
27 & 74	OLE4	0.61%	0.71%	16.39%
28 & 75	LP	0.50%	0.48%	-4.00%
30 & 77	LP	0.38%	0.38%	0.00%
31 & 78	LP	0.54%	0.48%	-11.11%
32 &79	LP	0.54%	0.48%	-11.11%
33 & 80	CLE6	0.94%	1.26%	34.04%
35 & 82	CLE6	0.93%	1.61%	73.12%
36 & 83	CLE6	0.93%	1.33%	43.01%
37 & 84	CLE6	0.92%	1.33%	44.57%
38 & 85	CLE4	1.16%	1.17%	0.86%
40 & 87	CLE4	1.17%	1.22%	4.27%
42 & 89	CLE4	1.21%	1.19%	-1.65%

7.6 Yield and Post-yield Behavior

An important aspect of this experiment was to assess the yield and post-yield behavior of container cranes. The structure reached yield during several ground motions. This section presents and discusses the data for the yield and post yield behavior.

7.6.1 Observations

After the structure yielded, it took progressively higher levels of excitation to cause the structure to uplift. For example, for run 168, in which the structure uplifted, the peak base excitation was 0.53g; in contrast, for run 188, the structure was subjected to a peak base excitation of 0.57g and did not uplift. Both run 168 and run 188 excited the structure in a single horizontal component of the CLE4 ground motion.

7.6.2 Yield

The first ground motion during which yield was achieved was run 168, which consisted of 90% of the H1 component of the CLE4 ground motion. The maximum moment achieved for this ground motion was measured at the top of the south landside portal leg. The values for the maximum moments for the four readings ranged from 170 kip-in to 186 kip-in. giving an average of 178 kip-in and a standard deviation of 7 kip-in. Figure 7.12 shows the drift vs. moment of the south landside portal leg. It can be seen that the maximum moment corresponds to when the maximum drift occurs. The maximum drift in the south portal frame is 2.20%, (1.3 in.). During the same ground motion, the north portal frame has a maximum drift of 3.14%, (1.9 in.). The values for the maximum moments of the four moment readings in the north frame ranged from 156 kip-in to 160

kip-in, for an average of 157 kip-in, with a standard deviation of 3 kip-in. The moment-drift relationship of the north frame can be seen in Figure 7.13.

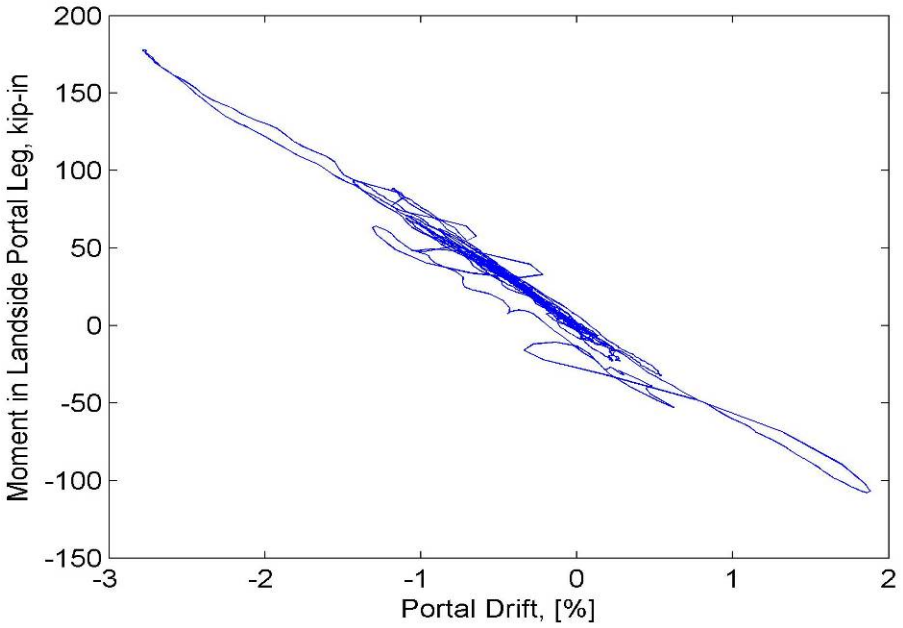

Figure 7.12: Moment versus portal drift in south portal frame during CLE4 ground motion

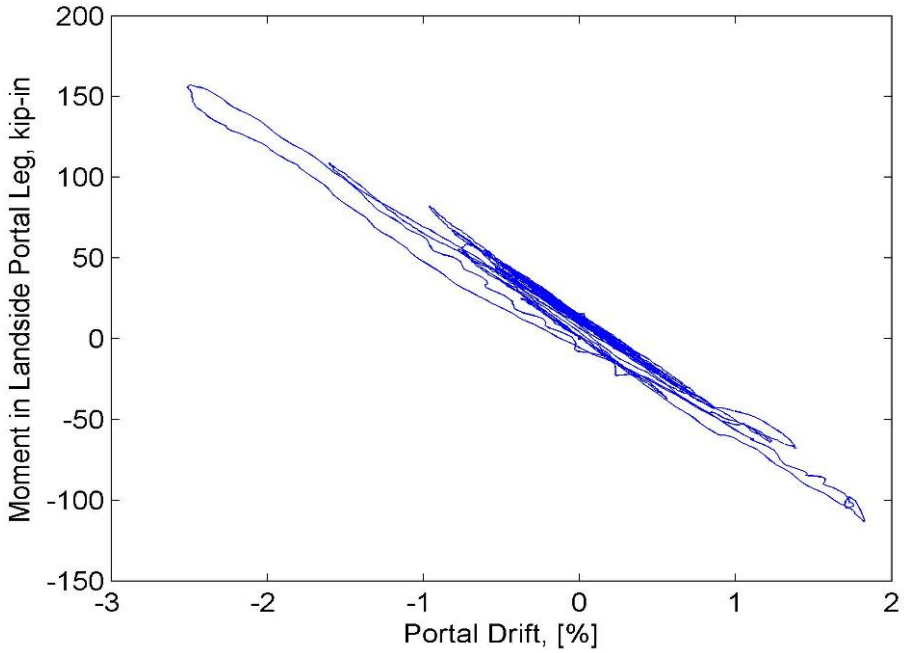

Figure 7.13: Moment versus portal drift in north portal frame during CLE4 ground motion

7.6.3 Post Yield

The first ground motion during which damage was achieved was run 169, which consisted of 95% of the H1 component of the CLE4 ground motion. The maximum moment achieved for this ground motion was measured at the top of the south landside portal leg. The values for the maximum moments for the four readings ranged from 183 kip-in to 202 kip-in, giving an average of 192 kip-in and a standard deviation of 8 kip-in. Figure 7.14 shows the drift vs. moment of the south landside portal leg. It can be seen that the maximum moment corresponds to when the maximum drift occurs. The maximum drift in the south portal frame is 2.20%, (1.3 in.). During the same ground motion, the north portal frame has a maximum drift of 3.14%, (1.9 in.). The values for the maximum moments of the four moment readings in the north frame ranged from 163 kip-in to 164 kip-in, for an average of 163 kip-in, with a standard deviation of 0.4 kip-in. The moment-drift relationship of the north frame can be seen in Figure 7.15. The moment-portal drift curve has a different slope before and after the maximum drift is achieved, which indicates that not only did yield happen, but permanent damage occurred as well.

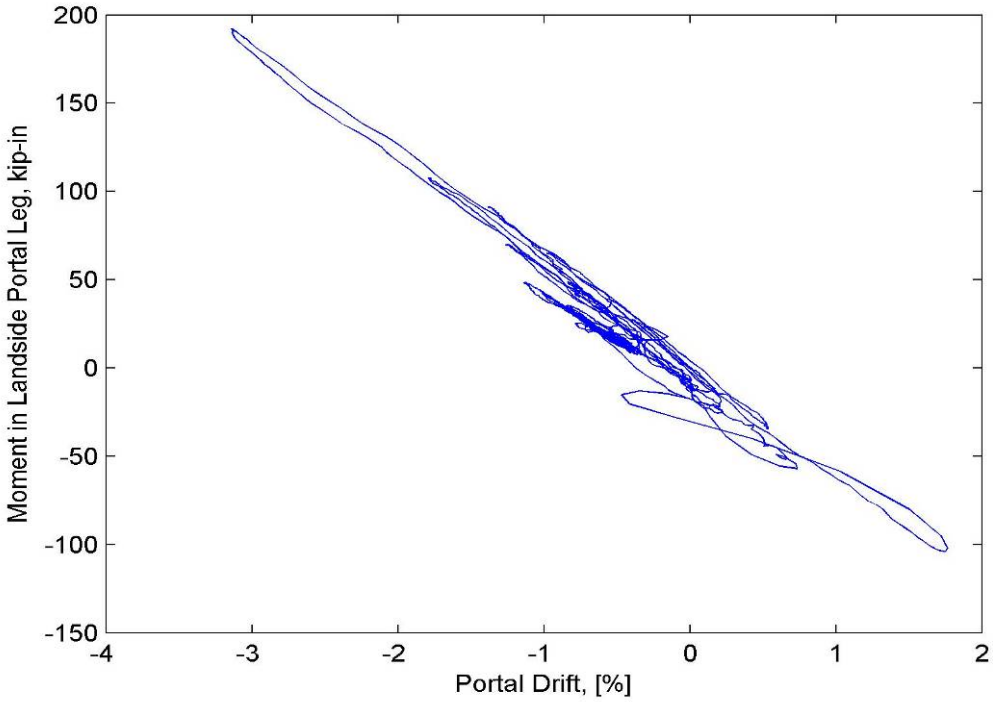

Figure 7.14: Moment versus portal drift in south portal frame during CLE4 ground motion

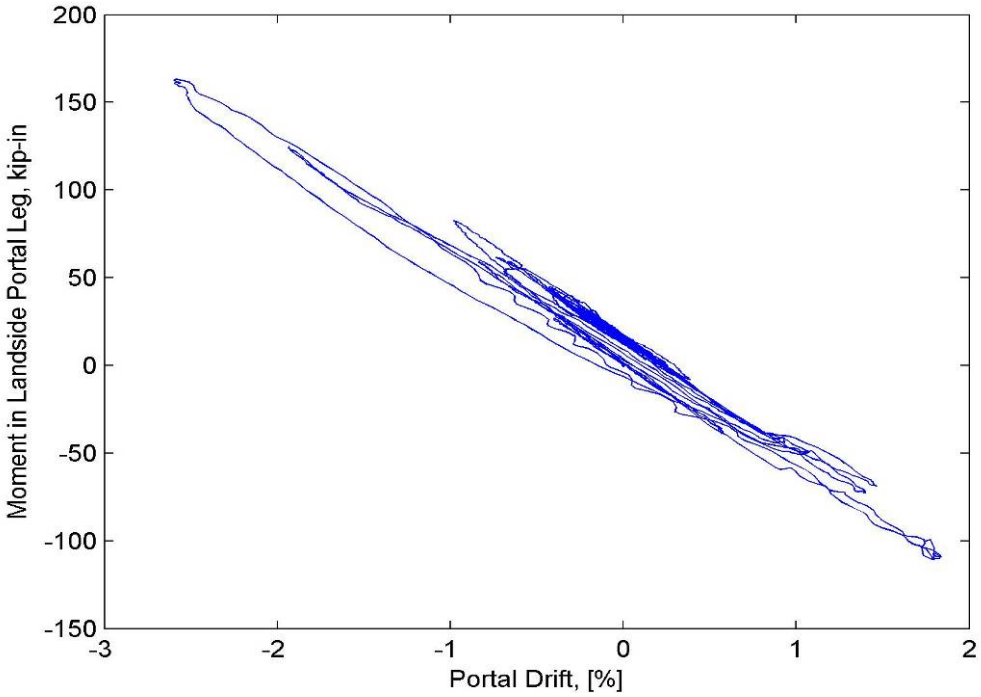

Figure 7.15: Moment versus portal drift in north portal frame during CLE4 ground motion

The phenomenon of the changing slope of the moment-portal drift curve happened during multiple tests. Table 7.6 summarizes the slopes in various sections of the curves for the ground motions in which damage occurred. There are a couple of important things to note from this data. First, a shim was added under the south landside leg prior to test 175, which resulted in a shift in the slope of the moment-portal drift curve from approximately -55 to approximately -35. The reduction of the slope means that the structure is more flexible, because it experiences higher drifts at lower moments than before. Second, the damage occurred in the south landside leg, but not in the north landside leg. The south landside leg is the one that uplifted, while the north landside leg remained on the rail. Thirdly, the slope at the end of the test was usually smaller than the slope at the start of the test when uplift occurred. This would indicate a change in stiffness due to the change of the boundary condition.

Table 7.7: Summary of the slope of the moment drift relationship in the 1/10th scale container crane

Test	*Ground Motion*	*Spectral Accleration (g)*	*South Pre-uplift Slope*	*South Post-uplift Slope*	*North Pre-uplift Slope*	*North Post-uplift Slope*
168	CLE4	0.602	-68.7	-67.4	-68.3	-65.2
169	CLE4	0.634	-67.5	-51.6	-68.1	-66.3
172	NJM	0.799	-66.6	-44.0	-64.7	-66.5
192	NJM	1.04	-33.8	-28.7	-60.2	-55.5
193	NJM	1.15	-31.19	-21.7	-62.8	-61.6

Prior to yield, the ground motions exhibited linear moment-drift relationships. After yield, the drifts continued to increase, while the moments stayed nearly constant, as shown in Figure 7.16 and Figure 7.17. Additionally, the drifts and moments did not

return to zero when the shaking stopped, indicating that permanent deformations occurred because of yielding in the structure.

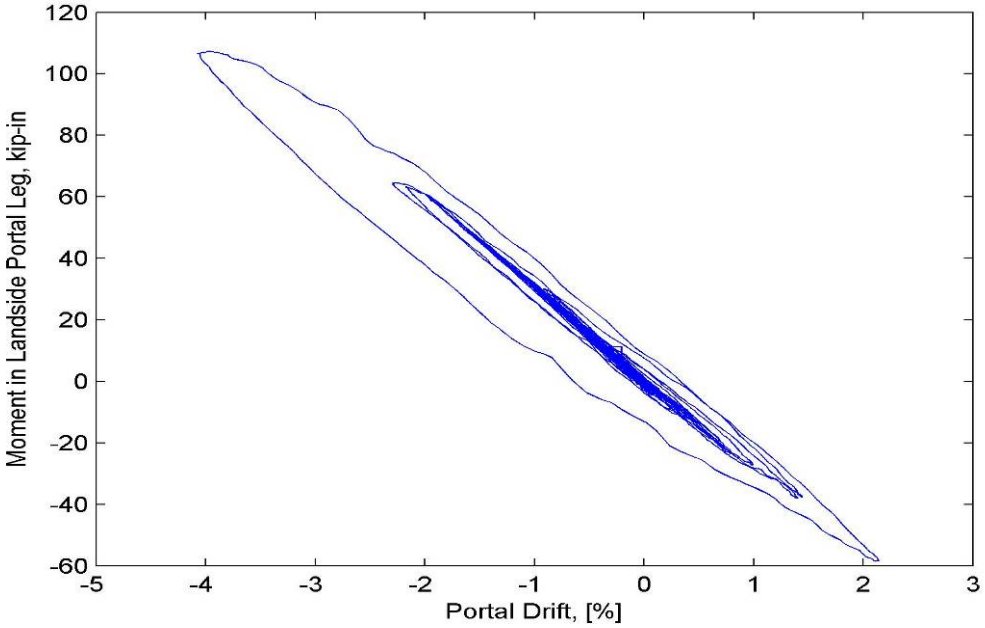

Figure 7.16: Moment versus portal drift in north portal frame during CLE4 ground motion

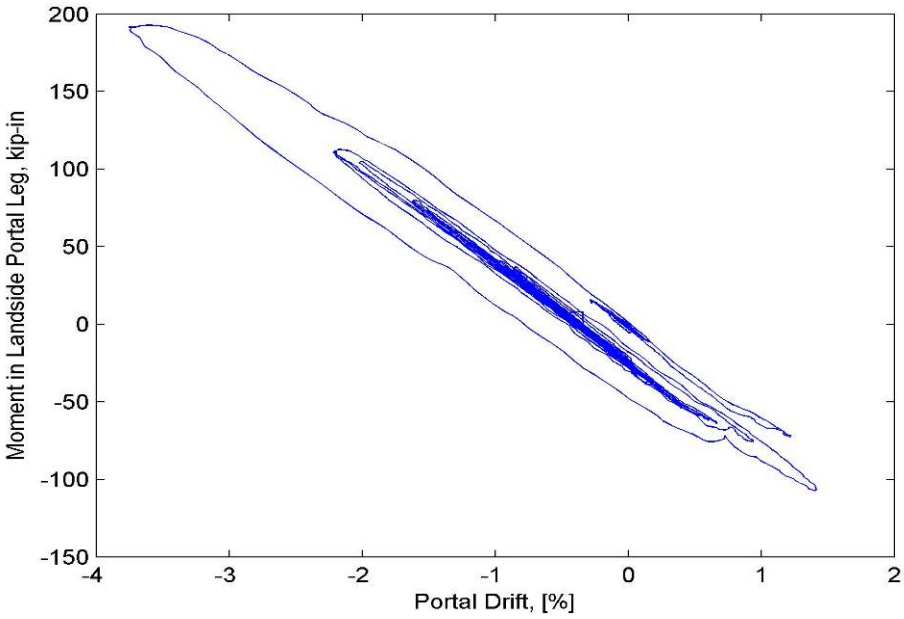

Figure 7.17: Moment versus portal drift in north portal frame during NJM ground motion

7.6.4 Ultimate

The structure experienced irreparable damage during the last test. All four columns experienced local buckling near the portal joints (Figure 7.18.) Additionally, all four columns exhibited permanent sway deformations (Figure 7.19.) The permanent sway deformation made the structure unstable. The welds connecting the top frame to the portal frame fractured (Figure 7.20.) The waterside portal beam connections ripped the walls of the columns (Figure 7.21) and the portal beam punched through the walls of the landside columns. The moment-portal drift curves (Figures 7.22 and 7.23) show that drifts of 5.66% and 4.75% occurred in the south and north frames respectively. The curves also show very large permanent drifts, confirming the observations from Figure 7.19.

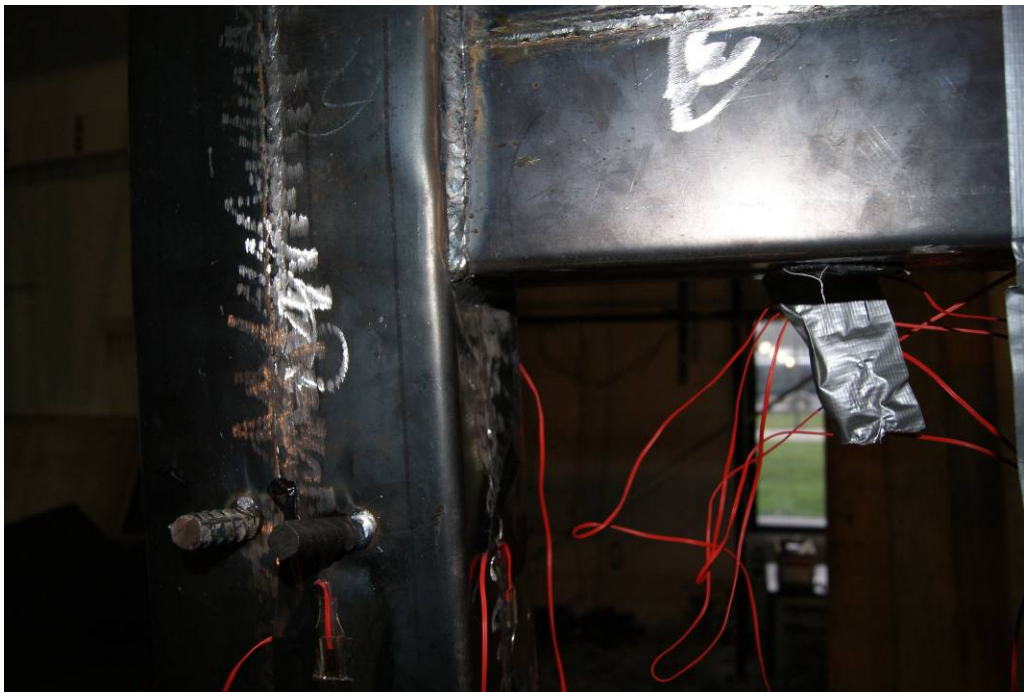

Figure 7.18: North landside leg of the 1/10th scale model, showing the typical buckling of the legs near the portal joints

Figure 7.19: 1/10th scale crane model after last test with permanent sway

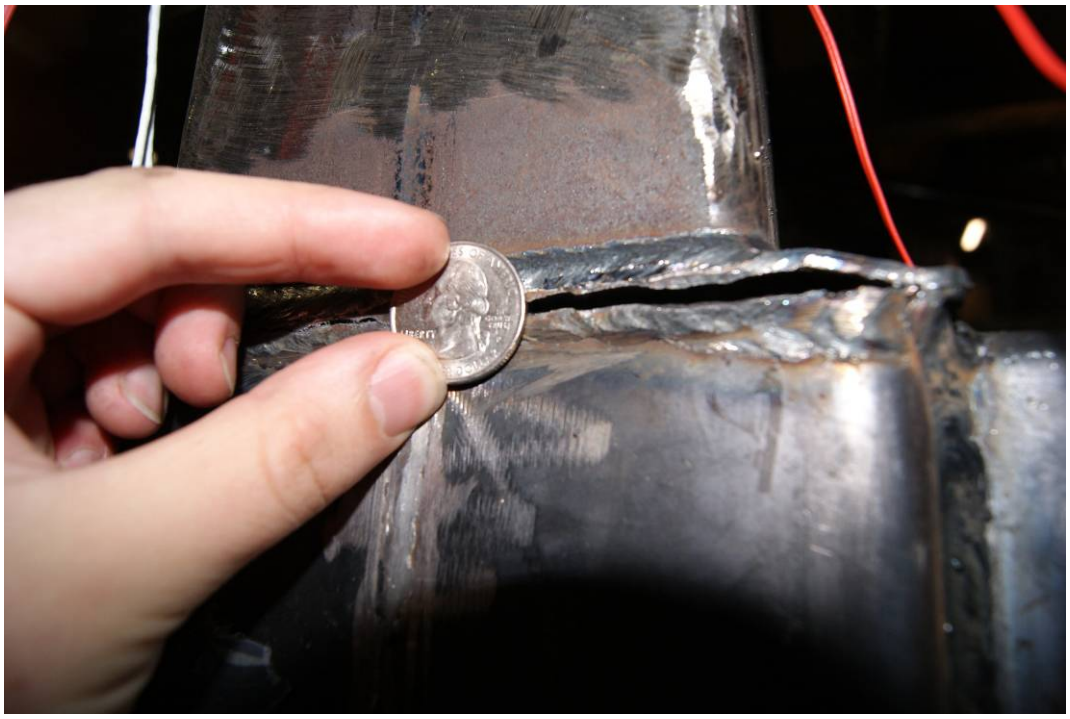

Figure 7.20: Connection between the northeast side of the portal frame and the top frame for the 1/10th scale crane

Figure 7.21: South waterside portal joint

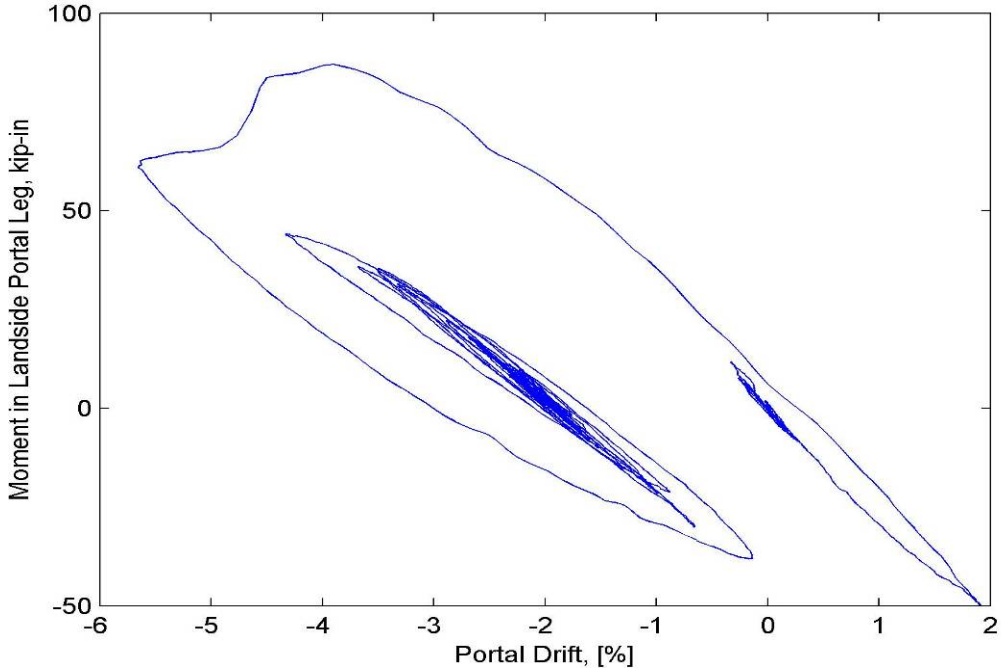

Figure 7.22: Moment versus portal drift in south portal frame during NJM ground motion

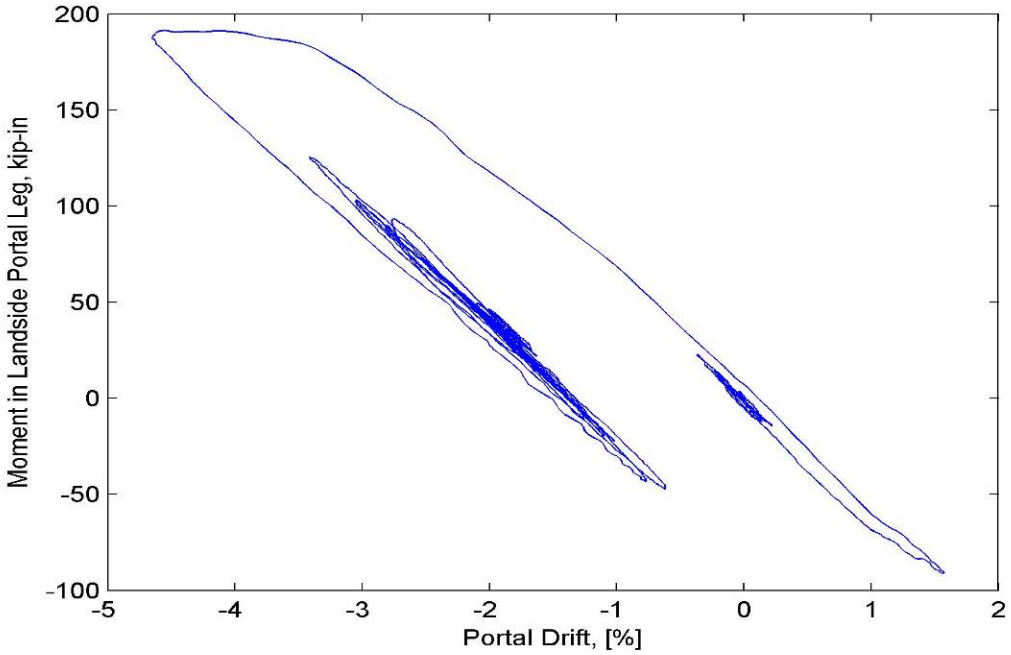

Figure 7.23: Moment versus portal drift in north portal frame during NJM ground motion

7.7 Conclusions

The 1/10th scale experiment structure had a primary bending mode frequency of 0.74s with a damping value of 2.4%. The damping in this test was higher than in the first test, because of the slack in the truck assembly.

The predicted uplift/derailment threshold was 0.35g, based on the location of the center of mass. The data is in good agreement with this value, supporting earlier findings (Chapter 4, Sugano et al, 2008) that it is possible to predict when uplift and derailment will occur based on the acceleration of the structure. Additionally, it is possible to predict when derailment will occur based on the drift. At drifts of 1.8% and above, derailment occurs. The value of 1.8% agrees with the value of drift predicted for 0.35g acceleration based on the relationship developed for the test data.

Prior to an uplift event, the wheels move almost vertically while restrained by the wheel flanges. After the wheel moves vertically beyond the wheel flange, the wheels continue to rise, with a slight horizontal movement. After reaching the top of uplift, the wheel starts to descend, accompanied by large horizontal motions in the longitudinal direction. After the wheel lands, it slides on the concrete before coming to a rest at the end of the motion. In the experiment, the crane goes directly from elastic behavior to tipping, rather than exhibiting the sliding behavior modeled in the FEA. The restraint provided by the wheel flanges is responsible for this difference in behavior.

There is a linear relationship between moment and drift with little scatter in the data prior to drifts of 1.8%, corresponding to pre-uplift behavior. Between drifts of 1.8% and 3.1% there is a linear relationship, although the slope of that line is different than the pre-uplift phase. There is also more scatter in the data in that range. For ground motions where drifts in excess of 3.1% occurred, the moment was fairly constant while the drift continues to increase. Yield occurred at 198 kip-in., which is in good agreement with the predicted value based on the expected material properties.

After yielding, a change in the structural stiffness was observed, indicating that damage occurred. It took larger excitations and drift levels to achieve uplift after the structure was damaged, due to the increase in flexibility. At the ultimate failure, the structure experienced local buckling, permanent deformations of the columns and failure of the welds.

The effects of the various components of ground motions varied by component and by ground motion. For the transverse excitation alone, the largest drift that was seen was 0.07%. When the two horizontal components were used at the same time, there was

little change in the overall response, with the exception of the CLE6 ground motion. For the CLE6 ground motion, two of the three tests saw a significant increase (larger than 10%) in the response. There is no discernable trend when the vertical ground motion is included. The only time there was a significant increase in response was when the spectral acceleration was larger than 0.35g, indicating that for moderate to large earthquakes, the vertical component should be considered.

Two different boundary conditions were used in the experiment: pinned and free. The damping in the free condition was lower than that of the pinned condition. For OLE6 and CLE6, the crane experienced a higher peak drift when the free condition was used. During the CLE4 and LP ground motions, the crane experienced higher peak drift when the crane was pinned. This result supports the industry claim that pinning a crane to the wharf during an earthquake could lead to larger forces and an undesirable response.

Chapter 8

Fragility Analysis

Decision makers at ports need to understand the vulnerabilities of the components of the port, such as container cranes, in order to most efficiently allocate resources and make emergency plans. Fragility curves are a useful tool to provide such information. Fragility curves provide the probability of meeting or exceeding a limit state given the intensity measure of the earthquake. There are two types of fragility curves: empirical and analytical. Empirical fragility curves make use of historical, experimental data, and engineering experience. Analytical fragility curves use finite element models and simulations. This study is primarily concerned with the former. This section presents and demonstrates a methodology for application to the seismic fragility analysis of container cranes.

Quantifying uncertainty is critical in any fragility analysis. The fragility methodology presented in Chapter 2 will be utilized. The results of previous sensitivity studies, also presented in Chapter 2, will be used to update the uncertainty values as they apply to container cranes. Subsequently, a fragility analysis will be performed on the test specimen for the derailment damage state. The derailment damage state is considered due to a sufficient number of data points to determine the threshold for the derailment damage state. The yield and collapse damage state are not considered, because only one data point for each damage state are available, which does not provide enough information to set a threshold for the damage states. To do this, test data, capacity estimates and seismic demand estimates are required. The author's intent is that this curve can be used as a general fragility curve for a jumbo container crane. It is intended

to incorporate data from the most accurate representation of the working boundary condition of these cranes.

Complete details of fragility formulation are presented in Chapter 2. A review of the formulation and how it applies to the present study are presented in the following sections.

8.1 Risk framework

The concept of risk includes hazards, consequences and context, (Ellingwood et al, 1980). The theorem of total probability provides the framework to consider the aspects of risk assessment:

$$P\left[Loss > c\right] = \sum_{s}\sum_{LS}\sum_{d} P\left[Loss > c \mid DS = d\right] P\left[DS = d \mid LS\right] P\left[LS \mid SI = s\right] P\left[SI = s\right] \quad (8.1)$$

where $P[SI=s]$ is the probability of a seismic event with $SI=s$, from the standard hazard curve; $P[LS|SI=s]$ is probability of achieving the limit state LS, given the occurrence of a seismic event, $SI=s$; P$[DS=d|LS]$ is the probability of the damage state DS, given the limit state LS; and $P[Loss>c|DS=d]$ is the probability that loss exceeds c, given that $DS=d$. The term $P[LS|SI=s]$ is the fragility term, and it describes the conditional probability that a limit state is achieved, given an earthquake intensity, and will be further developed in this section.

In a previous study by Kosbab (2010), it was shown that it was most appropriate to define (a) limit states in terms of an engineering demand parameter (EDP) of maximum portal drift, and (b) the seismic intensity in terms of spectral acceleration at the portal sway mode. The fragility term for container cranes can therefore be written as:

$$P[D > \theta \mid S_a = s] \quad (8.2)$$

where D is the EDP of maximum portal drift; θ is a specific value of D; S_a is the seismic intensity measure of spectral acceleration; and s is a specific values of S_a. The traditional lognormal cumulative distribution function is assumed for the fragility relationship:

$$F_R(x) = \Phi\left[\ln(x / m_R) / \beta\right] \tag{8.3}$$

where m_R represents the median capacity with a logarithmic standard deviation β representing the combination of the inherent randomness and uncertainty; $\Phi[\cdot]$ is the standard normal probability integral; x is a specific value of EDP.

8.2 Seismic Demand Model

To use Equation 8.3 to develop fragility curves, it is necessary to develop a relationship between the seismic intensity and the limit states in terms of the EDP. These relationships are characterized by seismic demand models, which is a way to relate spectral acceleration to portal drift as well as to quantify the uncertainty related to the choice of the demand model. The most efficient way to develop this model is to fit a function to data points from the series of tests and to quantify the dispersion of data points from the assumed function.

The seismic demand model is typically assumed to be a log-log linear relationship:

$$\theta_{\max} = aS_a^b\varepsilon \tag{8.4}$$

where ε is a lognormal random variable with a median of 1 and a log standard normal $\sigma_{ln\varepsilon}$

One point from each run in the Phase II tests with a free boundary condition is plotted in Figure 8.1 on a logarithmic scale. A linear regression is performed on $ln\ \theta_{max}$

vs. $ln\ S_a$ to characterize the mean and standard deviation results in a seismic demand model. The best-fit line is also plotted in Figure 8.1. The equation noted on the plot follows the form of Equation 8.4. The equation is similar to that determined by Kosbab (2010), which was $\theta_{max} = 3.16*S_a^{0.917}$. The values for the exponents differ by 9% between the experimental results and Kosbab's analytical results. The values for the constant in the equation based on Kosbab's analytical results were nearly twice that for the experimental results. Differences in the seismic demand models are expected since the experimental model was designed to be representative of a "typical" crane rather than being a model of the crane utilized by Kosbab to develop the seismic demand model, and as such there are differences in the geometries, mass properties and natural frequencies between the models.

The distribution of the experimental data points is assumed to be lognormal about the log-log linear best-fit line. The dispersion of data is quantified by $\beta_{D|Sa} = 0.164$. This dispersion constant is smaller than the dispersion found by Kosbab (2010) when using a single dispersion constant for a jumbo container crane, which was 0.268. A likely reason for the dispersion in the experiment being smaller than Kosbab's is due to the fact that fewer ground motions were used in the experiment than in Kosbab's analytical study. The uncertainty from the experiment is also smaller than the other sources of uncertainty in the modeling. A single dispersion constant is a good fit for the experimental data.

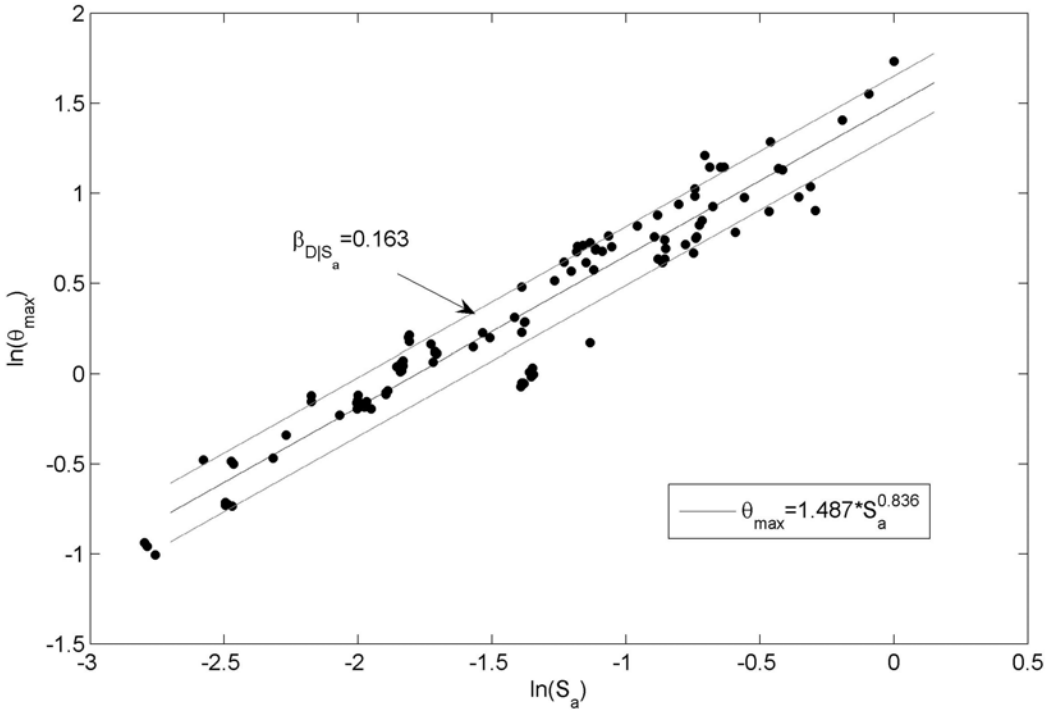

Figure 8.1: Seismic demand model for the experimental container crane

8.3 Uncertainty

The term β in Equation 8.3 represents the combination of all of the inherent randomness and uncertainty in the fragility formulation. The factor β can be broken down into categories: aleatory randomness and epistemic uncertainty. Epistemic uncertainty comes from a lack of knowledge and can be reduced with further investigation. Aleatoric uncertainty comes from physical sources of randomness and cannot be reduced by increased knowledge. Aleatoric uncertainty can be further divided into randomness in demand and capacity. The combination of the effects can be expressed as:

$$\beta = \sqrt{\beta_{RD}^2 + \beta_{RC}^2 + \beta_u^2} \tag{8.5}$$

where β_{RD} and β_{RC} represent randomness in demand and capacity, respectively; β_u represents the epistemic uncertainty. The following paragraphs will describe in further detail how the parameters are estimated for the application to container crane fragility.

The randomness in demand is based on the dispersion of data points around the assumed seismic demand model. The logarithmic standard deviation is used to approximate β_{RD}, also written as $\beta_{D|Sa}$ because it represents the variability in the demand given a specific earthquake. The previous sensitivity study by Kosbab (2010) highlighted that the ground motion intensity and profile characteristics dominated the demand randomness for container cranes. Therefore, it is possible to do a single excitation of the model with the uncertain parameters evaluated at their best estimate.

The randomness in capacity is more difficult to quantify. It must account for the uncertainty associated with the assumptions that derailment can be identified from static analysis. An assumed value of $\beta_{RC} = 0.25$ has been identified as a reasonable estimate for the randomness in capacity (Ellingwood et al, 2007).

The epistemic uncertainty in the fragility analysis of the model crane incorporates the simplifications, assumptions and limitations in creating the model. First, the structure was simplified for ease of construction and testing. The assumptions made in the simplifications, which includes that the critical response is that of the portal deformation, contribute to the uncertainty. Second, the uplift behavior prediction makes assumptions that must be accounted for. Third, a single crane model is used, rather than multiple models, leading to some uncertainty. Based on the work by Kosbab (2010), the epistemic modeling uncertainty can be assumed to be $\beta_u = 0.25$.

8.4 Fragility Curves

Equation 8.3 can be applied with the uncertainty treatment developed in section 8.3, and the seismic demand model from section 8.2 to develop a fragility curve, shown in Figure 8.2. Additionally, a fragility model from the experimental data was developed by dividing the spectral accelerations at the portal sway mode into bins and then the number of tests in each bin where derailment occurred is divided by the total number of tests in the bin. The probability in each bin is then plotted. The fragility model developed for the test specimen is compared to the fragility curves developed by Kosbab (2010) for a J100 crane, shown in Figure 8.2. Kosbab (2010) developed the curves using a log-log linear fit and a trilinear fit using portal uplift theory.

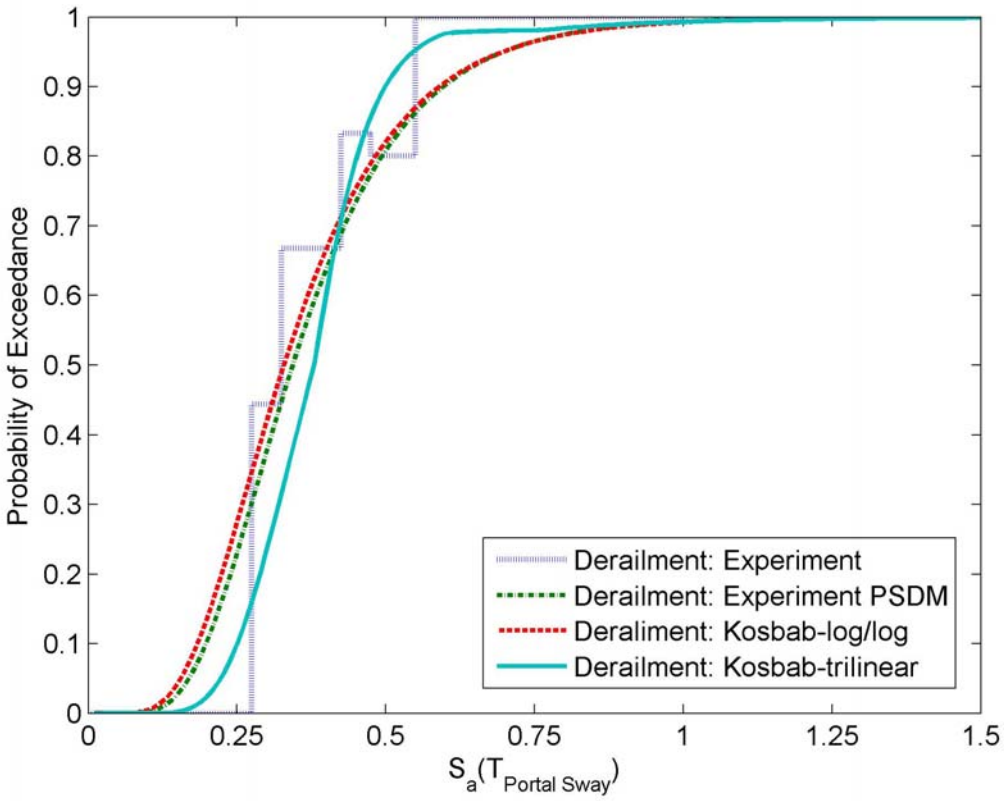

Figure 8.2: Fragility curve for the derailment damage state based on experimental data, and previous study by Kosbab (2010)

It can be seen that the fragility function developed using a log-log linear fit to the test data is in good agreement with the fragility model in Kosbab's study that utilizes a log-log linear fit to the analytical data. There is a significant difference between the fragility models developed using a log-log linear fit of the experimental data and Kosbab's trilinear fit. For $S_a < 0.4g$, the model developed from the experimental data predicts a higher probability of failure than Kosbab's trilinear model. For $S_a > 0.4g$, the model developed from the experimental data predicts a lower probability of failure than Kosbab's trilinear model. It can also be seen that the fragility functions developed using a log-log linear fit to the data tends to follow the trend of the fragility model from the experimental data, indicating that the lognormal assumption for fragility is valid. It can be seen that for Sa < 0.25g, all of the analytical models predict higher probabilities of derailment than was observed in the experiment. For Sa > 0.25g to Sa < 0.68, Kosbab's trilinear model shows lower probability of failure than the experiment. But, in the same range, the log-log linear models follow similar trends as the experimental data.

As presented in Section 2.4.6, the HAZUS program (FEMA, 2003) provides fragility curves for rail-mounted port container cranes. The damage levels are defined as minor, major and extensive/complete as described in Section 2.4.6, with an associated assumed randomness and uncertainty. The minor damage state most closely relates to the derailment damage state, and is recreated in Figure 8.3.

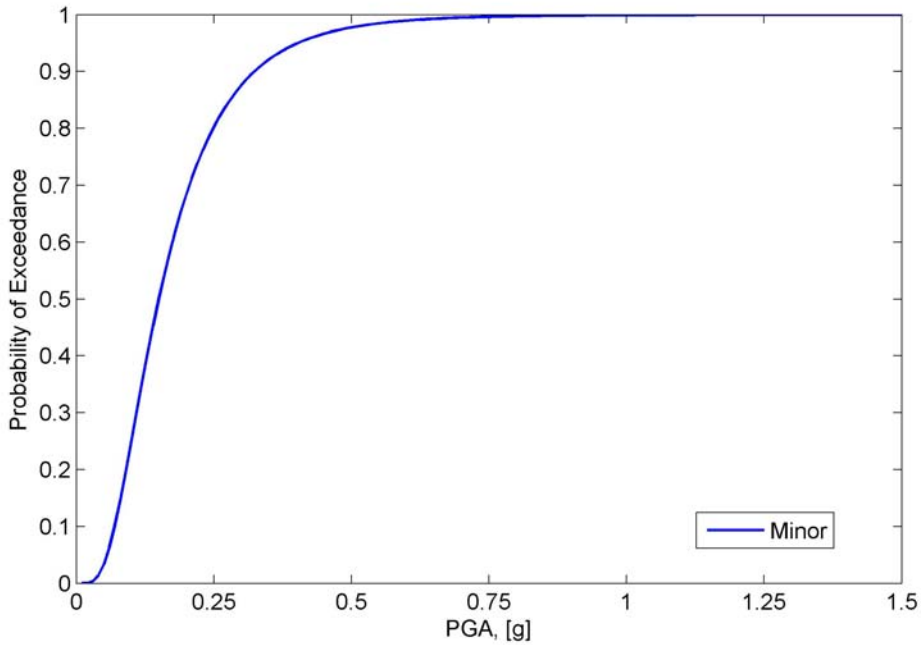

Figure 8.3: Fragility curve from HAZUS (FEMA, 2003)

The HAZUS curves are developed using a similar formulation to the one utilized in this study. They are developed using a lognormal distribution defined by a median capacity and lognormal standard deviation. However, there are some significant differences. One noticeable difference is that the HAZUS curves are created from expert opinion using the capacity spectrum method. Additionally, the formulation utilizes the peak ground acceleration for an intensity measure, rather than S_a. The definition of damage states does not separate minor damage from derailment. For these reasons, it is difficult and misleading to plot the fragility curve developed using experimental data along side the HAZUS curve for direct comparisons.

Although, it is difficult to make comparisons between the probabilities from the fragility model developed here versus the HAZUS curve, comparisons can be made between the methodologies. As previously mentioned, the HAZUS curves do not distinguish between derailment and minor structural damage. During the experiment,

derailment was seen at significantly lower excitations than minor structural damage for the crane modeled. Additionally, minor structural damage requires a different type of repair and has a different length of downtime than derailment. It is logical to define derailment and minor structural damage as distinct damage states in order to better predict the downtime and repair costs associated with the types of damage.

The HAZUS curve has a larger β value (0.6) than the one considered from the experiment (0.36). The HAZUS curve is intended to represent all container cranes. However, considering that the industry experts have recognized that older, smaller cranes have a significantly different response than the larger modern cranes, the single HAZUS curve may not be the most informative representation of crane response. Instead, it may be more informative to develop separate fragility curves for distinct classes of cranes, such as the one developed here, which was developed for a J100 container crane.

8.5 Conclusions

The methodology for quantifying uncertainty and developing fragility curves for J100 container cranes is presented and applied to the experimental data collected in this study. A log-log linear fit for the data is most appropriate for the seismic demand model. The fragility curves developed from the experimental data is compared to the fragility curves developed in the study by Kosbab (2010) for a J100 crane. There is excellent agreement between the fragility curve developed using probabilistic seismic demand models developed from the experimental data and Kosbab's fragility curve developed using a log-log linear fit for the analytical data. Additionally, the fragility curves developed using only the experimental data agreed well with the fragility curved

developed using a log-log linear fit, suggesting that the lognormal assumption of the distribution of the seismic demand model. The intention of the fragility model developed from the experimental data is to validate the use of a frictional contact element, utilized by Kosbab (2010) for the prediction of derailment.

The experimental structure was designed to be a "typical" J100 container crane, rather than being a scale model of the crane used by Kosbab to develop fragility models. As such, geometry, mass properties, and periods differed between the two models. Despite these differences in the structures, nearly identical fragility models were developed in this study as in Kosbab's study. This result suggests that a single fragility model for a class of crane can be robust enough to capture the response of the cranes with in that class.

The methodology utilized in this study has several advantages over the HAZUS program. Due to the differences in downtime and repair costs between minor structural damage and derailment, it is logical to define distinct damage states for derailment and minor damage. Additionally, the HAZUS curves are intended to represent all rail mounted port container cranes. However, due to the large differences in the responses between older cranes and modern cranes, having separate fragility curves for distinct classes of cranes is more accurate and more informative than a single function.

CHAPTER 9

SUMMARY, CONCLUSIONS AND RECOMMENDATIONS

The most important conclusions from this study are highlighted in this chapter. This chapter also provides recommendations for practitioners and code committees to improve the seismic analysis, design, and performance of container cranes. It concludes with recommendations for future studies to further enhance our understanding of the seismic behavior of container cranes.

9.1 Summary

The main goal of this work was to experimentally investigate the seismic behavior of container cranes from the elastic behavior level through the initiation of collapse. Of particular interest is the characterization of the uplift and derailment behavior, because that is a phenomenon that is difficult to model accurately. Additionally, no previous experimental studies had been conducted on container cranes to gather information about buckling, yield and collapse.

The testing was divided into two phases. Phase I was conducted on a $1/20^{th}$ scale model and focused on the uplift and elastic behavior of container cranes. The results of this experiment were used to validate finite element models developed as part of a parallel study conducted by Kosbab (2010). Additionally, the results of the Phase I test were used to design the Phase II test. The Phase II test was conducted on a $1/10^{th}$ scale model and looked at the behavior of container cranes in both the elastic and inelastic range as well as characterized uplift when using a realistic boundary condition of a wheel on a rail. In both phases, the models were tested on the six-degree-of-freedom shake

tables at the University at Buffalo. The models were subjected to a suite of ground motions that included various directional components as well as amplitude scaling. Additionally, white noise tests were used for the determination of the natural frequencies of the system.

In support of the experiments, finite element models were developed. The finite element models were used to determine the simplifications that could be made to the structure while maintaining a dynamically equivalent structure. The models were also used to determine the forces the model would be subjected to, in order to determine the necessary capacities of the members. Finally, the finite element models were used to ensure that the overturning moment capacity of the shake table was not exceeded during the course of testing.

9.2 Conclusions

Sugano et al. (2008) proposed a simple method for determining the uplift acceleration of a container crane utilizing statics. The experimental results of this study verified that their method of predicting the uplift acceleration is valid and effective. It goes further to show that it is possible to predict the acceleration and drift levels at which the crane will derail by the use of Equation 2.18.

A typical container crane in the United States will uplift at an acceleration of 0.3-0.4g at the center of mass. However, the current design practice and codes use the value of 0.2g for the lift acceleration, (PIANC, 2001). Under the current design standard, cranes will not have sufficient strength to withstand seismic forces and will be exceedingly vulnerable.

9.2.1 Phase I

The most important mode of the crane was the portal sway mode, accounting for as much as 90% of the response. The primary bending mode for the scale model occurred at a period of 0.31s, which is in good agreement with the theoretical value based on the finite element analysis. The prototype value for the primary bending mode was 1.4s. The value of damping, calculated using the half power bandwidth calculation, was 0.84%.

The drift levels in the portal frame were at least an order of magnitude larger than the drift levels of the inter-story drift between the O-frame and portal fame. These results indicate that most of the deformation occurs within the portal frame. The response being concentrated in the portal frame indicates that models that include careful modeling of the portal structure, but simplifications to the remaining elements of the crane structure can be used for analysis and testing with good accuracy.

The best predictor of the amount of drift and moments experienced in the crane is the spectral acceleration at 0.31s, the natural period of the primary bending mode of the structure. This conclusion indicates that the best intensity measure to be used for the jumbo crane response is the spectral acceleration at the fundamental period of the structure.

The torsion response has a negligible effect on the overall response of the structure. Therefore, a two dimensional model should be sufficient to capture the seismic response of jumbo container cranes, which leads to large savings in computational requirements for crane modeling.

There was no consistent trend for the drift response of the model crane when the vertical excitation was included. In some cases the response was increased by as much as 16%, but in other cases the response was decreased by as much as 31%. In 5 of 9 cases, the amount of uplift displacement was substantially increased. In two cases there was no difference in the uplift displacement, and in the remaining two cases the uplift displacement was decreased. With a lack of consistent trends, it would be prudent to run analyses with and without a vertical excitation to get the most extreme case.

9.2.2 Modeling

The most significant conclusion from the modeling is that it is possible to simplify a jumbo crane model and maintain the dynamic properties. The portal frame is the most important section of the crane, and care must be taken in modeling the portal frame properly. The mass of the portal frame must be distributed along the members due to the P-Δ effects when large deformations of the portal frame occur. The center of mass of the crane must also be placed in a realistic location, so that the uplift of the crane will occur at the correct time. However, the rest of the structure of the crane has little influence on the portal sway mode, and thus the dynamic response.

9.2.3 Phase II

The $1/10^{th}$ scale model had a natural frequency of 0.74s for the primary bending mode. The damping value for the primary bending mode was 1.87%. The bending mode was a longer period than the predicted value based on the finite element models due to

the flexibility of the truck assembly, which was assumed to be rigid in the FEM. The damping value was higher than the previous test due to the slack in the truck assembly.

Based on the location of the center of mass, uplift/derailment threshold was 0.38g. The experimental data is in good agreement with this value, and supports the theory that it is possible to predict when uplift and derailment will occur based on the acceleration of the structure.

The test structure uplifted when the drift levels exceeded 1.8%. During the experiments yielding was observed when the drift levels exceeded 3.1%. Irreparable damage was observed in the test structure when the drift levels reached 5.7%. The structure failed shortly after yield. After yielding, a change in the structural stiffness was observed, indicating that damage occurred. Due to the increase in flexibility, it took larger excitations and drift levels to achieve uplift after the structure was damaged. At the ultimate failure, the structure experienced local buckling, permanent deformations of the columns and failure of the welds.

Two different boundary conditions were used in the experiment: pinned and free, in order to validate FEM with both boundary conditions. The damping in the free condition was higher than that of the pinned condition. During most of the ground motions, the structure experienced higher peak drift when the crane was free to uplift than when it was pinned. This result supports the industry claim that pinning a crane to the wharf during an earthquake could lead to larger forces and an undesirable response.

9.3 Recommendations for Practitioners

This study only looked at jumbo container cranes, and as such the following recommendations should be applied to the design and analysis of jumbo container cranes.

1. The primary response of a jumbo crane is in the portal sway mode, which accounts for 90% of the response. Therefore, any performance based design criteria should use the portal drifts as an engineering demand parameter.
2. The best intensity measure for the seismic response of container cranes is the spectral acceleration at the natural period of the portal sway mode. Seismic analysis and design of container cranes should utilize the spectral acceleration as an intensity measure.
3. Stiffener patterns for the portal frame should be designed such that the desired levels of ductility are achieved, as well as ensuring that panel buckling rather than wall buckling occurs, because panel buckling occurs at larger levels of load.
4. Requirements for seismic detailing and analysis of container cranes should be included in a code; otherwise these issues will continue to be ignored.
5. Seismic qualification tests would be useful to ensure the performance of the cranes. Qualification tests can either be performed experimentally on physical models or analytically. For both types of tests, the base motions are important and should be selected with care. For example, when liquefaction of the soil beneath the wharf occurs, the dynamic characteristics of the wharf system change dramatically, sometimes making the natural period of the wharf correspond to that of the crane. Therefore, it is necessary to account for the soil conditions at the site where the crane will be located as well as the dynamic properties of the wharf. It

would be best if a non-linear dynamic time history can be done with several ground motions on a model of the wharf with the site-specific soil conditions, giving the most realistic base excitation possible. If that type of analysis is unavailable, the analyst could use wharf motions generated as part of the NEES Grand Challenge project on the seismic risk assessment of port systems.

6. For physical qualification tests, a simplified model that carefully represents the portal structure will provide useful information. The specimen should be designed such that the center of mass of the test specimen is in the proper location for a crane that is in operation, as that represents the extreme load case. Large scale testing should be performed, particularly if there is an interest in yielding, buckling and collapse. Useful information can be gathered from a $1/10^{th}$ scale model.

7. For analytical qualification tests, simplified models that explicitly model the portal structure are sufficient to capture the dynamic properties. Additionally, 2-D models will capture the seismic response of container cranes. It is necessary to model the crane with a boundary element that allows uplift and does not restrain the base horizontally while the base is uplifted. For all test earthquakes, a horizontal motion in the trolley travel direction and a vertical motion should be used. Time histories should be run for the horizontal motion alone and the horizontal and vertical combined should be run, since there are cases where either will govern.

9.4 Impact

This work represents the most sophisticated, and comprehensive shake table tests performed on container cranes to date. As such there are many benefits of the work, including the following:

- This was the first test in the world to consider nonlinear effects. All of the previous tests assumed that if a crane remained elastic until uplift, then it would not experience inelastic behavior during a ground motion. This assumption is also seen in US design guidelines where it is stated that the maximum possible internal force is that at incipient uplift (ASCE 1998). This was based on the fact that early container cranes had small gage lengths, and thus could tip at relatively low lateral loads. As a result, it became typical for US port designers to adopt a lateral seismic design force of 0.2g as standard for new container cranes (Soderberg et al. 2009). This test showed modern jumbo cranes will tip at larger forces than the 0.2g assumption. Therefore, if the 0.2g value is used for modern cranes, the expected seismic forces will be significantly underestimated. Additionally, this test provided data to show that the jumbo crane will experience higher forces during and after uplift than those at incipient uplift. In fact, the internal forces that lead to yielding and collapse occurred after the point of incipient uplift. Therefore, the design assumption that the maximum possible force is at incipient uplift is incorrect for jumbo container cranes.
- All previous tests neglected the influence of the vertical component of ground motion. This study showed that there are instances in which the inclusion of a vertical excitation increased the critical portal sway response. Additionally, the

amount of vertical displacement can be increased with the inclusion of a vertical excitation. Therefore, vertical excitations should be considered in the analysis of container cranes to determine the most extreme load case.

- One of the most difficult aspects of modeling a container crane is the boundary condition of a wheel on a rail. This study provides complete data of how the wheel flange affects the uplift behavior. When the wheel begins to uplift, the flanges of the wheels prevent horizontal motion until they clear the rail. This restraint translates into a tendency of the wheels to lift straight up before the large horizontal displacements occur. A consequence of this larger vertical motion is that there is less horizontal motion than is predicted by the frictional contact elements. This information can be used to help develop more accurate models for uplifting wheels, which would include some restraint during the time the wheel flanges would be on the rails.
- The test structure was designed to be a "typical" J100 container crane, rather than being a scale model of the crane used by Kosbab to develop fragility models. As such, the periods, geometry and mass properties differed between the two models. Despite the differences in the structures, nearly identical fragility models were developed in this study as in Kosbab's study. This result suggests that a single fragility model for a class of crane can be robust enough to capture the response of the cranes with in that class.
- During the course of this study, the test structure had to be simplified. This study showed that a simplified test structure can provide all of the critical response quantities that one can obtain from a full, detailed model, such as the timing and

duration of uplift and the portal sway behavior, as long as the portal structure is properly modeled and the center of mass is in the correct location. This finding has strong implications for practitioners because they can save time and computational power by considering simplified models.

- The data generated during testing was used to validate sophisticated finite element models that are going to be used as part of a port wide risk assessment.
- The nonstructural components within a structure account for a significant portion of the losses due to seismic events. Many nonstructural components are free to slide and uplift. A variety of finite element software programs have developed frictional contact elements, yet many modelers lack confidence in the performance of those elements. This study provides data that demonstrate the applicability of the use of these elements in seismic, structural applications.

9.5 Recommendations for Future Work

There is more work that needs to be done to gain a complete understanding of the seismic response of modern container cranes.

- One of the limitations of scale models is that nonlinear effects cannot be scaled up. Therefore, it is difficult to make conclusions about the nonlinear damage states of a full-scale model based solely on a scale model. Therefore, full-scale component tests should be performed on the portal legs in order to determine their rotation capacity and ductility capacity. Additional studies need to be completed to determine how stiffener patterns affect the ductility of the portal structure.

- There are no simple methods to account for the vertical effects of ground motions. A full, nonlinear time history is currently necessary to account for the vertical excitation. Studies need to be completed to determine simplified ways to account for the vertical components for large ground motions.
- It was shown that the ground motion that had liquefied soil had a large influence on the input and thus response of the crane. Studies need to be completed on the impact of local site effects on the wharf and crane response.
- During testing, it was observed that tiedowns could cause an increase in demand of the structure. Further analysis and testing should be done to quantify this effect. This information would be particularly applicable to the cranes at the Port of Charleston, which would likely be tied down during an earthquake.
- With the vulnerabilities in many container cranes in ports today, effective retrofit strategies need to be developed. Testing and analysis should be done to evaluate the effectiveness of various retrofit strategies. Some suggested retrofit strategies include adding viscous dampers to the portal structure, which would dissipate the energy in the portal structure. The machinery house contributes the largest amount of mass other than the structure itself. For a jumbo crane, it accounts for about 6% of the total mass. Isolating the large machinery house may have some effect on the structure and it may be possible, with some minor modifications, to use it as a tuned mass damper. Isolation at the base or portal beam level can limit the accelerations at the center of mass, thus decreasing the likelihood of damage. Isolation will result in large displacements of the portion of the structure above the isolator.

APPENDIX A

DATA PROCESSING

During the course of this work, it was necessary to process various types of data and do numerous calculations. This appendix highlights the different methods of data processing used through the course of this study. Some of the types of calculations include frequency responses, moments and axial loads, drift, displacements, and structural stiffness.

A.1 White Noise Test Results

There are two main types of information that can be calculated from a white noise test: natural frequencies and damping values. The natural frequencies are important because they characterize the can be used to predict the response of the structure. Damping is an important characteristic of a structure, but is difficult to quantify except through experimentation. This section describes in further detail how the calculations for natural frequencies and damping are done.

A.1.1 Natural Frequencies

The first step to determining the natural frequencies of a structure is to perform a fast fourier transform (FFT) on the data from the white noise test. The FFT is an efficient way to convert data from the time domain into the frequency domain. The peaks of the frequency domain response are the natural frequencies. To do an FFT, it is necessary to have input and structural response accelerations. The input accelerations are those measured on the shake table. The structural response accelerations are selected to give

the natural frequency of a particular mode, and will be addressed further in the following paragraphs.

In Phase I, there were four main modes of interest: portal sway, frame torsion, boom torsion and vertical boom motion. To calculate the portal sway mode, the signal from accelerometer X (Figure 3.Y) is used. To calculate the frame torsion mode, the signal from accelerometer Z is used. To calculate the boom torsion, the signal from accelerometer A is used. To calculate the vertical boom mode, the signal from accelerometer B is used. Figure A.1 show the results of the FFT analysis.

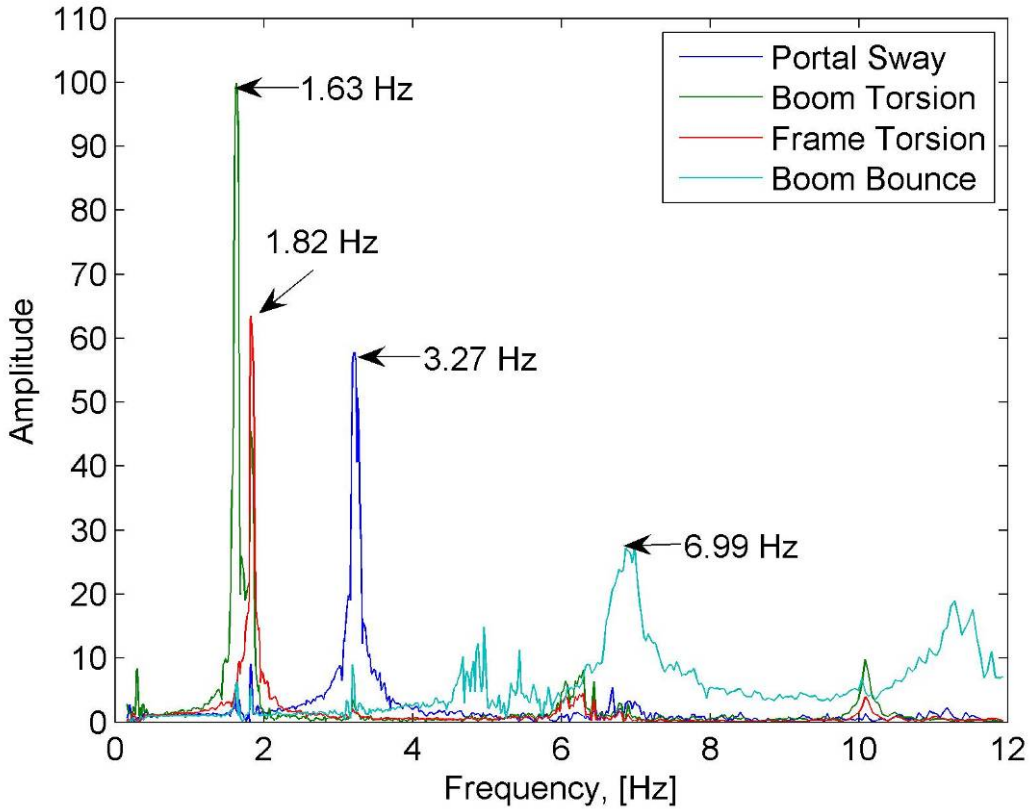

Figure A.1: Frequency response of the white noise tests for Phase I Test on a 1/20th scale container crane

In Phase II, there were two main modes of interest: portal sway and frame torsion. To calculate the portal sway mode, the signal from accelerometer 40 (Figure 6.7) is used. To calculate the frame torsion mode, the signal from accelerometer 41 is used. Figure A.2 shows the result of the FFT analysis.

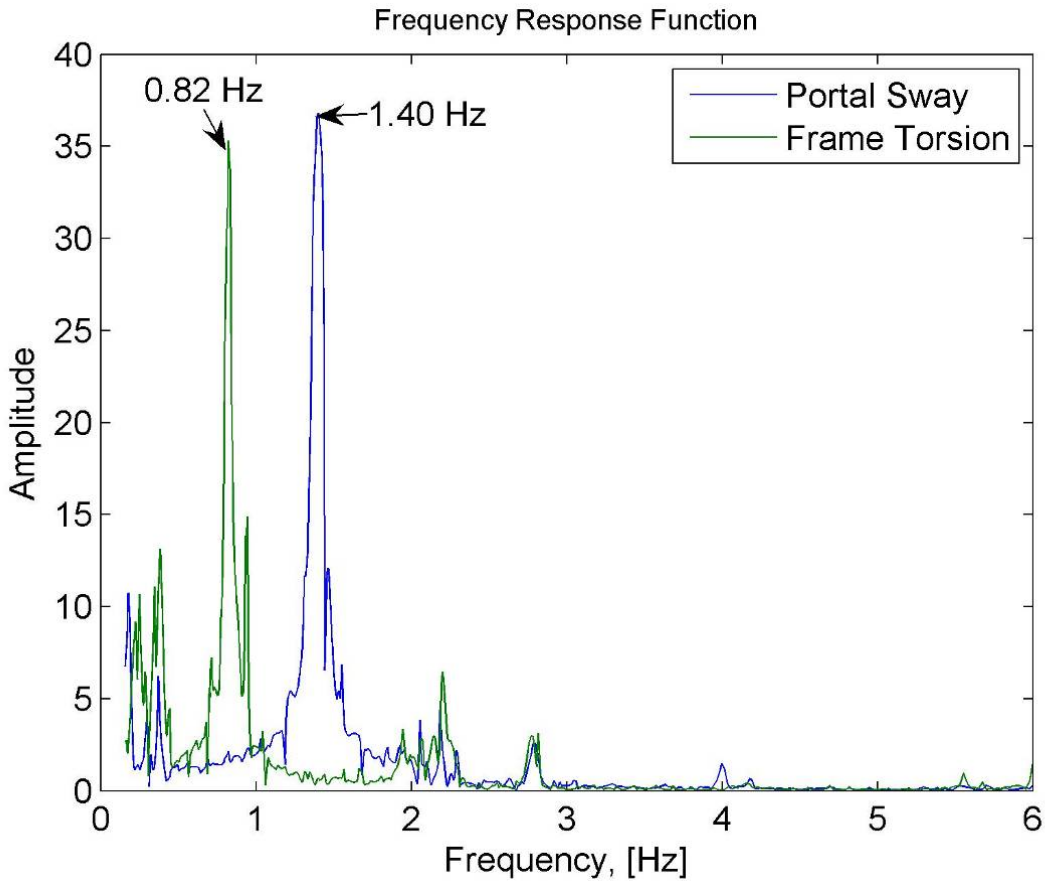

Figure A.2: Frequency response of the white noise tests for Phase II test on a 1/10th scale container crane

A.1.2 Damping Calculation

There are several techniques for calculating the damping values for a structure from the white noise results. One of the methods is the half power bandwidth method. This method utilizes the response in the frequency domain. The first step is to find the

natural frequency at each mode, ω_n, and the amplitude of the FRF at that frequency. Then the amplitude value is divided by the square root of two. The frequencies corresponding to the locations of the reduced amplitude are then determined, as shown in Figure A.3. The damping ratio is then calculated using Equation A.1.

$$2\zeta = \frac{\omega_2 - \omega_1}{\omega_n} \tag{A.1}$$

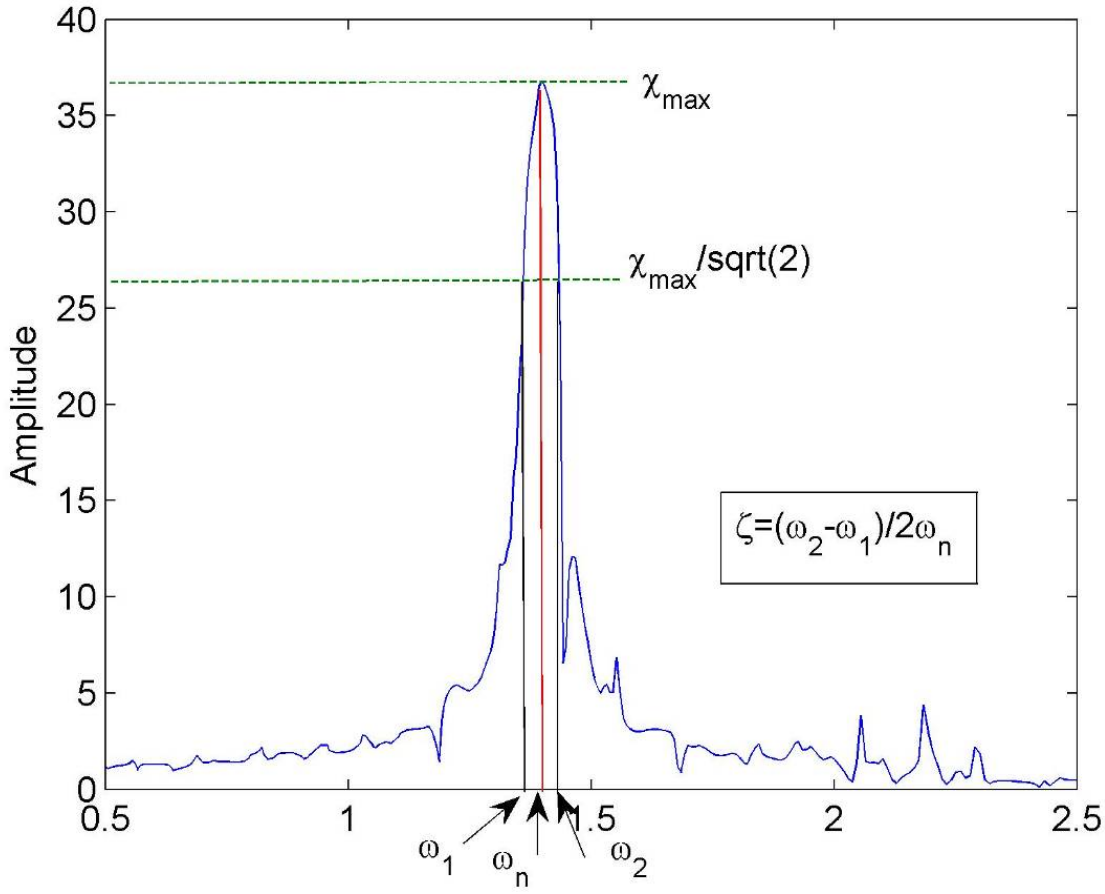

Figure A.3: Damping calculation example

A.2 Ground Motion Input

In order to investigate the effects of earthquakes on container cranes, it is necessary to come up with a single value to characterize the ground motion. There are a couple of ways to do that: peak base excitation and spectral acceleration. The methods used to calculate these values are discussed further in the following paragraphs.

The first ground motion characteristic is the peak base excitation. The accelerometers on the base of the shake table are the base excitations. There were three accelerometers oriented in three orthogonal directions. The values of the measurements from each of the accelerometers can be combined to determine the total acceleration by taking the square root of the sum of the squares of each of the values. This was done for each time step of each ground motion. Then, the maximum value of the time history is determined, and that is the peak base excitation value.

The second ground motion characteristic is the spectral acceleration. The spectral acceleration in this study is calculated using the methodology described by Nigam and Jennings (1969). The spectral acceleration is defined by the maximum response of a single oscillator subjected to a base acceleration. In order to solve the equations of motion to get the maximum response, there are a few necessary inputs, which include: the base acceleration time history, the natural frequency of the structure, and the damping value for the natural frequency. For the analysis on this study, the spectral acceleration at the primary bending mode is selected because the majority of the response occurs in that mode. The first step is to perform an analysis to determine the natural frequencies and damping values, as described in section A.1. The base acceleration is the accelerometer reading on the shake table in the direction of the primary bending mode.

A.3 Structural Response

There are several structural response quantities that are important for the characterization of the seismic behavior of container cranes: drift, displacements, and moments and axial loads. The following sections outline the data processing procedures and calculations used in the analysis of the data.

A.3.1 Drift

One of the most important values that had to be calculated for the analysis of the behavior of the container crane models was the portal drift, shown in Figure A.4. The portal drift is calculated for both the data from Phase I and Phase II. The treatment of the drift calculation for each phase is further discussed in the following paragraphs.

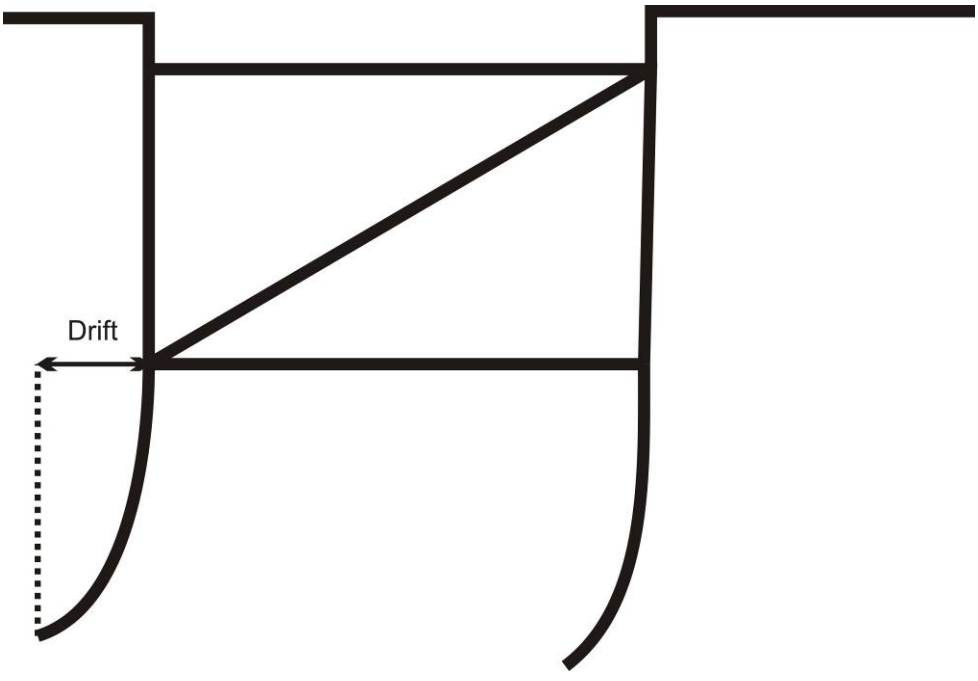

Figure A.4: Portal Drift Definition for Container Cranes

In Phase I, the drift is calculated for the north frame, the one instrumented with displacement gauges. The drift is calculated by subtracting the displacement of DX from DY. To remove the effects of rigid body motion, the relationship between the vertical displacement and the horizontal displacement is determined using geometry, Figure A.5. The rigid body displacement is then subtracted from the drift. To normalize the data, the drift is divided by the distance between gauges DX and DY and then multiplied by 100, to get the percent drift. This is completed for each time step of each of the time histories to get a time history of the percent drift.

In Phase II, the drift is calculated for each frame. There were displacement gauges on each of the trucks. To get the bottom x displacement for the columns to get the drift, the average of the x displacement of each of the two trucks under that column are averaged. The same is done for the z displacement. To determine the effects of the rigid body motion, the relationship between the vertical and horizontal displacements was determined using geometry (Figure A.5). To get the drift, the base x displacement and the rigid body effects are subtracted from the x displacement of the portal beam for each frame. To normalize the drift, the drift is divided by the height of the portal beam and then multiplied by 100, to get the percent drift. This is completed for each time step of each of the time histories to get a time history of the percent drift.

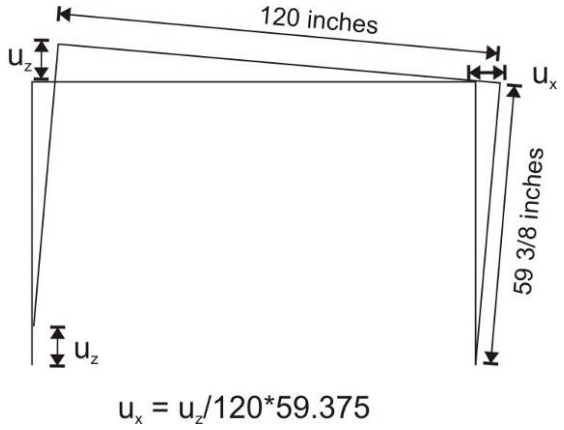

Figure A.5: Geometry for determining rigid body motion

A.3.2 Displacements

All of the displacements presented in this work are relative displacements, that is displacements relative to the top of the shake table. The x and y displacements are calculated by taking the measurements from the displacement gauges and subtracting the x and y table displacements. The z displacements of the structure were measured from the top of the table, so the displacement measurements in this direction are relative. To remove any initial offset in the displacement measurements due to the DC offset of the gauges, the first second of the recording, prior to the start of excitation, is averaged, and then subtracted from the entire time history.

A.3.3 Moments and Axial Loads

The moments and axial loads in the members were calculated using the measurements from the strain gauges. The precise location of each strain gauge was measured and recorded. The locations of the strain gauges and the strain readings were used to determine the polynomial that defines the plane on which they are located. The

values of strain and the polynomial are then used to determine the strain in the middle of each side of the member.

The axial load portion is calculated by determining the average value of the strains at the four mid-side locations. The average was then multiplied by the Young's Modulus and the area of the cross-section. The axial portion of the strain was then removed from all of the gauges.

The moments are calculated using a strain plane that is defined after the axial load is removed. The biaxial moments are then calculated assuming a linear strain profile, using the relationships:

$$M_x = E * \varepsilon * I_x / (b / 2) \quad \text{(A.2)}$$

$$M_y = E * \varepsilon * I_y / (b / 2) \quad \text{(A.3)}$$

where M_x and M_y are the moment about the X and Y axes respectively; E is the Young's Modulus; I_x and I_y are the moments of inertia about the X and Y axes respectively; ε is the strain.

The axial load and moment calculations are completed using all four combinations of three gauges at each location. The signals are assessed, and if all the gauges are functioning properly, the four time histories are averaged. However, if one of the gauges is broken, then the moment and axial load calculations using those values are discarded, and only the trace that does not include that gauge is used.

APPENDIX B

DETAILS OF 1/20TH SCALE MODEL

This appendix contains additional information of the 1/20th scale model of a jumbo container crane. Section B.1 provides detailed information on the prototype container crane. Section B.2 includes information on the dimensions of the various members, as well as the fabrication drawings. Section B.3 contains additional data from the experiment.

B.1 Prototype Structure

Container cranes are made up of a combination of three types of members: built-up hollow boxes, circular tubes and built-up wide-flange shapes. The dimensions of each of the types of sections are defined in Figure B.1. The hollow box sections have dimensions B and D, and flange and web thicknesses of t_f and t_w respectively. There are often longitudinal stiffeners in the built-up box sections. The number of stiffeners in the flange and web are denoted as n_f and n_w respectively. The tubes have a diameter, D and a thickness, t. The built-up wide-flange shapes flange dimensions B and t_f and and web dimensions D and t_w.

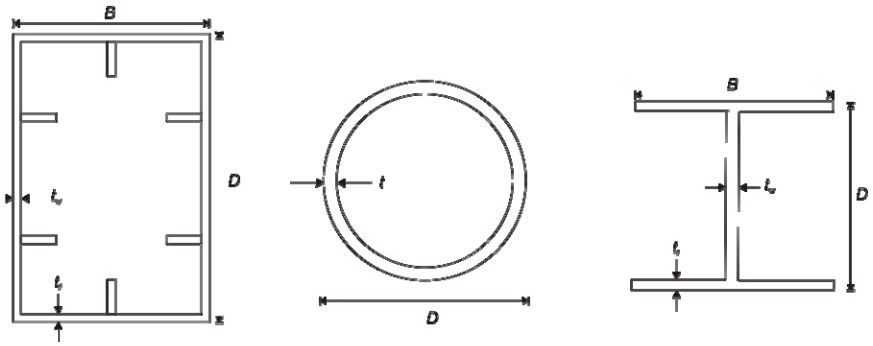

Figure B.1: Cross sections of members used in container cranes

The first step in creating a scale model is to determine the properties of the prototype structure. The structural properties can be categorized in three main classes: geometric, member and mass. The geometric properties characterize the general shape and layout of the crane, and are presented in Figure B.2. Dimensions for the various sections are presented in Table B.1 (built-up hollow boxes), Table B.2 (tubes), and Table B.3 (built-up wide-flange shapes).

Table B.1: Dimensions of J100 built-up hollow box sections

Section	*B (in)*	t_f *(in)*	n_f	*D (in)*	t_w *(in)*	n_w
A-A	60.00	0.625	1	90.00	0.375	2
B-B	60.00	0.500	1	90.00	0.328	2
C-C	52.76	1.102	1	80.94	0.709	2
C'-C'	52.76	1.102	1	80.94	0.787	2
D-D	52.76	1.102	1	80.94	0.630	2
D'-D'	52.76	1.102	1	80.94	0.787	2
E-E	52.76	0.472	1	67.87	0.394	2
F-F	52.76	0.787	1	68.19	0.551	2
G-G	111.34	1.024	2	68.19	0.630	2
H-H	52.76	0.630	2	68.50	0.787	2
I-I	111.81	0.787	2	68.50	0.787	2
J-J	52.76	1.417	1	101.26	0.787	2
J'-J'	52.76	1.417	1	101.26	0.945	2
K-K	52.76	0.787	1	100.00	0.551	2
K'-K'	52.76	0.787	1	100.00	0.630	2
L-L	67.75	0.472	2	119.06	0.315	4
M-M	49.61	0.787	1	72.44	0.630	2
N-N	52.76	0.945	2	68.82	0.787	2

Table B.2: Section dimensions of J100 tube sections

Section	*D (in)*	*t (in)*
O-O	39.37	0.630
P-P	47.24	0.630
Q-Q	19.69	0.394
R-R	39.37	0.551

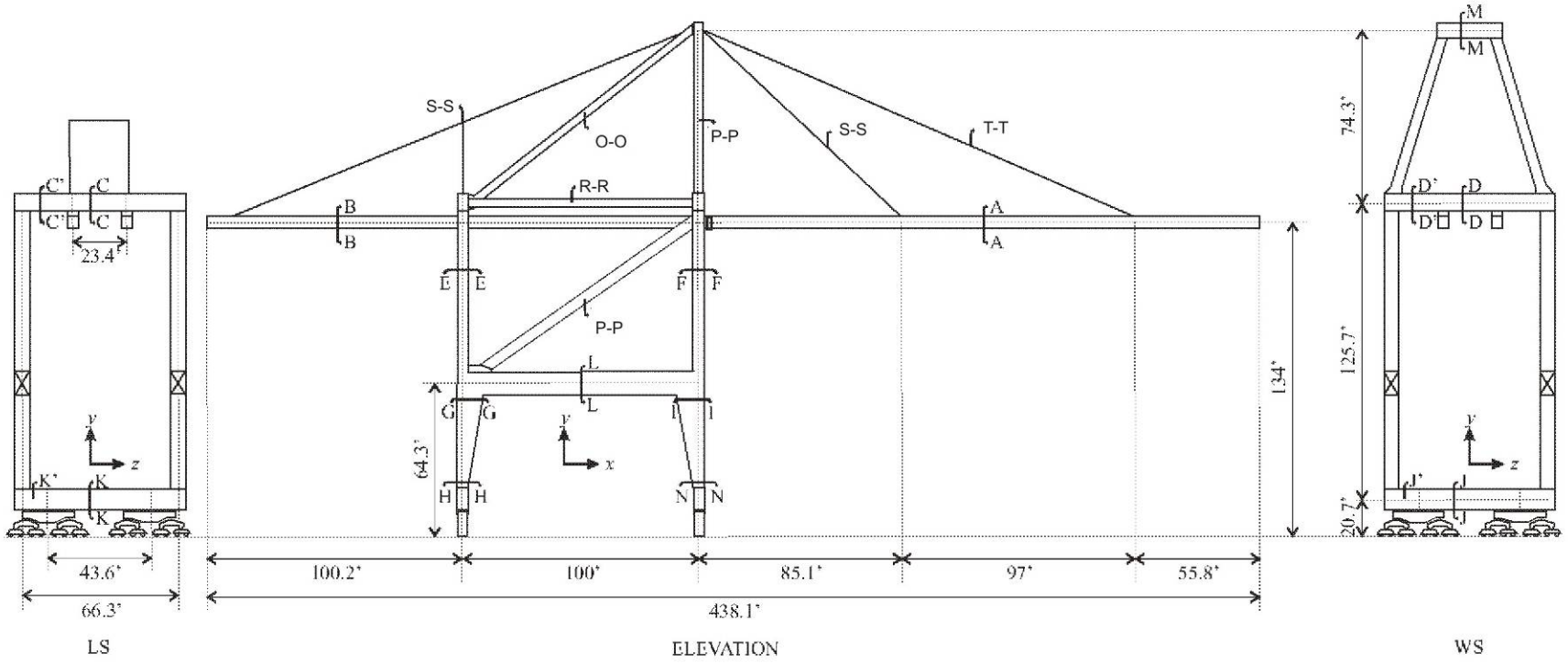

Figure B.2: Overall dimensions and section assignments for the prototype container crane

Table B.3: Section dimensions of J100 built-up wide-flange sections

Section	*B (in)*	t_f *(in)*	*D (in)*	t_w *(in)*
S-S	11.81	0.630	13.07	0.472
T-T	26.54	0.787	15.35	0.630

Mass is the final structural property needed to characterize the prototype structure. Dead load factors are assigned to each member to account for the distributed nonstructural masses attached to each member, and are presented in Table B.4. Table B.5 provides a summary of the overall weight, including the equipment and machinery.

Table B.4: Dead load factors for J100 structural members

Member	*Factor*
Legs	1.3
Sill	2.00
Portal Beam	1.30
Landside TGSB	1.76
Waterside TGSB	2.00
Pipes	1.00
Top Beam	4.50
Boom	1.65
Trolley Girder	2.00
Forestays	1.00
Boom Ties	1.30

Table B.5: Weight summary for J100 crane

Item	*Weight (kip)*
Structural Frame	2039.1
Stairs 1	10.7
Stairs 2	40.0
Stairs 3	19.0
Trucks (x4)	62.7
Machinery House (x2)	174.2
Service Crane	3.9
½ Festoon	8.8
Snag Device	03.9
Boom Hoist Rope	17.0
Trim & List	4.4
Total	**2773**

B.2 Scale Model Details

B.2.1 Member Details

Presented in Table B.6 are the dimensions of all of the members of the 1/20th scale model structure illustrated in Figure B.3 that give the moments of inertia presented in Table 3.2. The values of *D* and *B* correspond to the dimensions labeled in Figure B.1. The boxes have a uniform thickness, so t_f and t_w are represented by a single variable, *t*. The tubes have a diameter, *D* and a thickness, *t*, as illustrated in Figure B.1.

Table B.6: Member dimensions for 1/20th scale model jumbo crane

Box Member	*D in*	*B in*	*t in*
B1	2.5	1.5	0.12
B2	1	1.5	0.12
B3	2.875	2	0.164
B4	3	2	0.25
B6	3	1.5	0.188
B5	4	2	0.25
B12	2	1.25	0.083
B11	2	1.875	0.164
B10	2	3.75	0.164
B9	2	1.625	0.164
B8	2	3.5	0.164
B7	3	1.5	0.188
Tube Member	*D in*	*t in*	
C1	1.66	0.14	
C2	1.315	0.133	

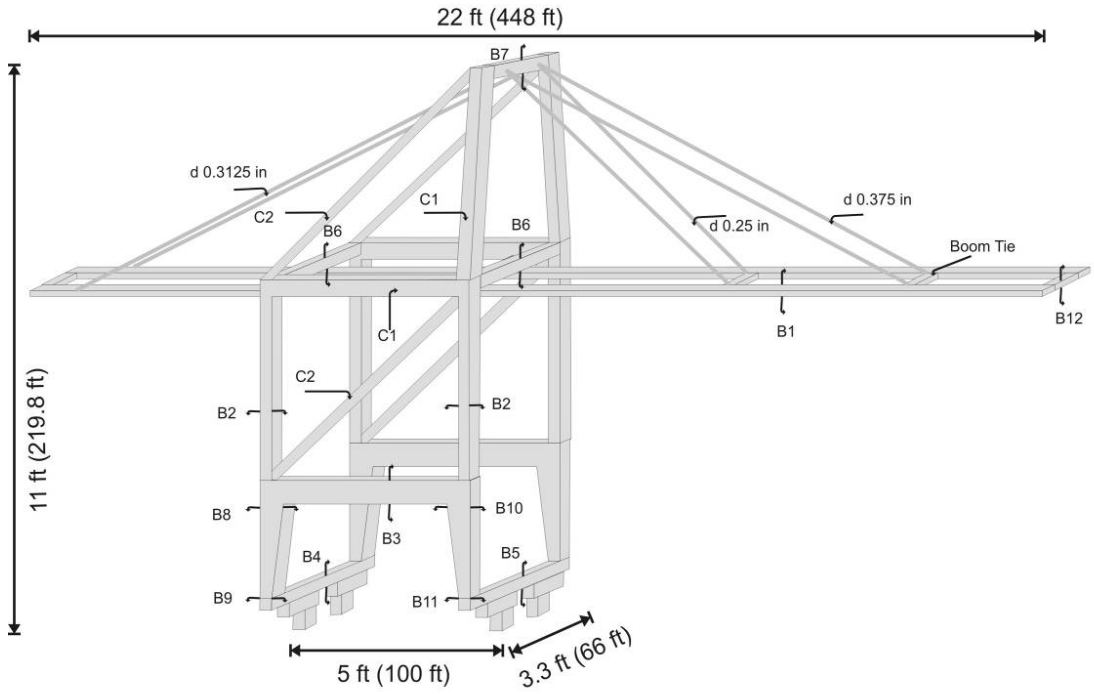

Figure B.3: 1/20th scale model of a jumbo container crane

B.2.2 Fabrication Drawings

The next 24 drawings are the fabrication drawings for the 1/20th scale model. Figure B.4 gives the overall dimensions and section and connection labels. Figure B.5 shows the cross-section dimensions and details for all of the members used in the model. Figures B.6 – B.13 give special member details. Figure B.14 gives the details for the boom and trolley girder. Figures B.15 – B.28 illustrate the connection details. Figure B.29 shows the details of the pseudo trucks.

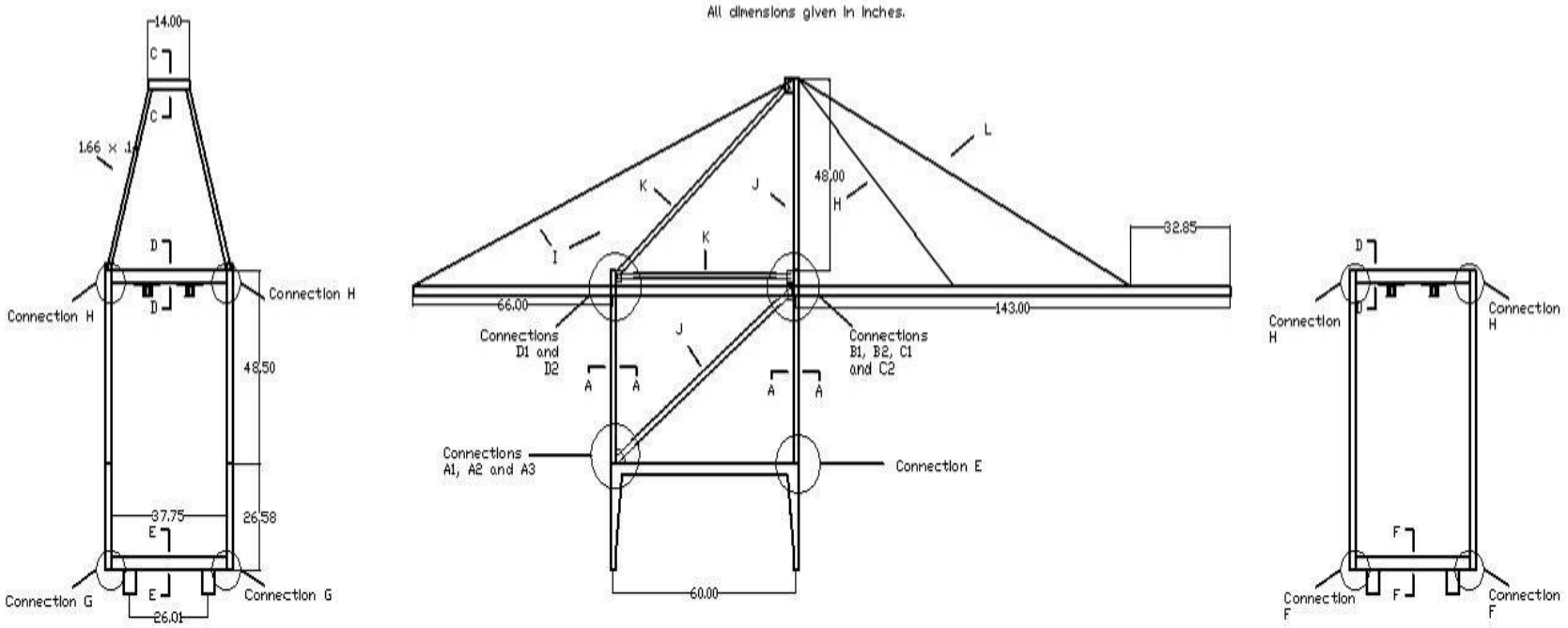

Figure B.4: Fabrication drawing overview of 1/20th scale model crane

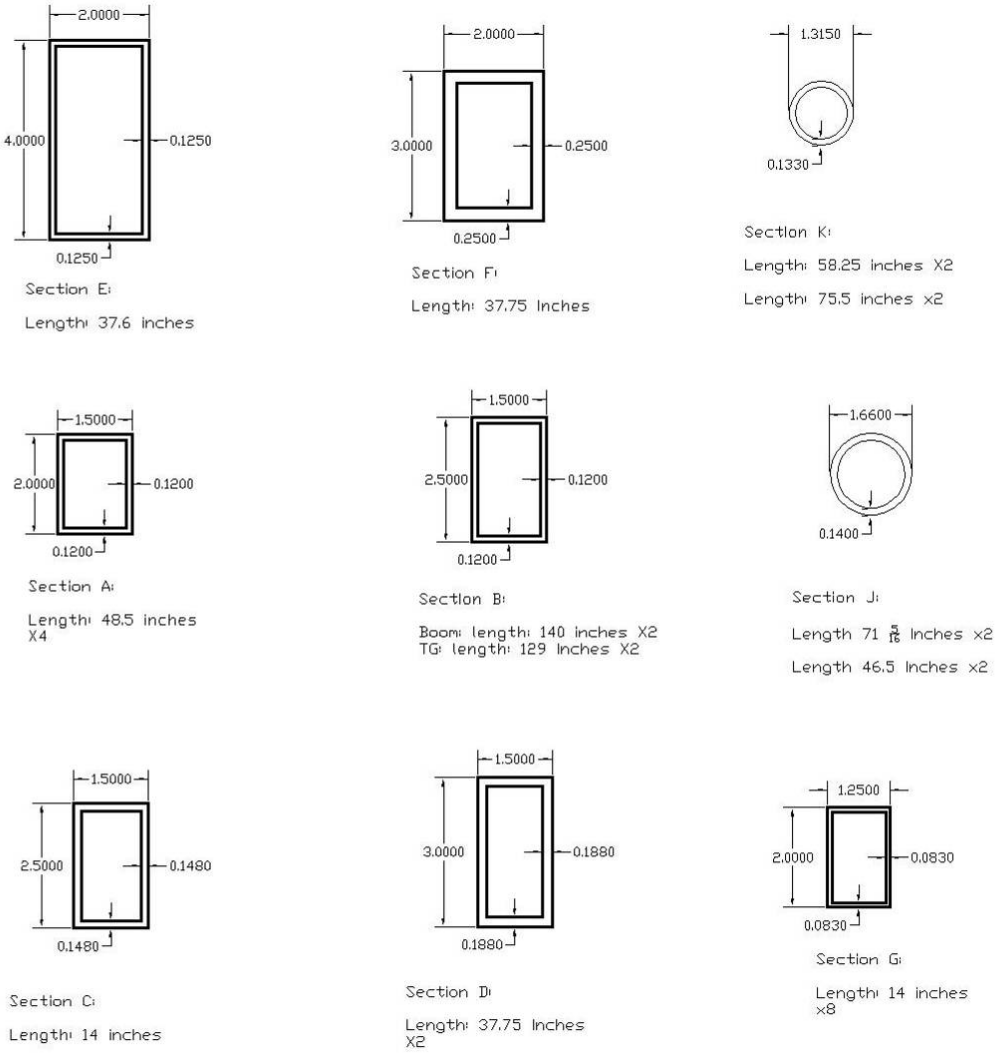

Figure B.5: Fabrication drawings of members used in 1/20th scale model

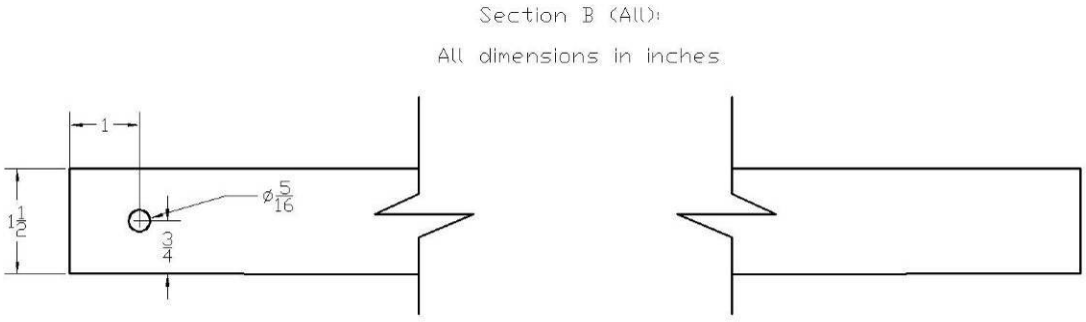

Figure B.6: Special details for section B

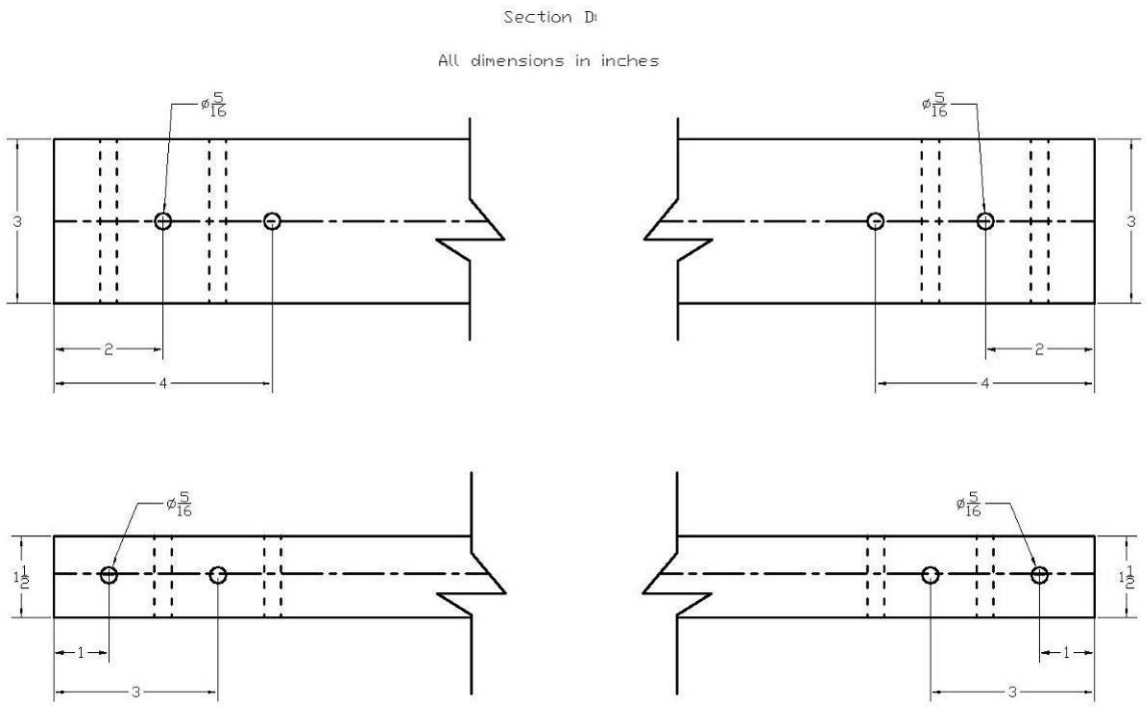

Figure B.7: Special details for section D

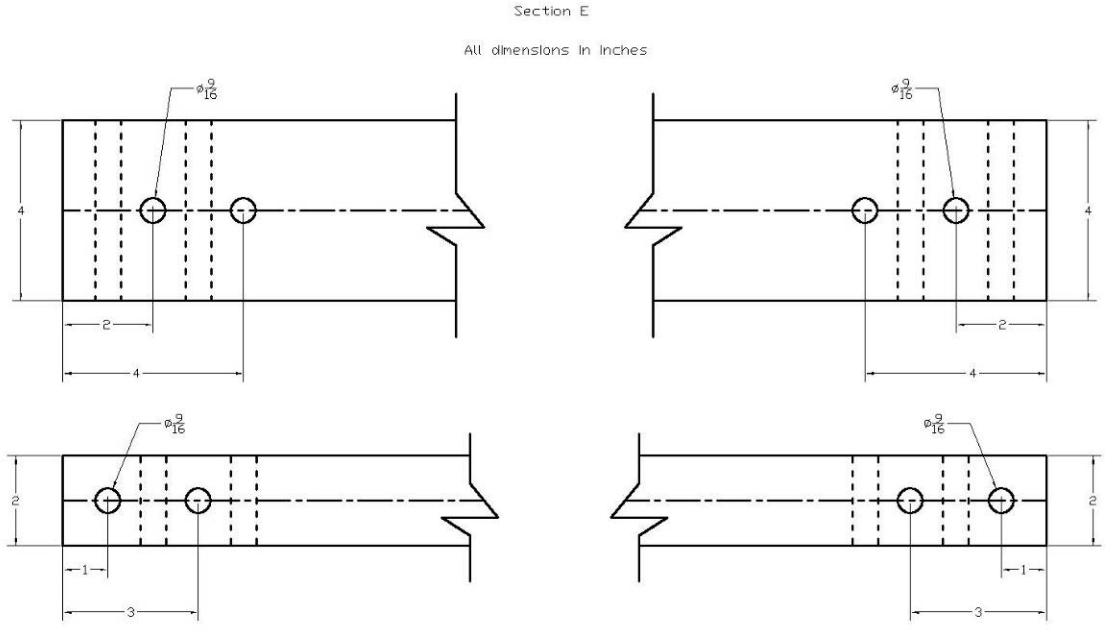

Figure B.8: Special details for section E

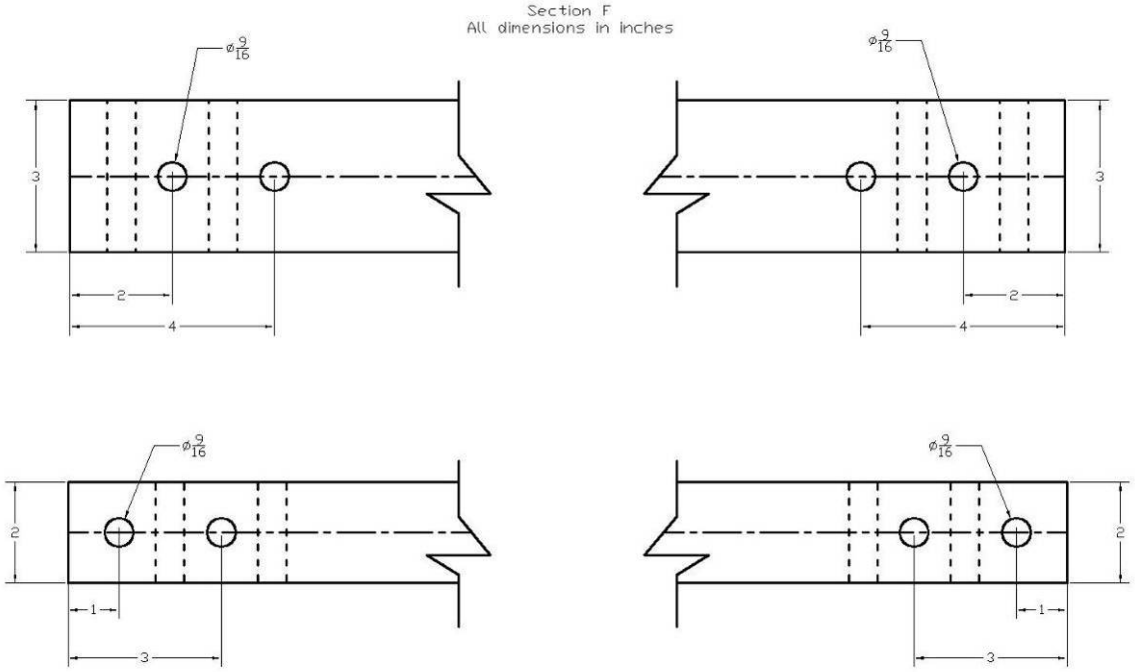

Figure B.9: Special details for section F

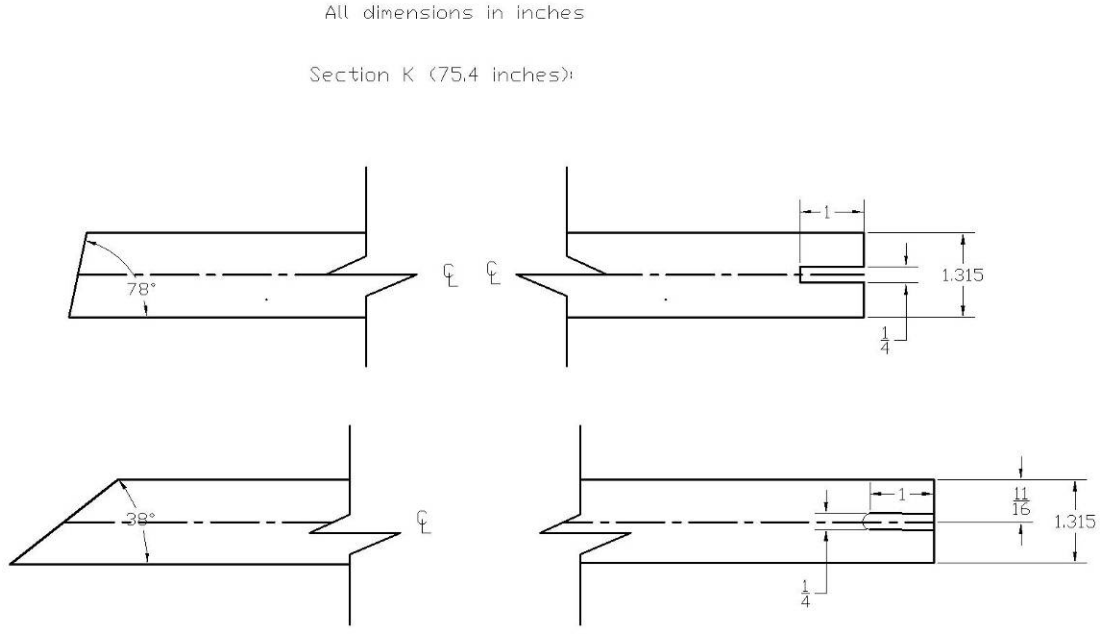

Figure B.10: Special details for 75.4 in long section K

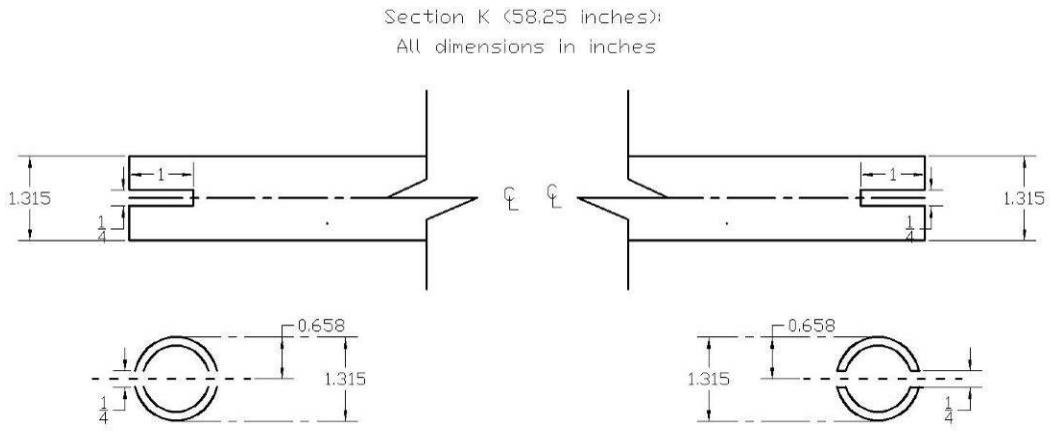

Figure B.11: Special details for 58.25 in long section K

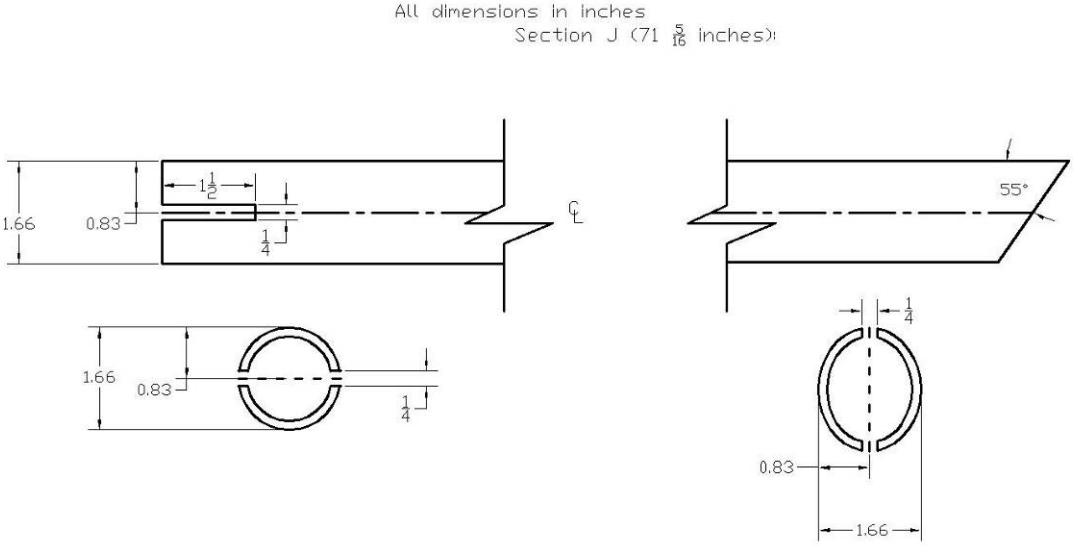

Figure B.12: Special details for 71 5/16 in long section J

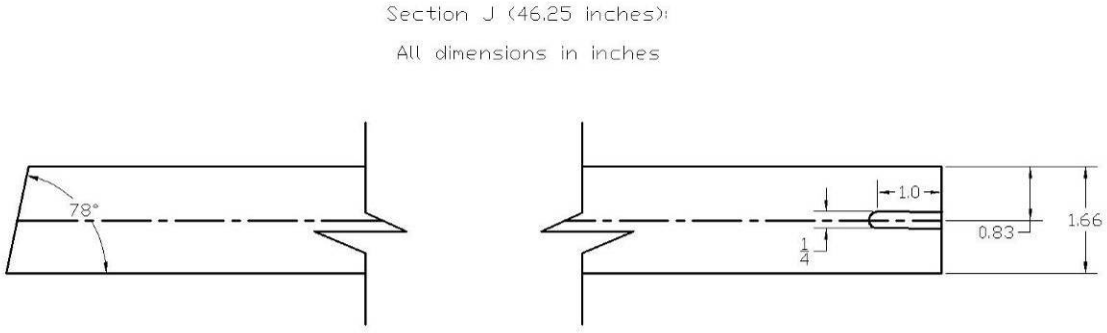

Figure B.13: Special details for 46.25 in long section J

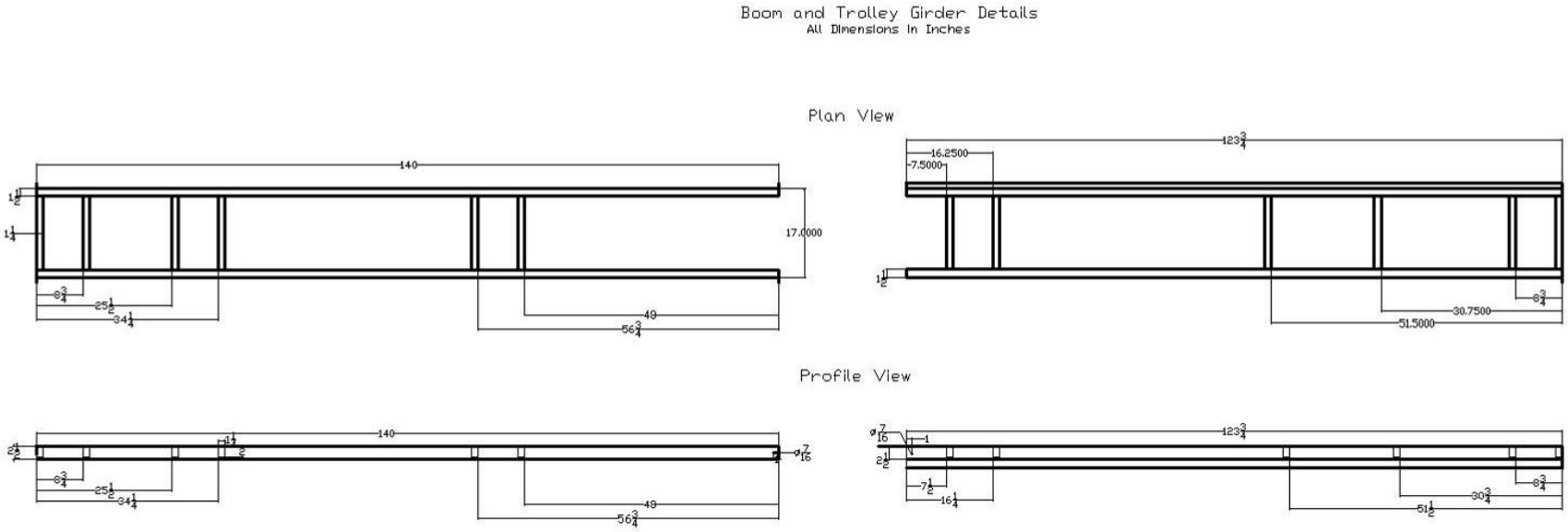

Figure B.14: Boom and trolley girder details

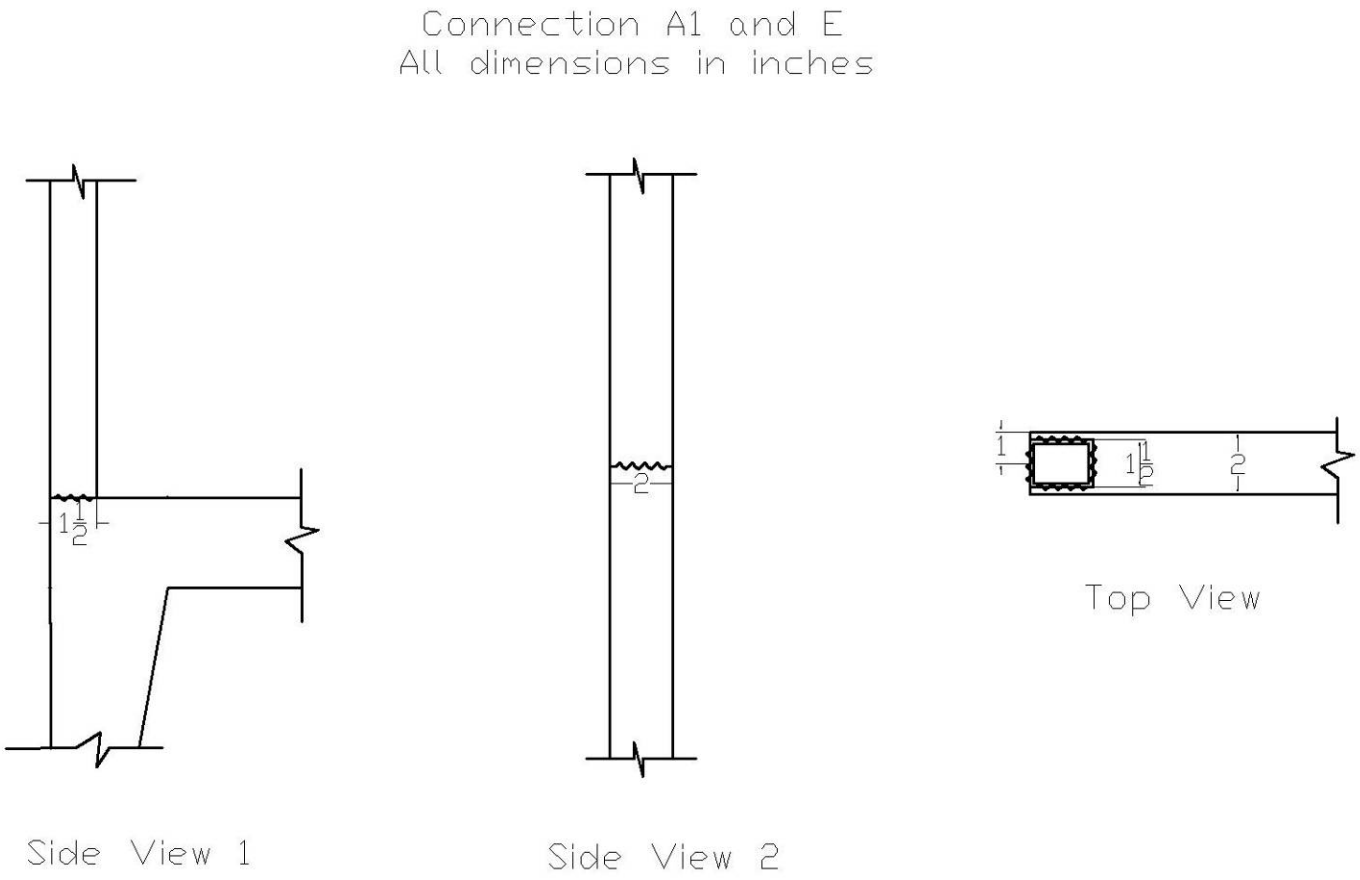

Figure B.15: Details for connections A1 and E

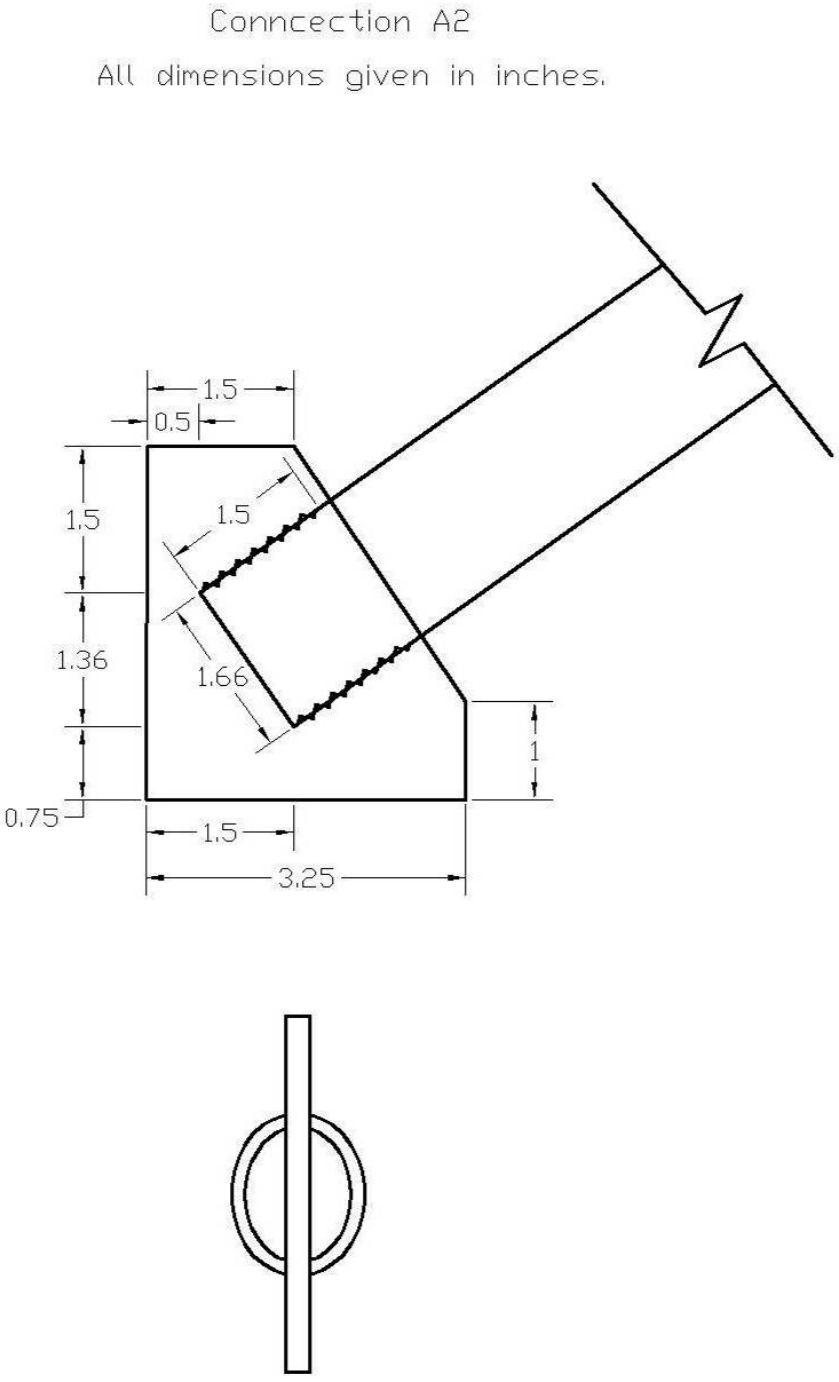

Figure B.16: Connection A2 details

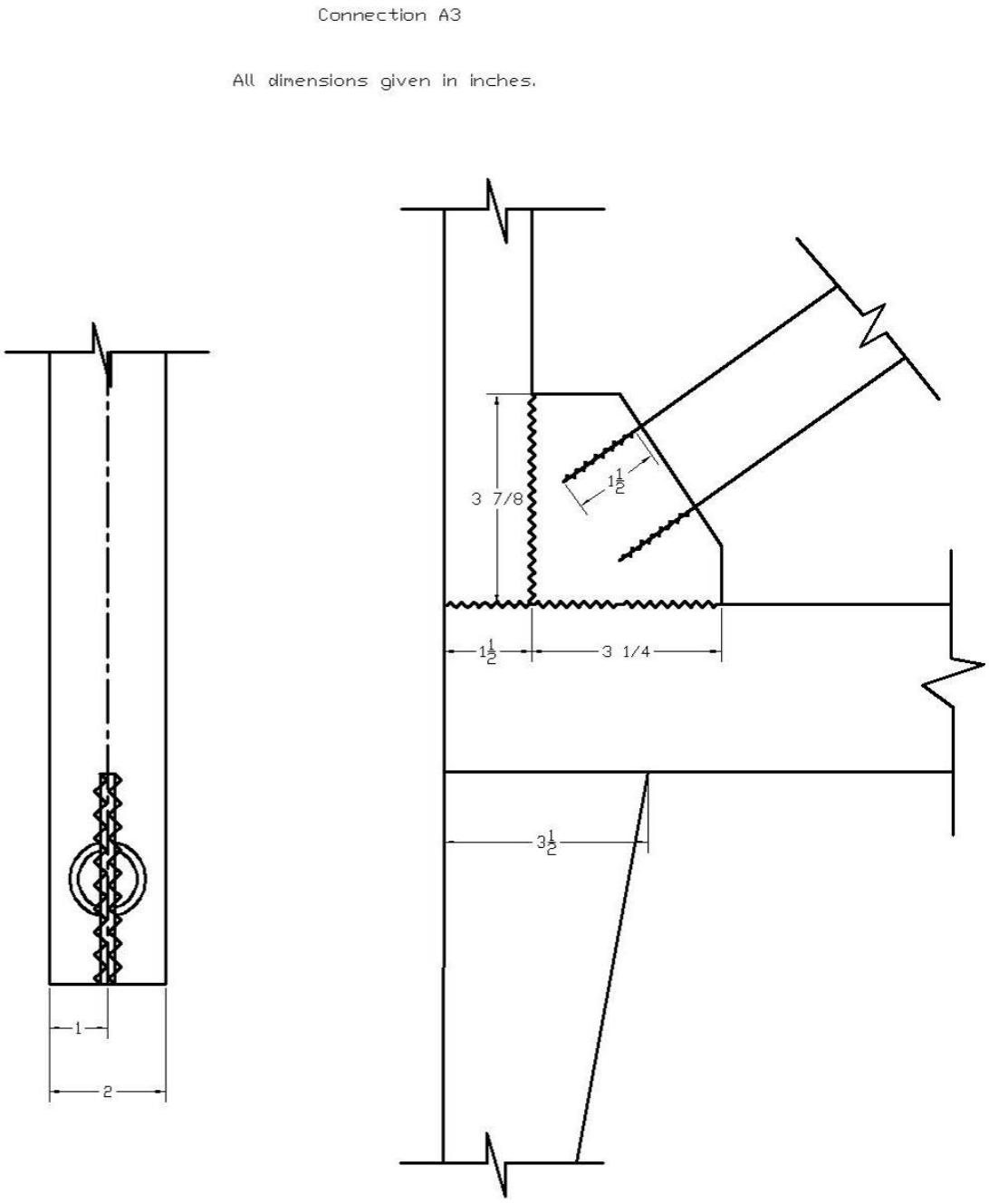

Figure B.17: Connection A3 details

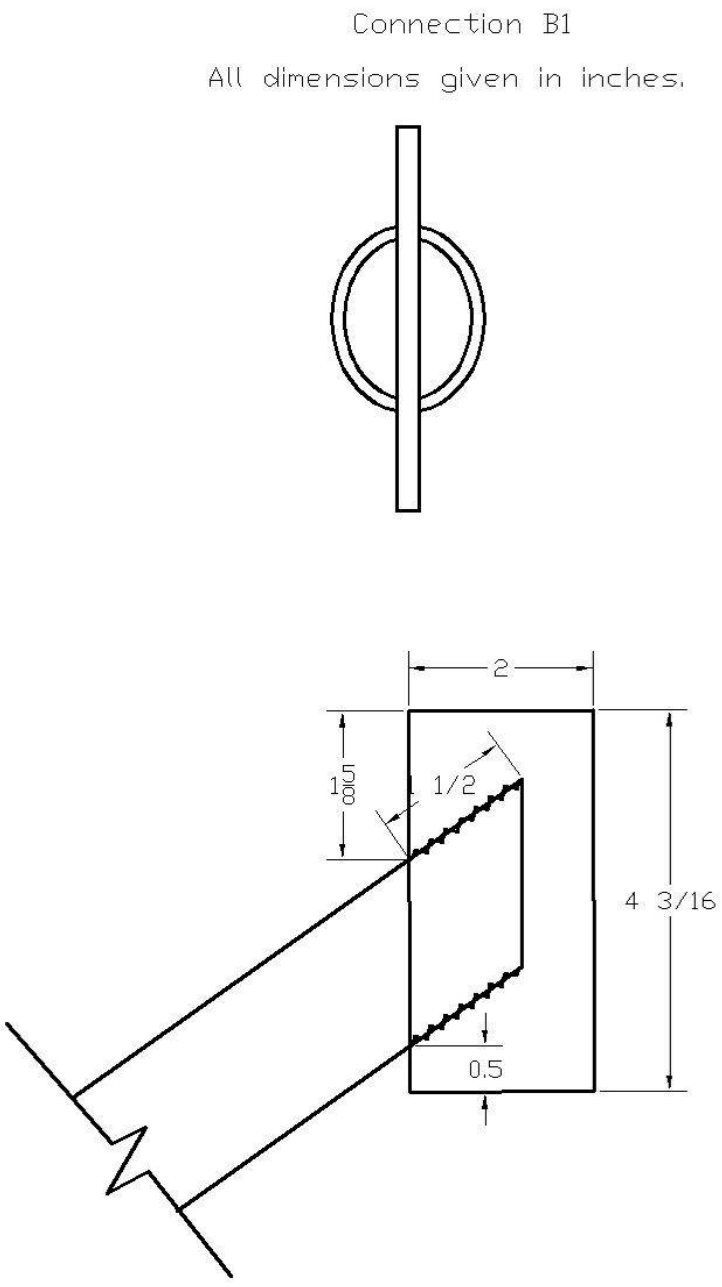

Figure B.18: Connection B1 details

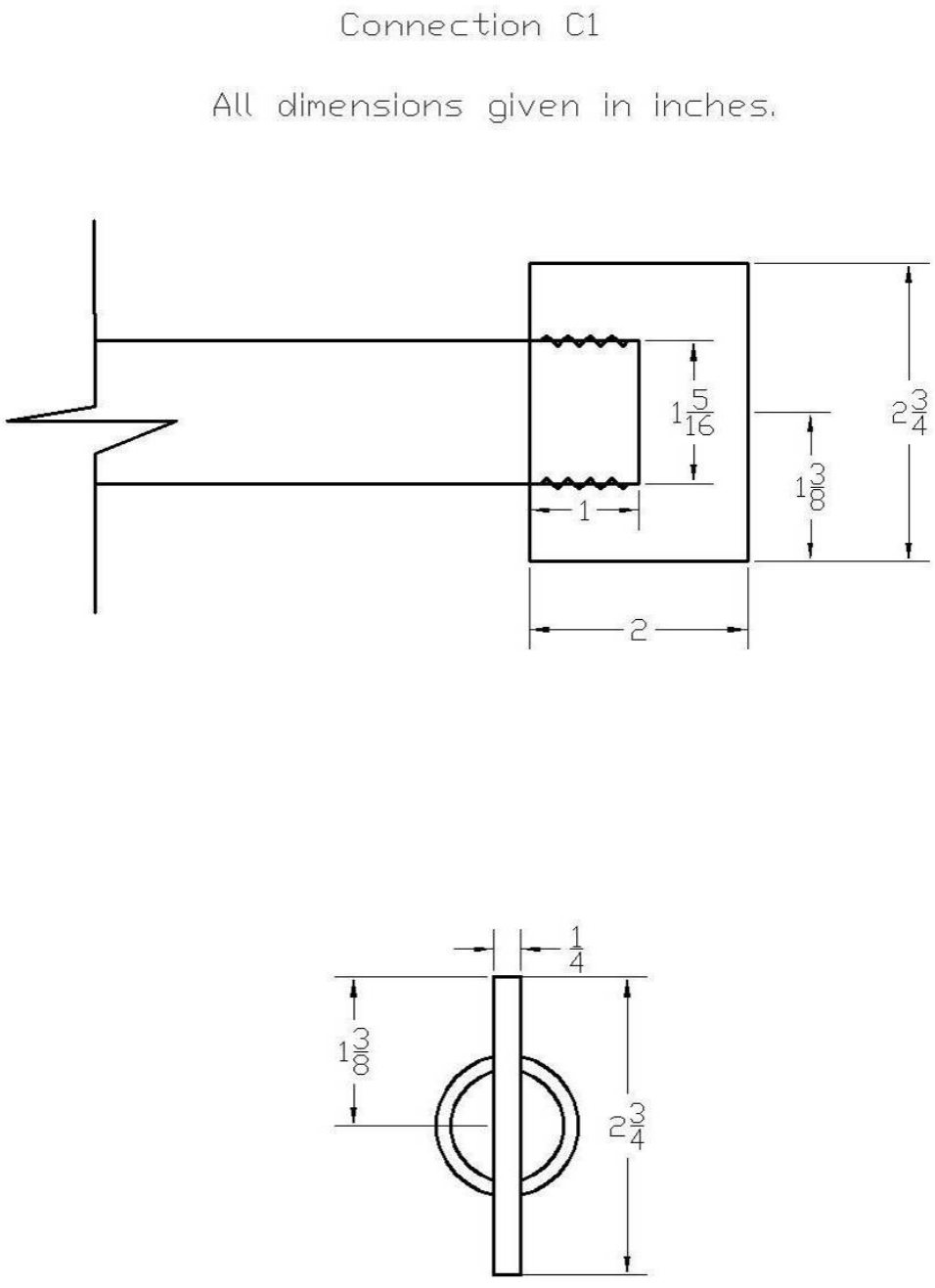

Figure B.19: Connection C1 details

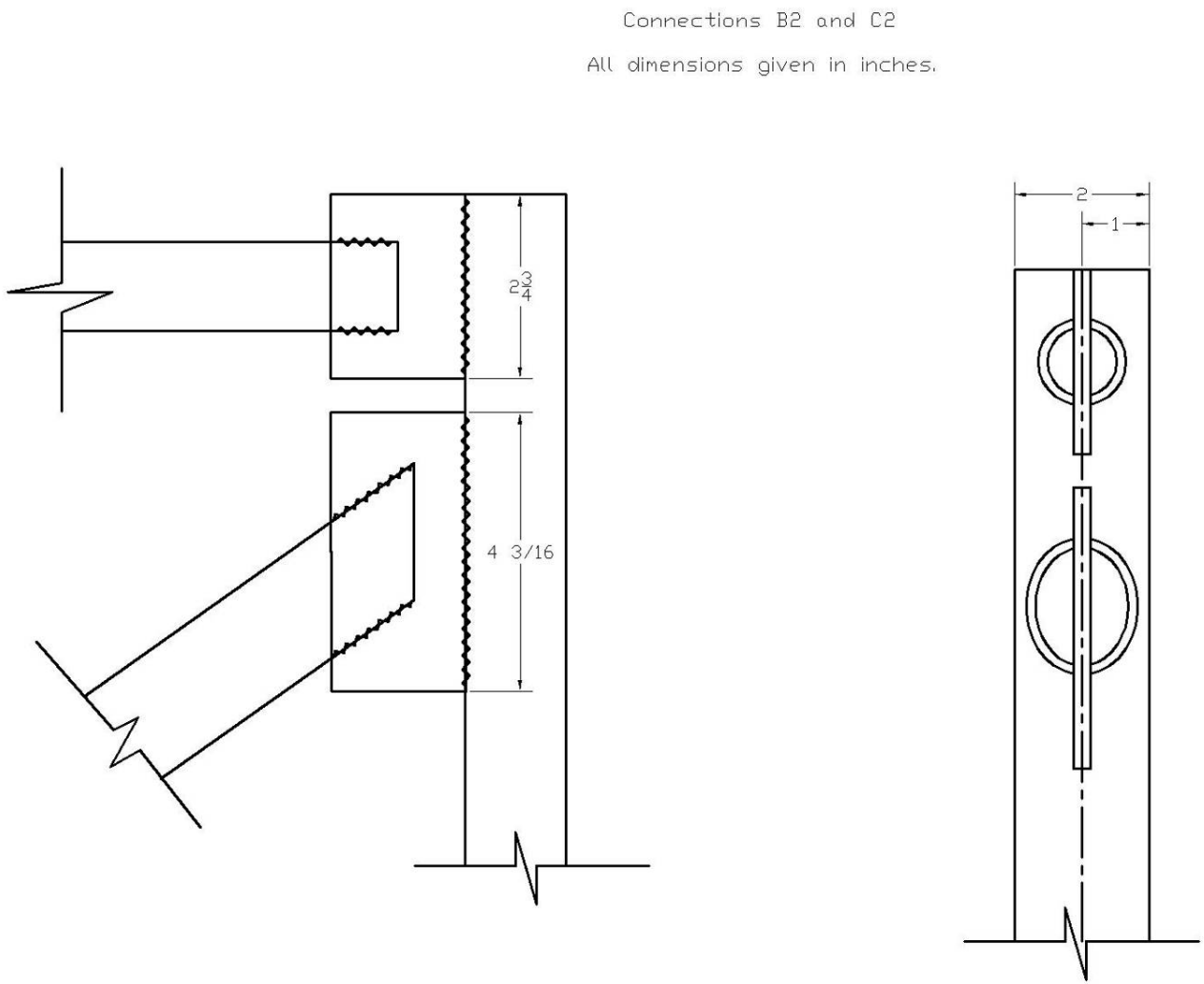

Figure B.20: Details for connections B2 and C2

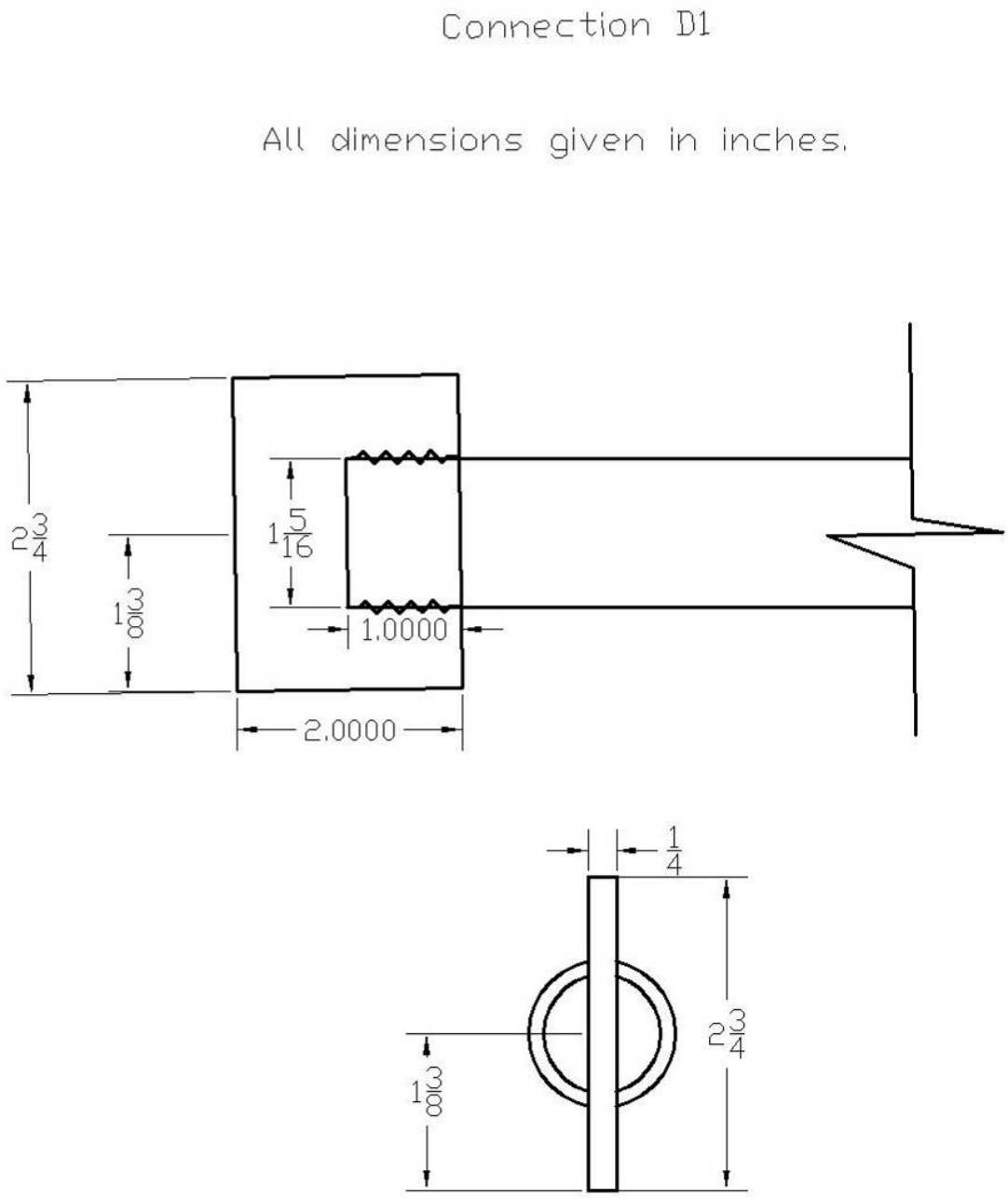

Figure B.21: Connection D1 details

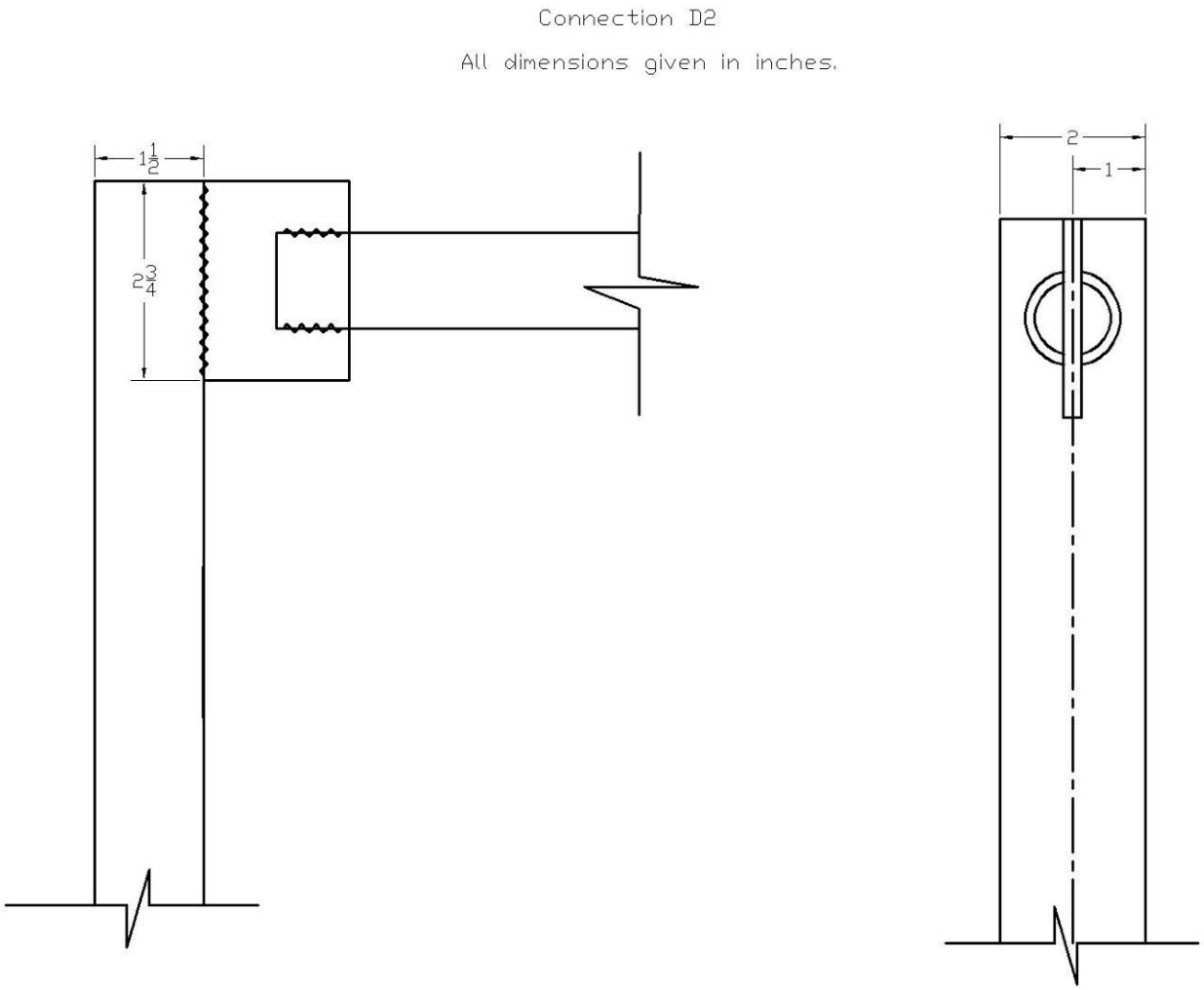

Figure B.22: Connection D2 details

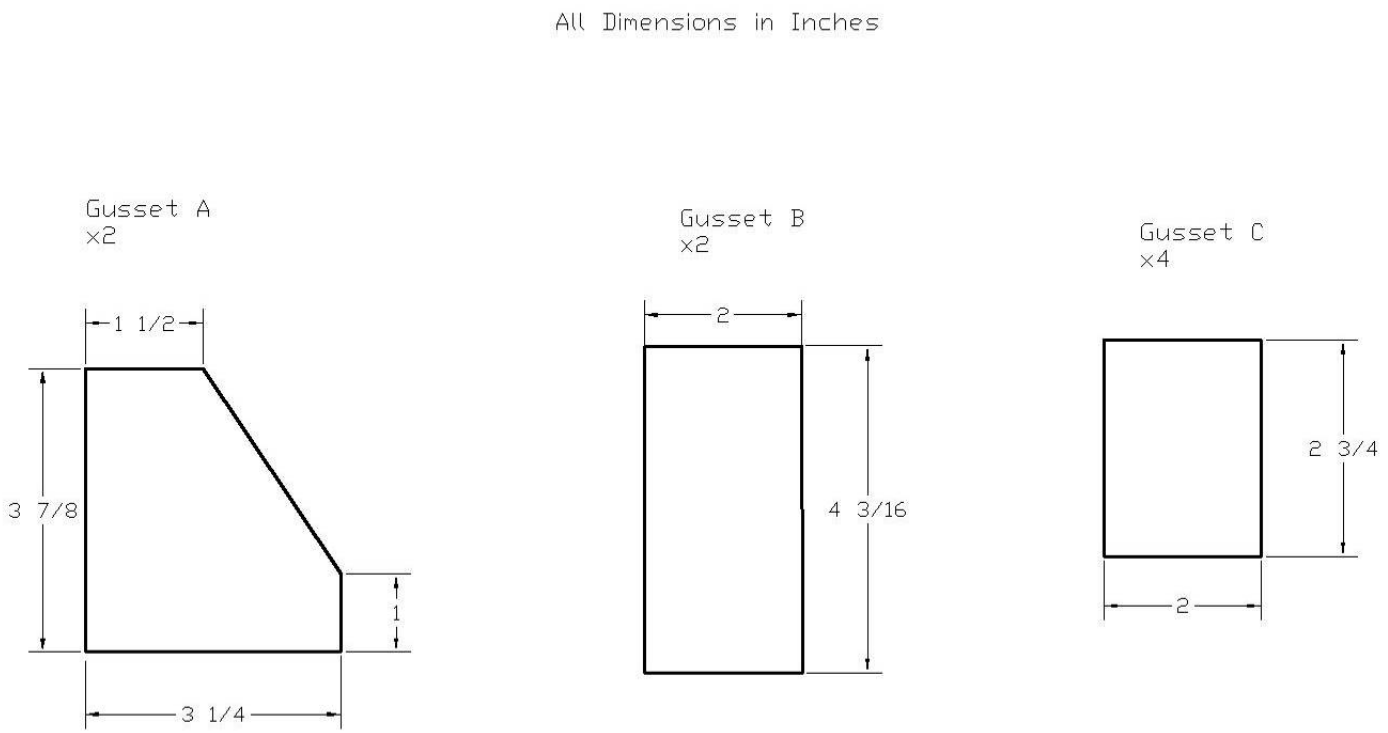

Figure B.23: Gusset plate details for gussets A, B and C

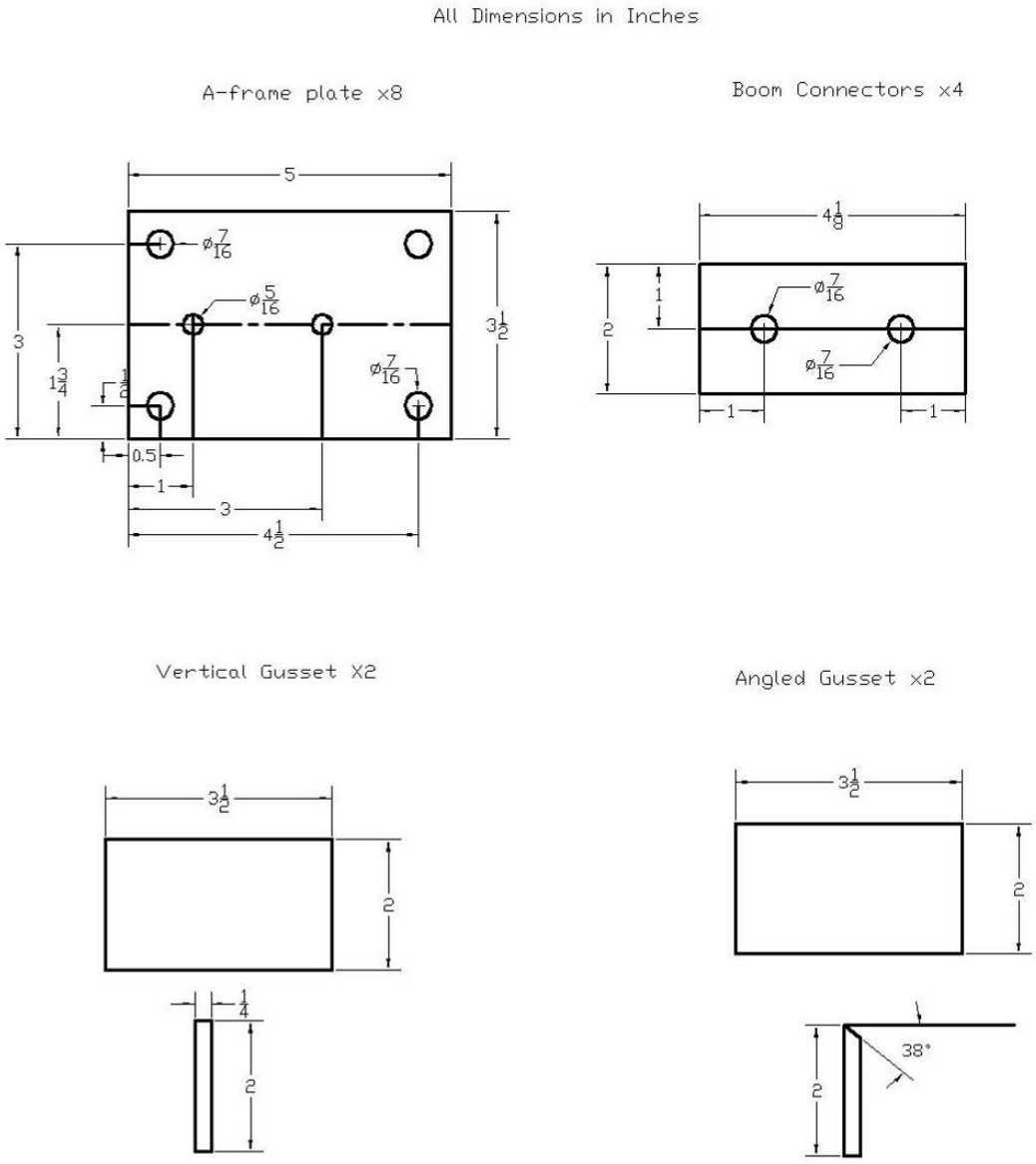

Figure B.24: Connection plate details

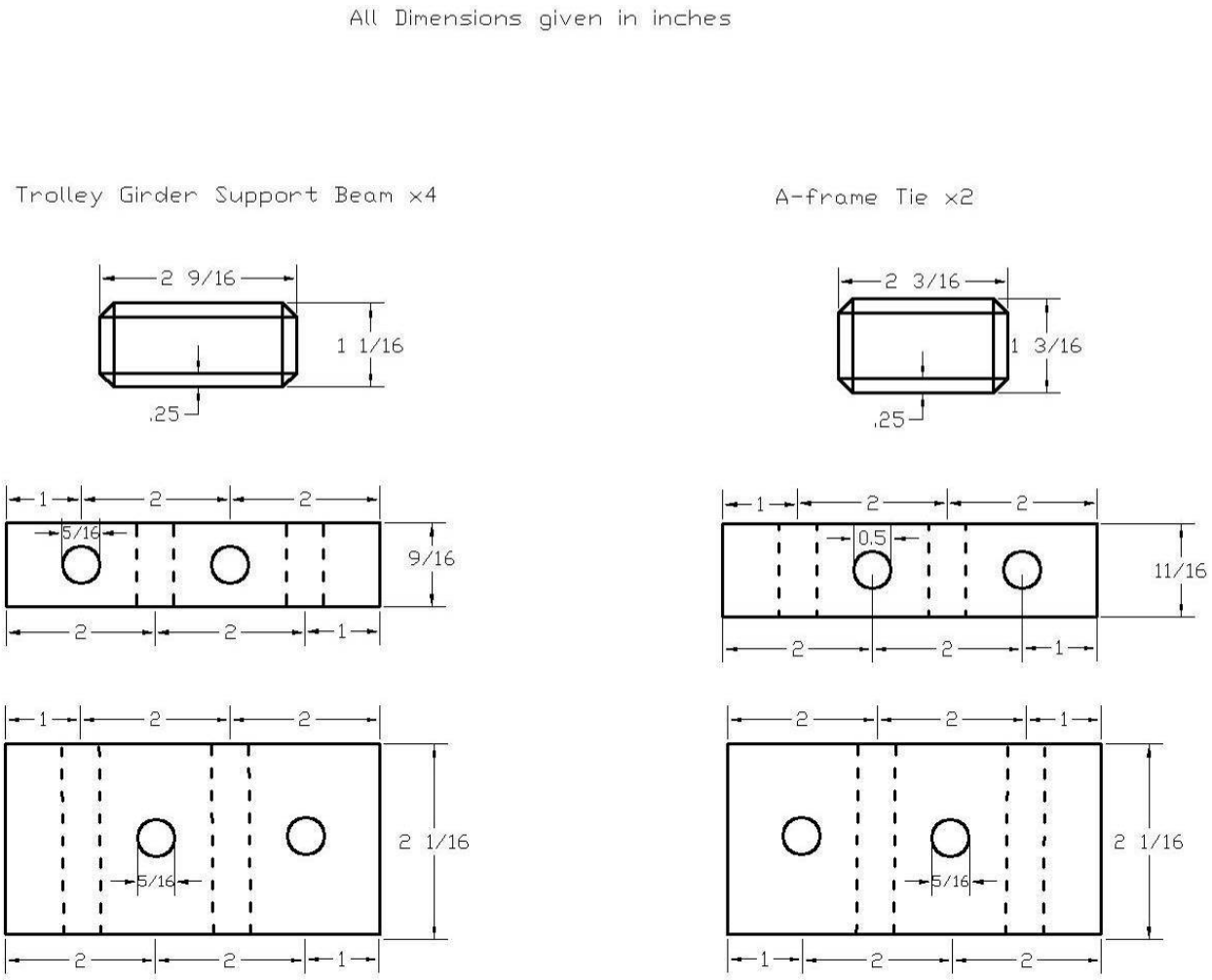

Figure B.25: Connection box details for bolted connections of the trolley girder support beam and A-frame

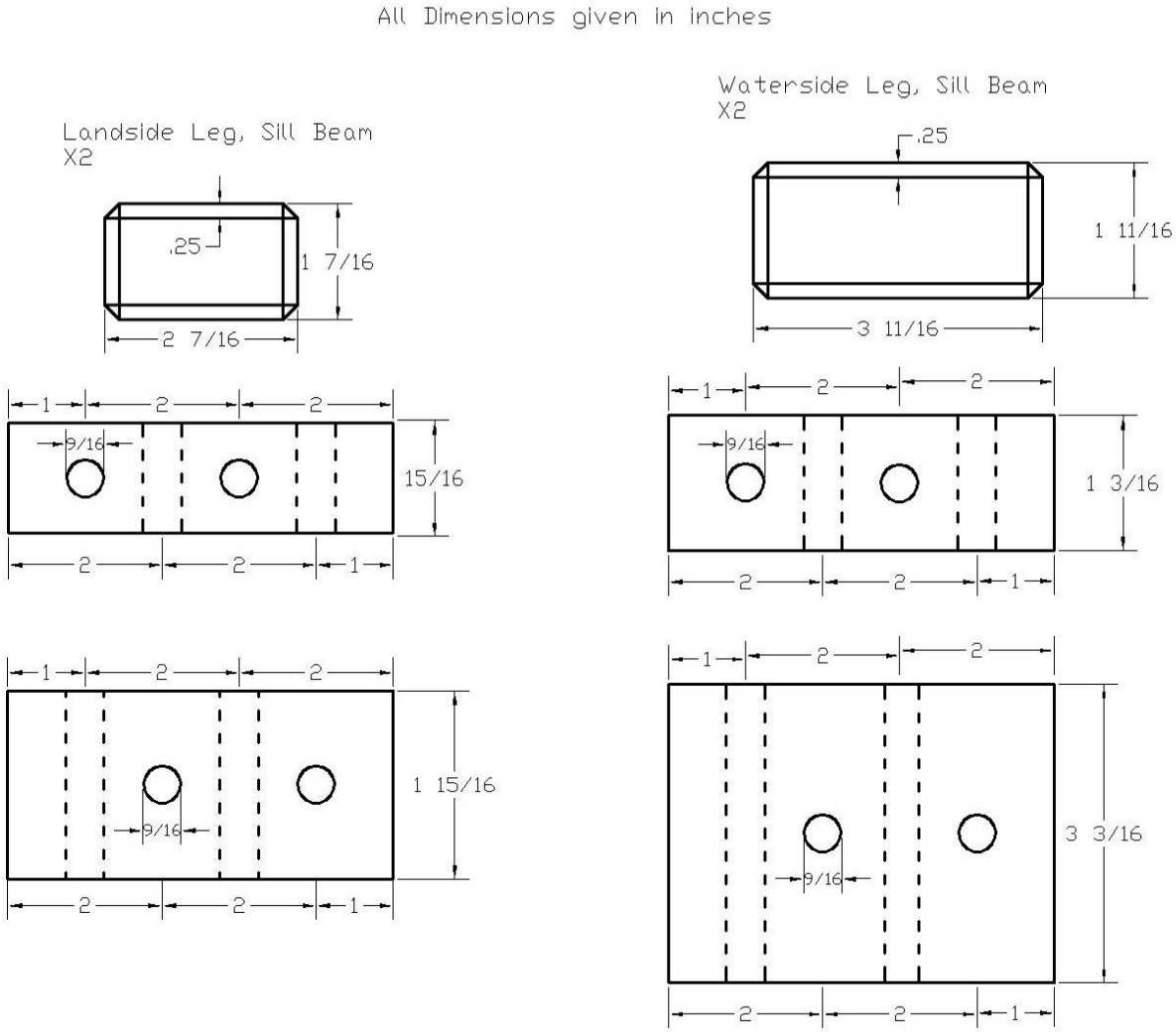

Figure B.26: Connection box details for the bolted connections of the sill beams

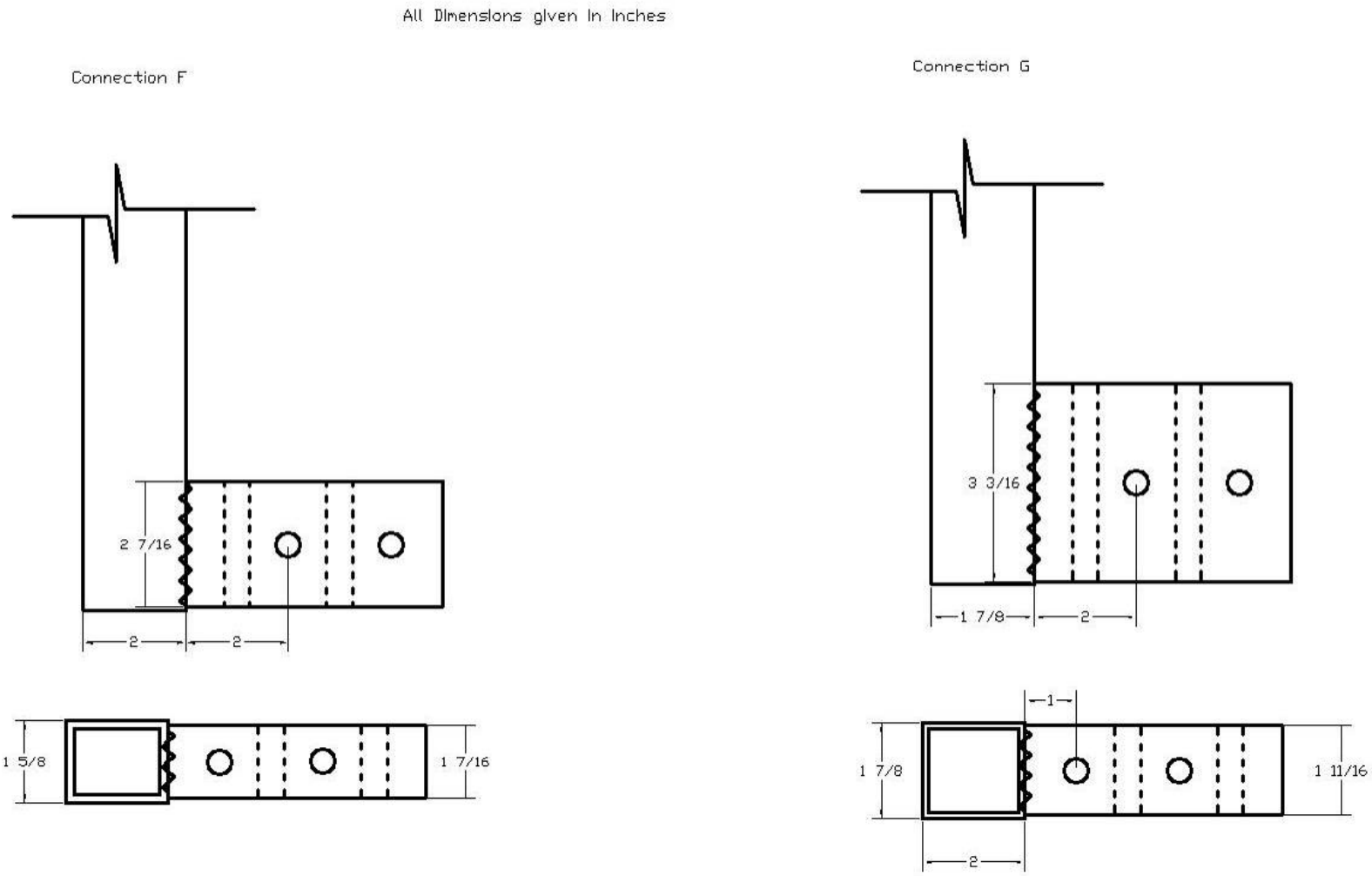

Figure B.27: Details for connections F and G

Connection H

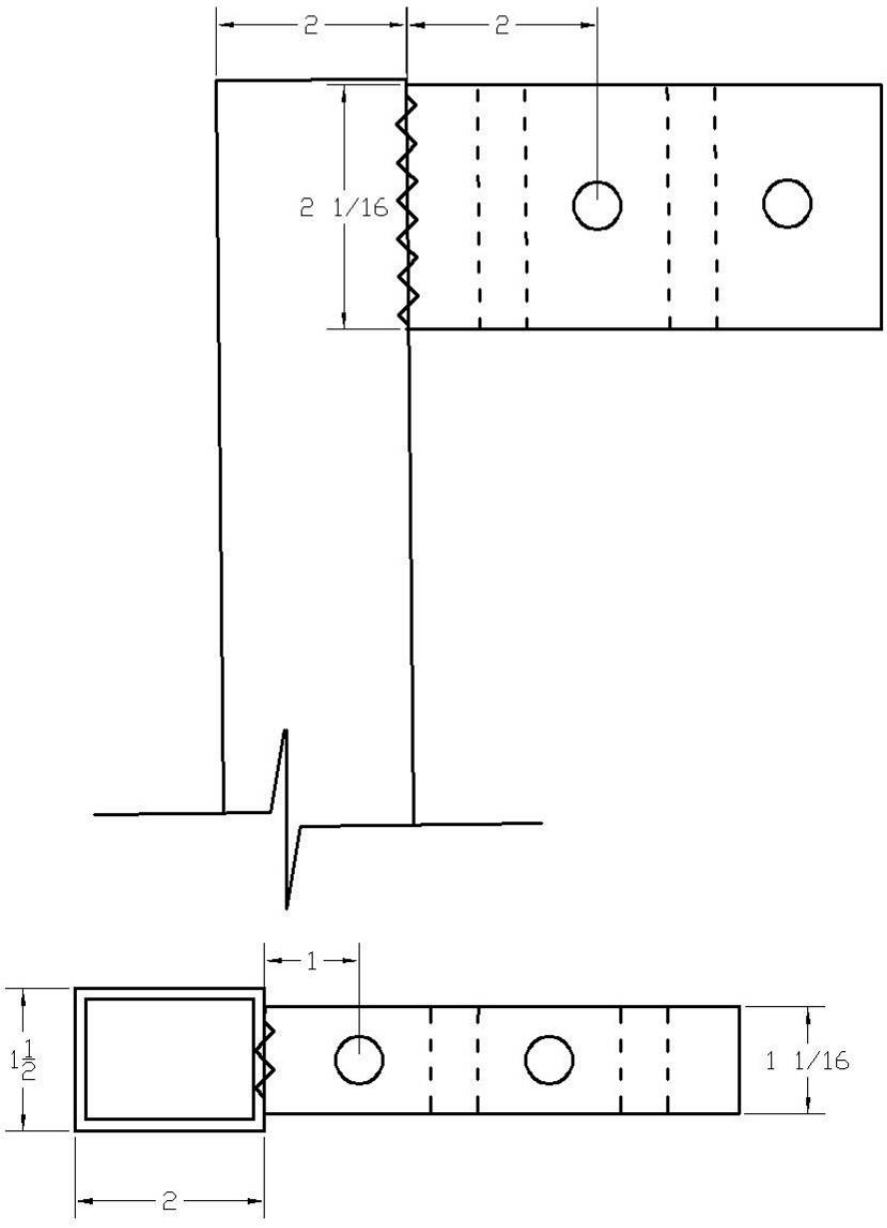

Figure B.28: Connection H detail

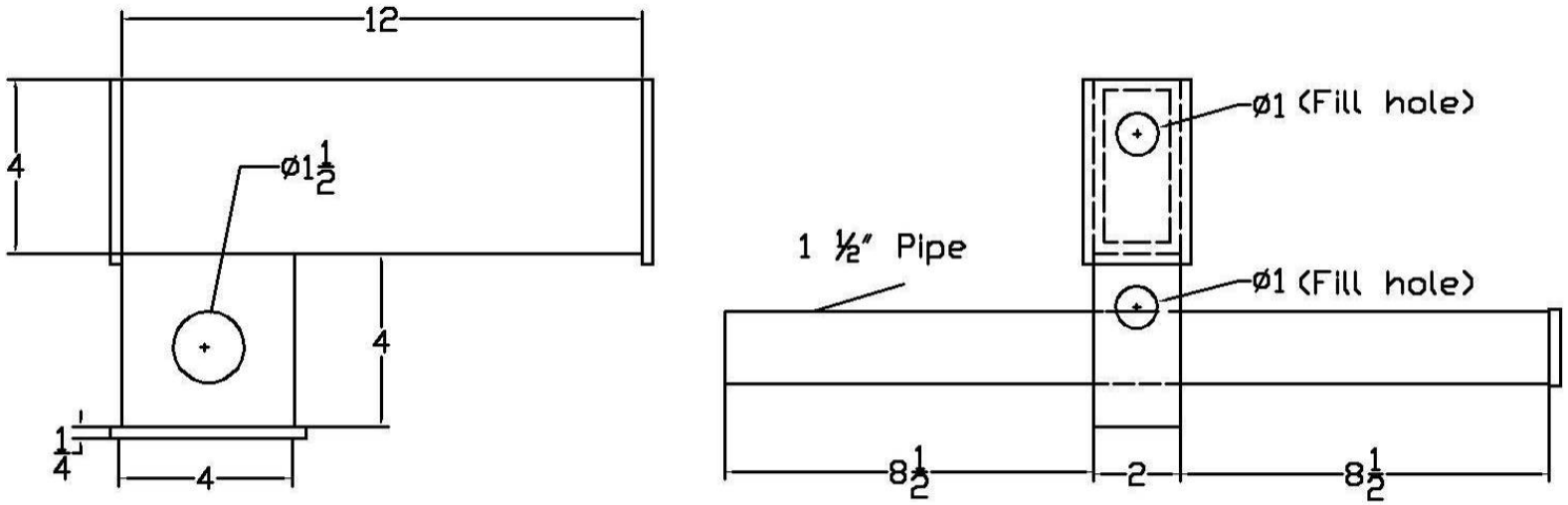

Figure B.29: Pseudo truck details

B.3 Raw Data

This section includes some of the raw data from the Phase I test. All of the data is available from the NEES central repository. As of publication, the location of the central repository is: https://nees.org/warehouse/experiment/970/project/86. The data included in this section from the OLE earthquakes is from the full scale, biaxial excitations. The data included in this section from the CLE and Loma Prieta earthquakes is from the full scale triaxial excitations.

The first figure in each subsection (Figures B.31, B.37, B.43, B.49, and B.55) show the measured acceleration data on the shake table in the X (trolley travel), Y (gantry travel) and Z (vertical) directions and the trolley travel boom acceleration. The second figure in each subsection (Figures B.32, B.38, B.44, B.50, and B.56) show the displacement time histories at the base in the trolley travel and vertical directions. Additionally the trolley travel direction displacements of the portal beam and the top of the O-frame. The gauges given for each time history correspond to the gauges labeled in Figure 3.9. The remaining figures show the raw strain gauge data from the portal frame. The gauges given for each of the time histories correspond to those in Figure 3.10. The strain gauge data was used to calculate the moments presented in Chapter 4.

B.3.1 Full Scale OLE4 Excitation

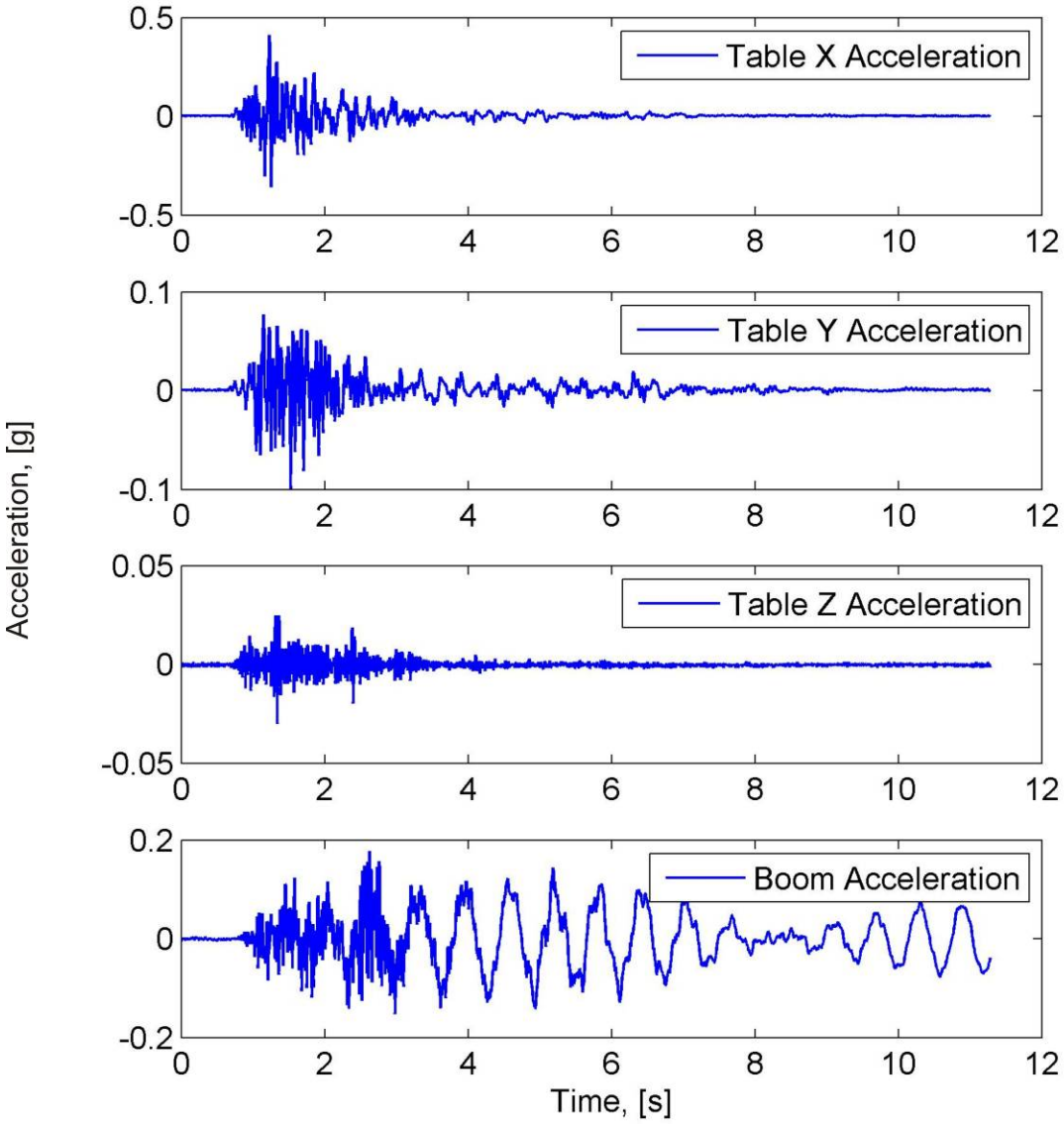

Figure B.30: Acceleration time histories for the full scale OLE4 excitation

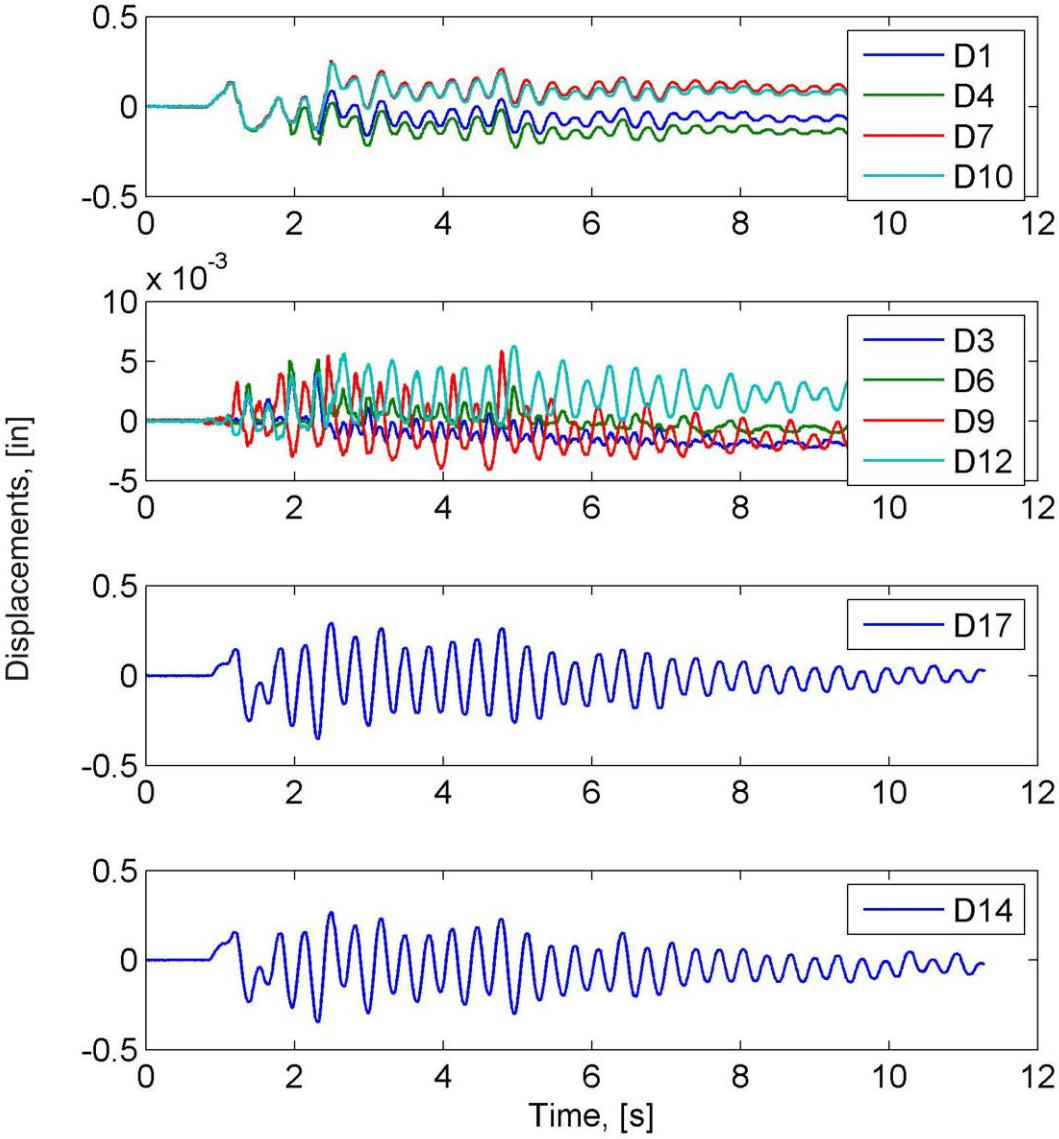

Figure B.31: Displacement time histories for the full scale OLE4 excitation

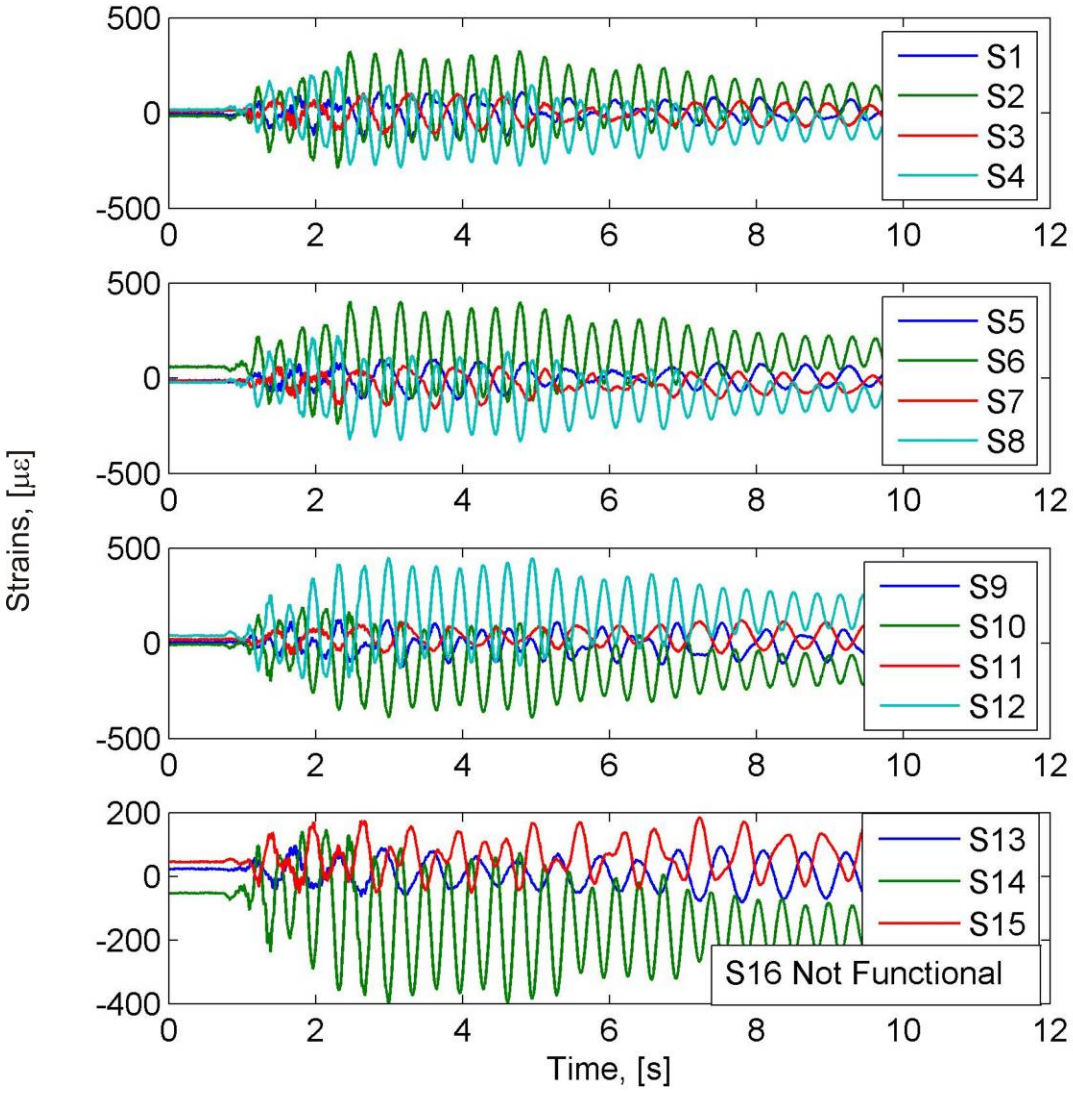

Figure B.32: Strain time histories at the bottom of the portal frame legs for the full scale OLE4 excitation

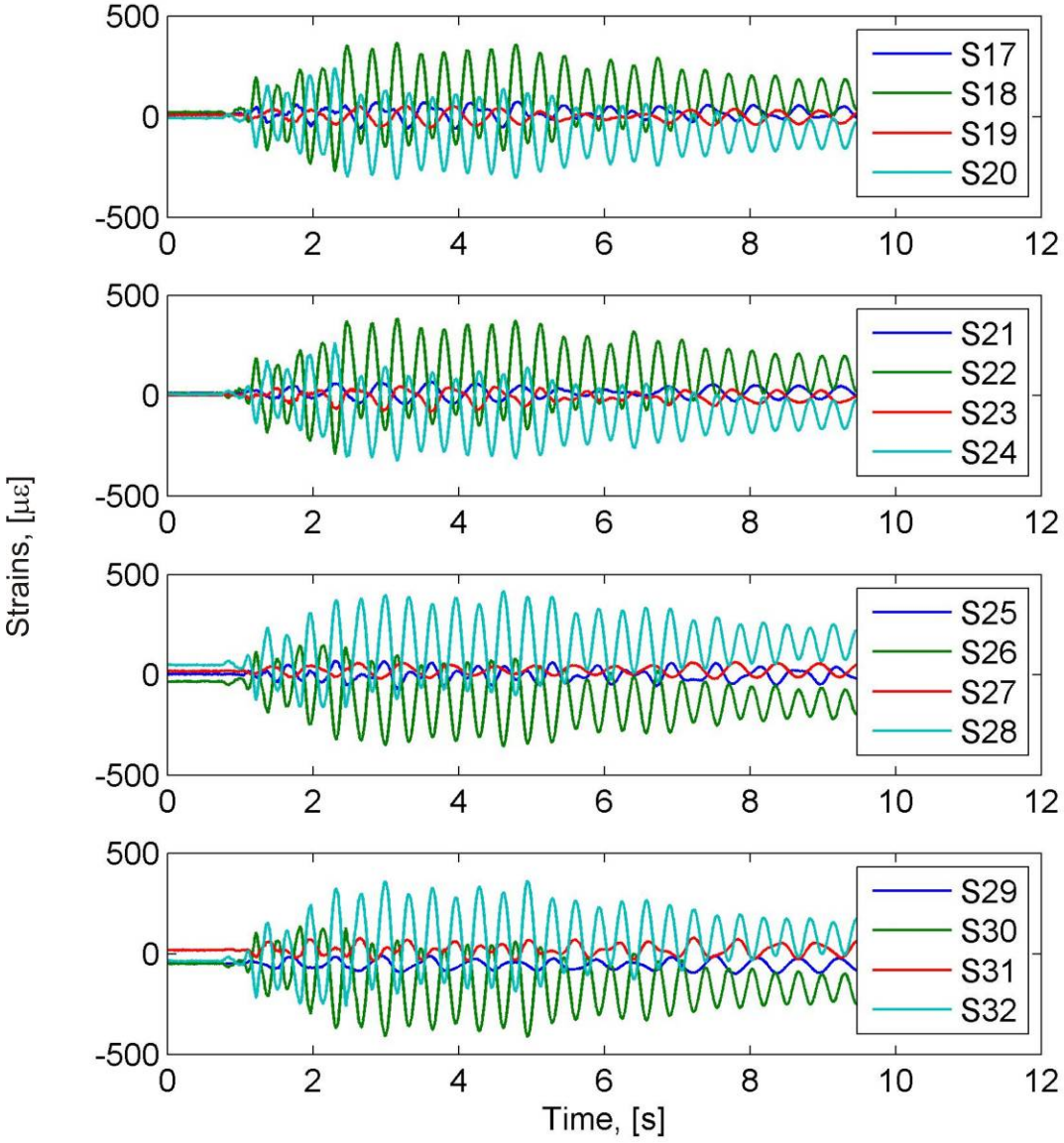

Figure B.33: Strain time histories at the middle of the portal frame legs for the full scale OLE4 excitation

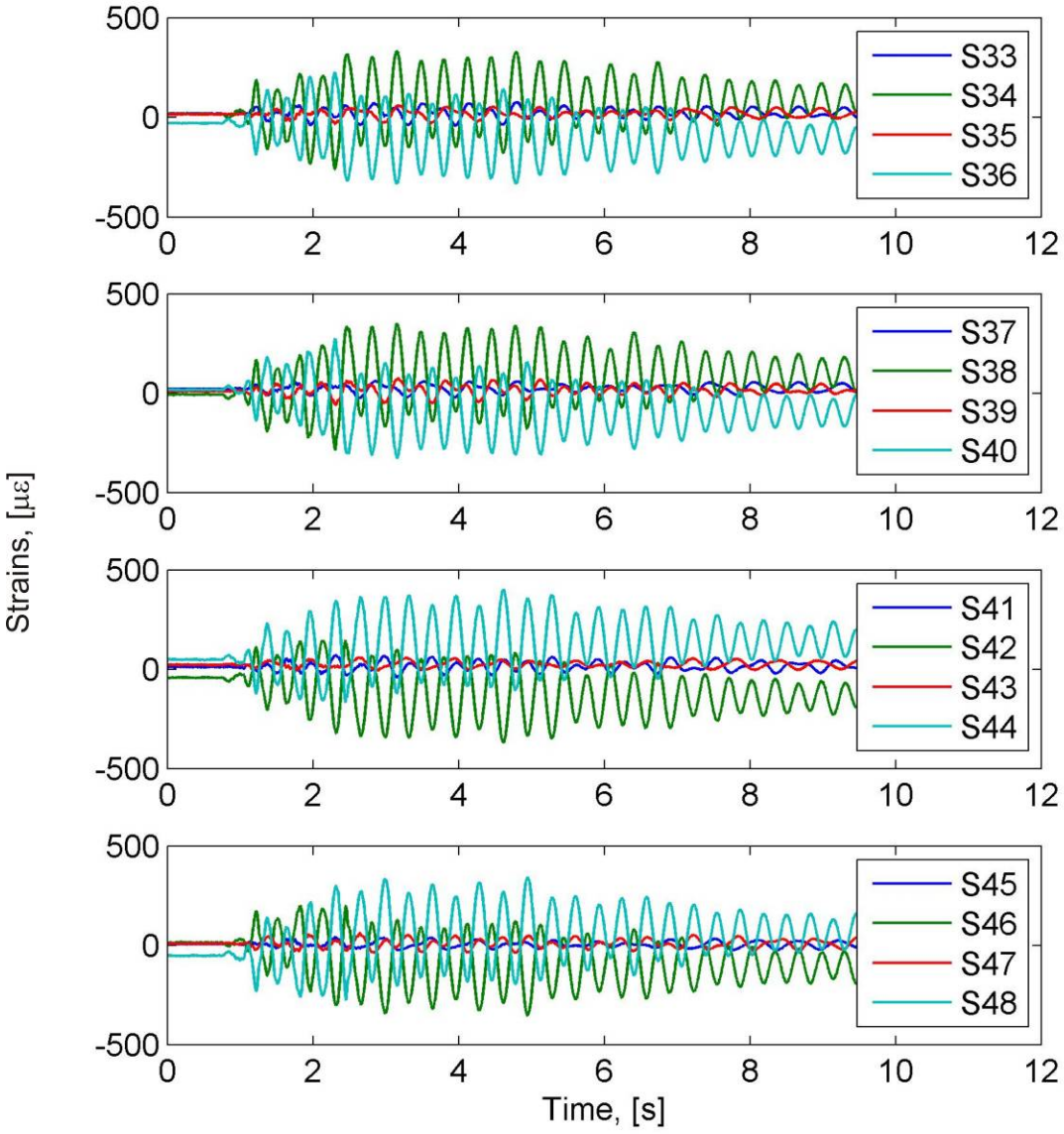

Figure B.34: Strain time histories at the top of the portal frame legs for the full scale OLE4 excitation

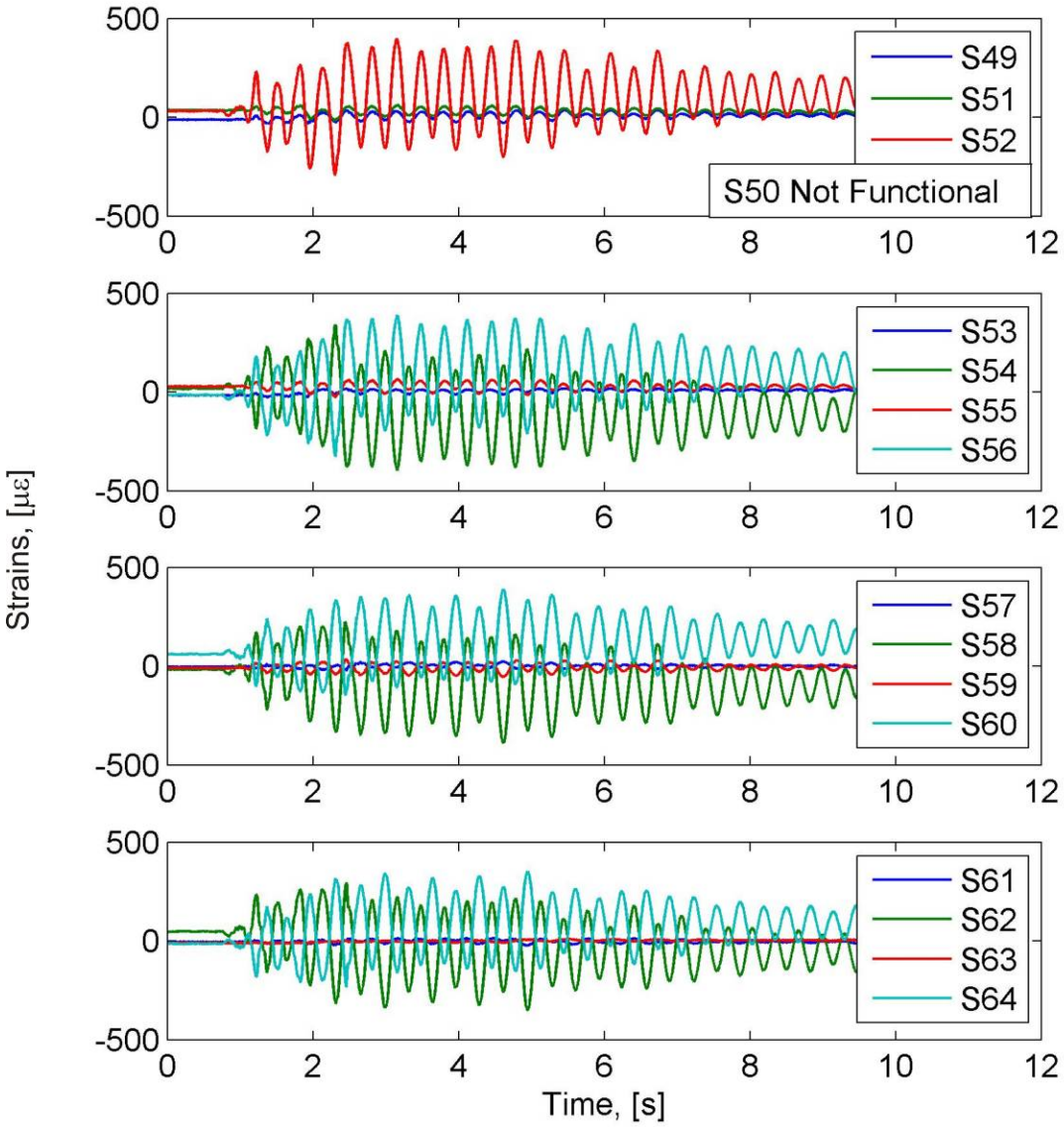

Figure B.35: Strain time histories in the portal beam for the full scale OLE4 excitation

B.3.2 Full Scale OLE6 Excitation

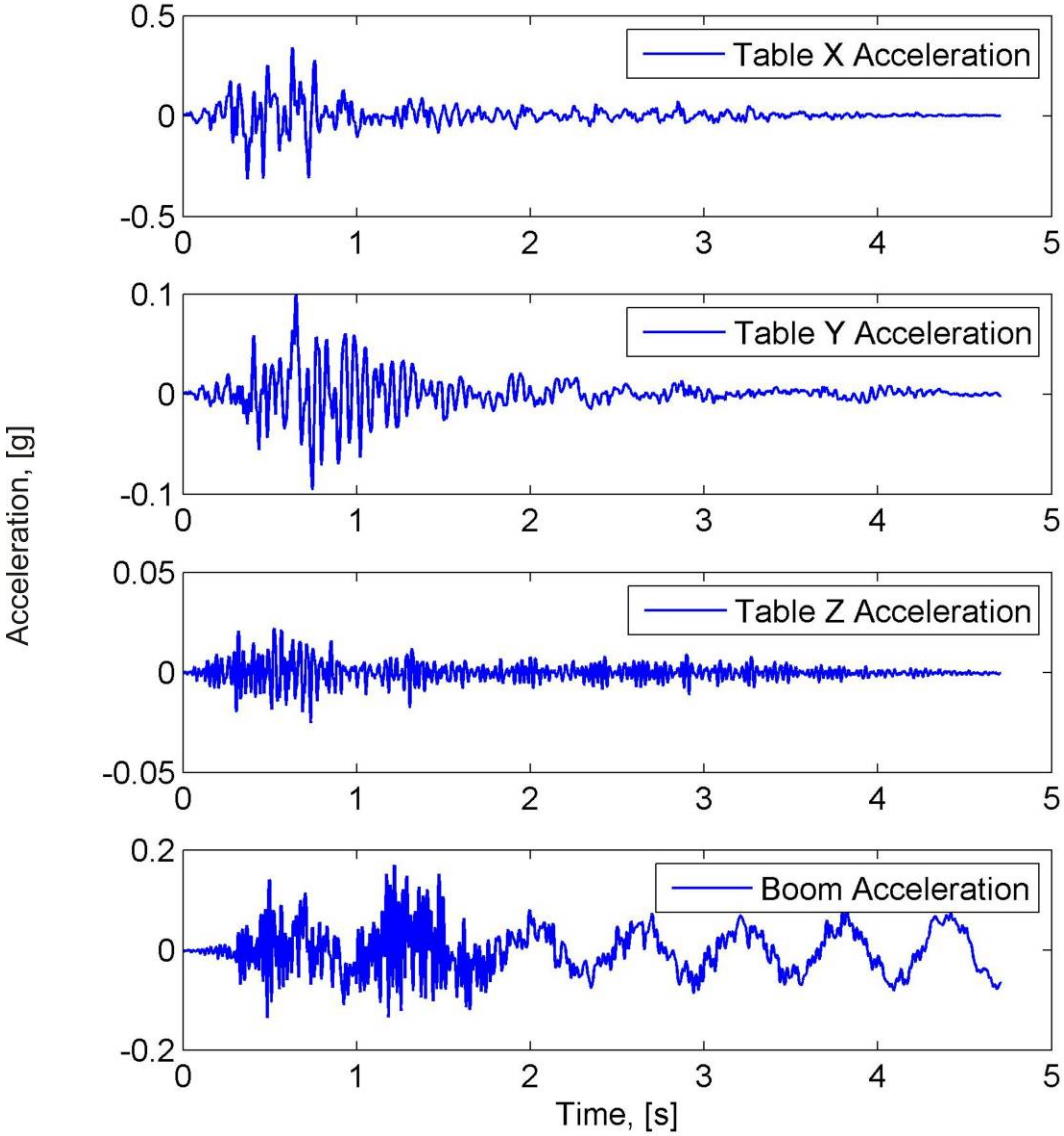

Figure B.36: Acceleration time histories for the full scale OLE6 excitation

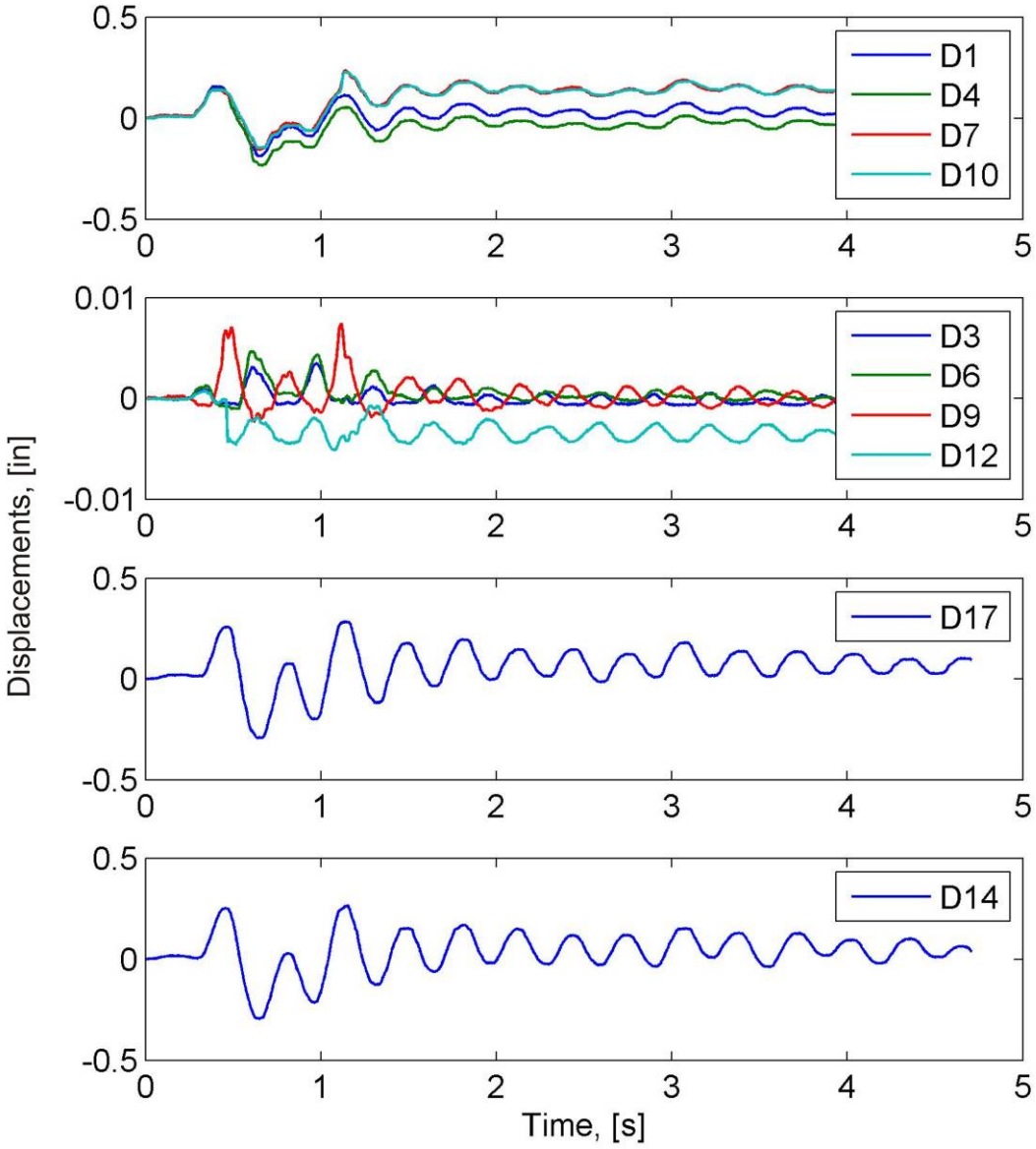

Figure B.37: Displacement time histories for the full scale OLE6 excitation

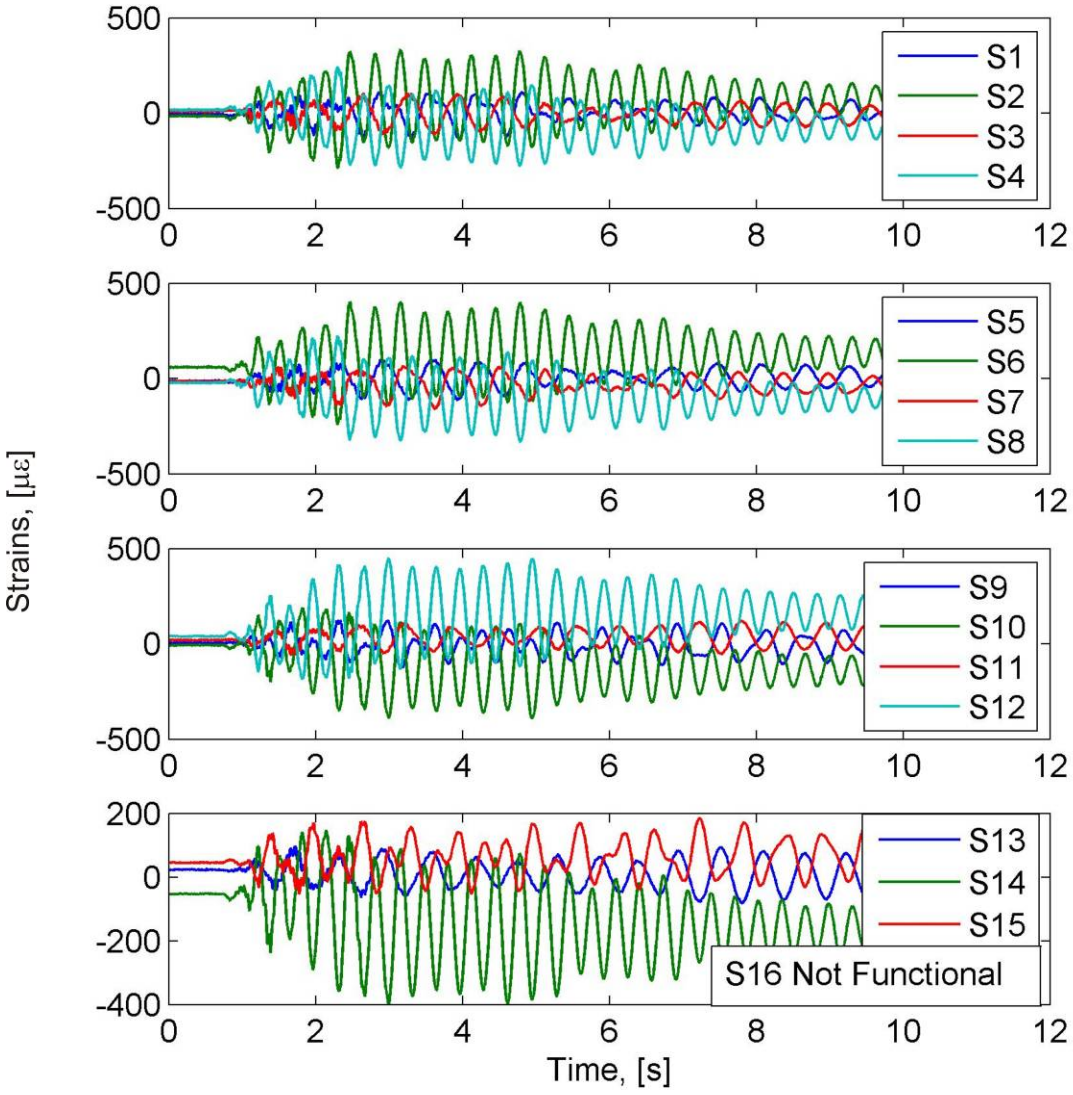

Figure B.38: Strain time histories at the bottom of the portal frame legs for the full scale OLE6 excitation

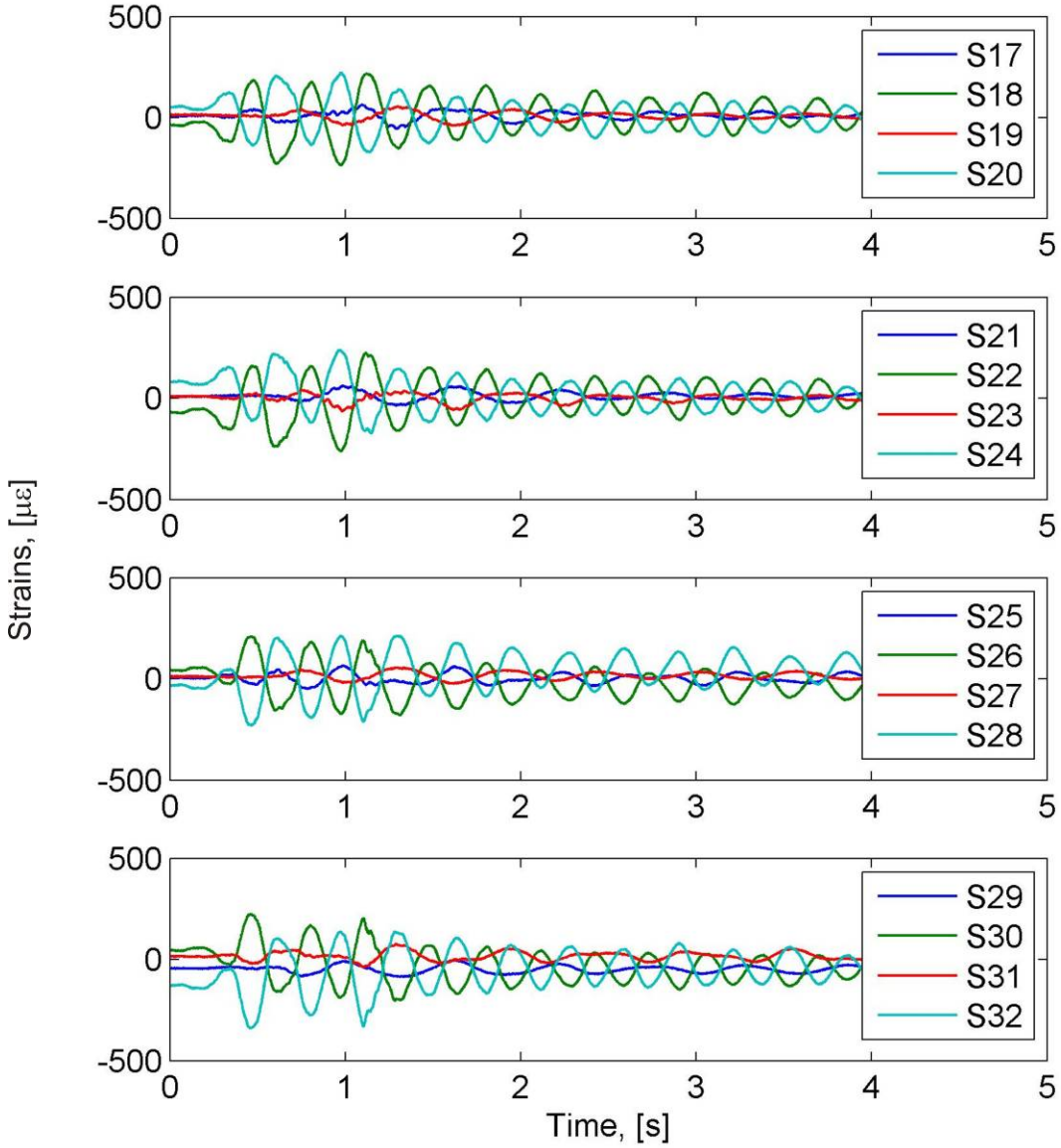

Figure B.39: Strain time histories at the middle of the portal frame legs for the full Sscale OLE6 excitation

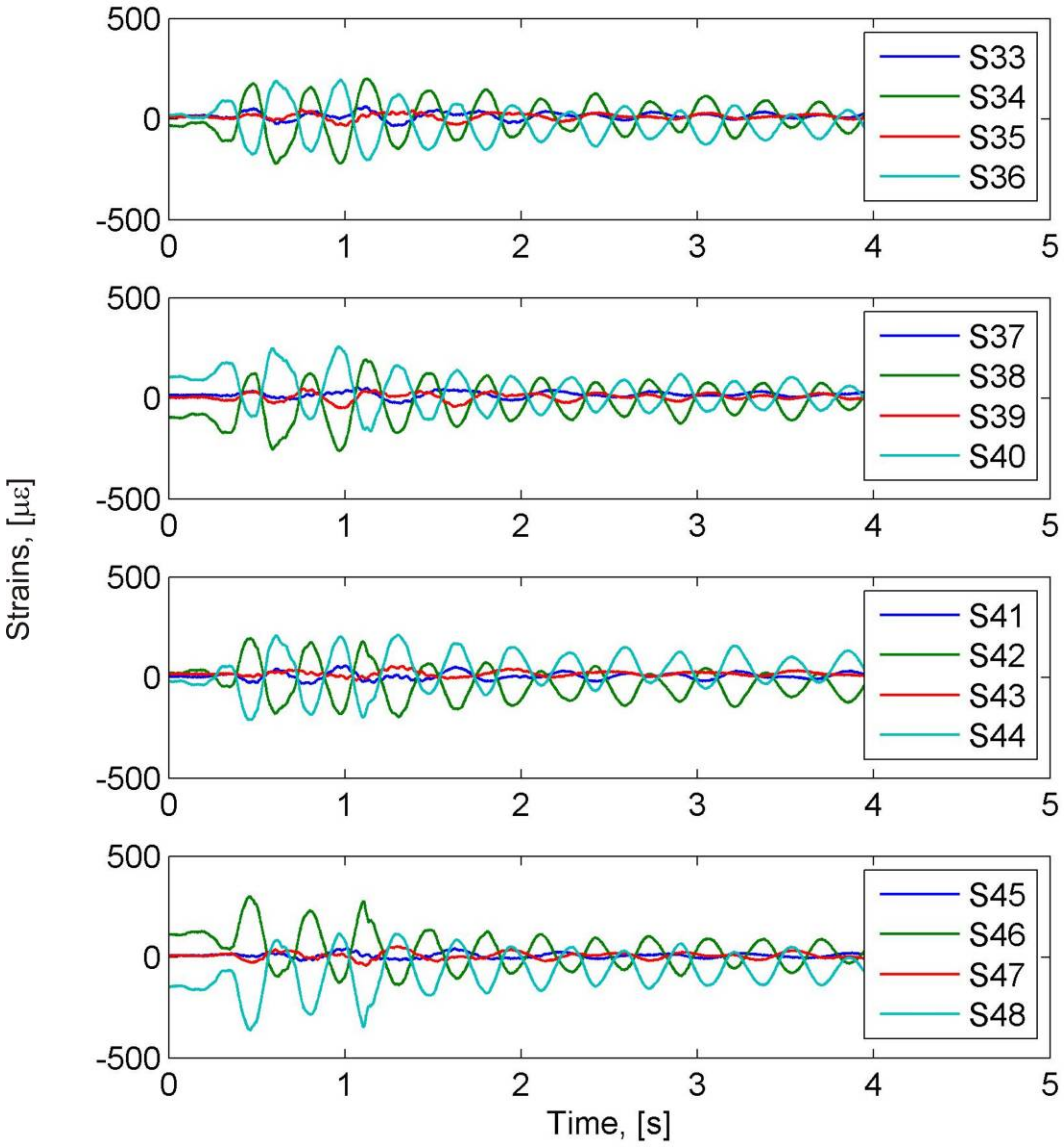

Figure B.40: Strain time histories at the top of the portal frame legs for the full scale OLE6 excitation

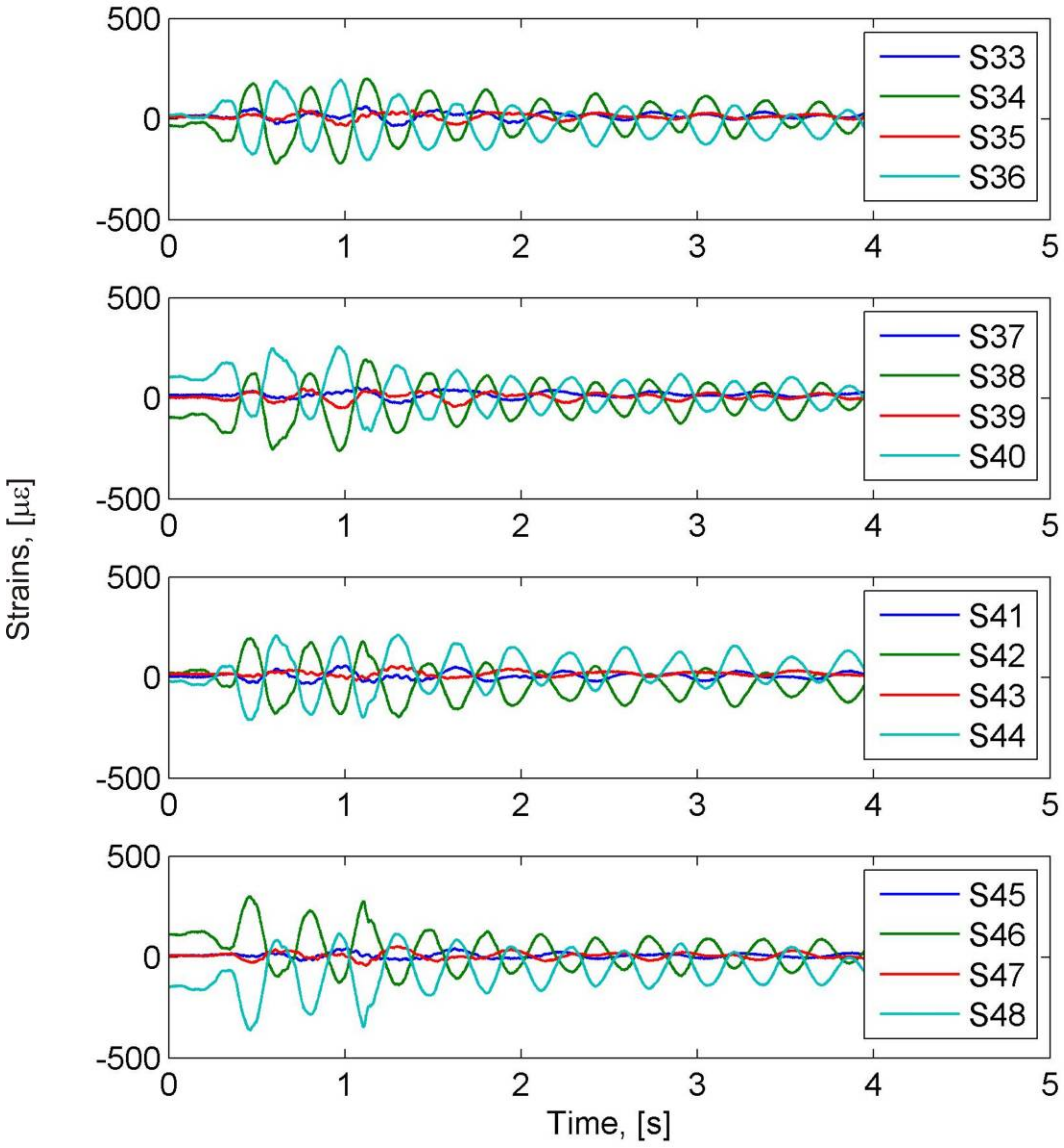

Figure B.41: Strain time histories in the portal beam for the full scale OLE6 excitation

B.3.3 Full Scale Loma Prieta Excitation

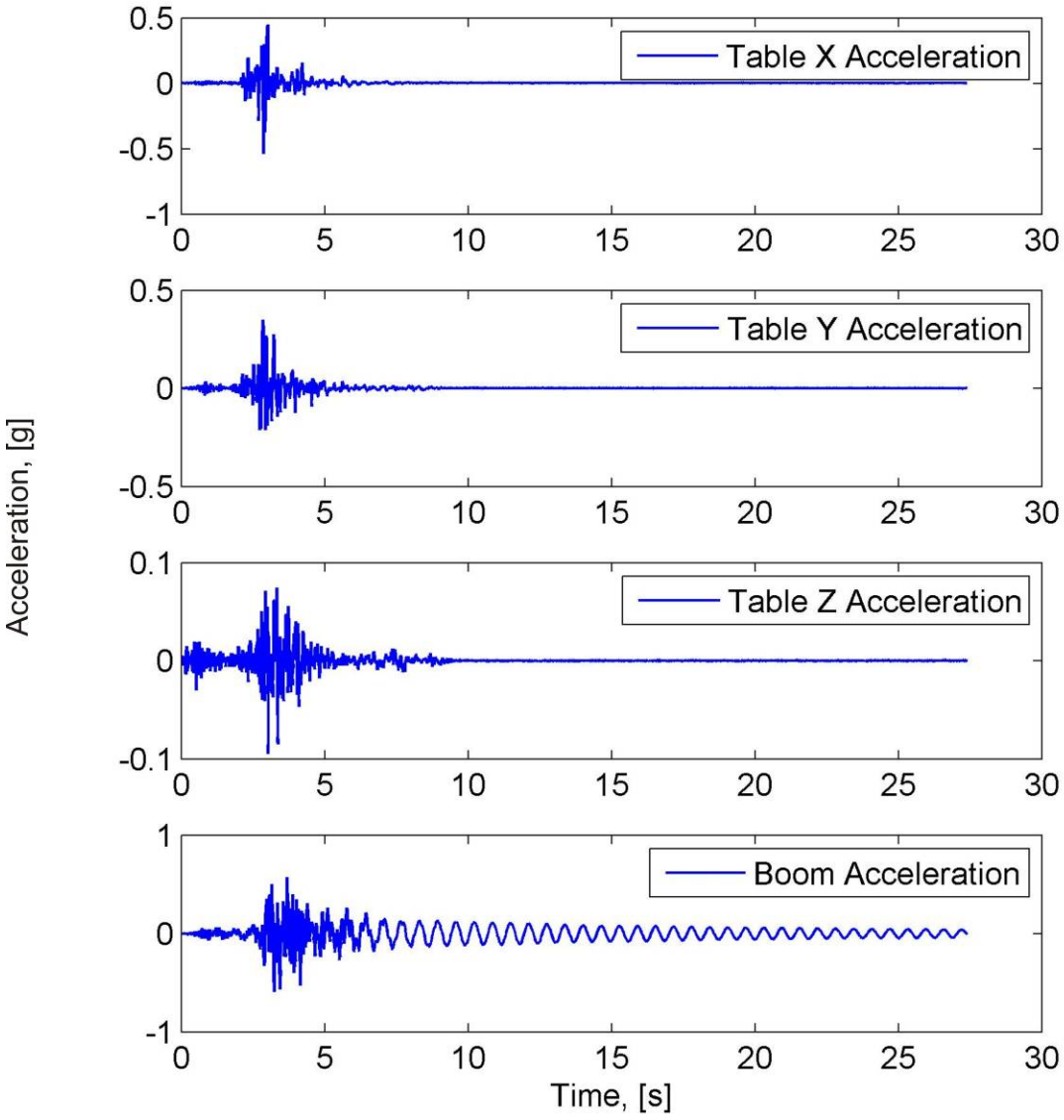

Figure B.42: Acceleration time histories for the full scale Loma Prieta excitation

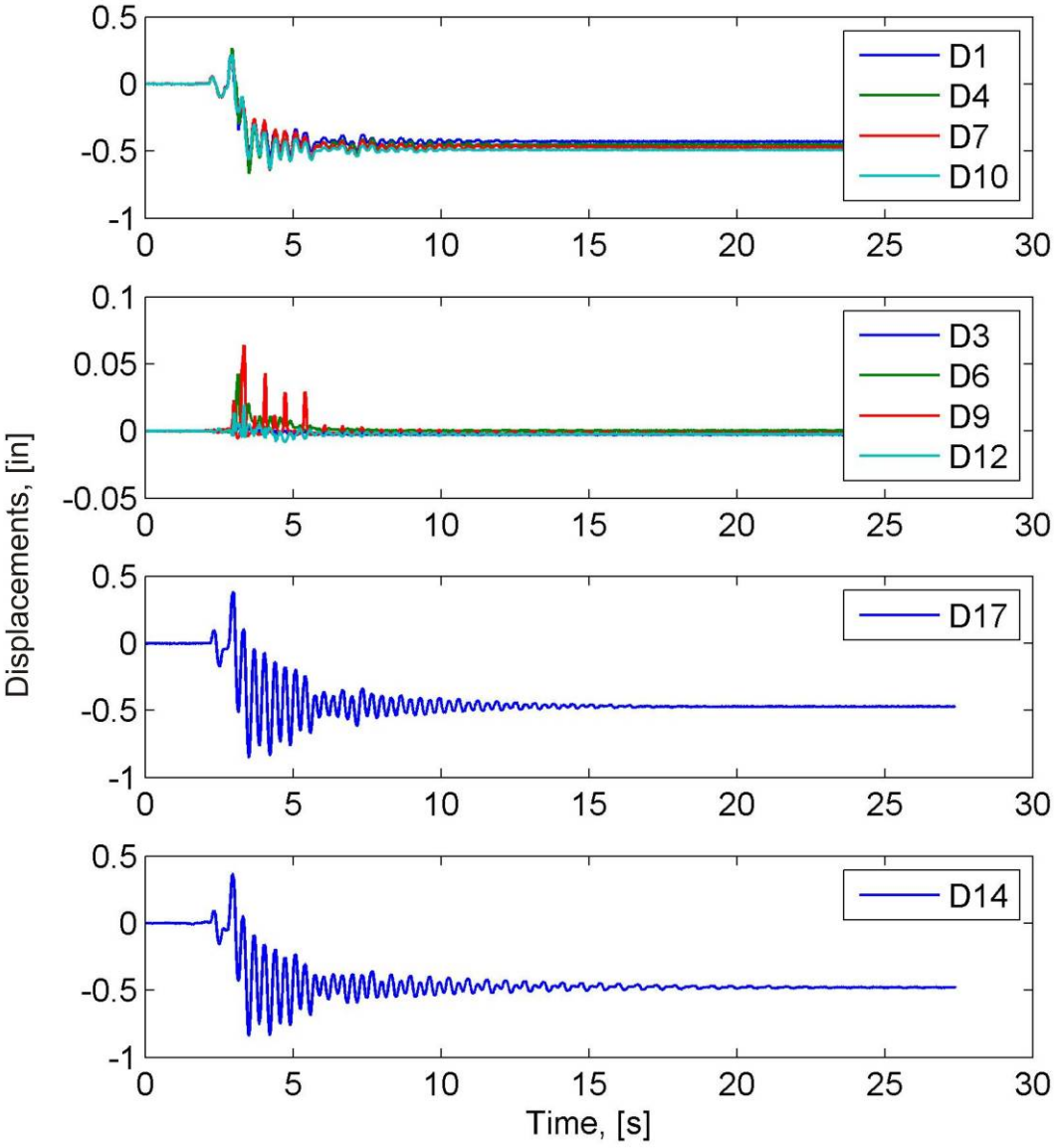

Figure B.43: Displacement time histories for the full scale Loma Prieta excitation

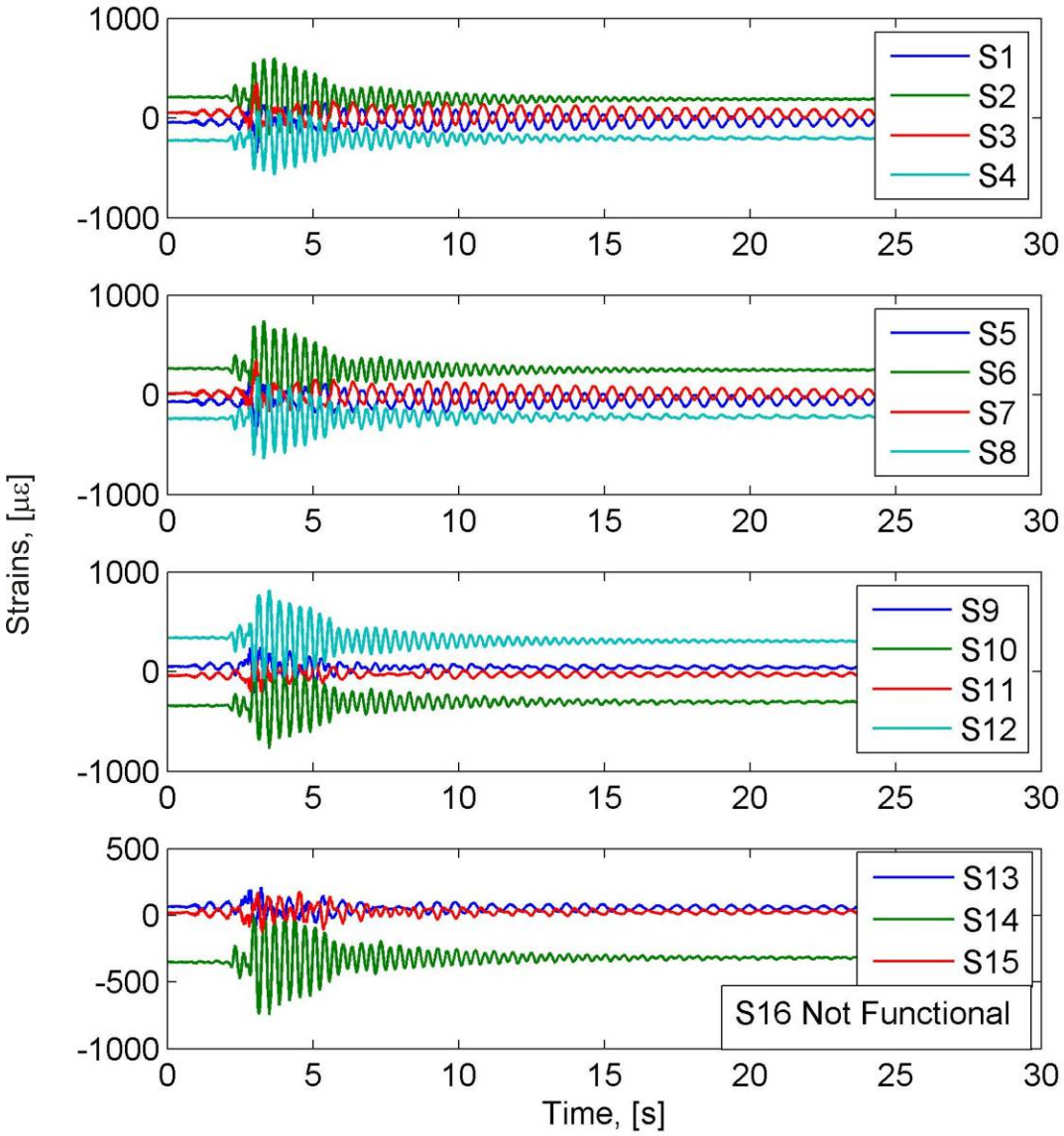

Figure B.44: Strain time histories at the bottom of the portal frame legs for the full scale Loma Prieta excitation

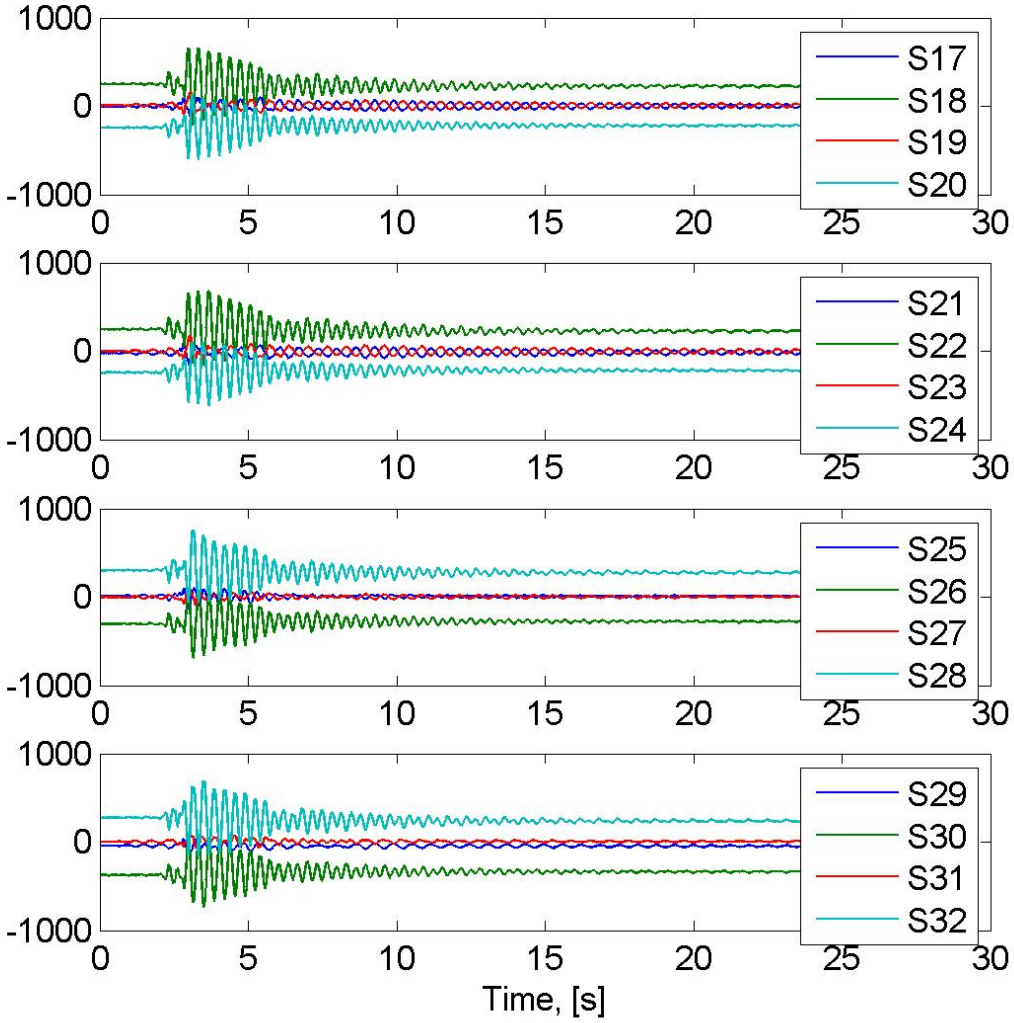

Figure B.45: Strain time histories at the middle of the portal frame legs for the full scale Loma Prieta excitation

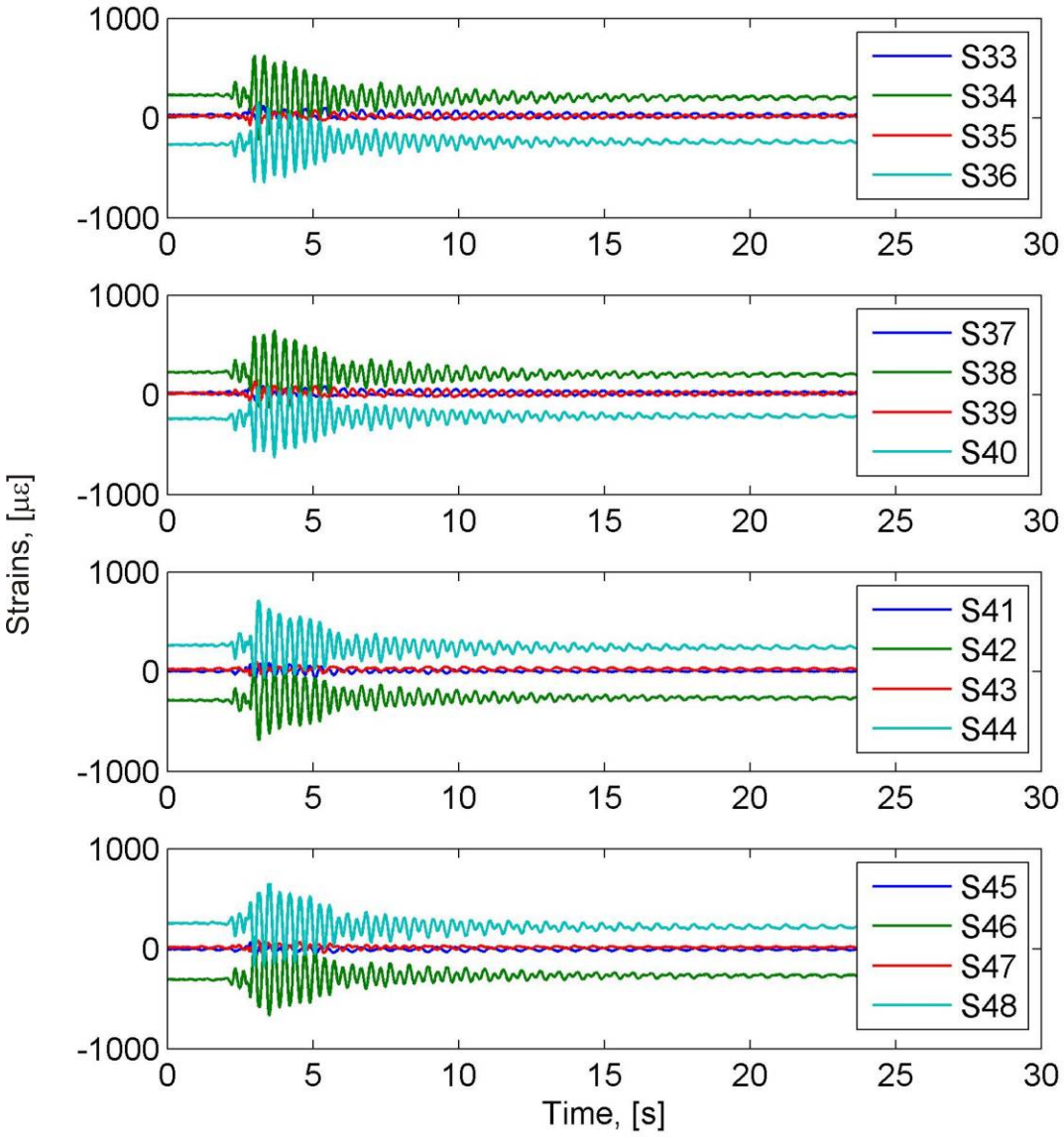

Figure B.46: Strain time histories at the top of the portal frame legs for the full scale Loma Prieta excitation

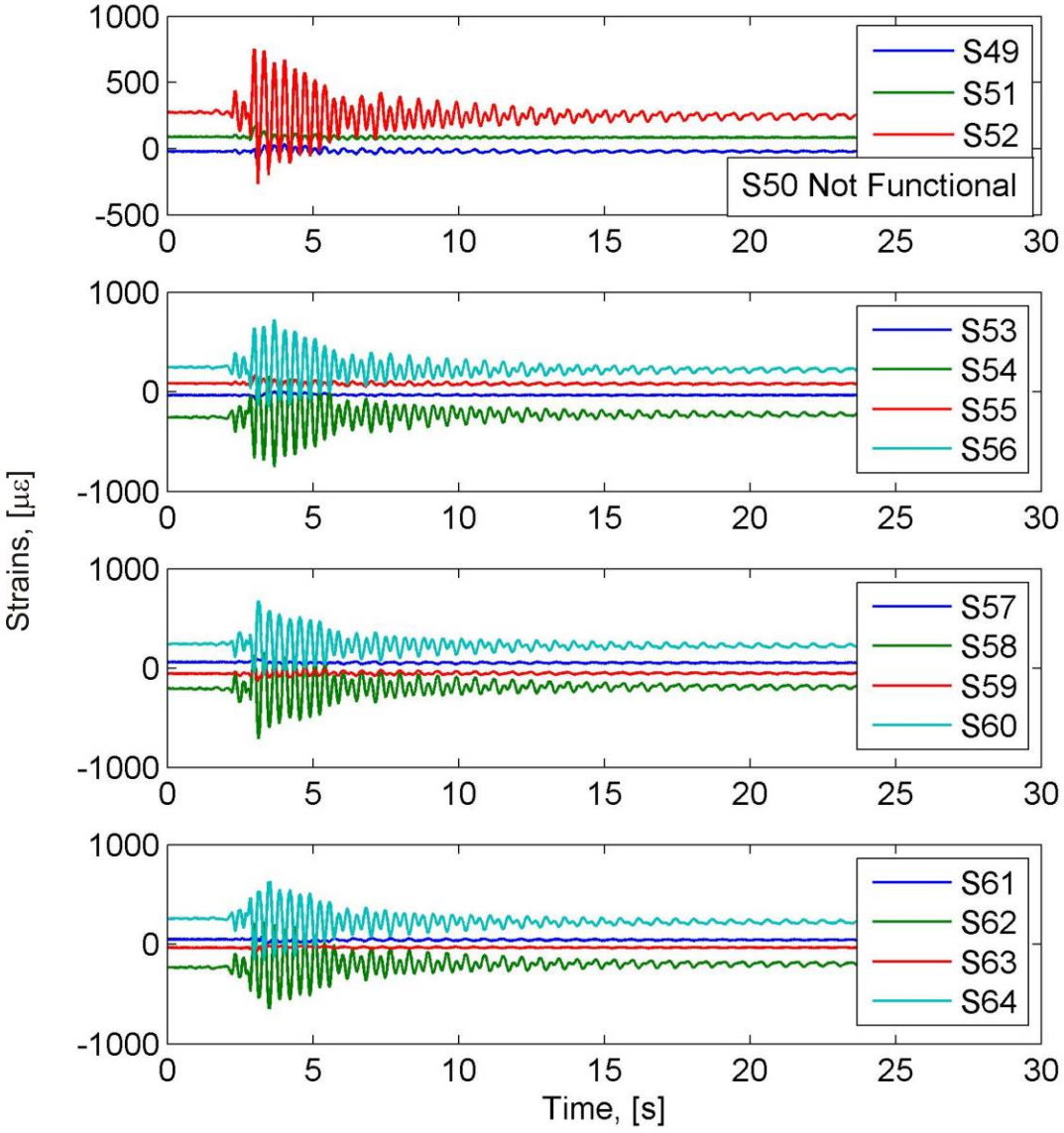

Figure B.47: Strain time histories in the portal beam for the full scale Loma Prieta excitation

B.3.4 Full Scale CLE4 Excitation

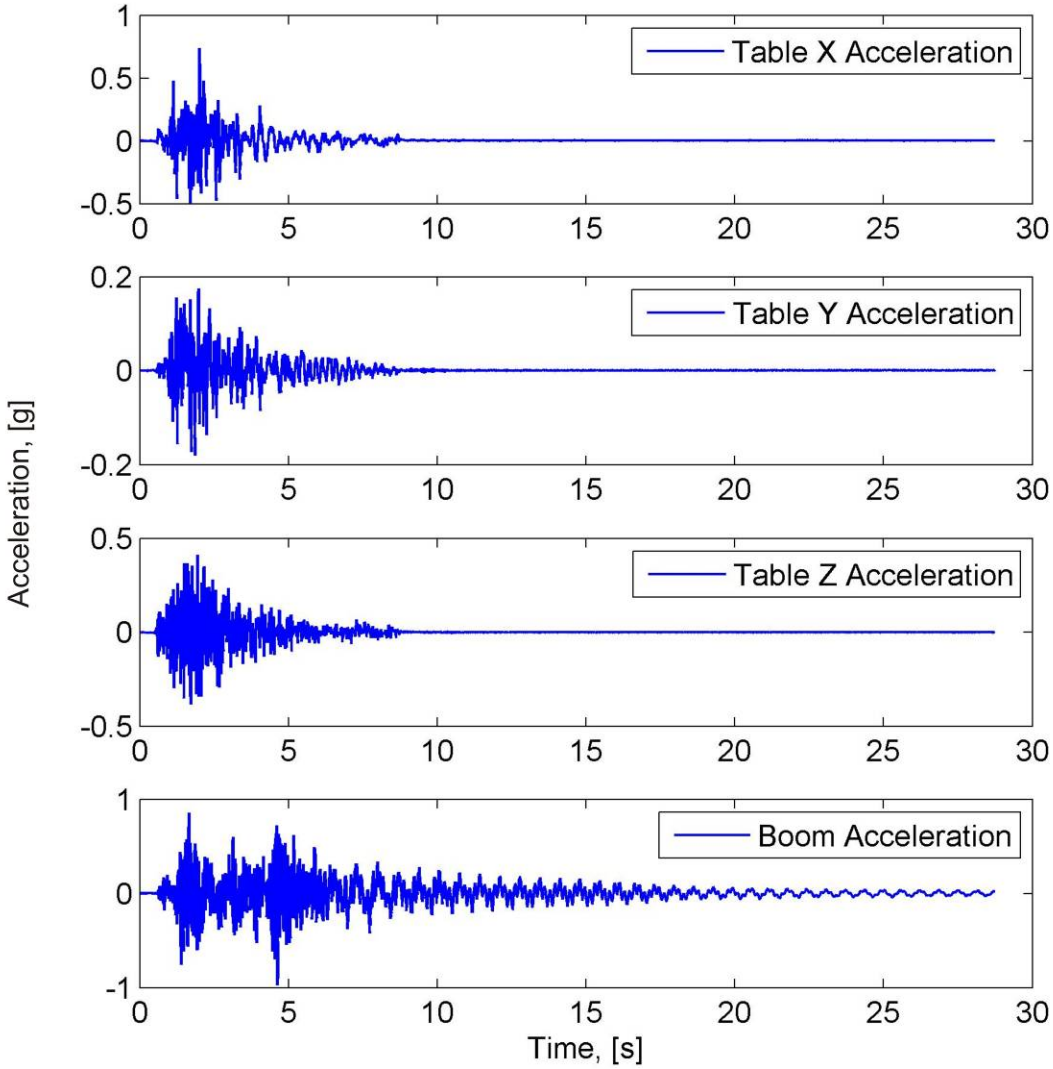

Figure B.48: Acceleration time histories for the full scale CLE4 excitation

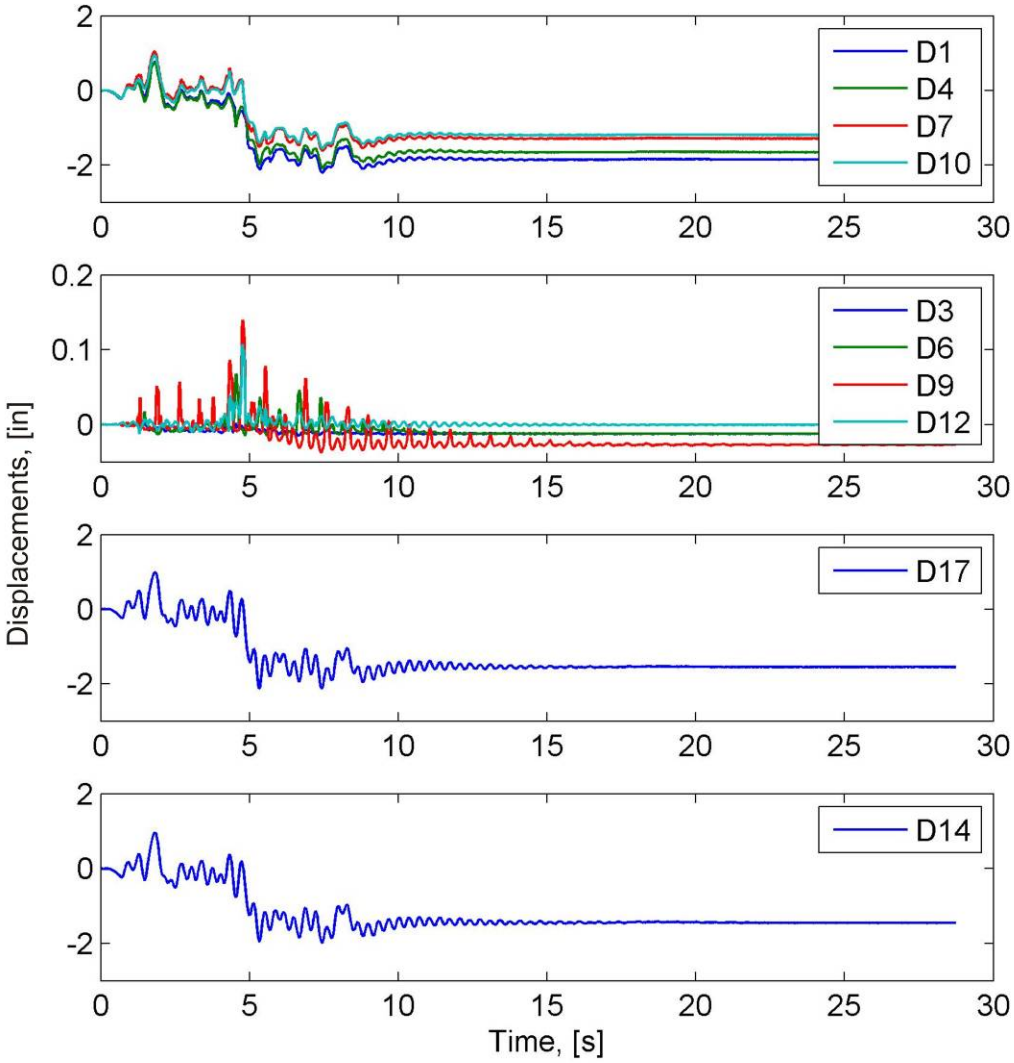

Figure B.49: Displacement time histories for the full scale CLE4 excitation

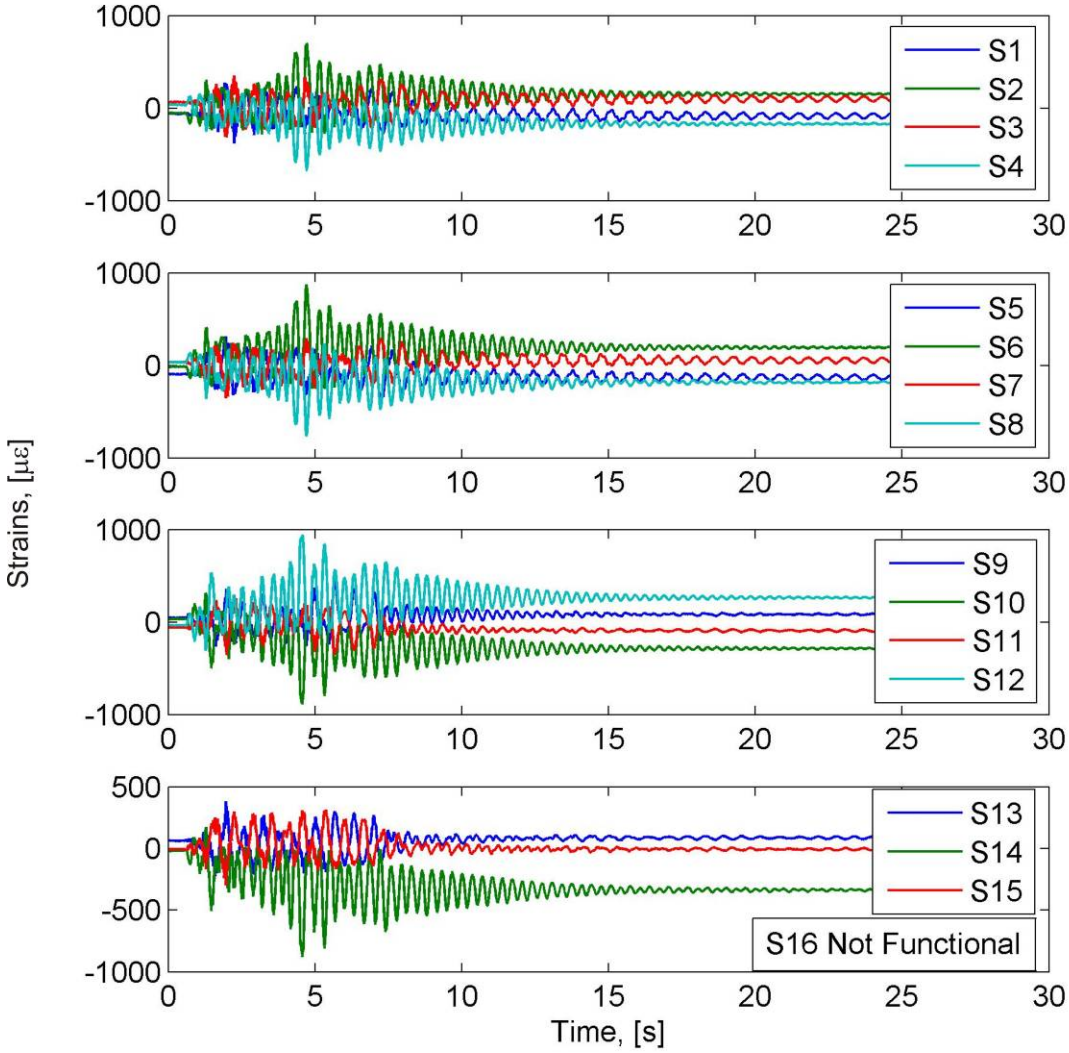

Figure B.50: Strain time histories at the bottom of the portal frame legs for the full scale CLE4 excitation

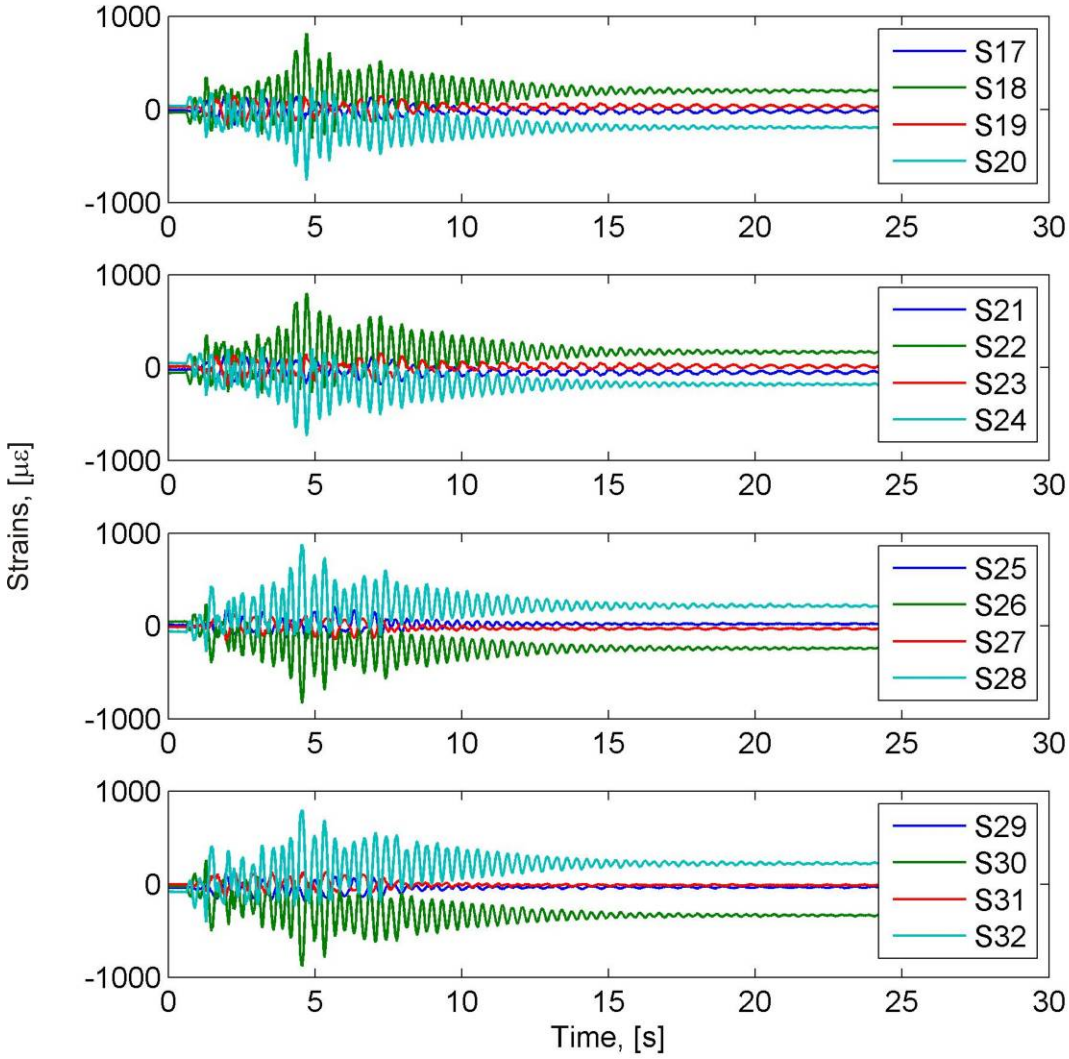

Figure B.51: Strain time histories at the middle of the portal frame legs for the full scale CLE4 excitation

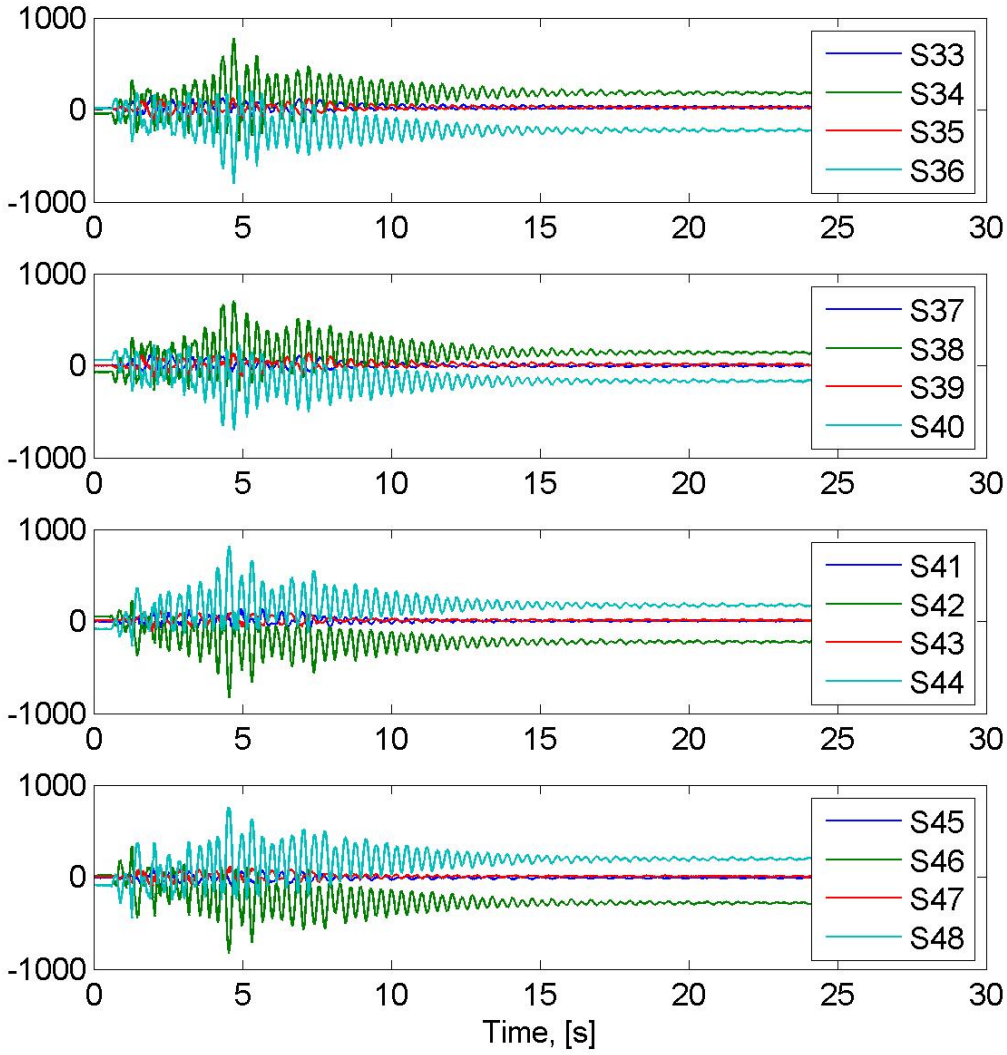

Figure B.52: Strain time histories at the top of the portal frame legs for the full scale CLE4 excitation

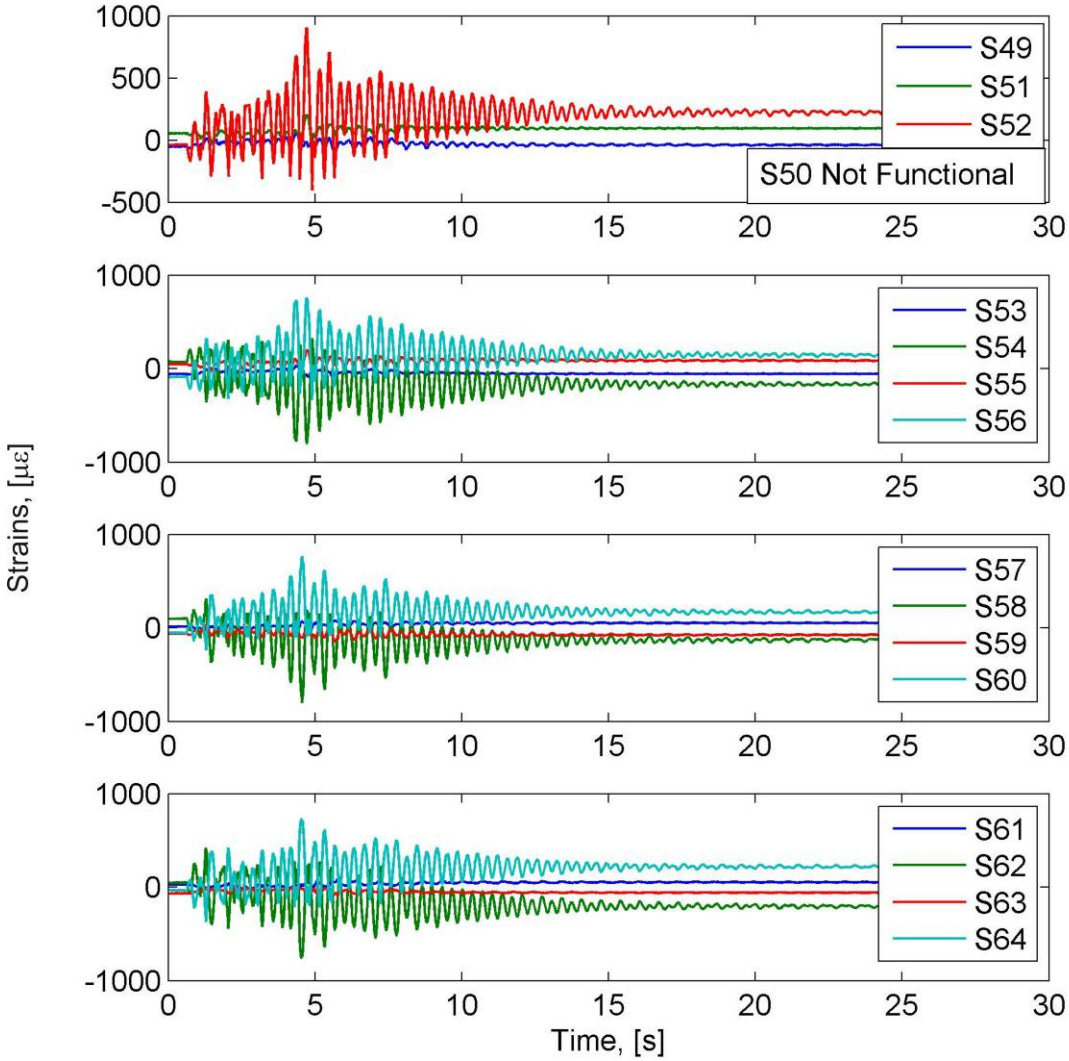

Figure B.53: Strain time histories in the portal beam for the full scale CLE4 excitation

B.3.5 Full Scale CLE6 Excitation

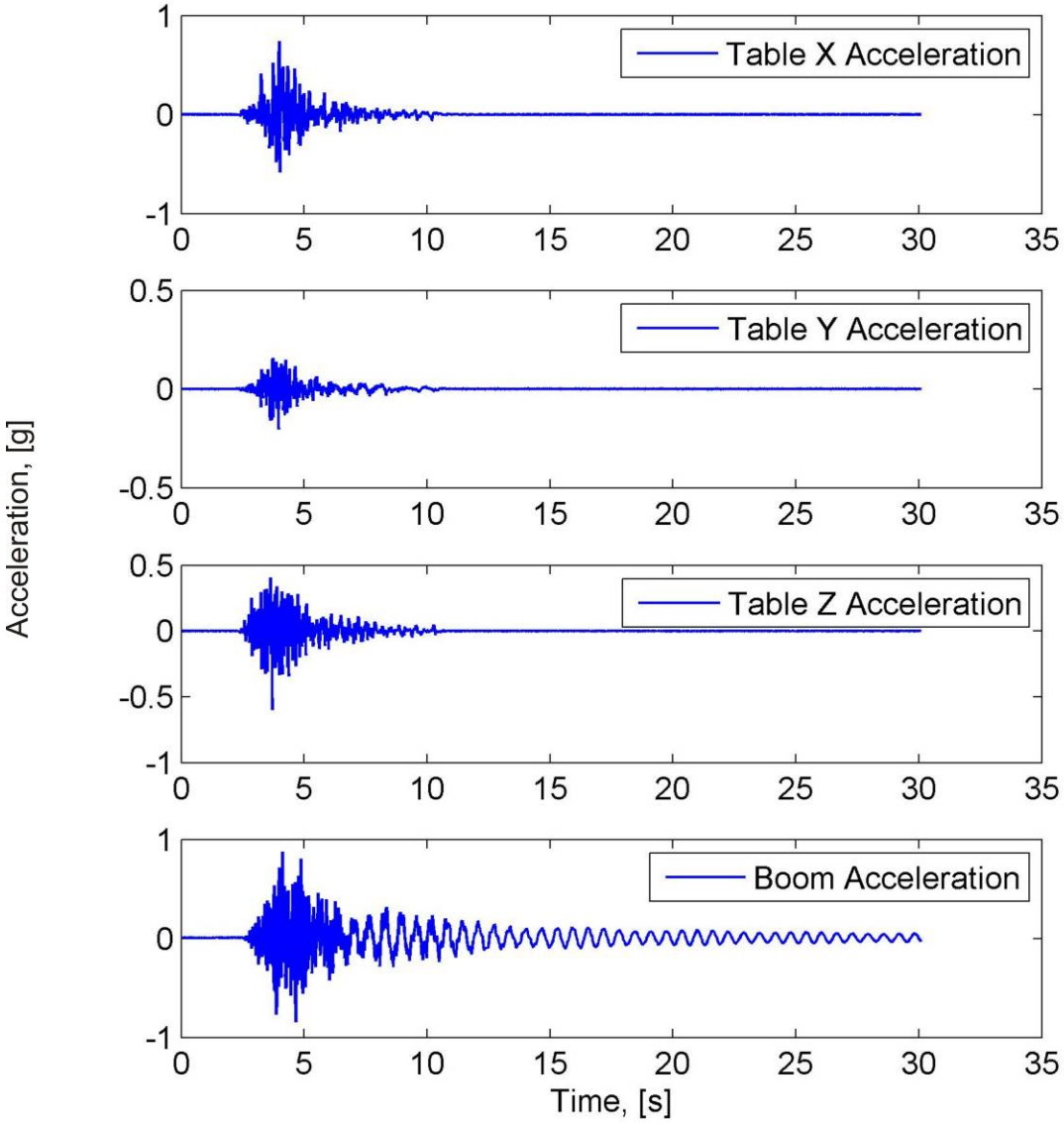

Figure B.54: Acceleration time histories for the full scale CLE6 excitation

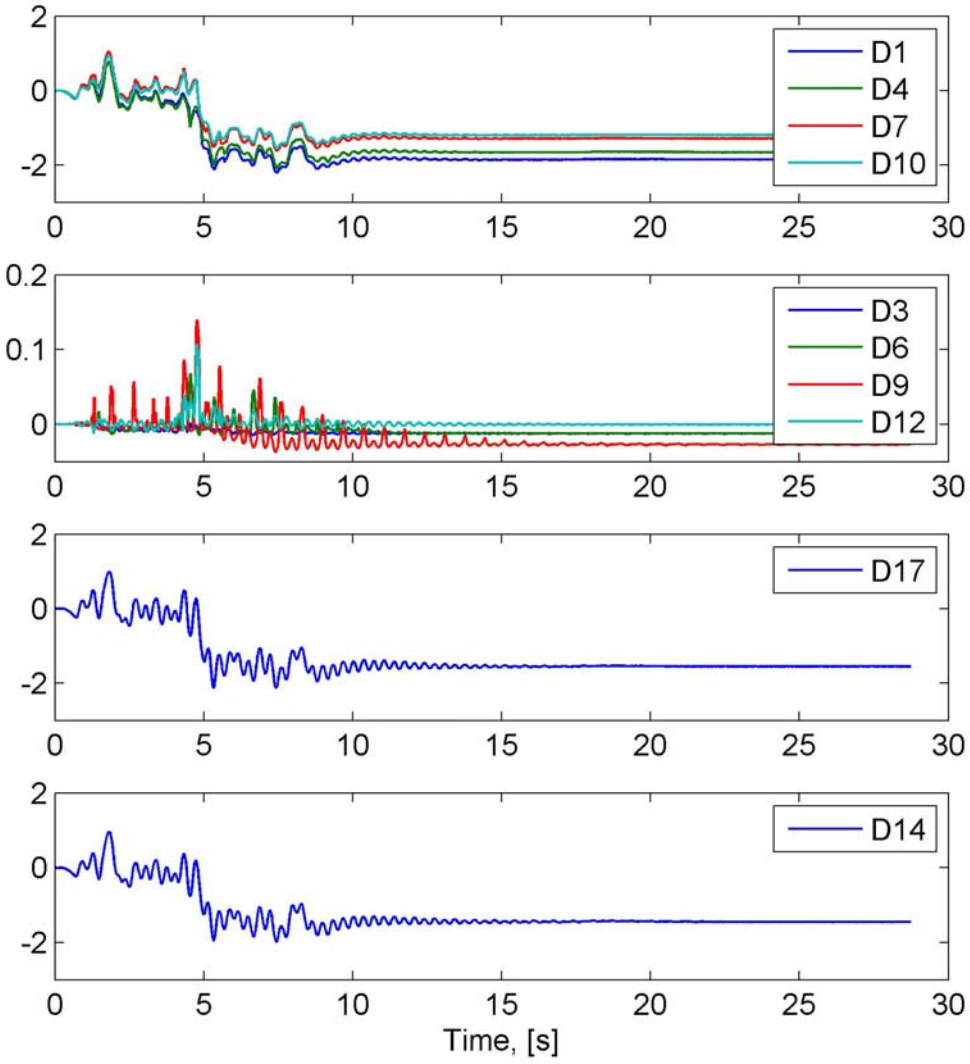

Figure B.55: Displacement time histories for the full scale CLE6 excitation

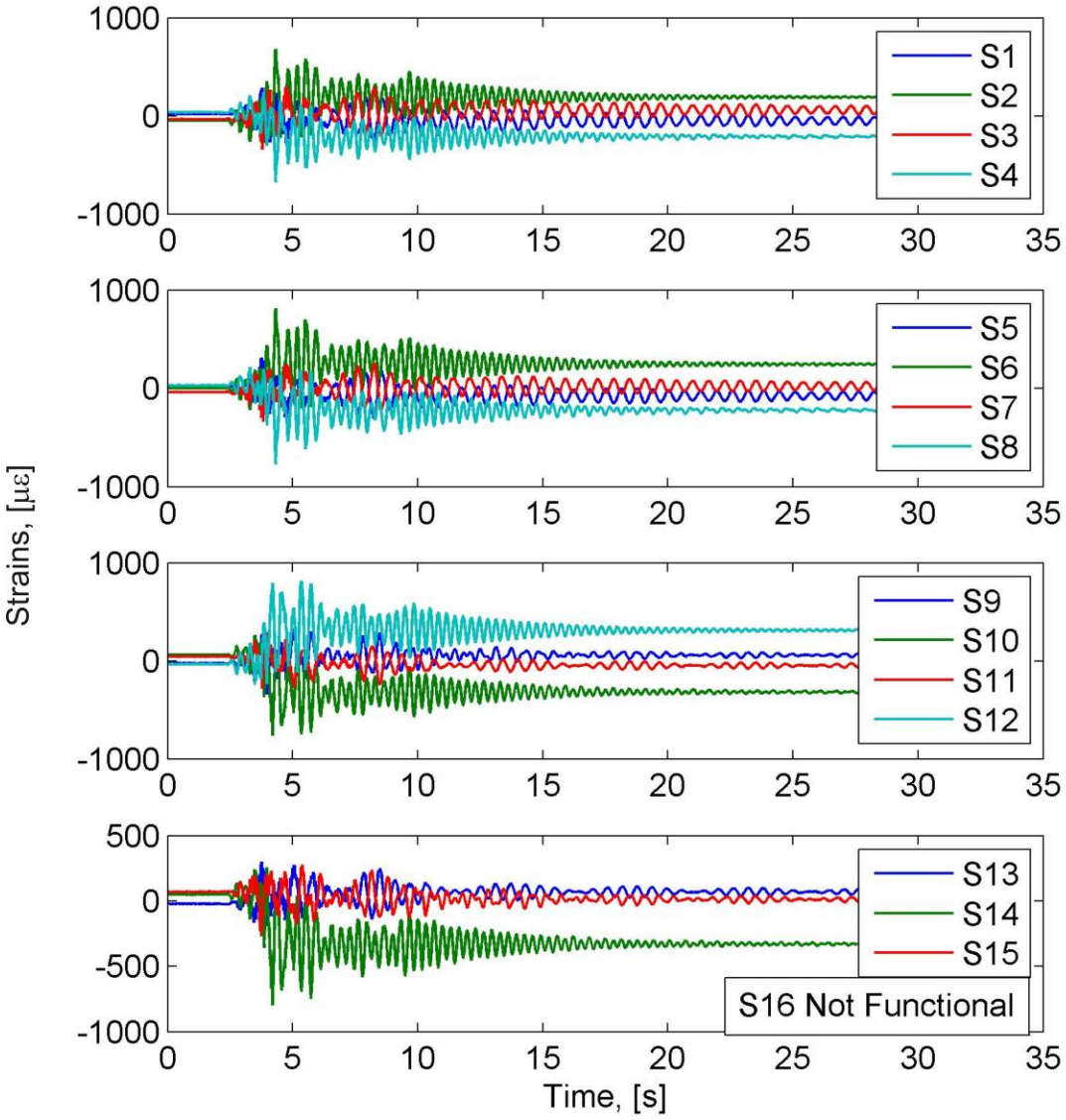

Figure B.56: Strain time histories at the bottom of the portal frame legs for the full scale CLE6 excitation

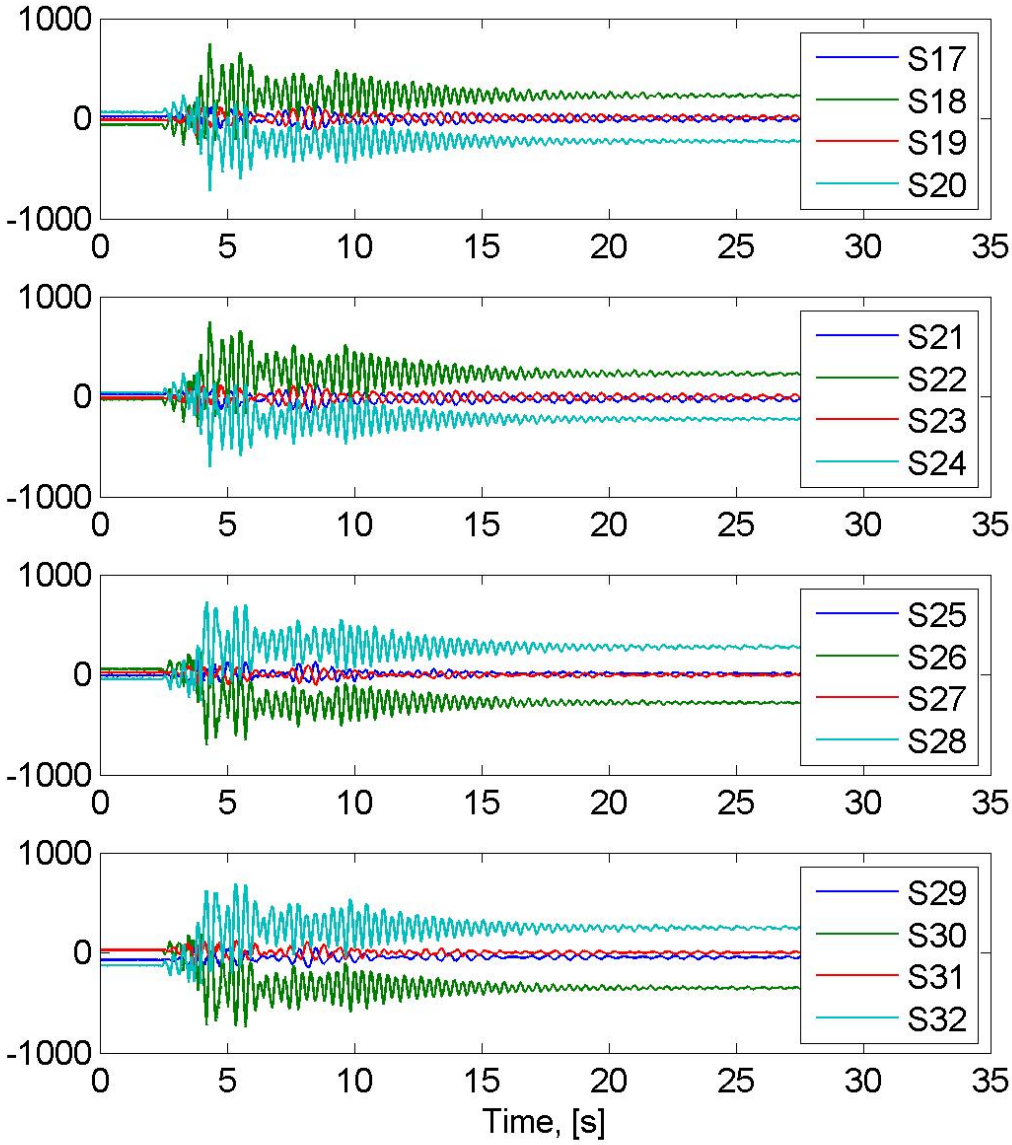

Figure B.57: Strain time histories at the middle of the portal frame legs for the full scale CLE6 excitation

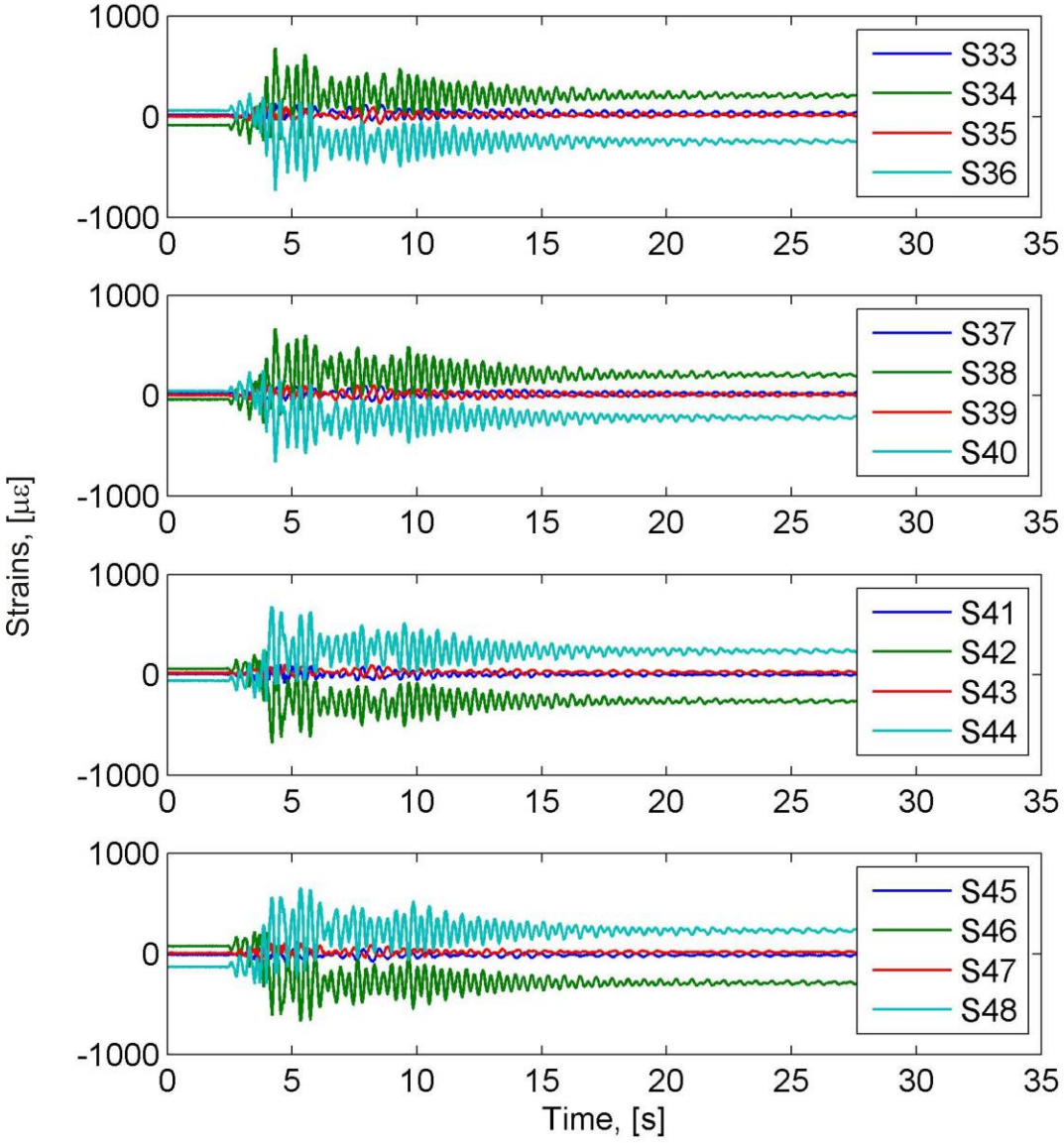

Figure B.58: Strain time histories at the top of the portal frame legs for the full scale CLE6 excitation

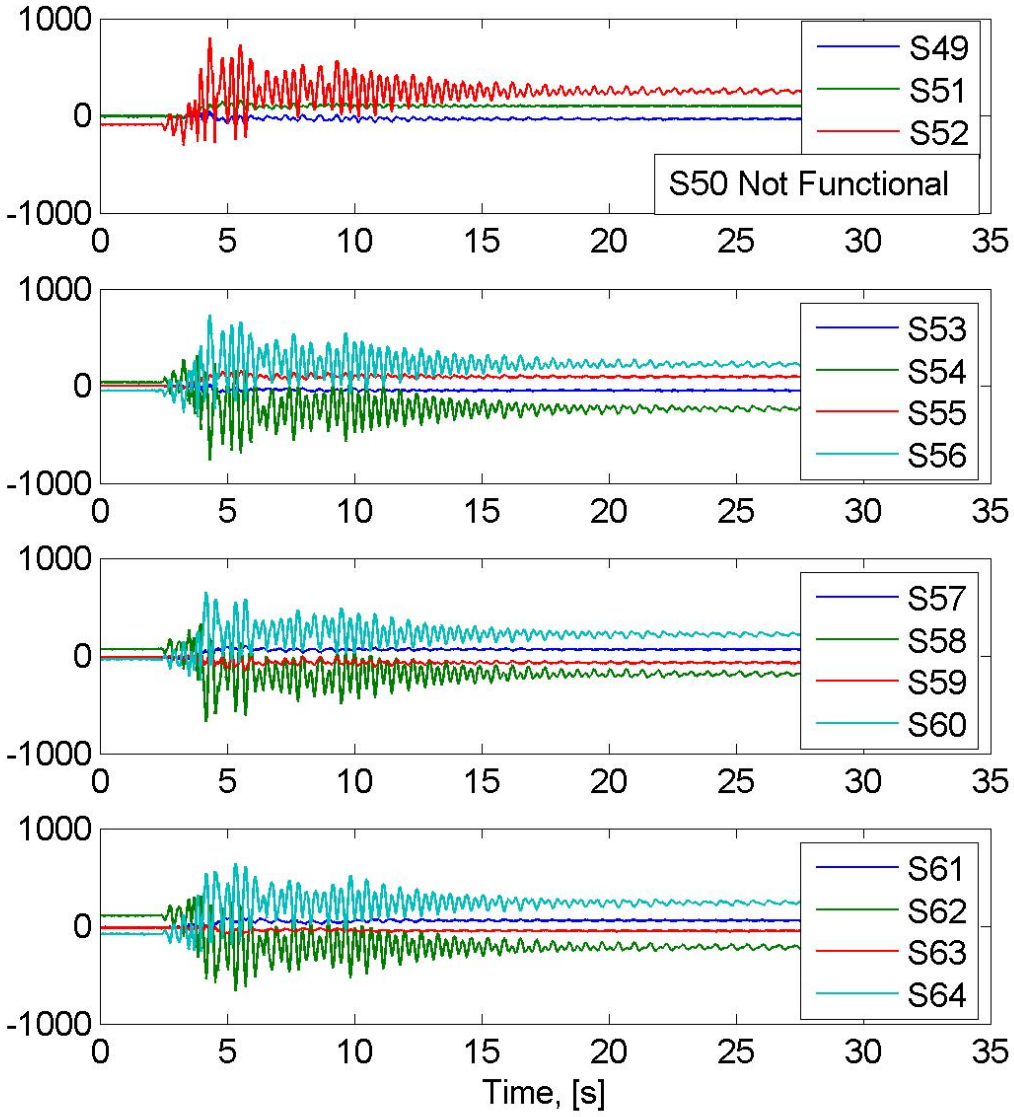

Figure B.59: Strain time histories in the portal beam for the full scale CLE6 excitation

APPENDIX C

DETAILS OF 1/10TH SCALE MODEL

This appendix contains additional information of the 1/10th scale model of a jumbo container crane. Section C.1 includes information on the dimensions of the various members. Section C.2 includes the fabrication drawings. Section C.3 contains additional data from the experiment.

C.1 Member Details

Presented in Table C.1 are the dimensions of all of the members of the 1/10th scale model structure illustrated in Figure C.1 that give the moments of inertia presented in Table 6.5. The values of D and B correspond to the dimensions labeled in Figure B.1. The boxes have a uniform thickness, so t_f and t_w are represented by a single variable, t.

Table C.1: Member dimensions for 1/10th scale model crane

Member	*B (in)*	*D (in)*	*t (in)*
A	4.0	7.0	0.188
B	4.0	5.0	0.188
C	6.125	3.825	0.125
D	6.825	3.825	0.125
E	3.0	8.0	0.188
F	6.0	8.0	0.625
G	2.75	7.25	0.125
H	3.0	5.0	0.5
L	2.5	3.5	0.188
M	1.5	3.5	0.188

C.2 Fabrication Drawings

The next 12 figures are the fabrication drawings for the 1/10th scale model.

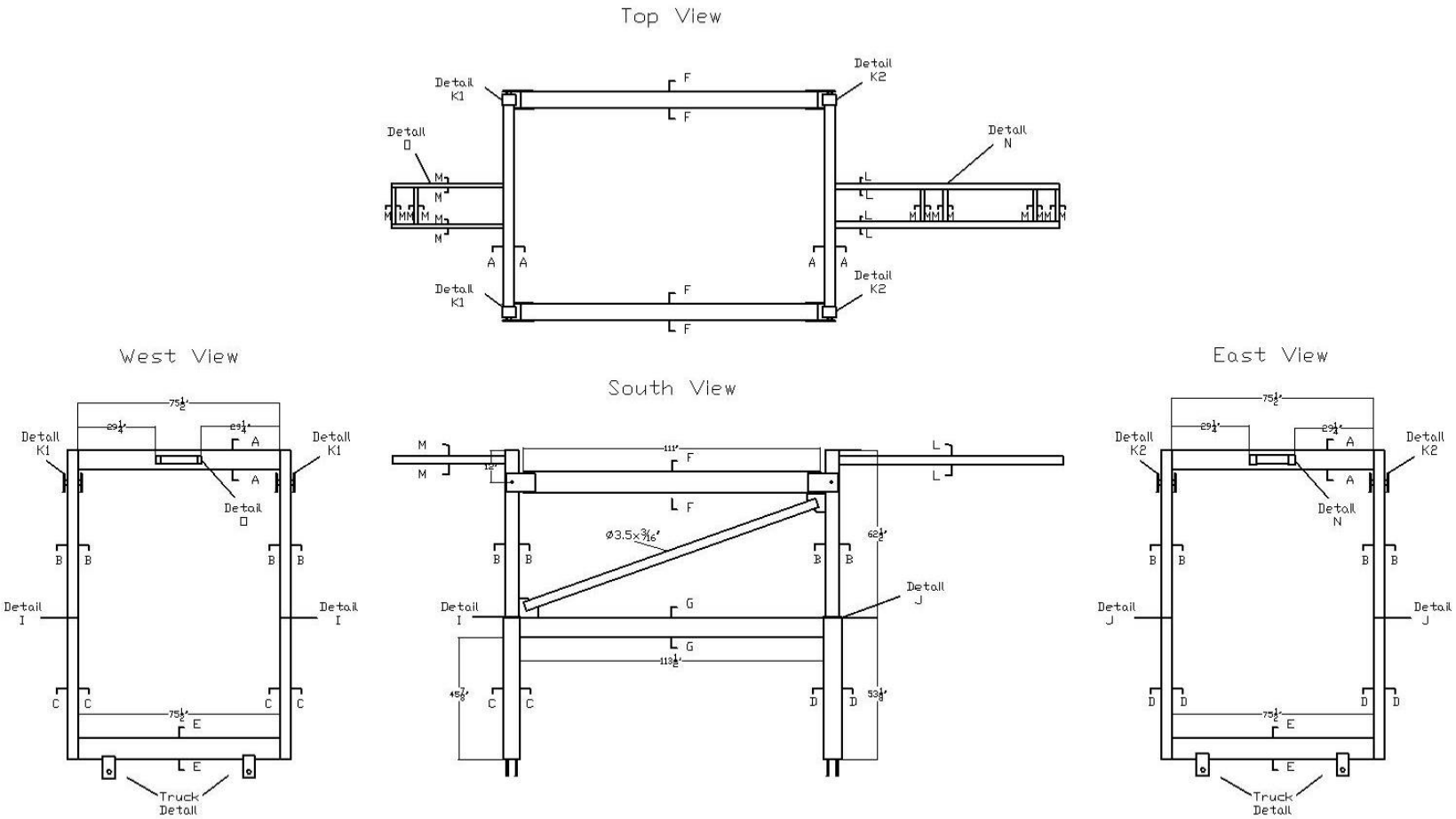

Figure C.1: 1/10th Scale model of a jumbo container crane

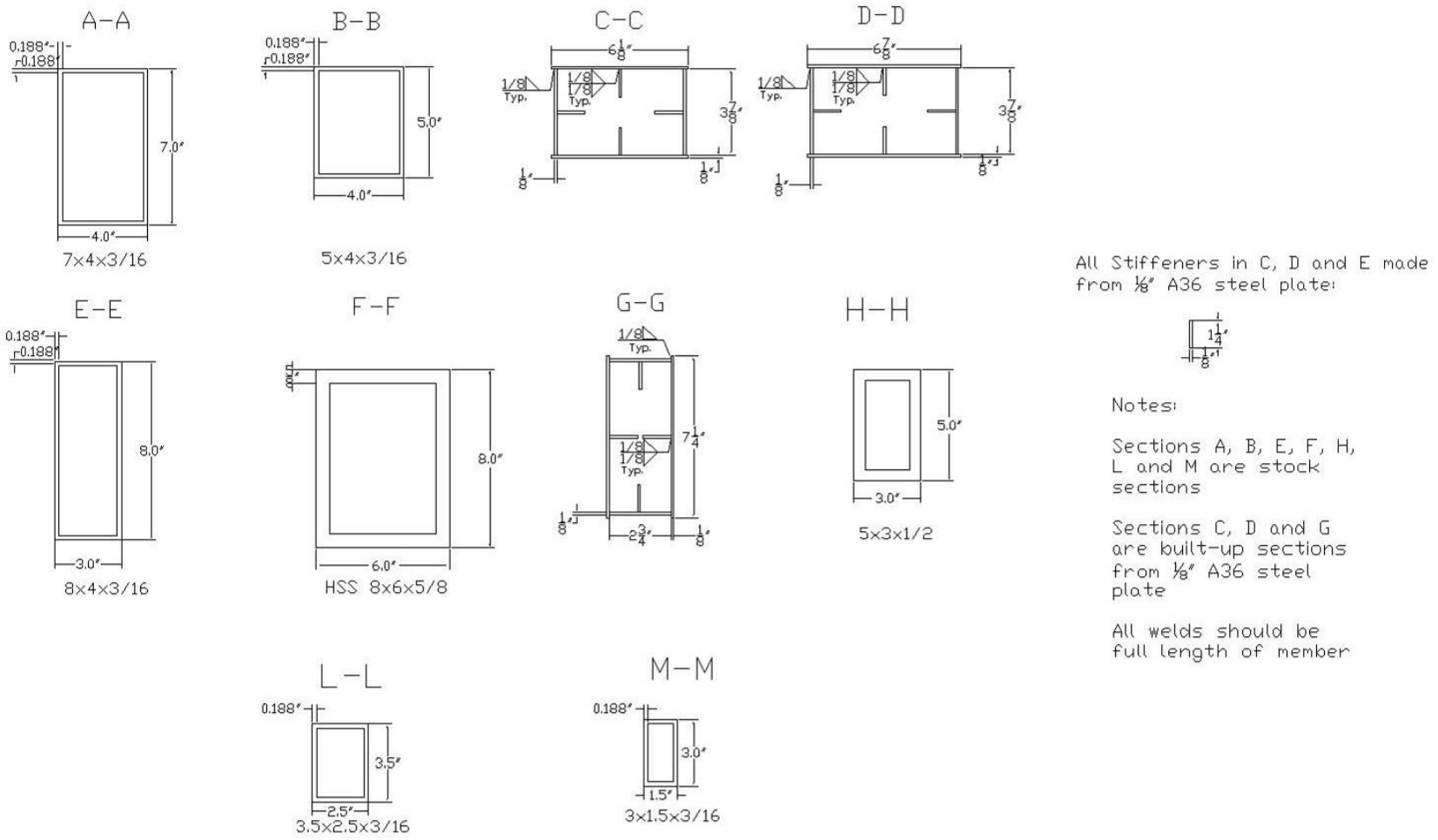

Figure C.2: Section details for 1/10th scale container crane

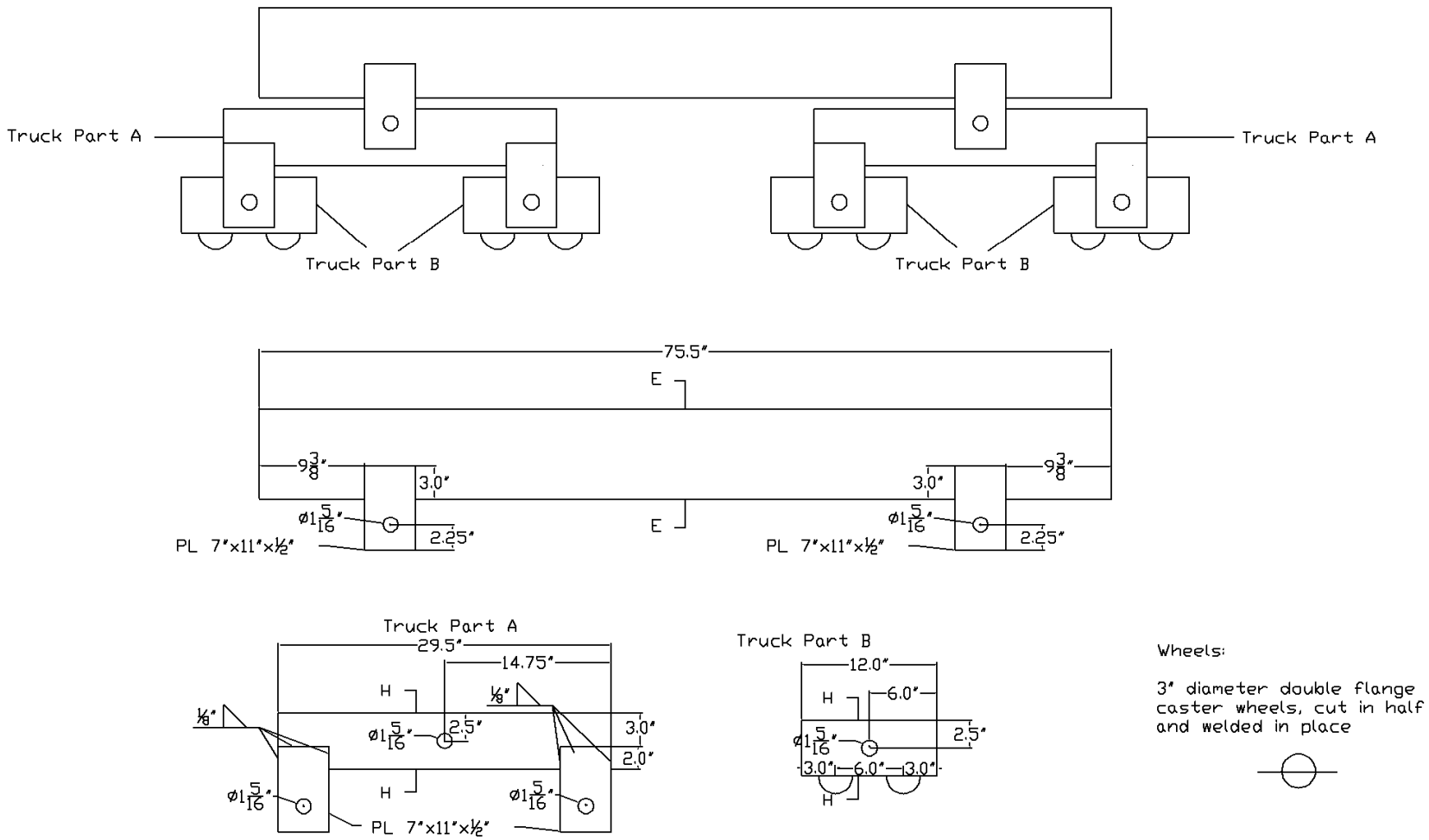

Figure C.3: Truck details for 1/10th scale model

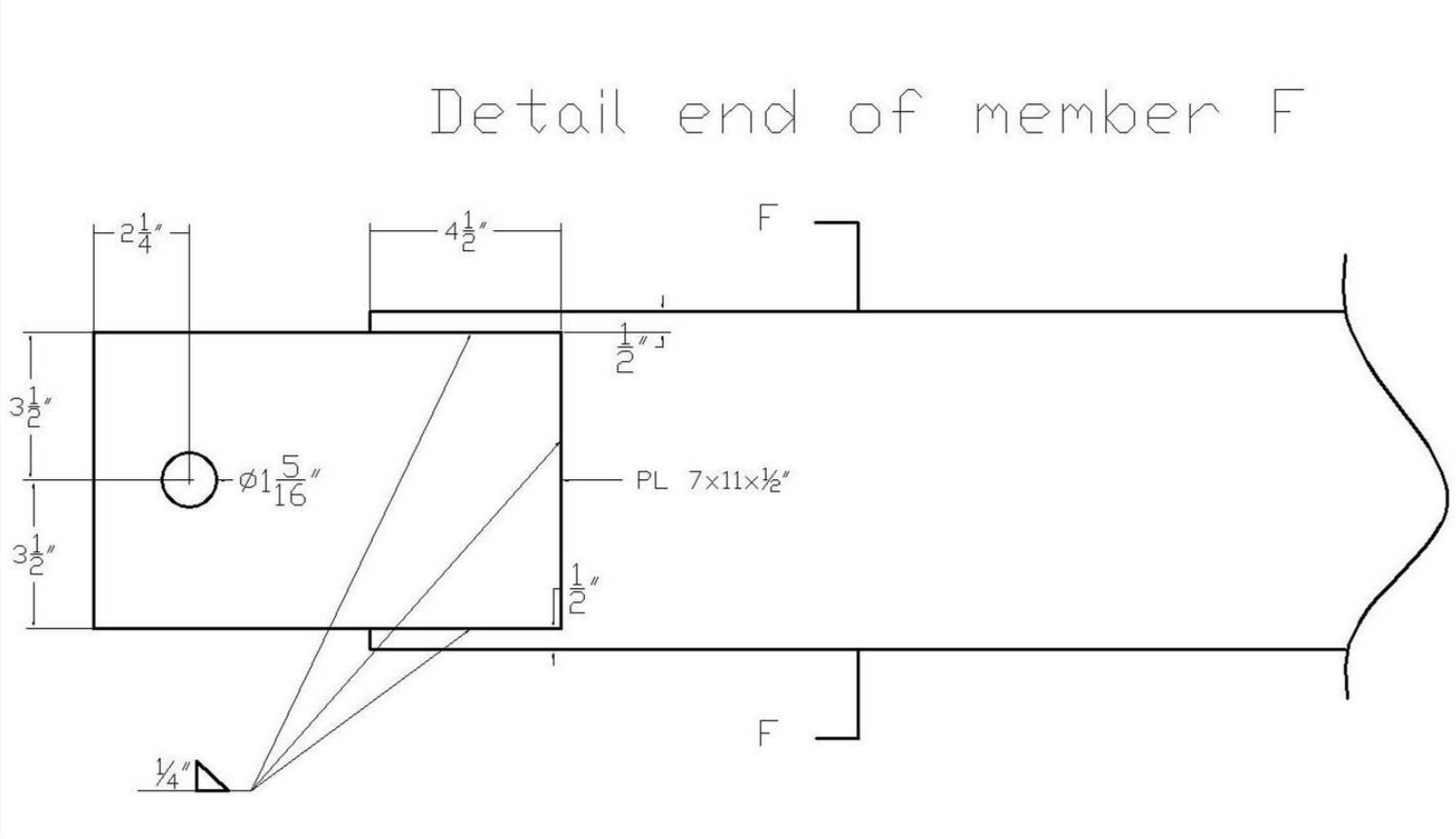

Figure C.4: Details for end of member F of 1/10th scale model

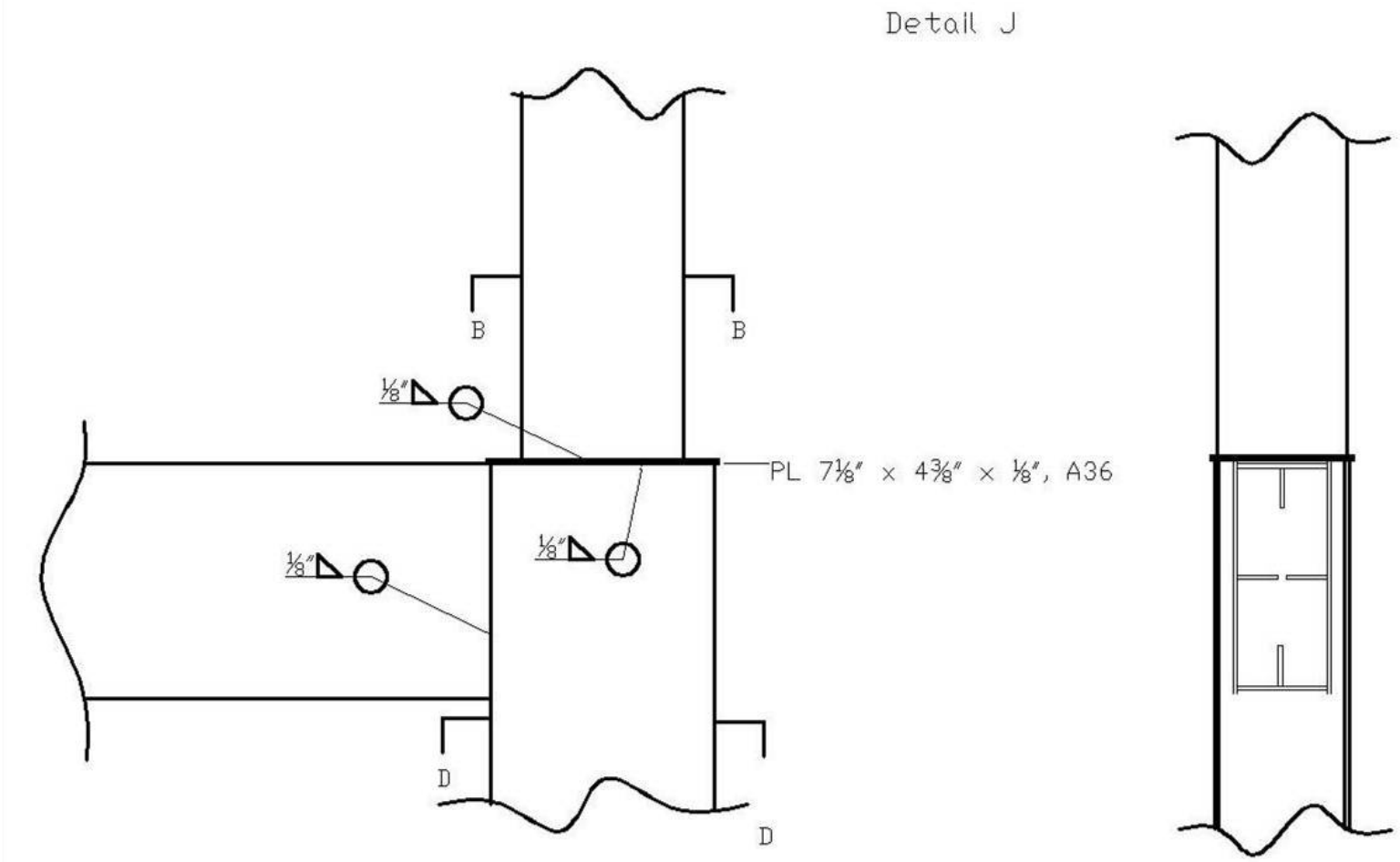

Figure C.5: detail J for 1/10th scale model

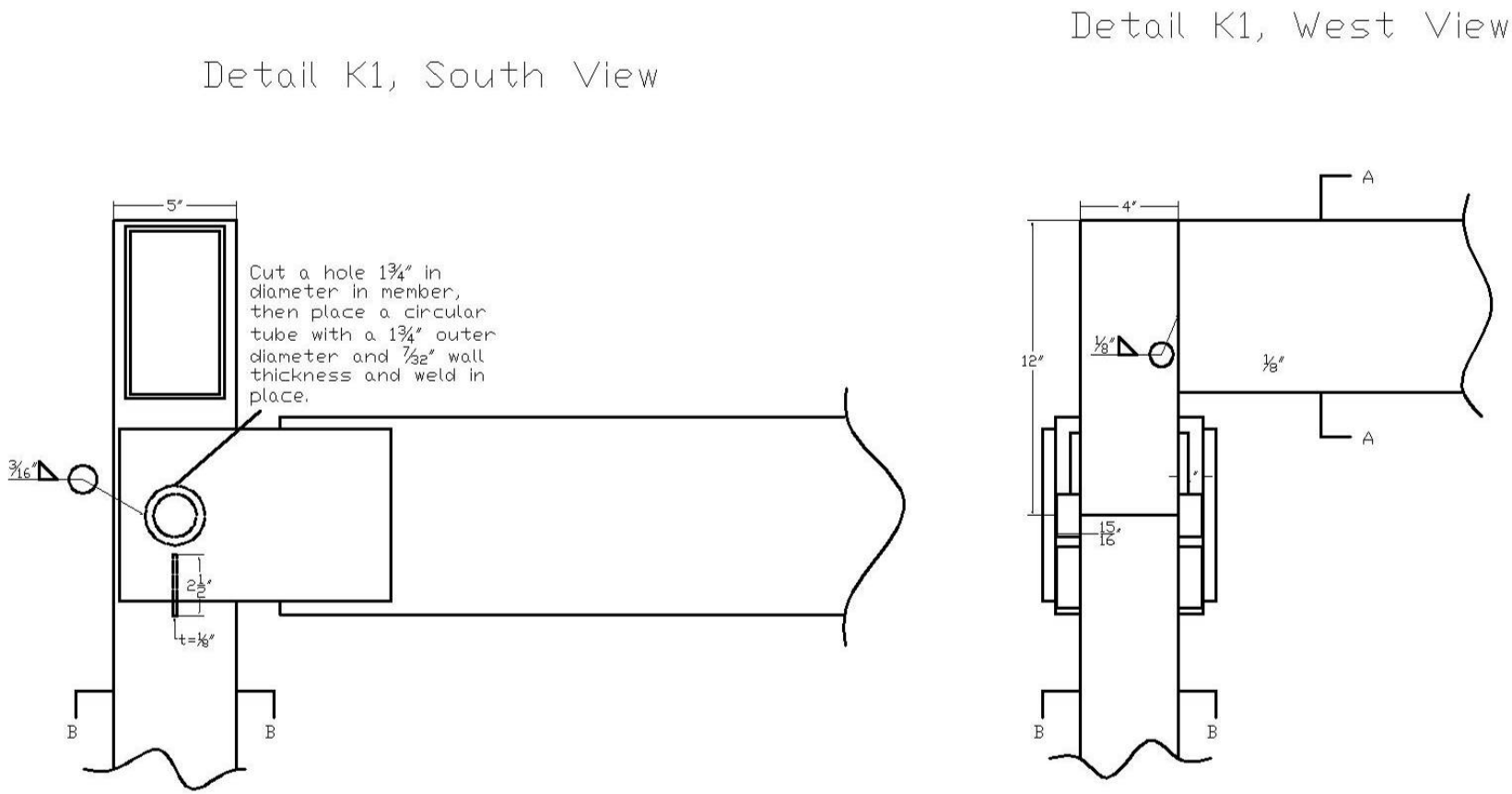

Figure C.6: Detail K1 for 1/10th scale model

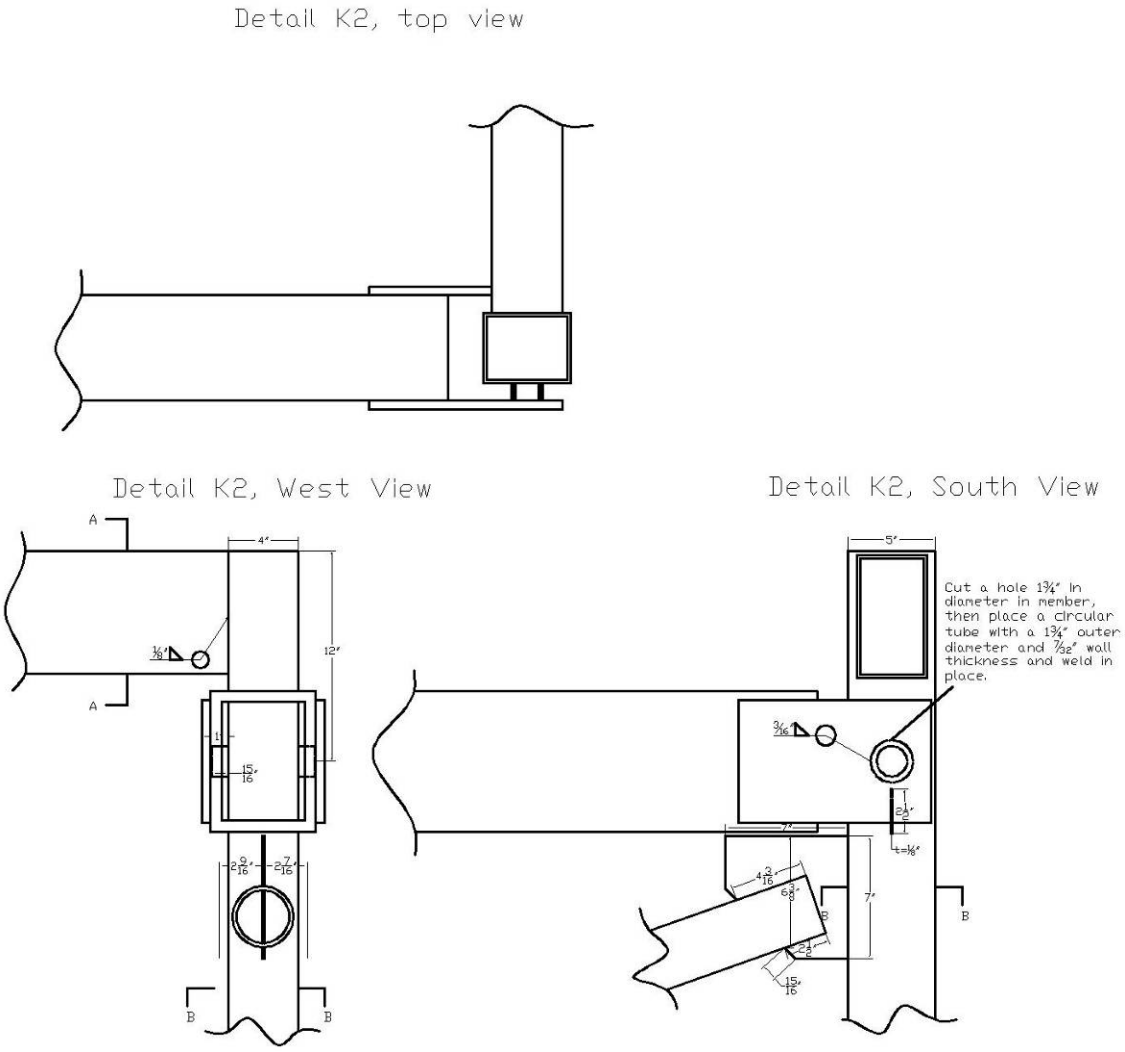

Figure C.7: Detail K2 for 1/10th scale model

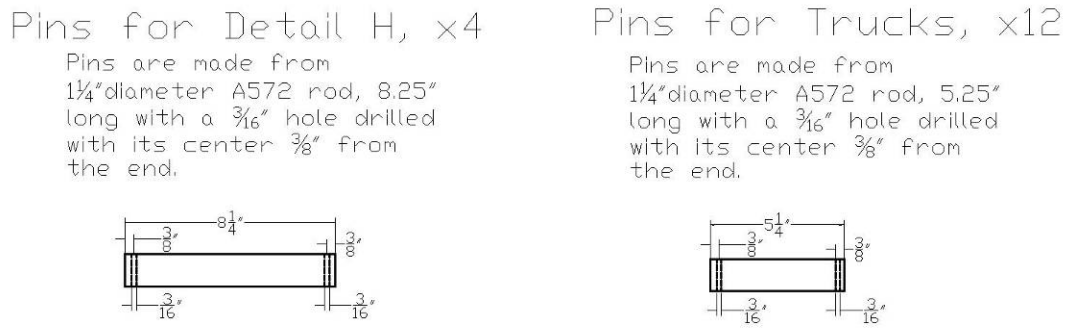

Figure C.8: Pin details for 1/10th scale model

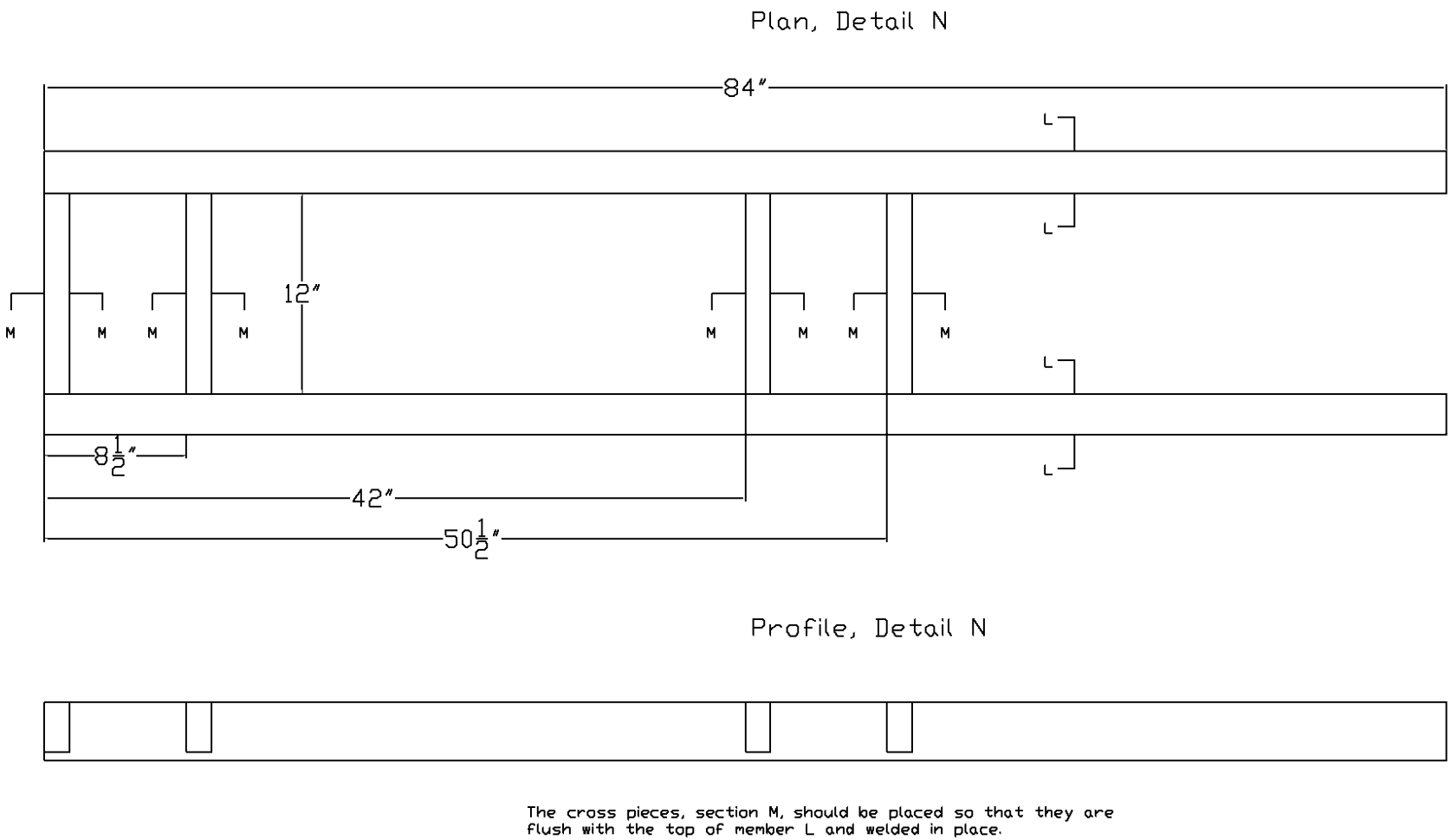

Figure C.9: Detail N for 1/10th scale model

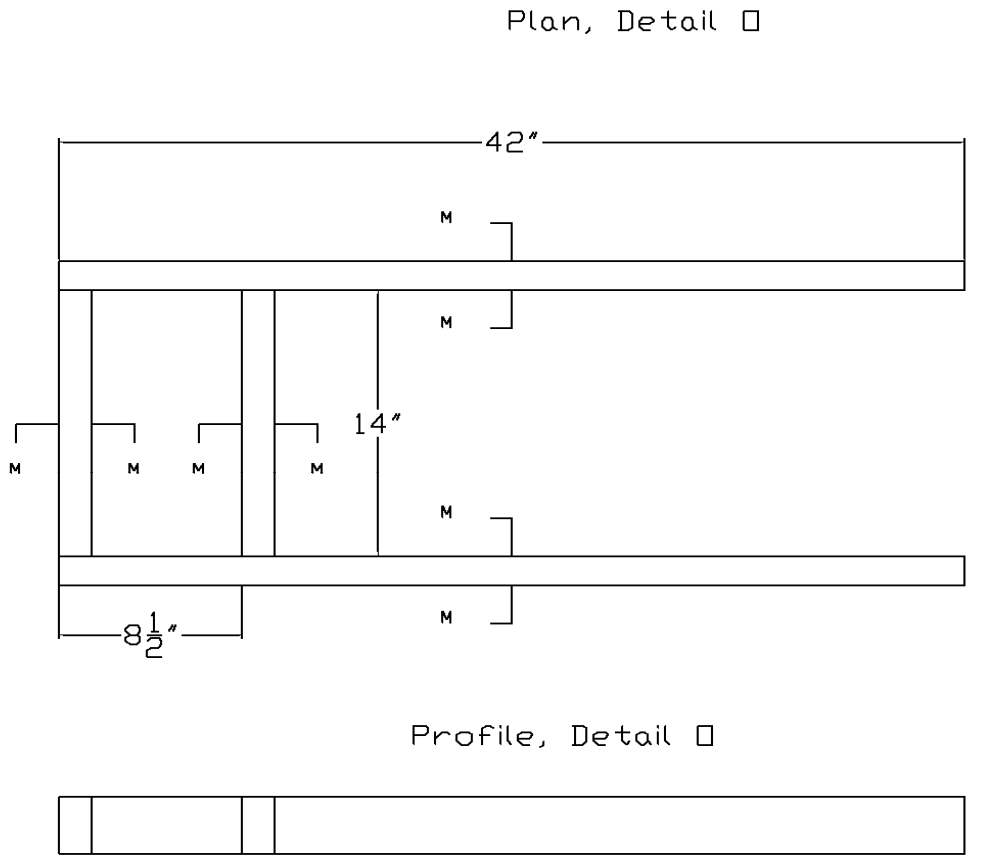

Figure C.10: Detail O for 1/10th scale model

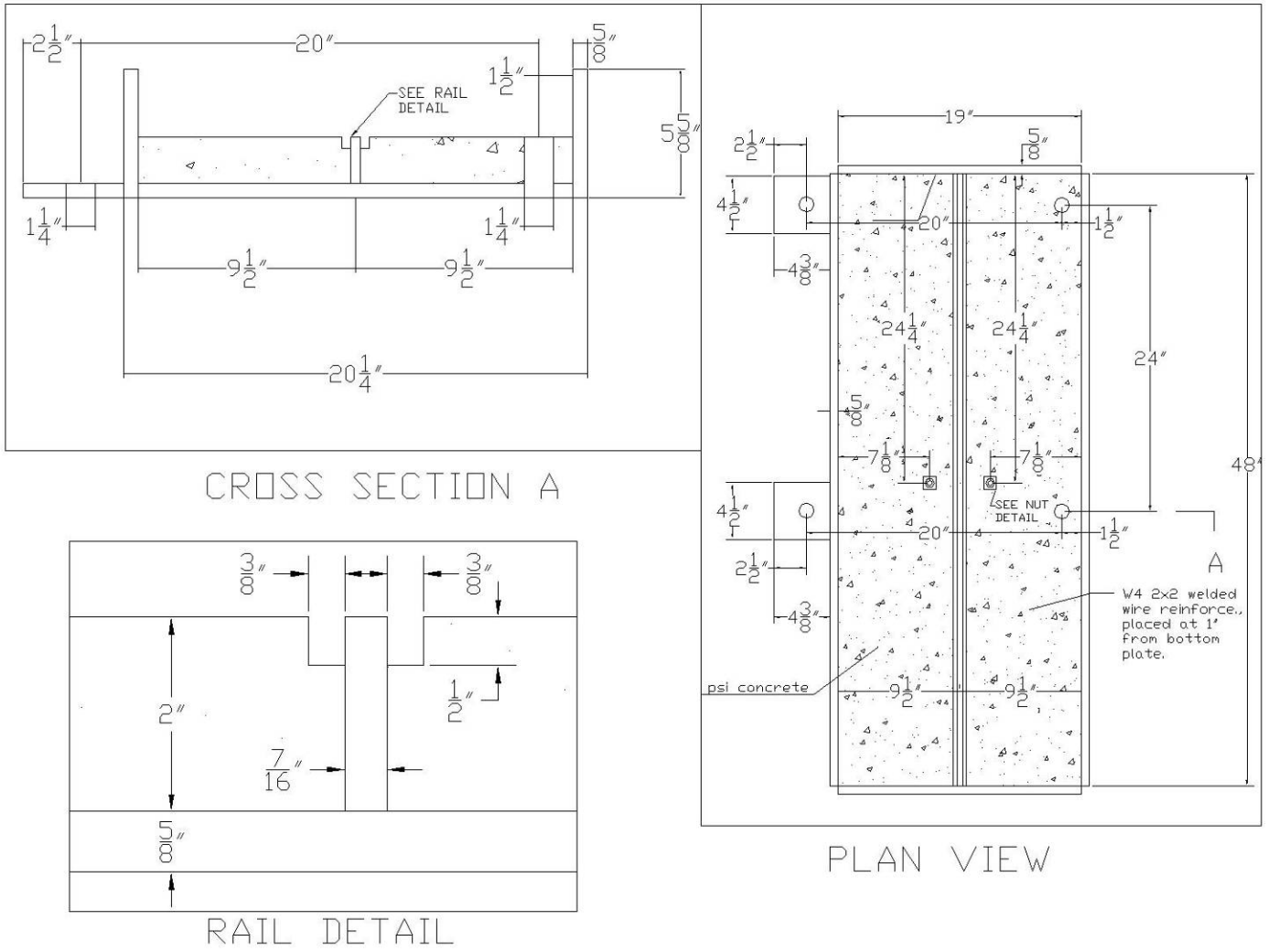

Figure C.11: Rail box diagrams for 1/10th scale model

C.3 Raw Data

This section includes some of the raw data from the Phase I test. All of the data is available from the NEES central repository. As of publication, the location of the central repository is: https://nees.org/warehouse/project/86. The data included in this section from the OLE earthquakes is from the full scale, biaxial excitations. The data included in this section for the CLE4 earthquake is from the 55% triaxial excitation. The data included from the CLE6 earthquake is from the 60% triaxial excitation. The data from Loma Prieta earthquake is from the 70% triaxial excitation. The data from the NJM record is from the 20% triaxial excitation.

The first figure in each subsection (Figures C.12, C.18, C.24, C.30, C.36 and C.42) show the measured acceleration data on the shake table in the X (trolley travel), Y (gantry travel) and Z (vertical) directions and the trolley travel boom acceleration. The second figure in each subsection (Figures C.13, C.319, C.25, C.31, C.37 and C.43) show the displacement time histories at the base in the trolley travel and vertical directions. Additionally the trolley travel direction displacements of the portal beam and the top of the O-frame. The gauges given for each time history correspond to the gauges labeled in Figure 6.12. The remaining figures show the raw strain gauge data from the portal frame. The gauges given for each of the time histories correspond to those in Figure 6.13. The strain gauge data was used to calculate the moments presented in Chapter 7.

C.3.1 Full Scale OLE4

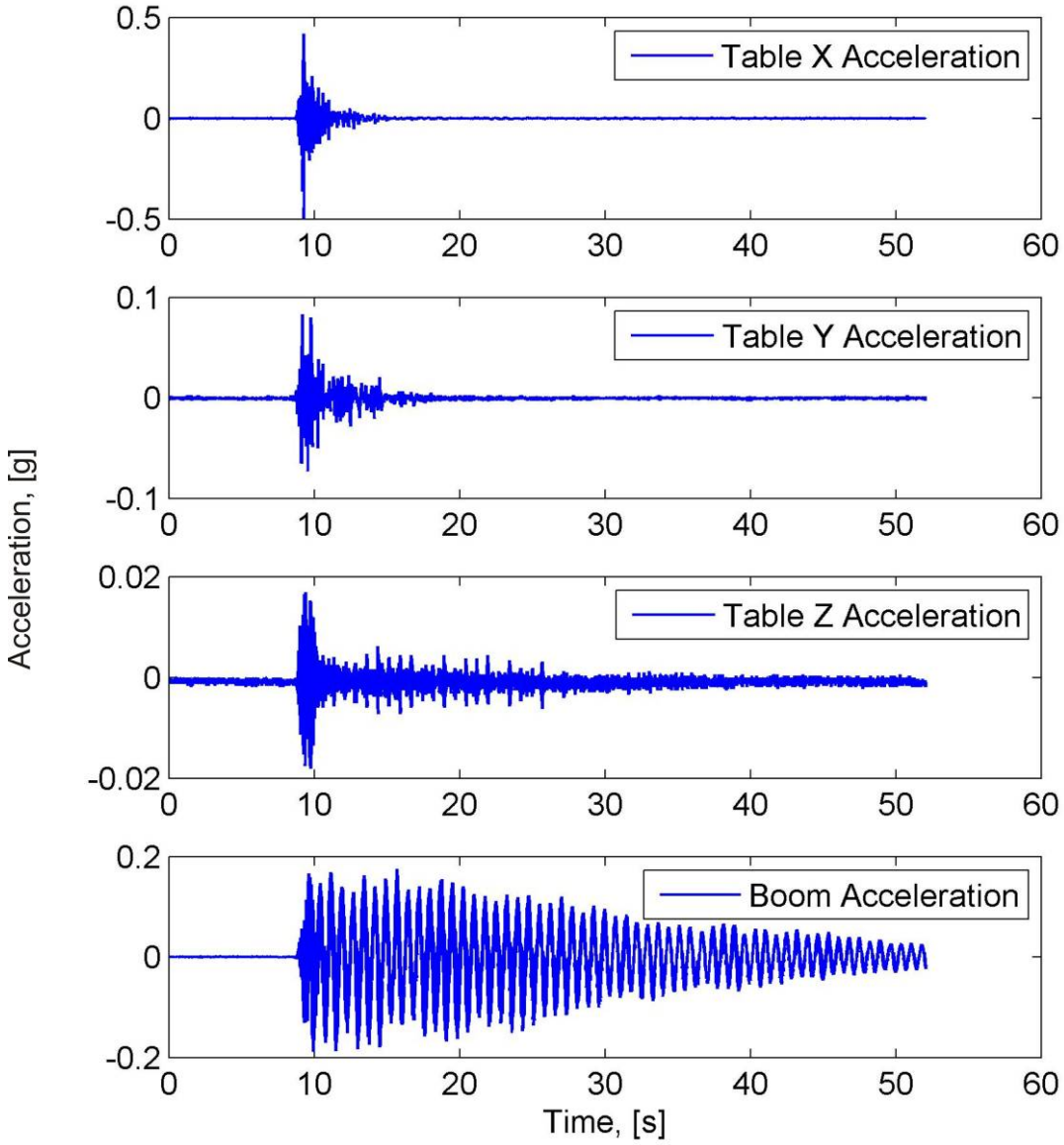

Figure C.12: Acceleration time histories for the full scale OLE4 excitation

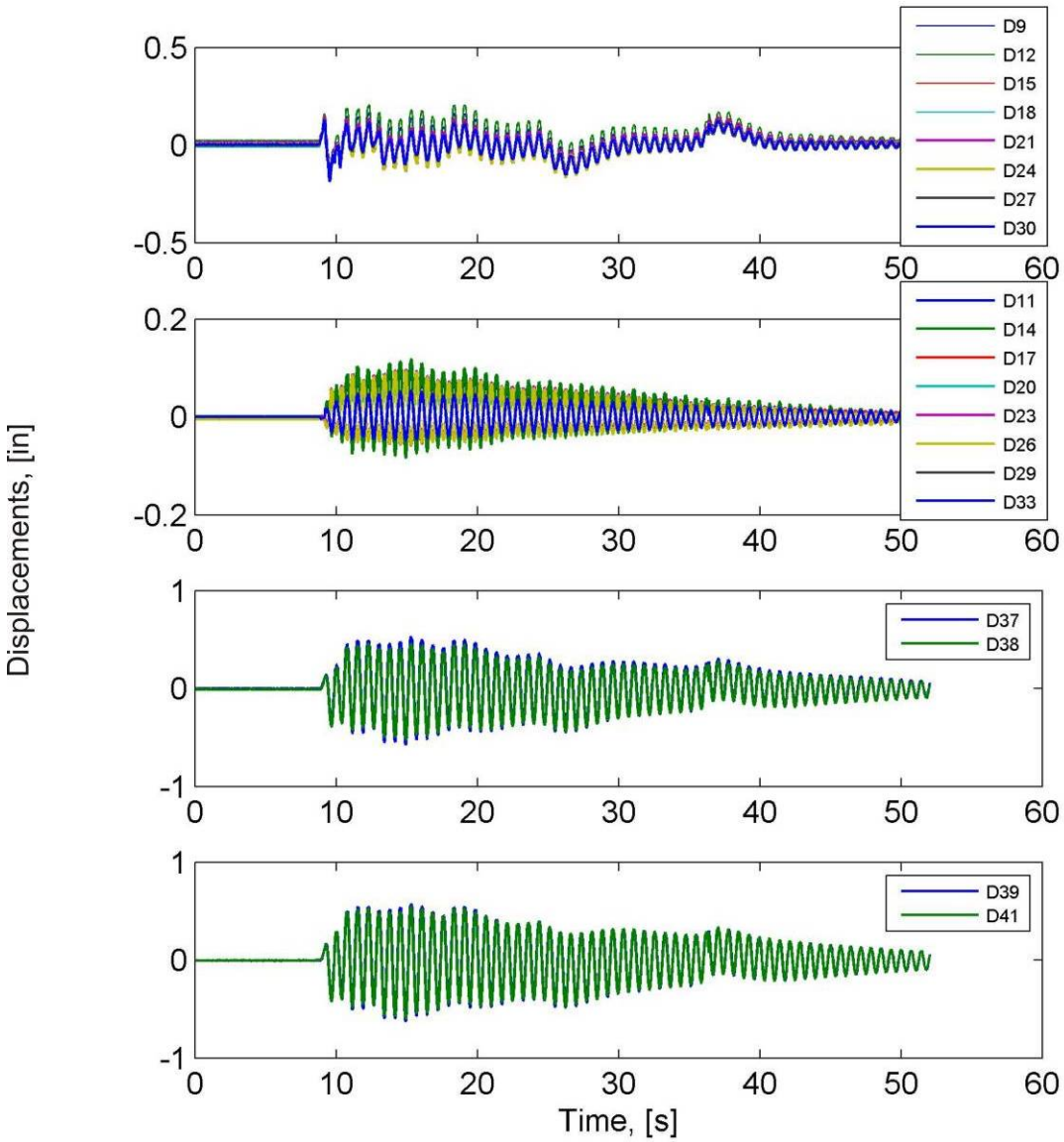

Figure C.13: Displacement time histories for the full scale OLE4 excitation

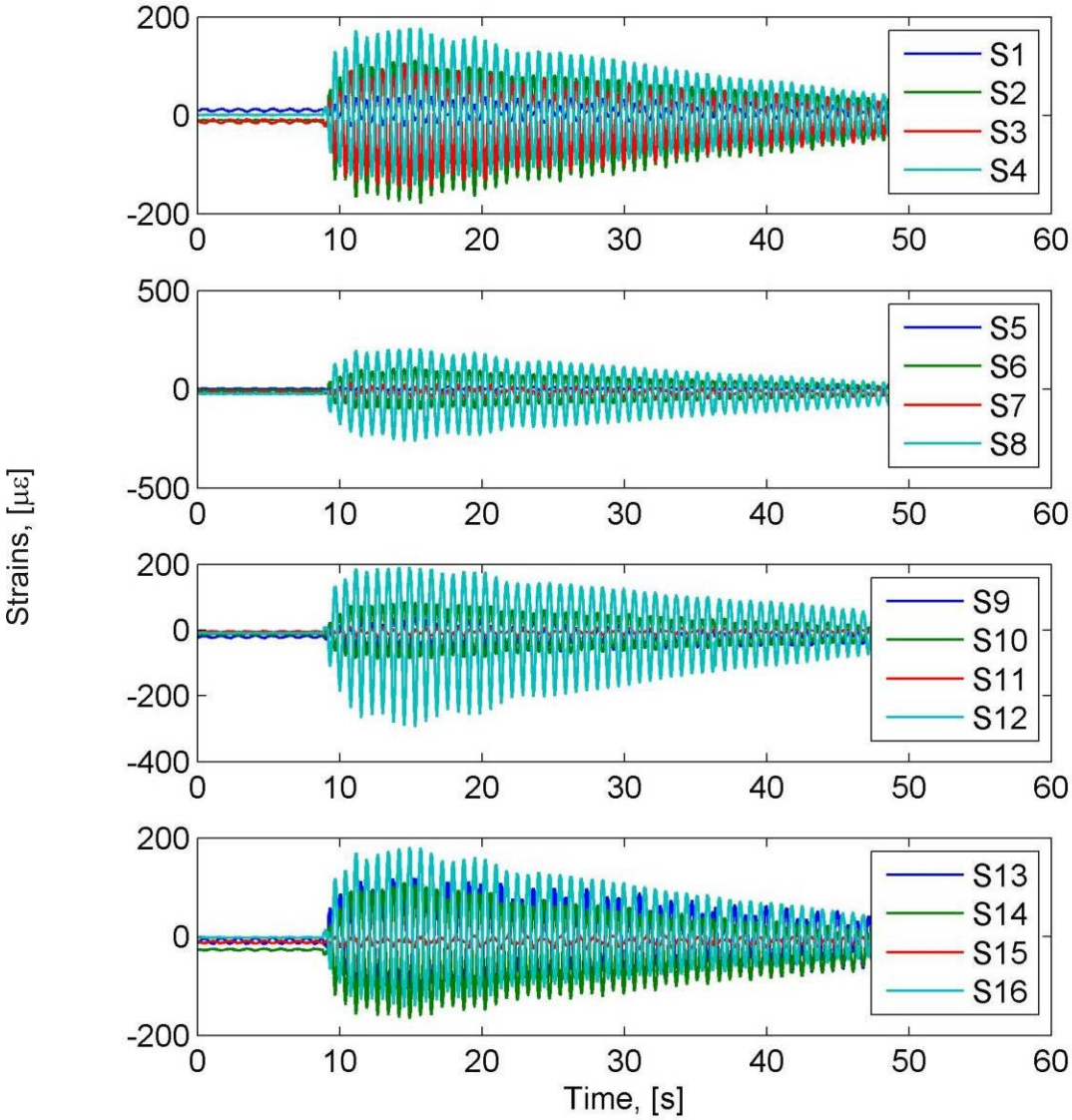

Figure C.14: Strain time histories at the bottom of the portal frame legs for the full scale OLE4 excitation

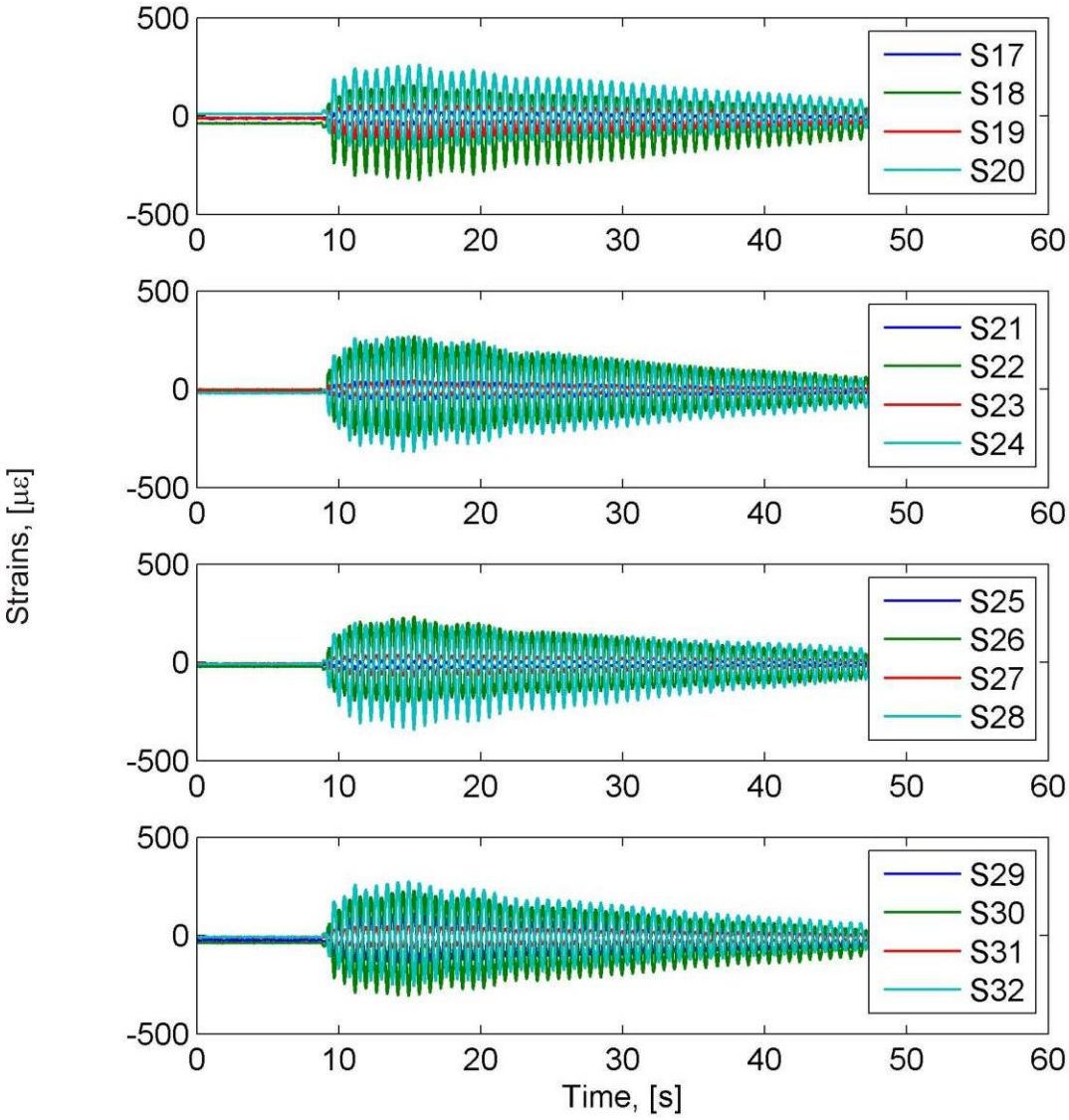

Figure C.15: Strain time histories at the middle of the portal frame legs for the full scale OLE4 excitation

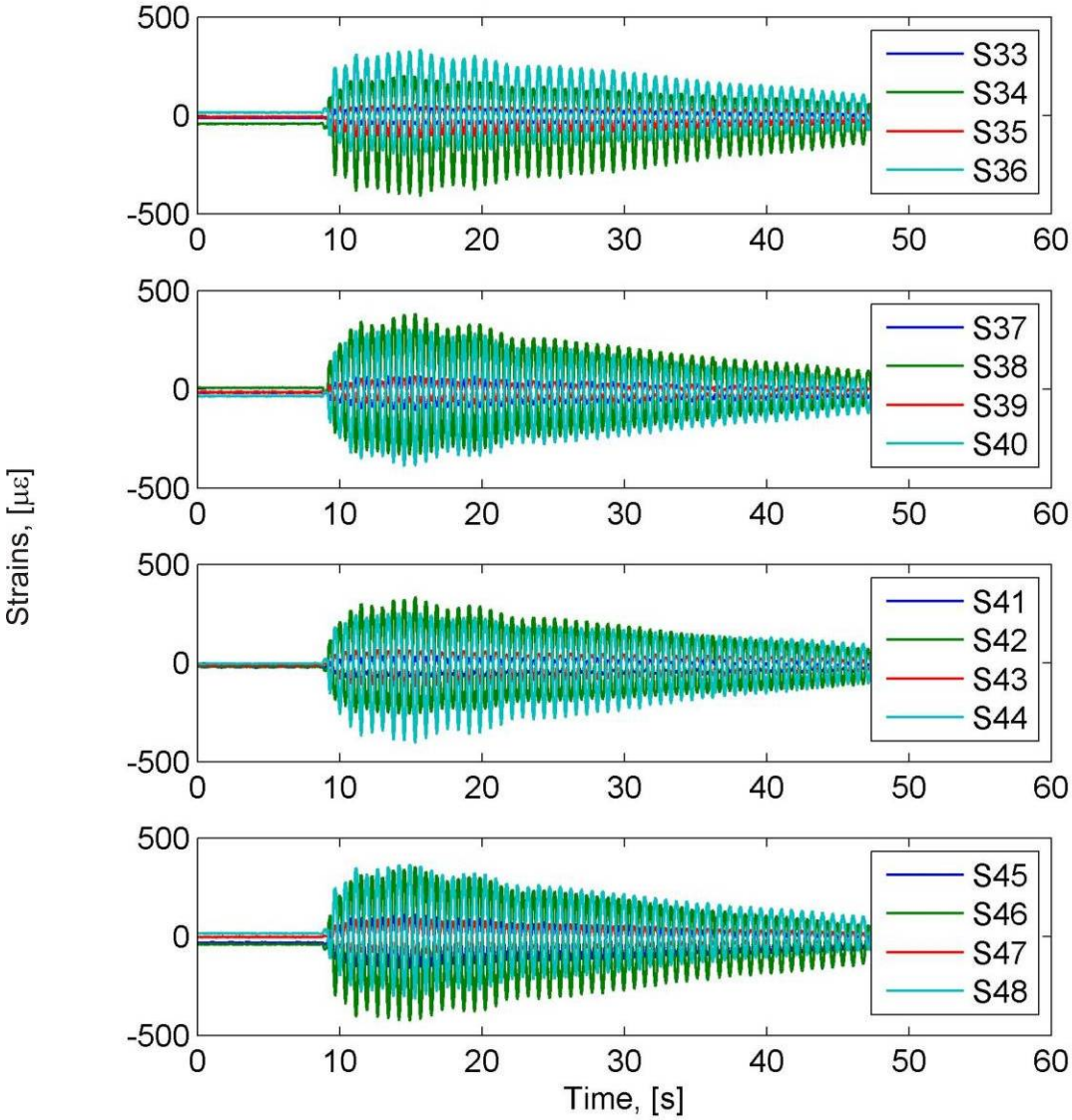

Figure C.16: Strain time histories at the top of the portal frame legs for the full scale OLE4 excitation

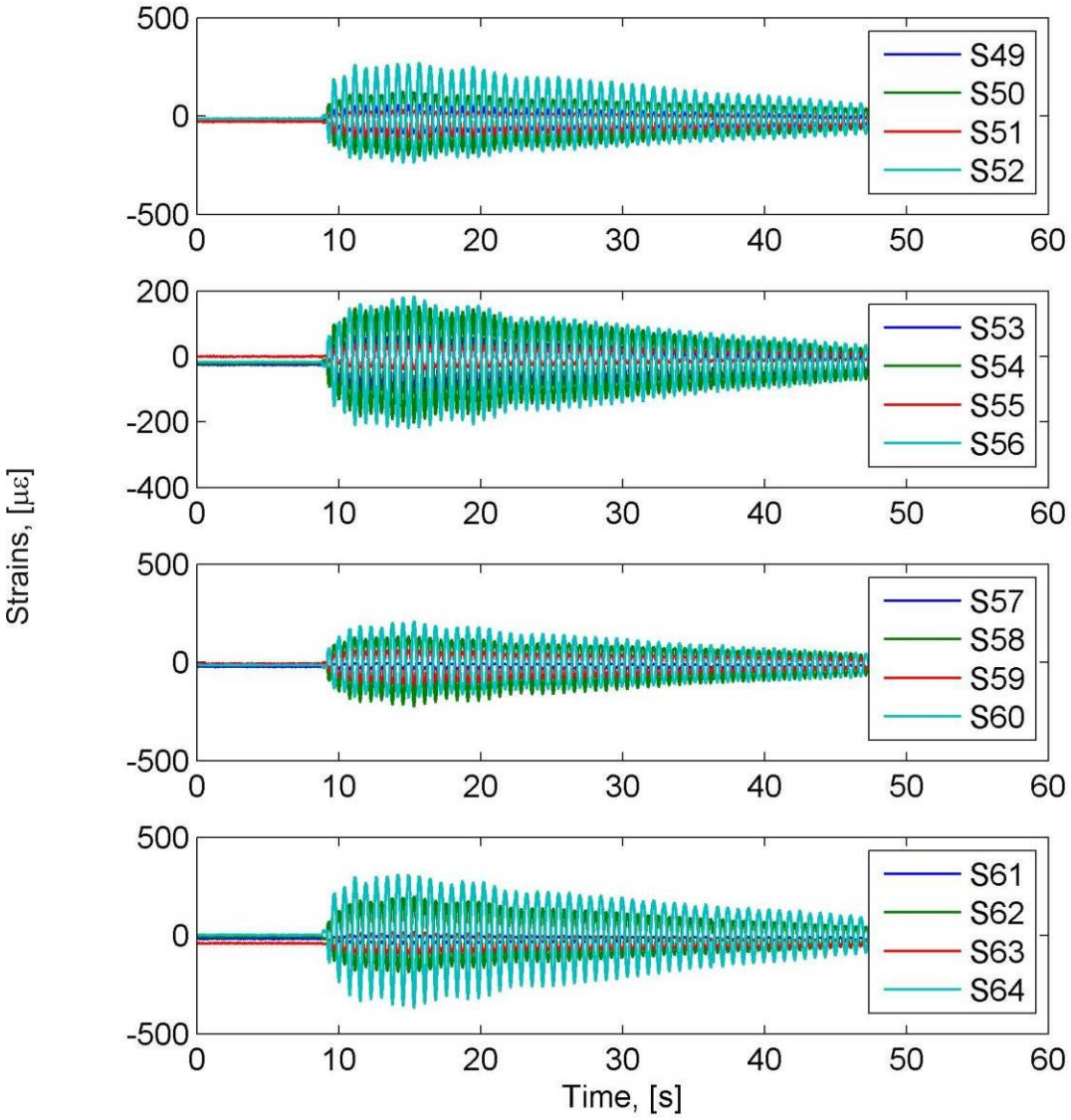

Figure C.17: Strain time histories in the portal beam for the full scale OLE4 excitation

C.3.2 Full Scale OLE6 Excitation

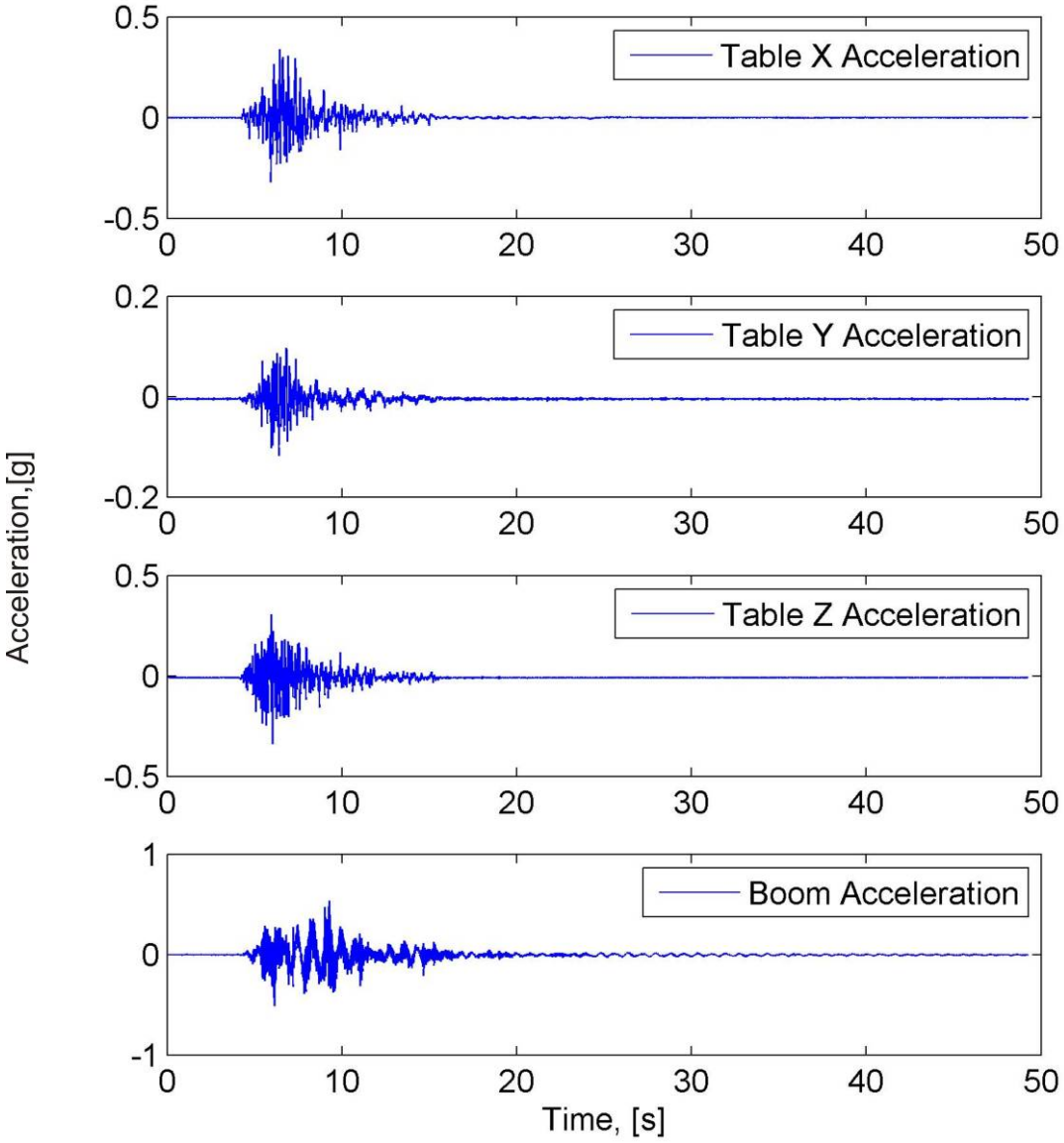

Figure C.18: Acceleration time histories for the full scale OLE6 excitation

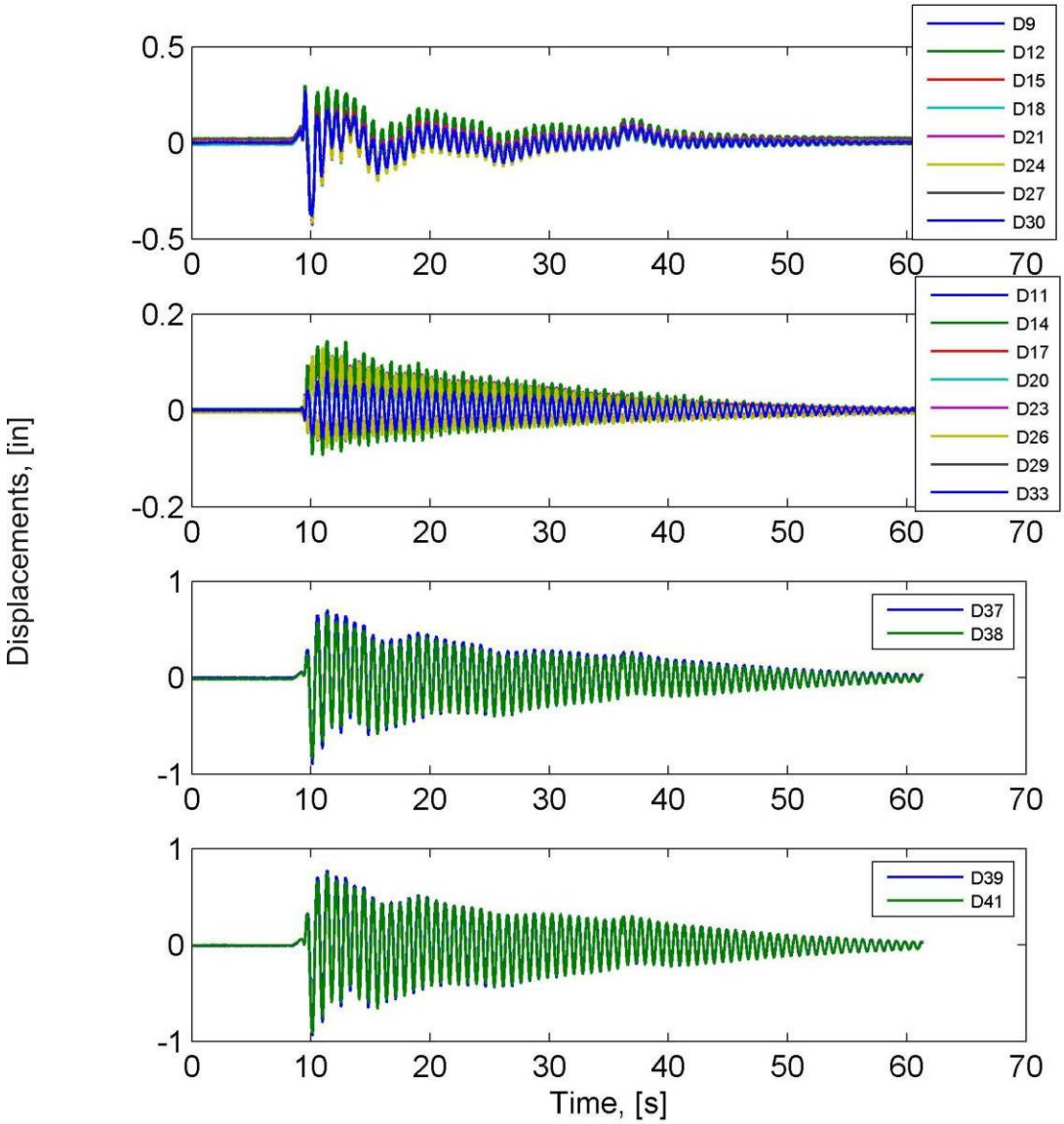

Figure C.19: Displacement time histories for the full scale OLE6 excitation

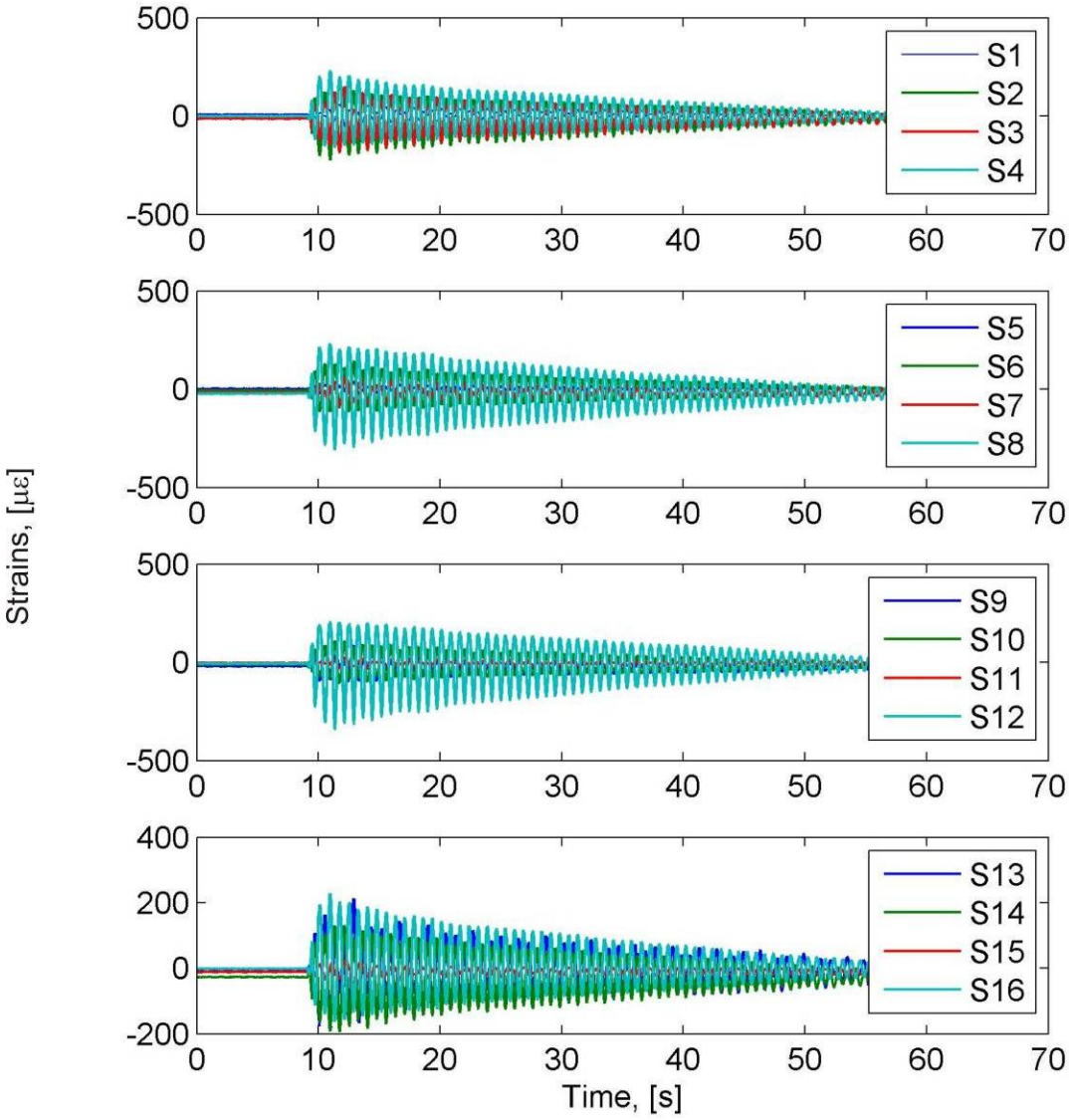

Figure C.20: Strain time histories at the bottom of the portal frame legs for the full scale OLE6 excitation

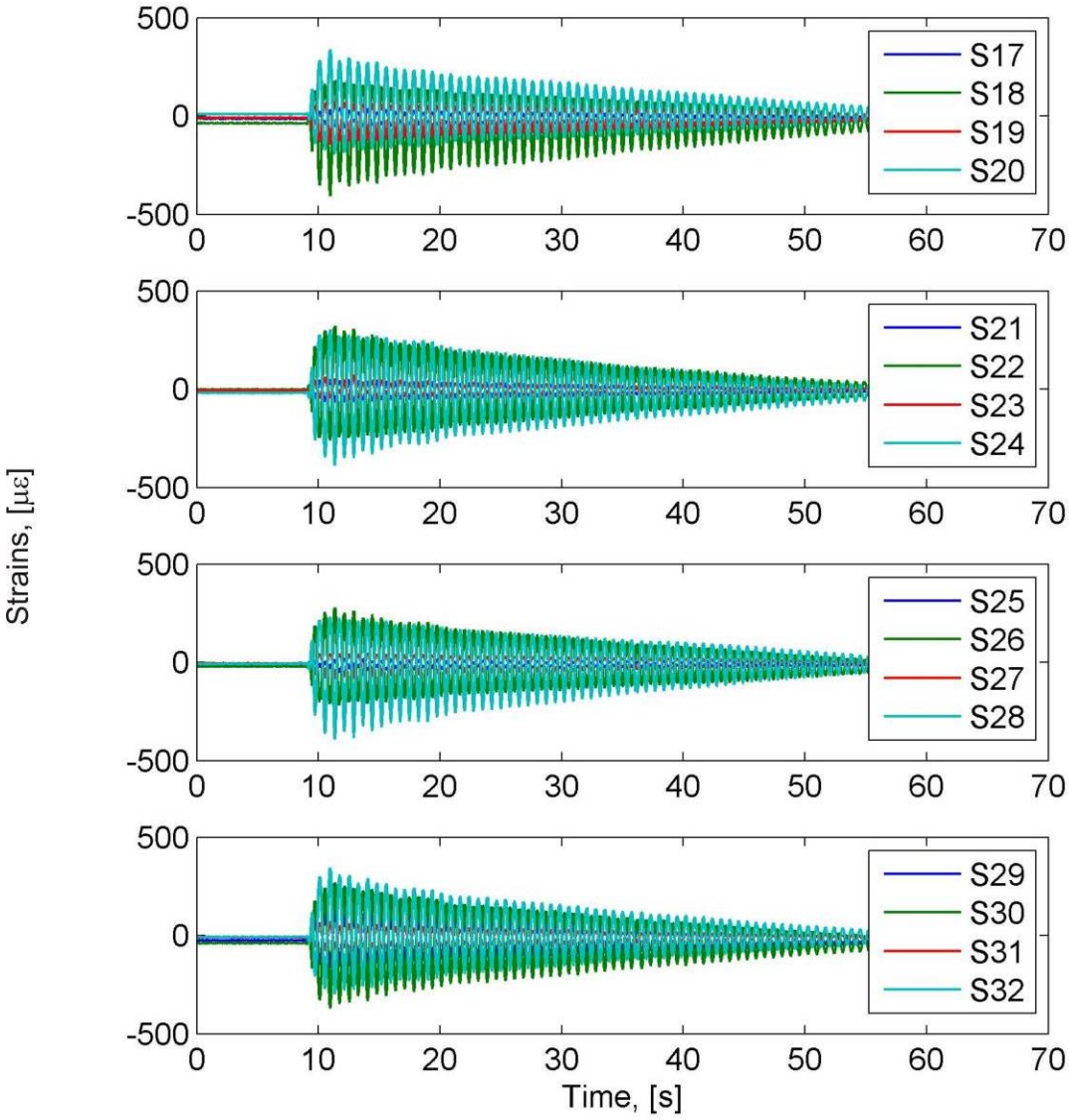

Figure C.21: Strain time histories at the middle of the portal frame legs for the full scale OLE6 excitation

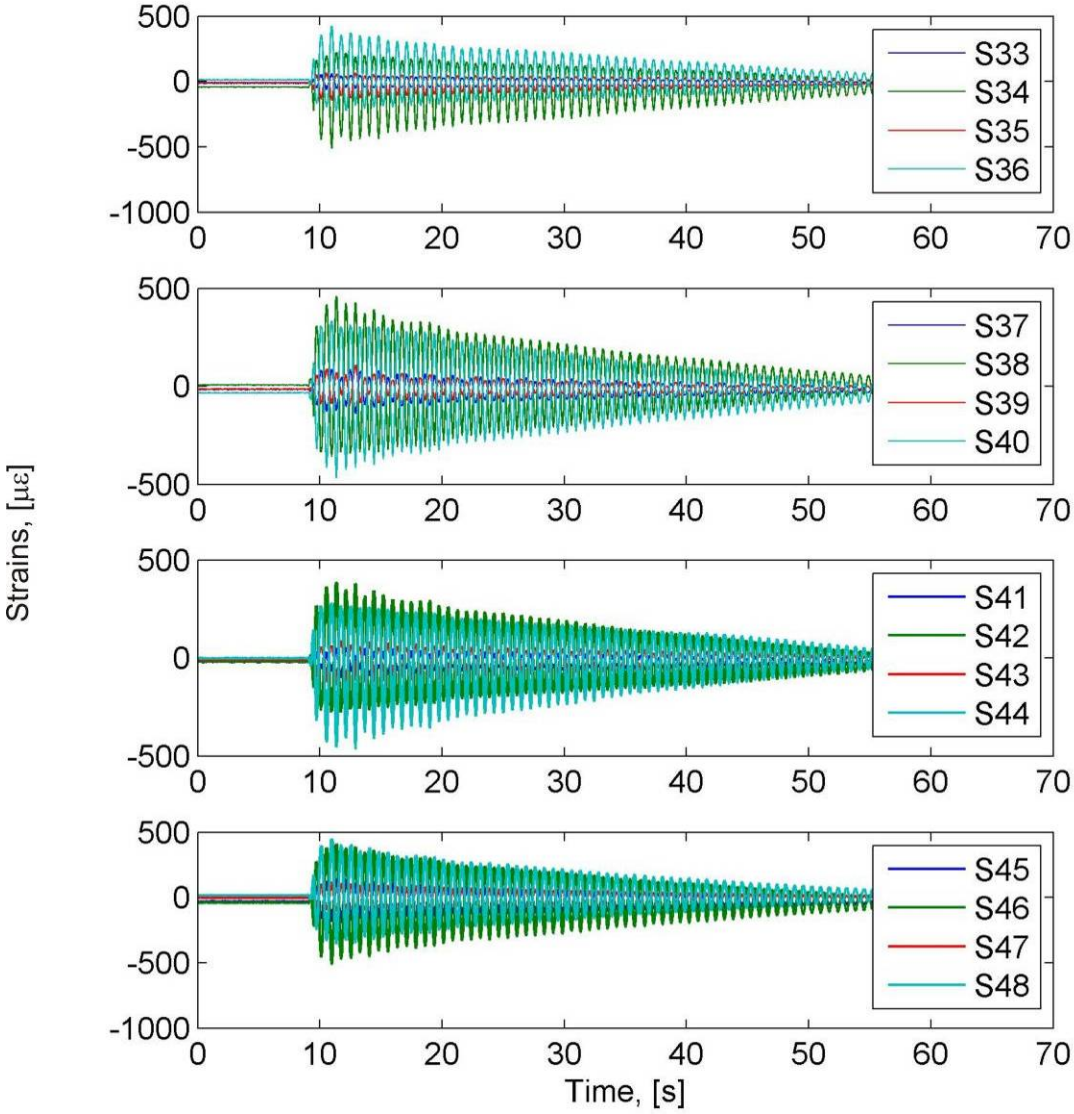

Figure C.22: Strain Time Histories at the top of the portal frame legs for the full scale OLE6 excitation

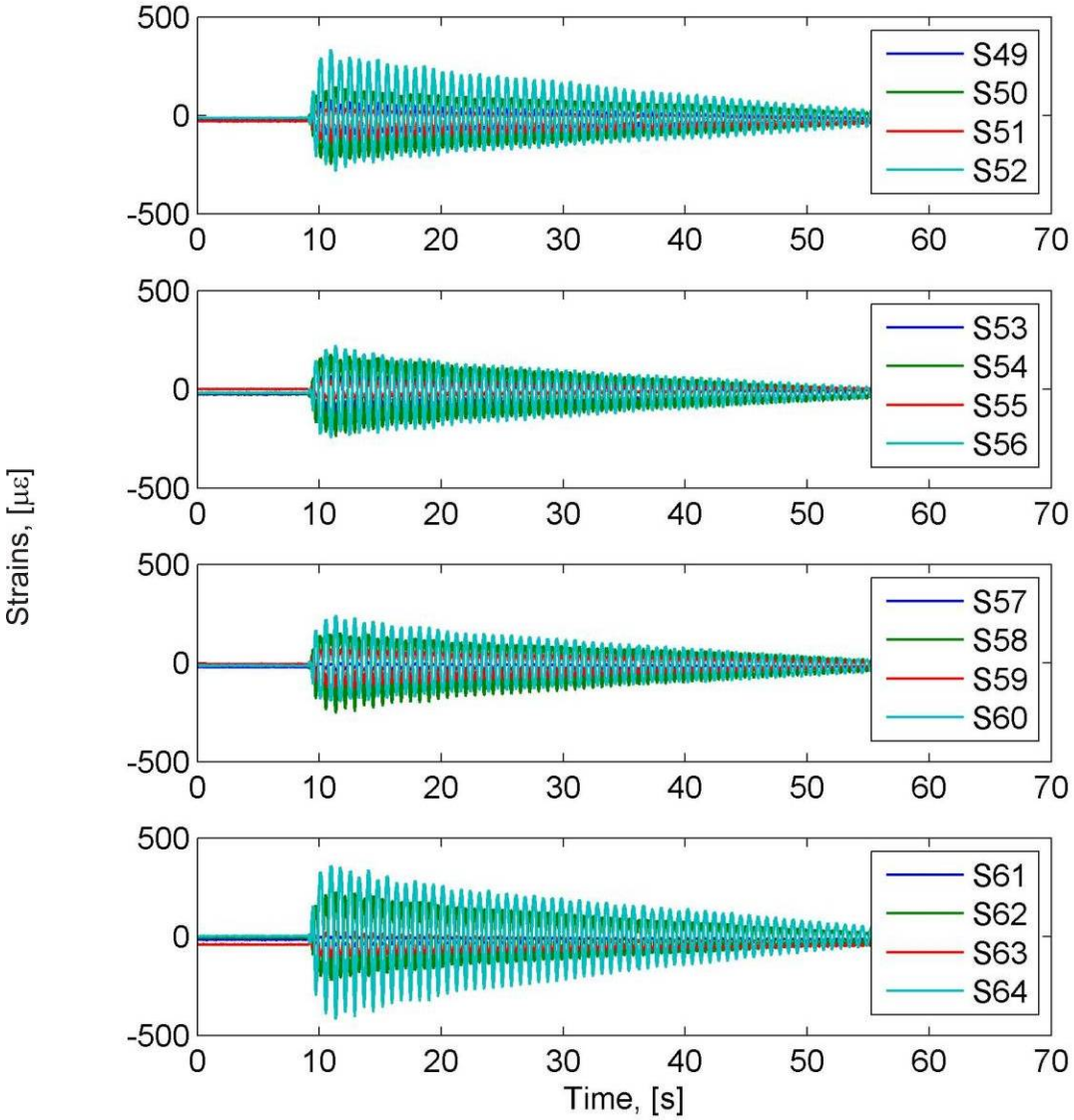

Figure C.23: Strain time histories in the portal beam for the full scale OLE6 excitation

C.3.3 70% Loma Prieta Excitation

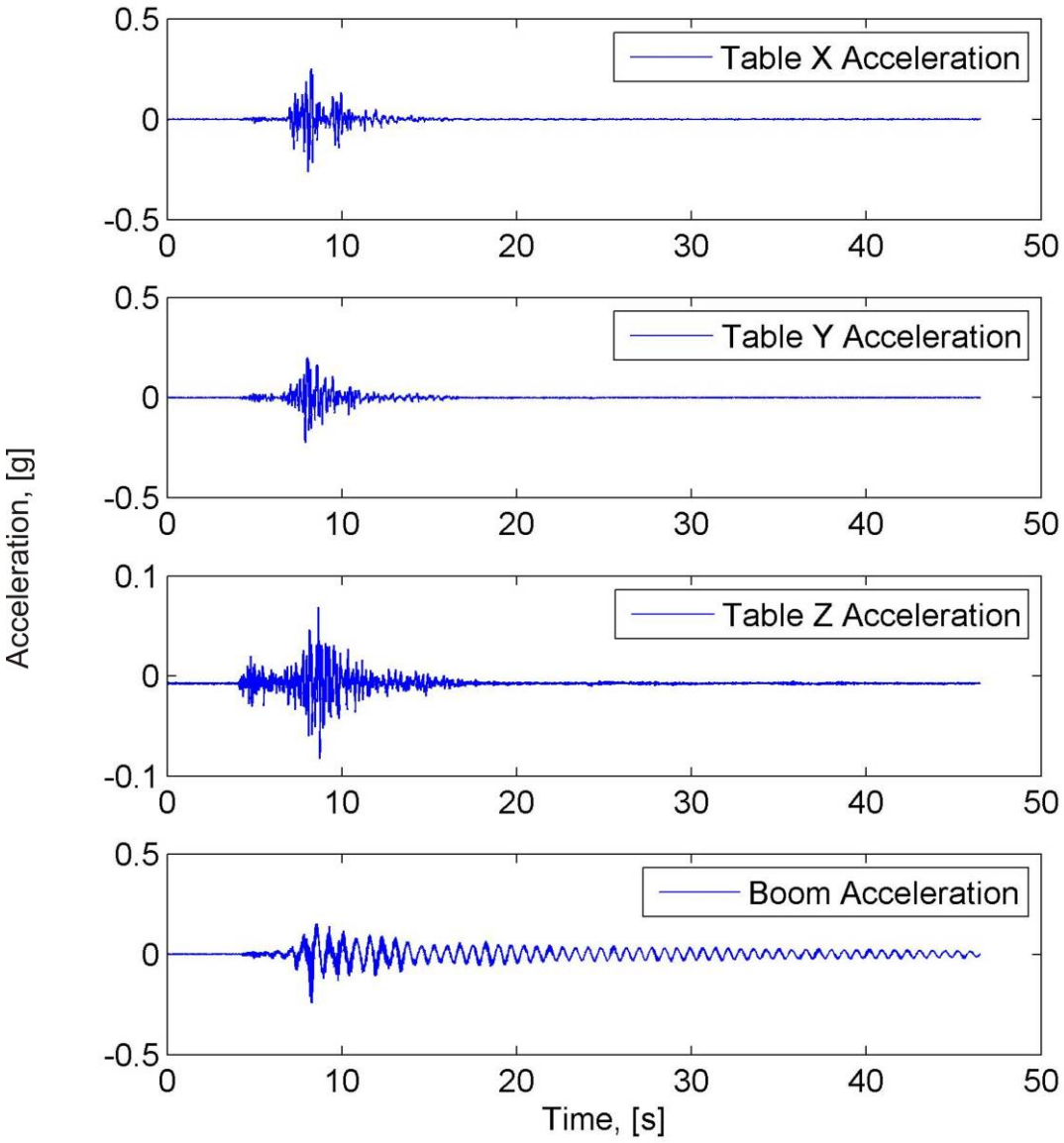

Figure C.24: Acceleration time histories for the 70% Loma Prieta excitation

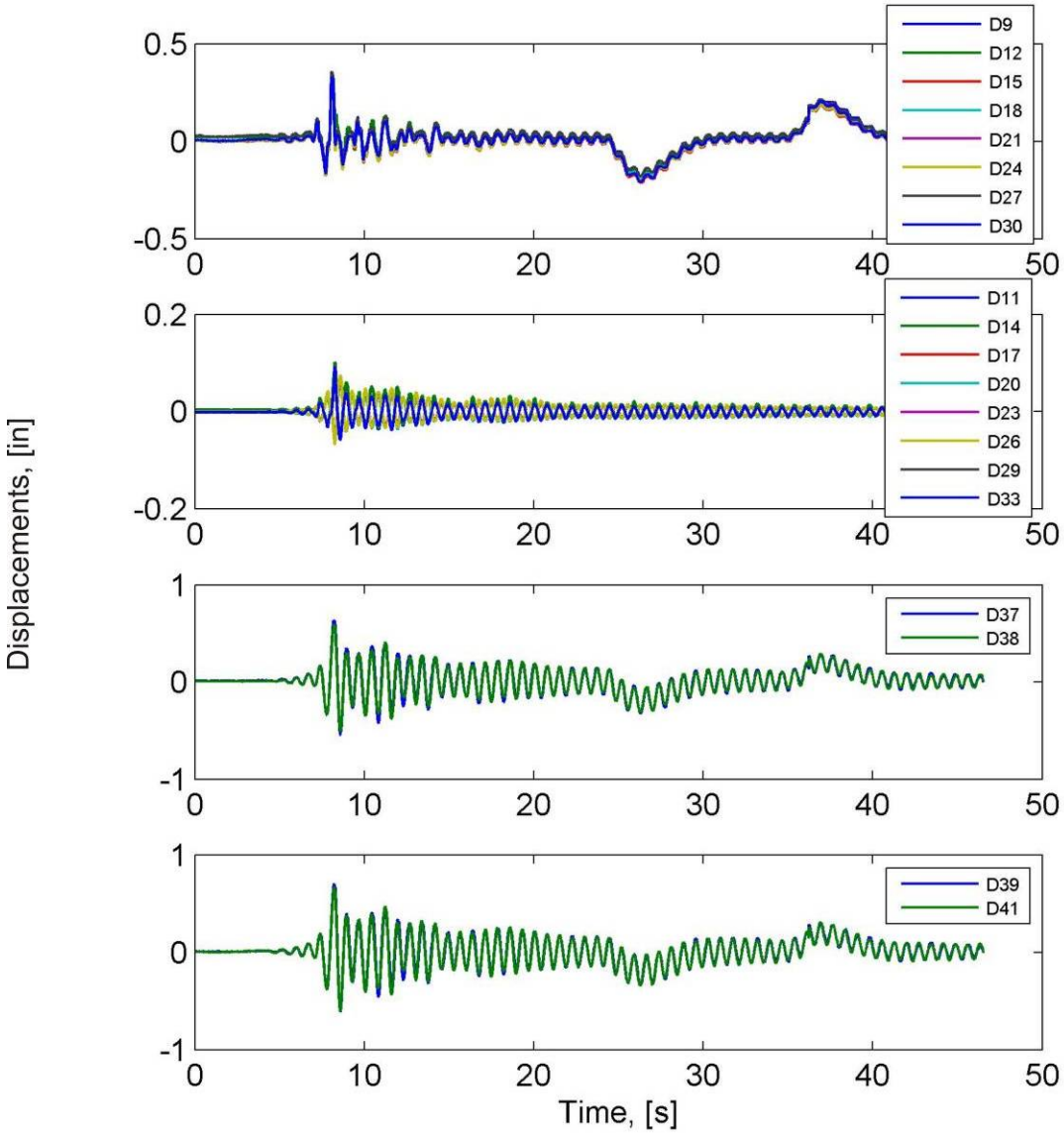

Figure C.25: Displacement time histories for the 70% Loma Prieta excitation

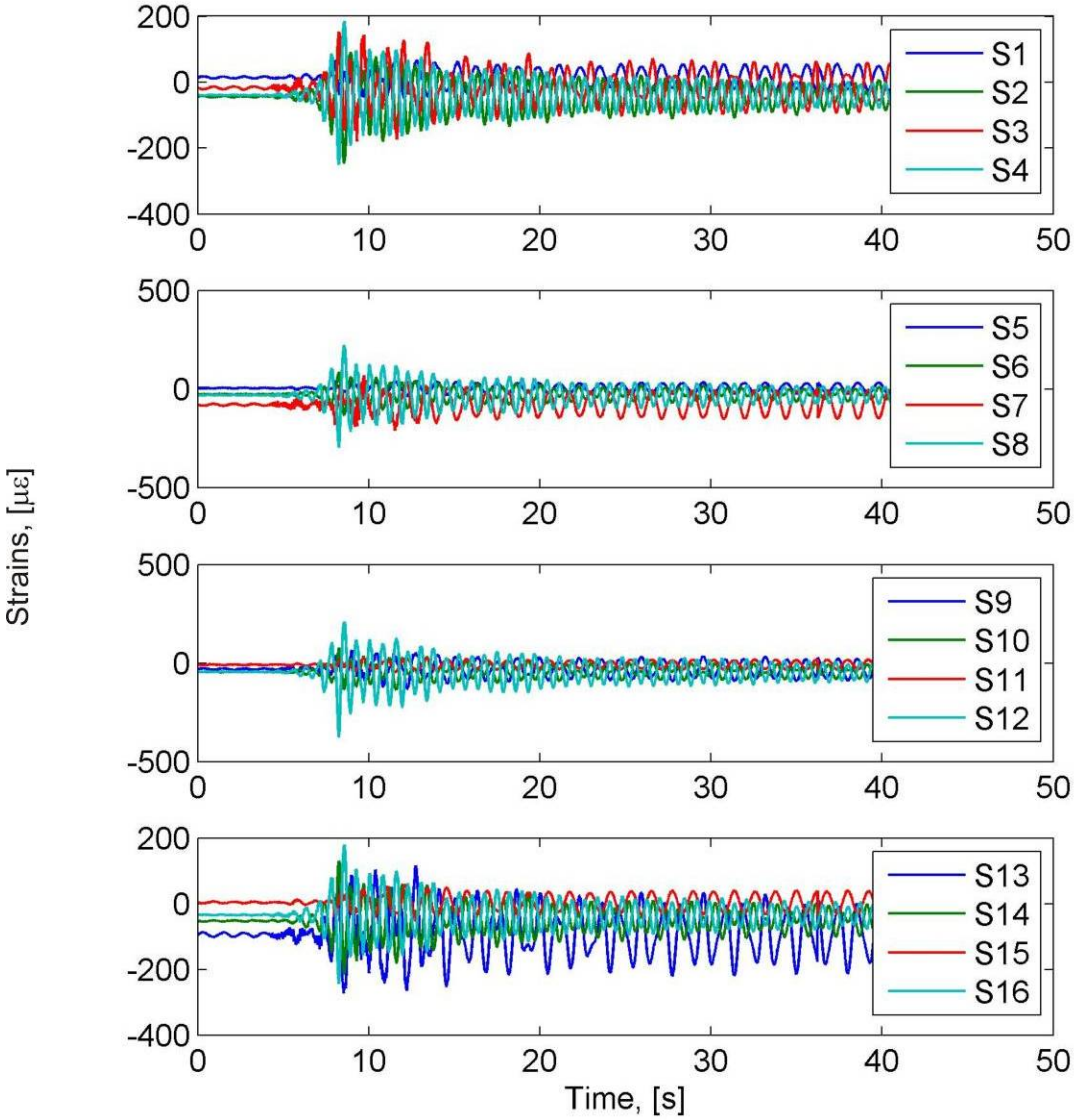

Figure C.26: Strain time histories at the bottom of the portal frame legs for the 70% Loma Prieta excitation

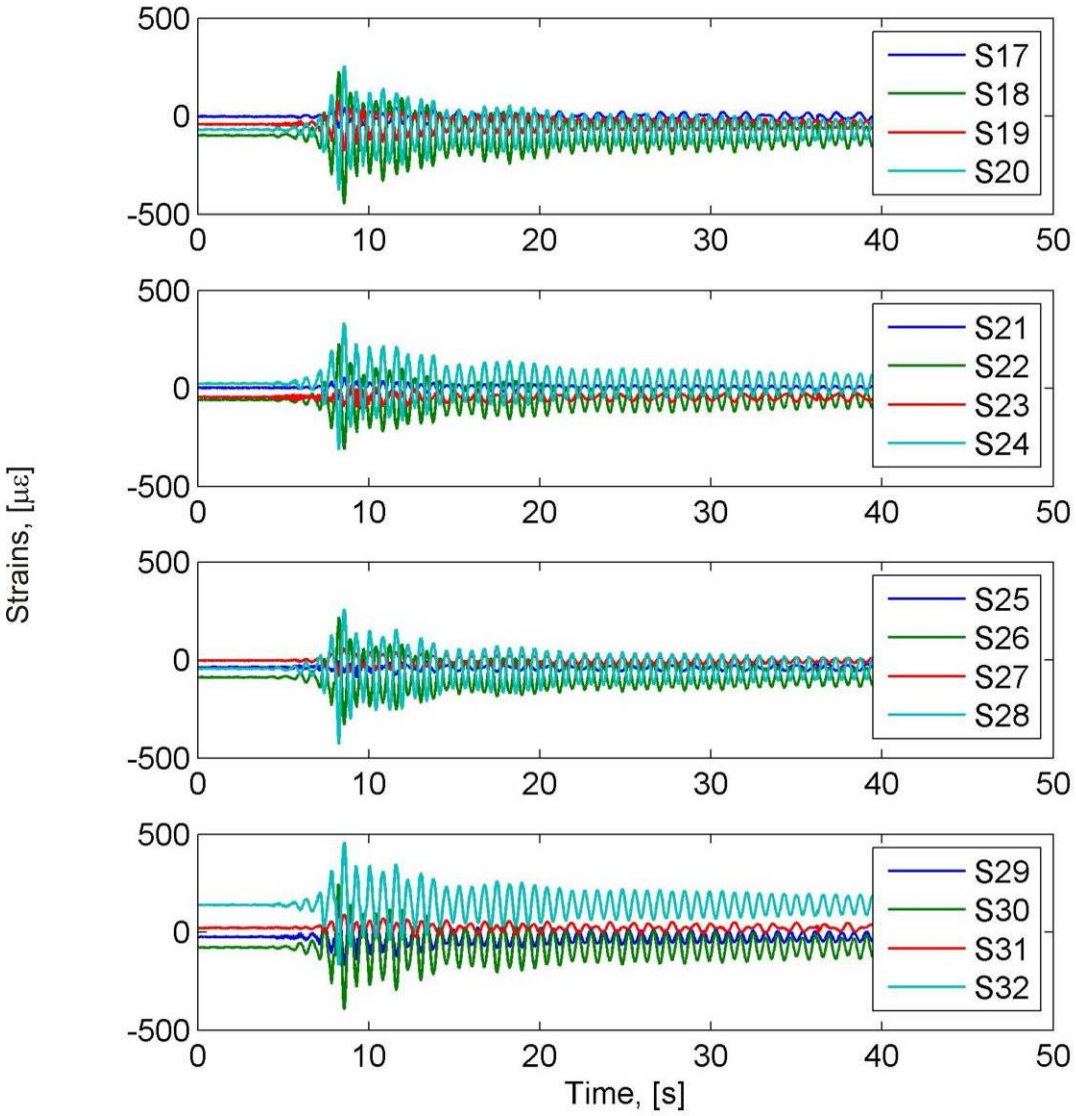

Figure C.27: Strain time histories at the middle of the portal frame legs for the 70% Loma Prieta excitation

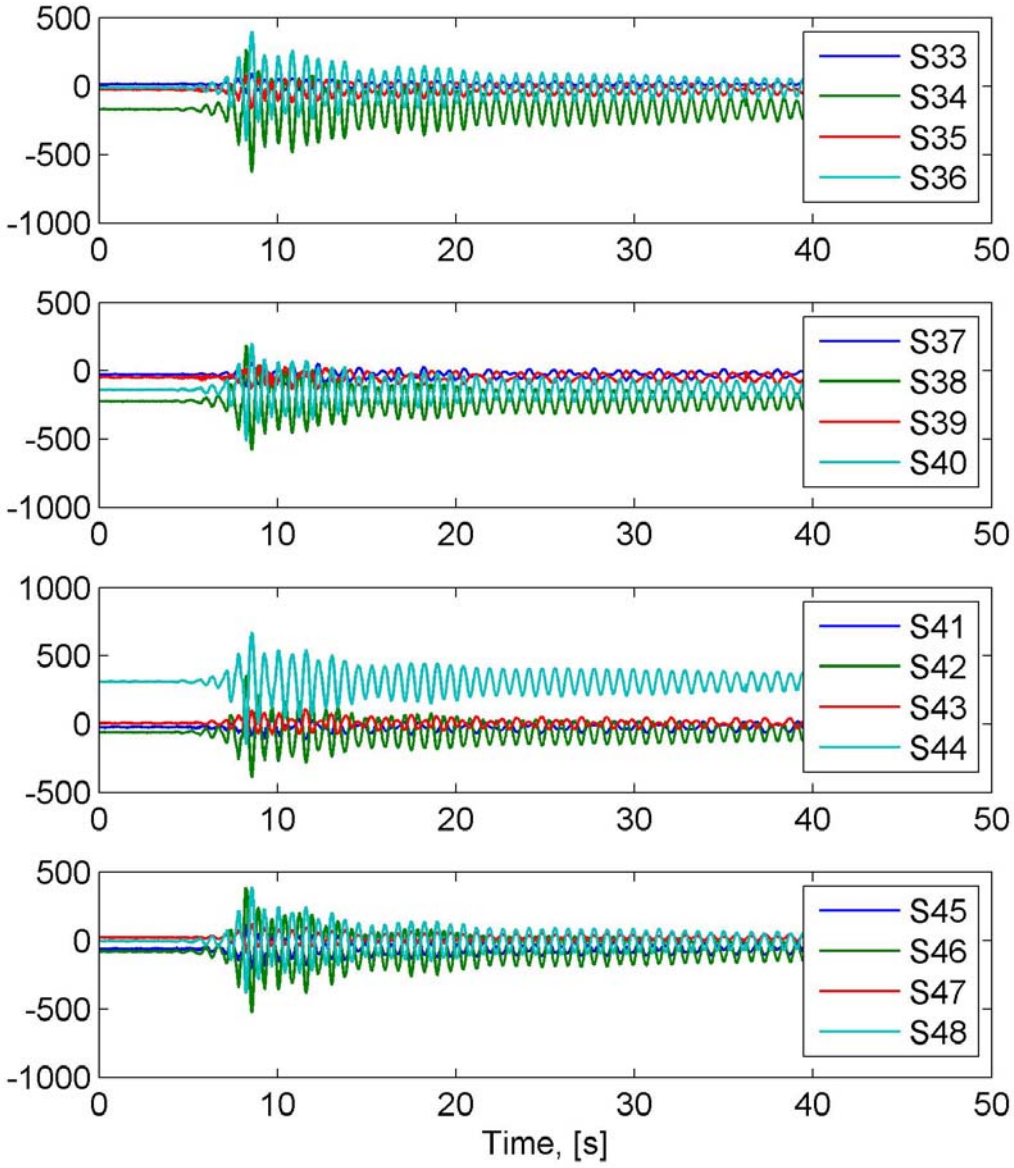

Figure C.28: Strain time histories at the top of the portal frame legs for the 70% Loma Prieta excitation

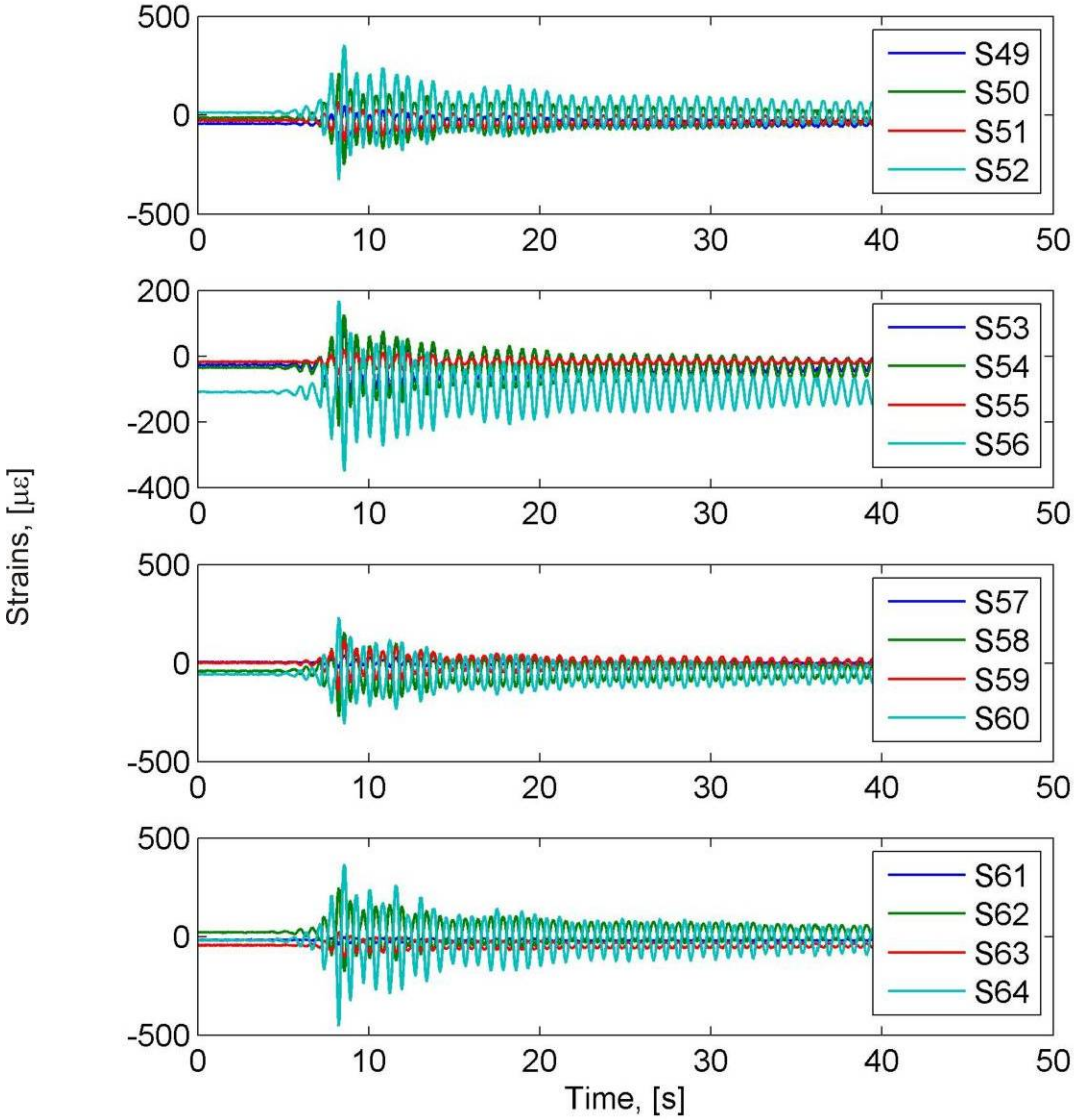

Figure C.29: Strain time histories in the portal beam for the 70% Loma Prieta excitation

C.3.4 55% CLE4 Excitation

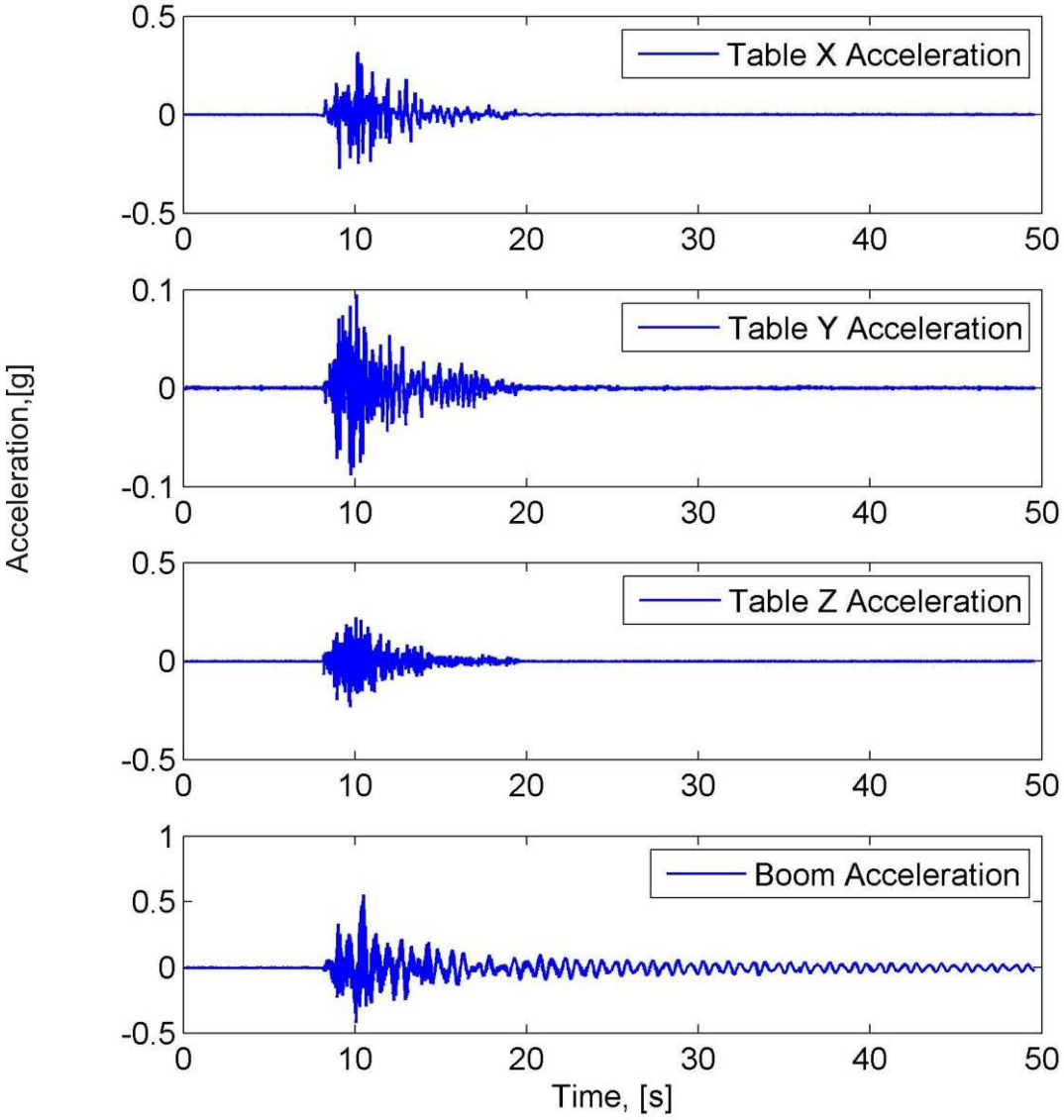

Figure C.30: Acceleration time histories for the 55% CLE4 excitation

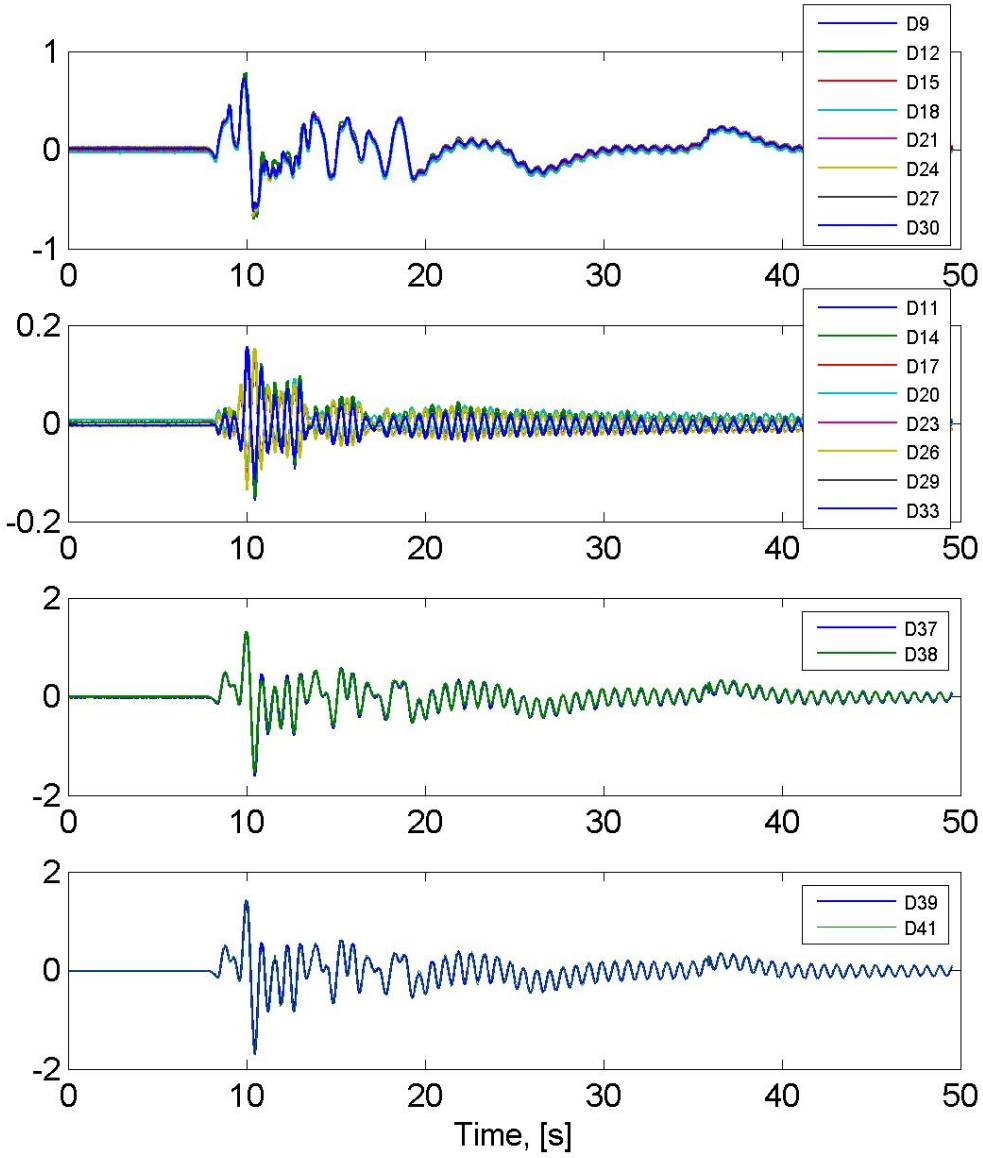

Figure C.31: Displacement time histories for the 55% CLE4 excitation

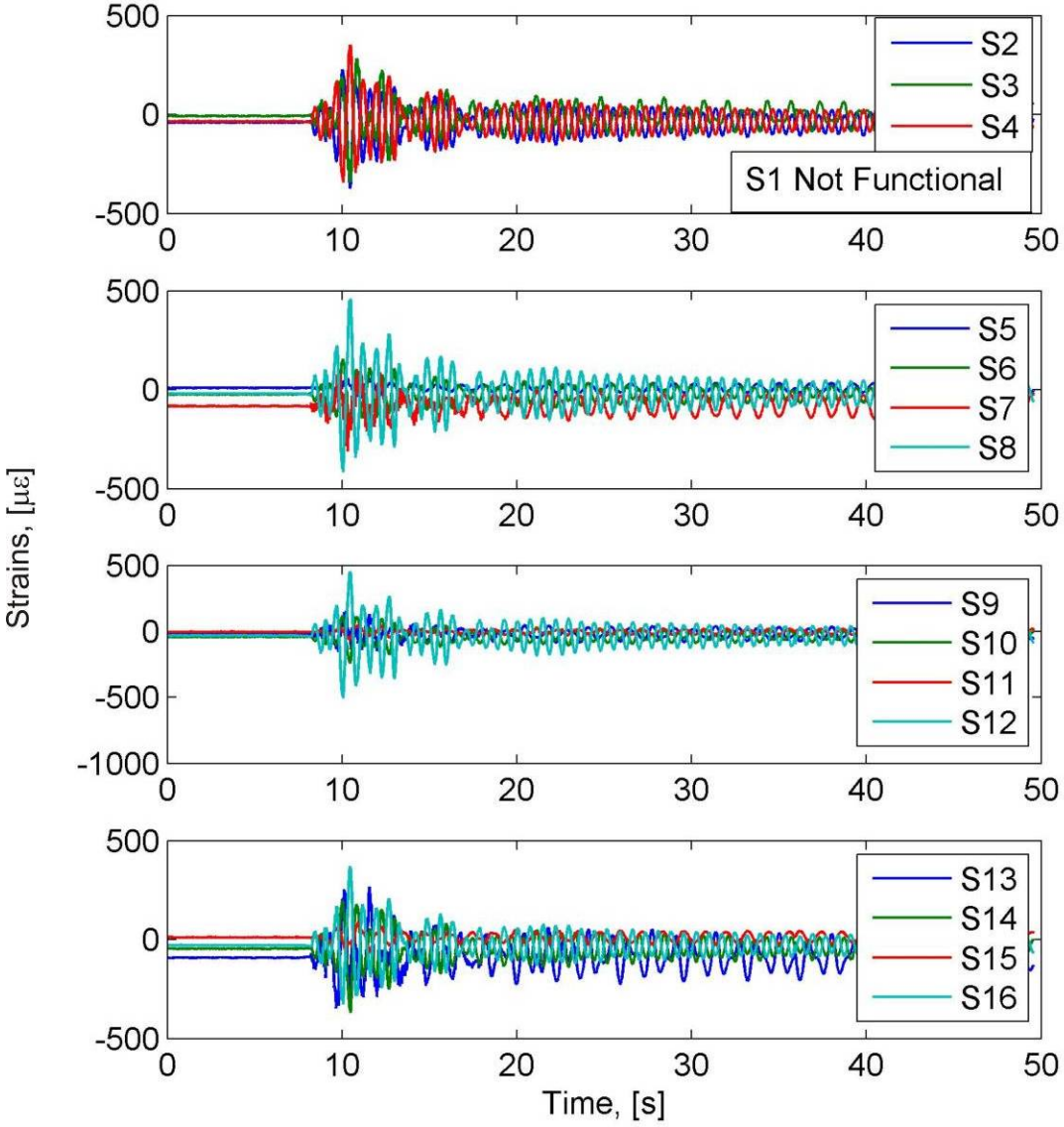

Figure C.32: Strain time histories at the bottom of the portal frame legs for the 55% of CLE4 excitation

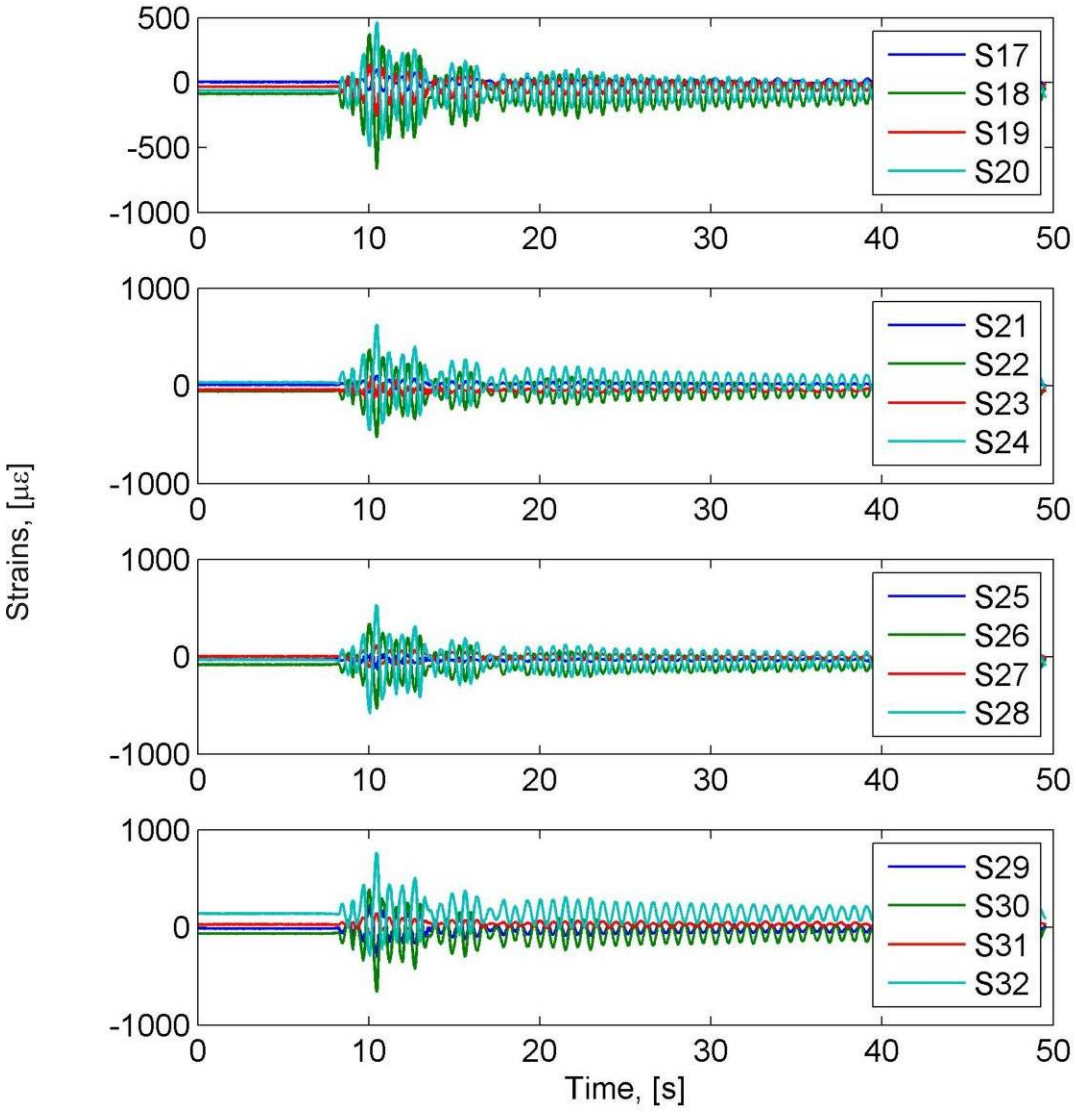

Figure C.33: Strain time histories at the middle of the portal frame legs for the 55% of CLE4 excitation

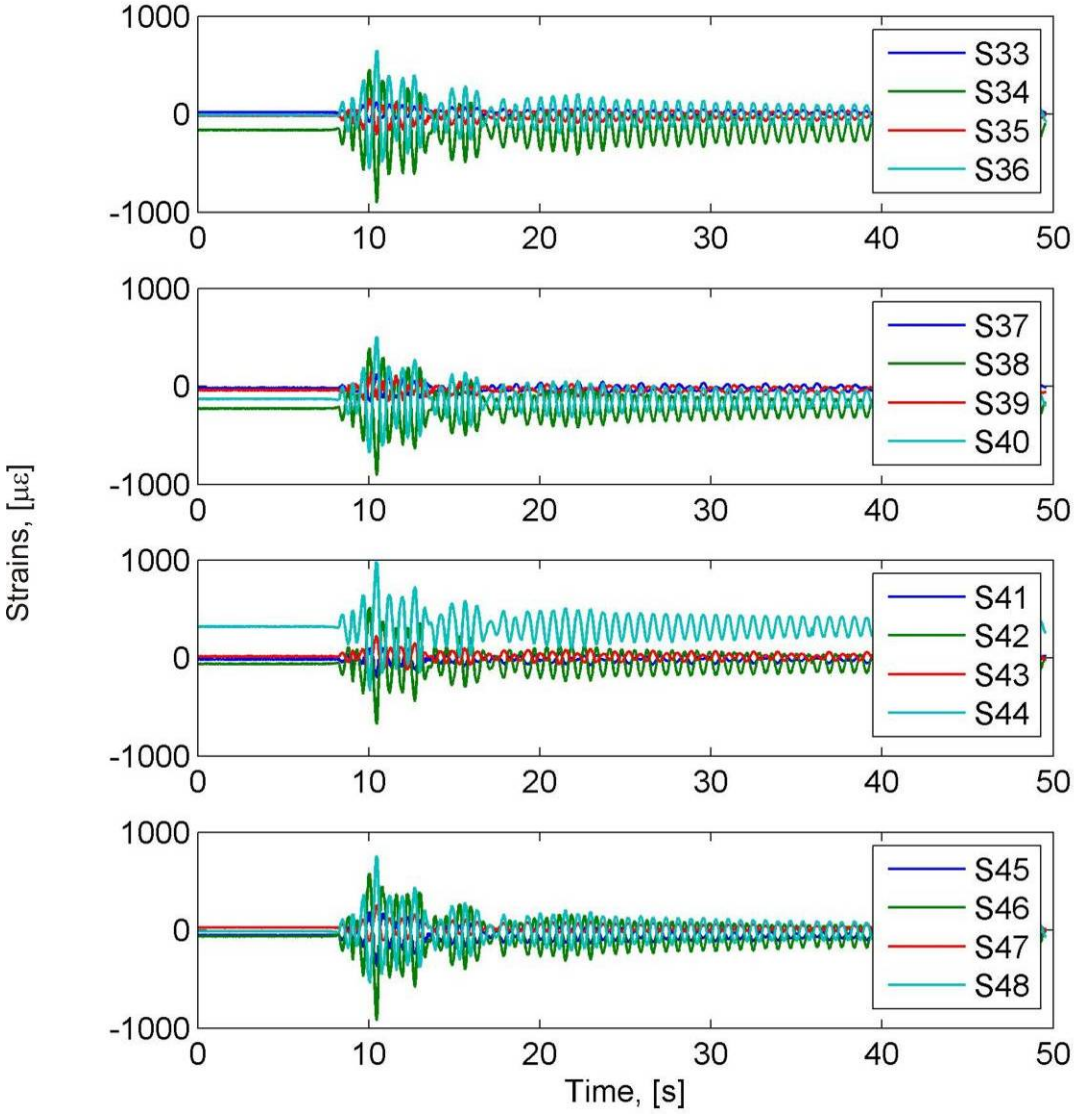

Figure C.34: Strain time histories at the top of the portal frame legs for the 55% of CLE4 excitation

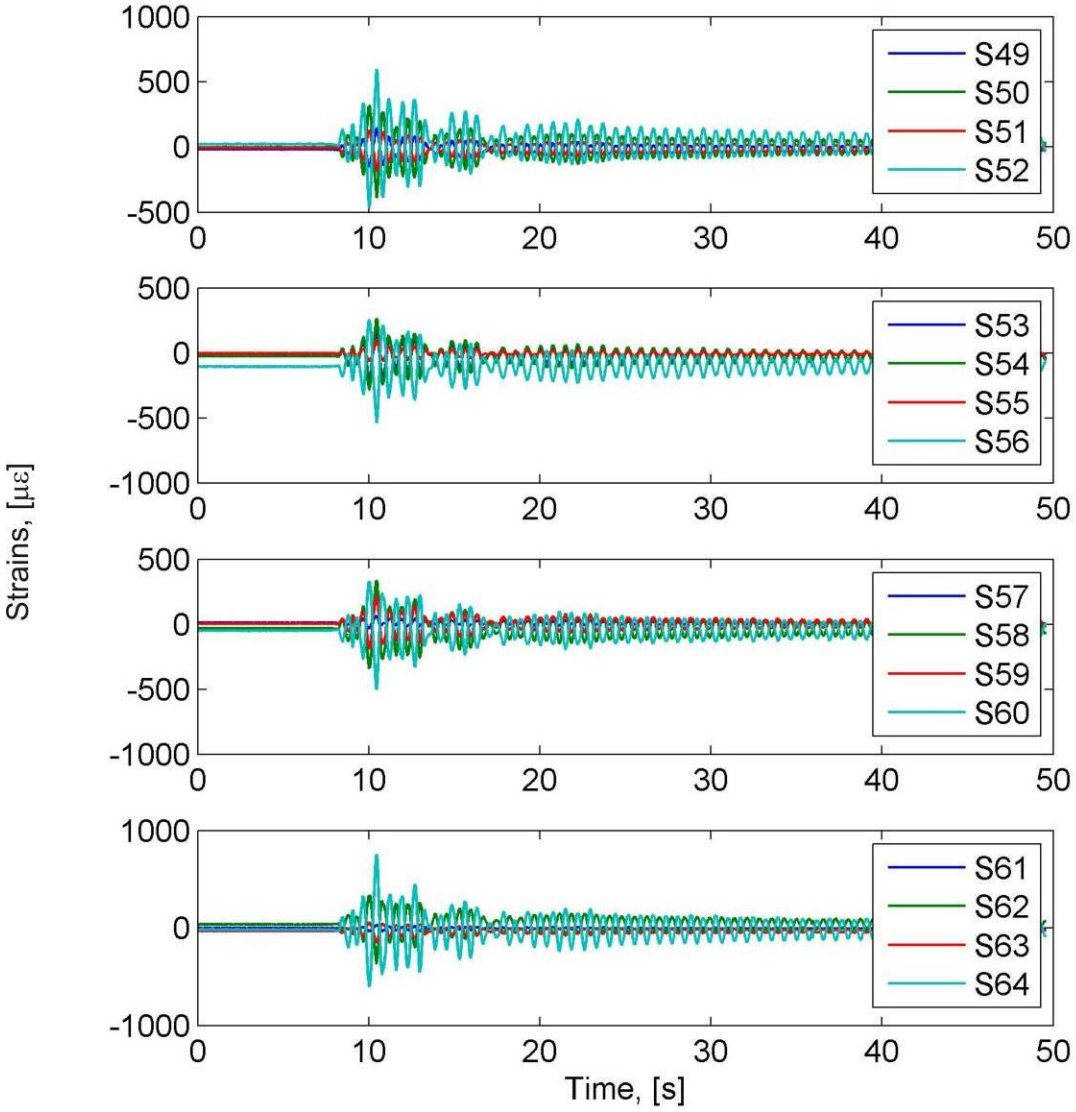

Figure C.35: Strain time histories in the portal beam for the 55% of CLE4 excitation

C.3.5 60% CLE6 Excitation

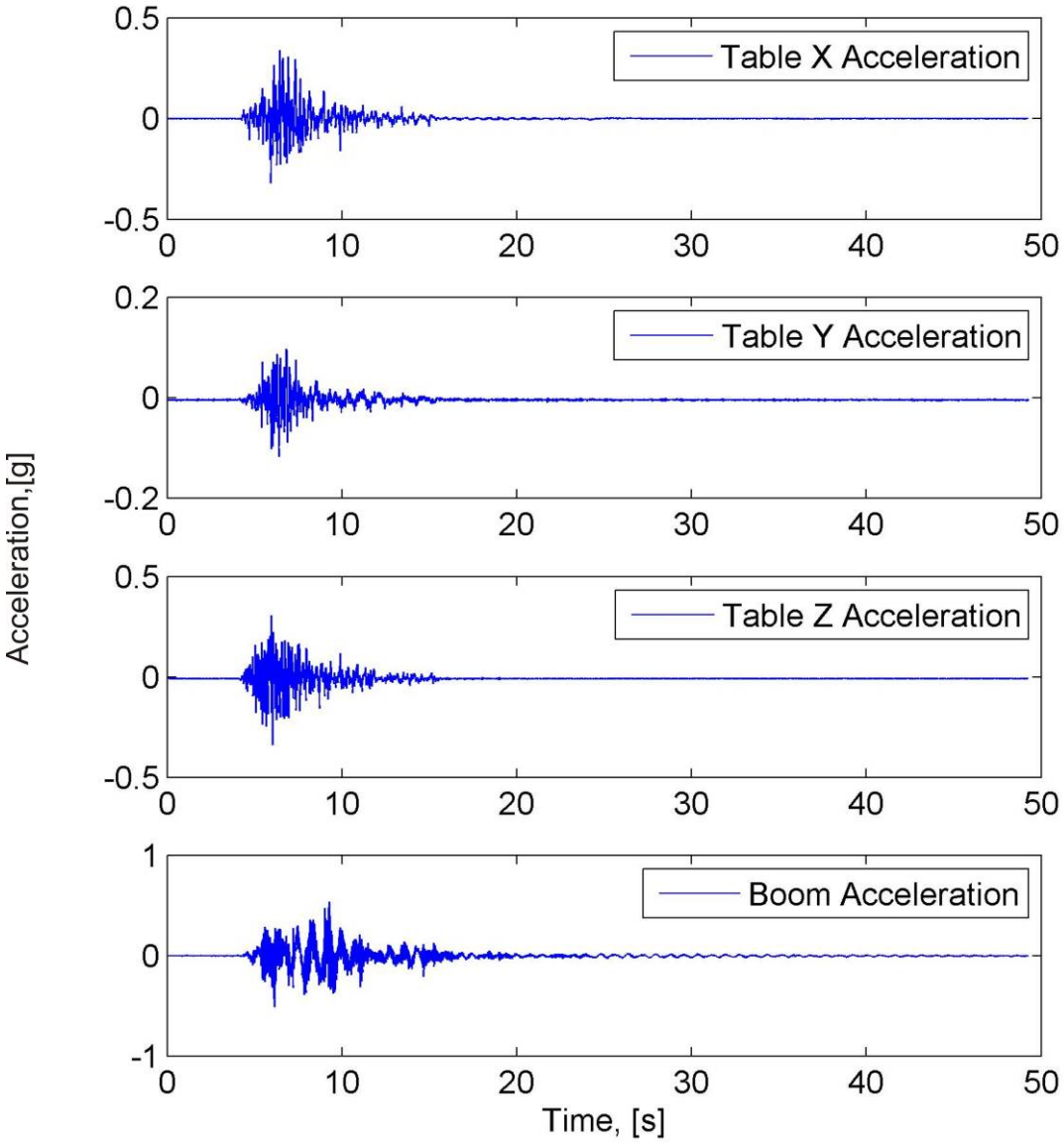

Figure C.36: Acceleration time histories for the 60% CLE6 excitation

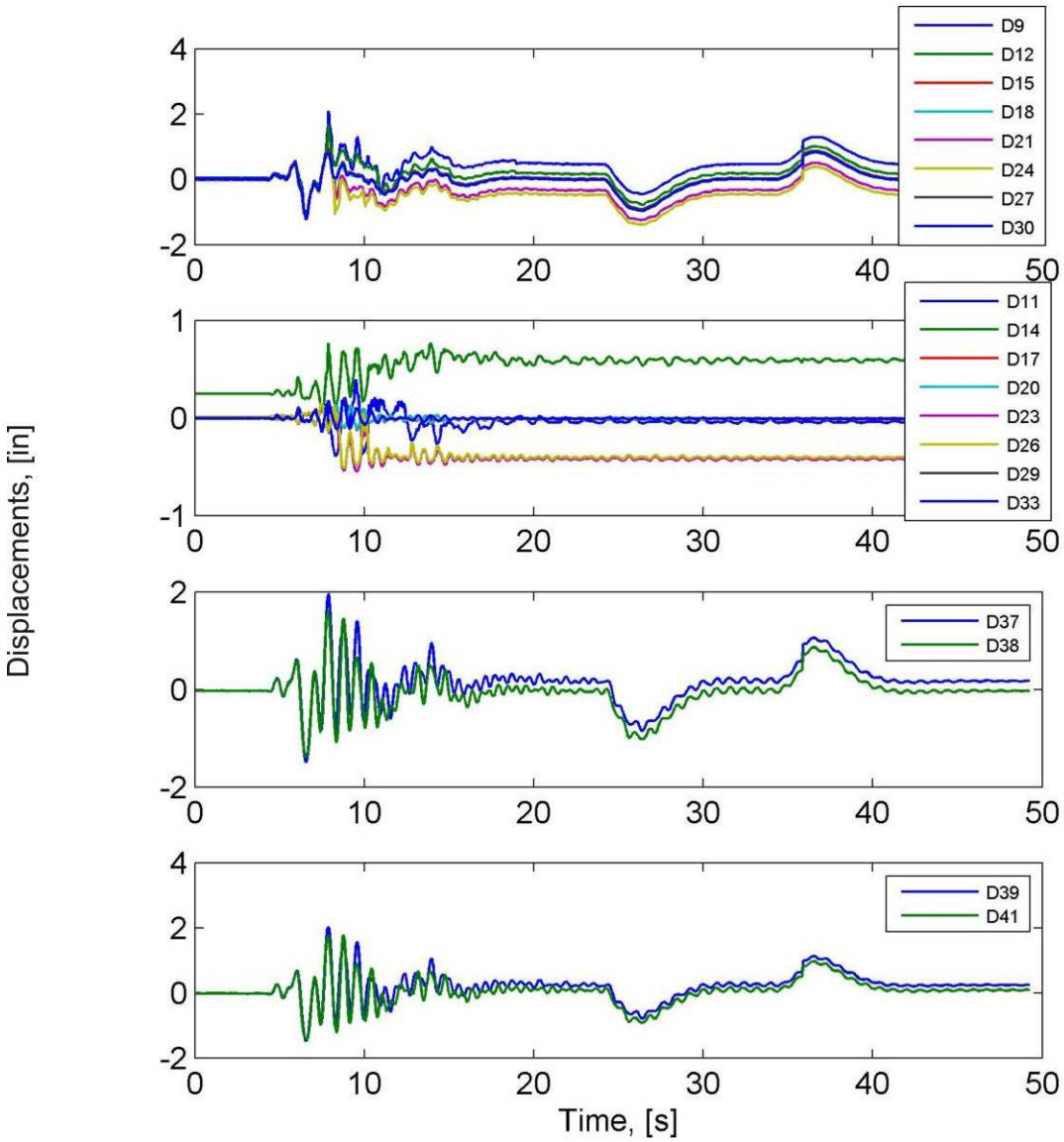

Figure C.37: Displacement time histories for the 60% CLE6 excitation

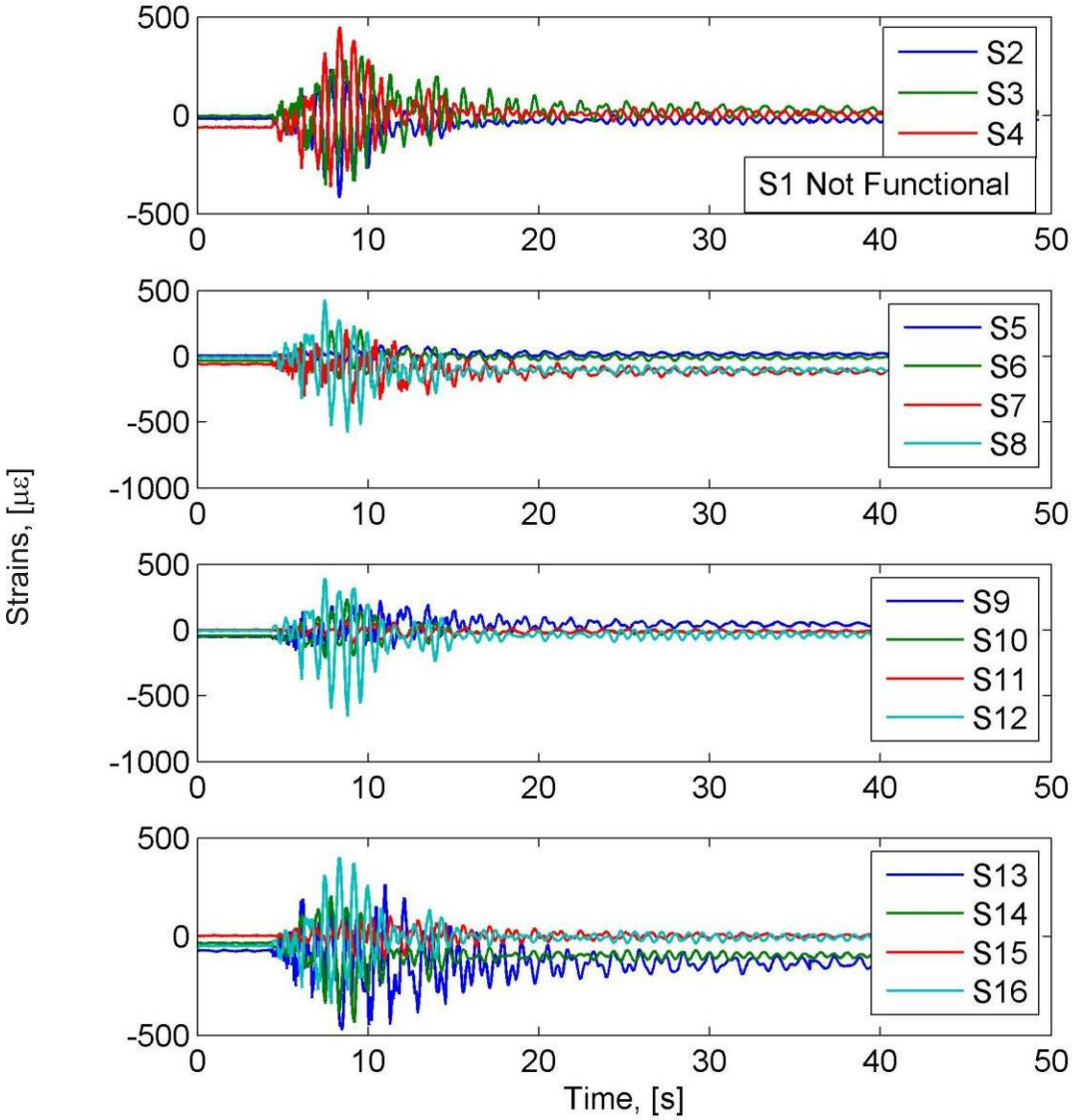

Figure C.38: Strain time histories at the bottom of the portal frame legs for the 60% of CLE6 excitation

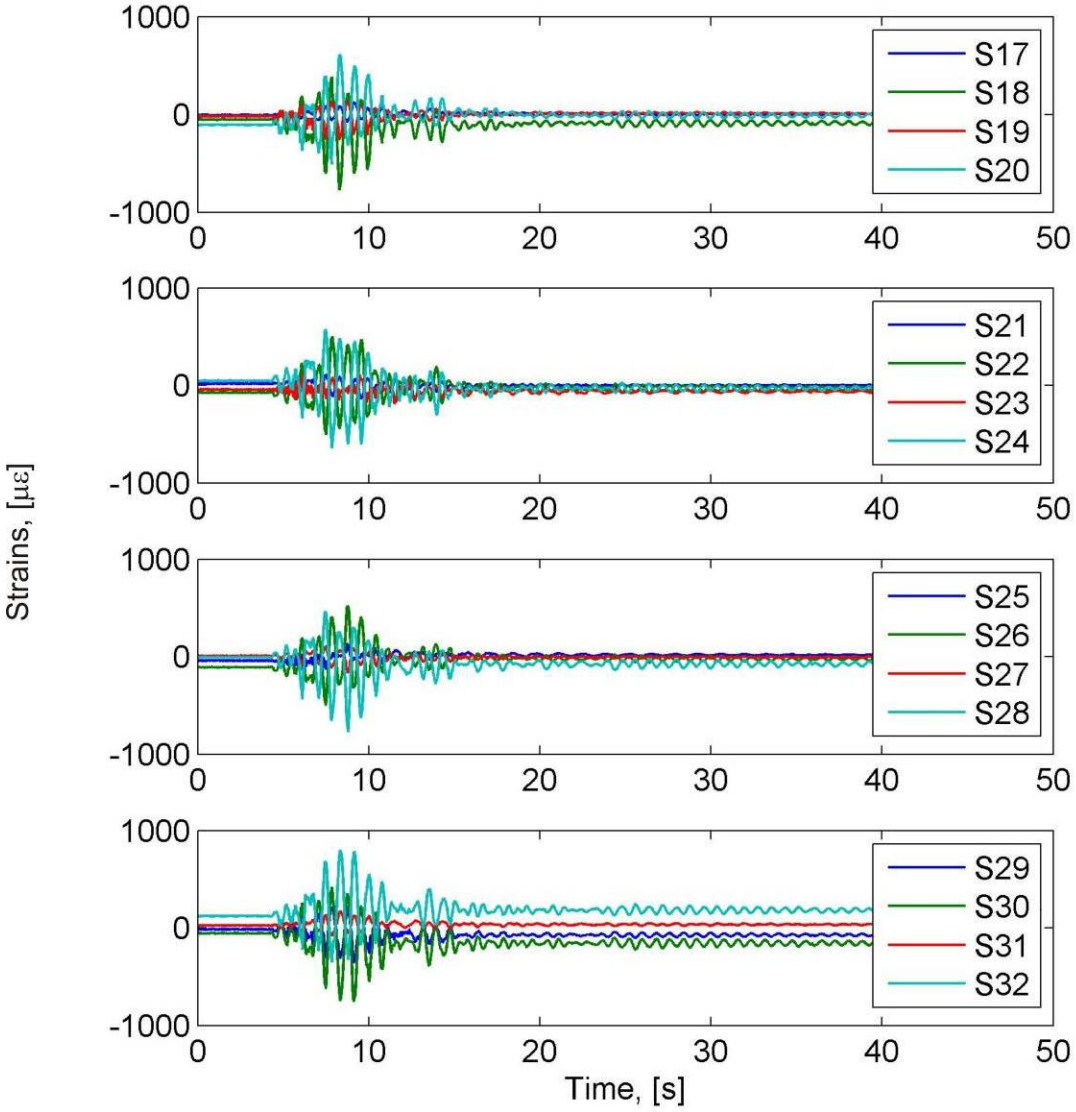

Figure C.39: Strain time histories at the middle of the portal frame legs for the 60% of CLE6 excitation

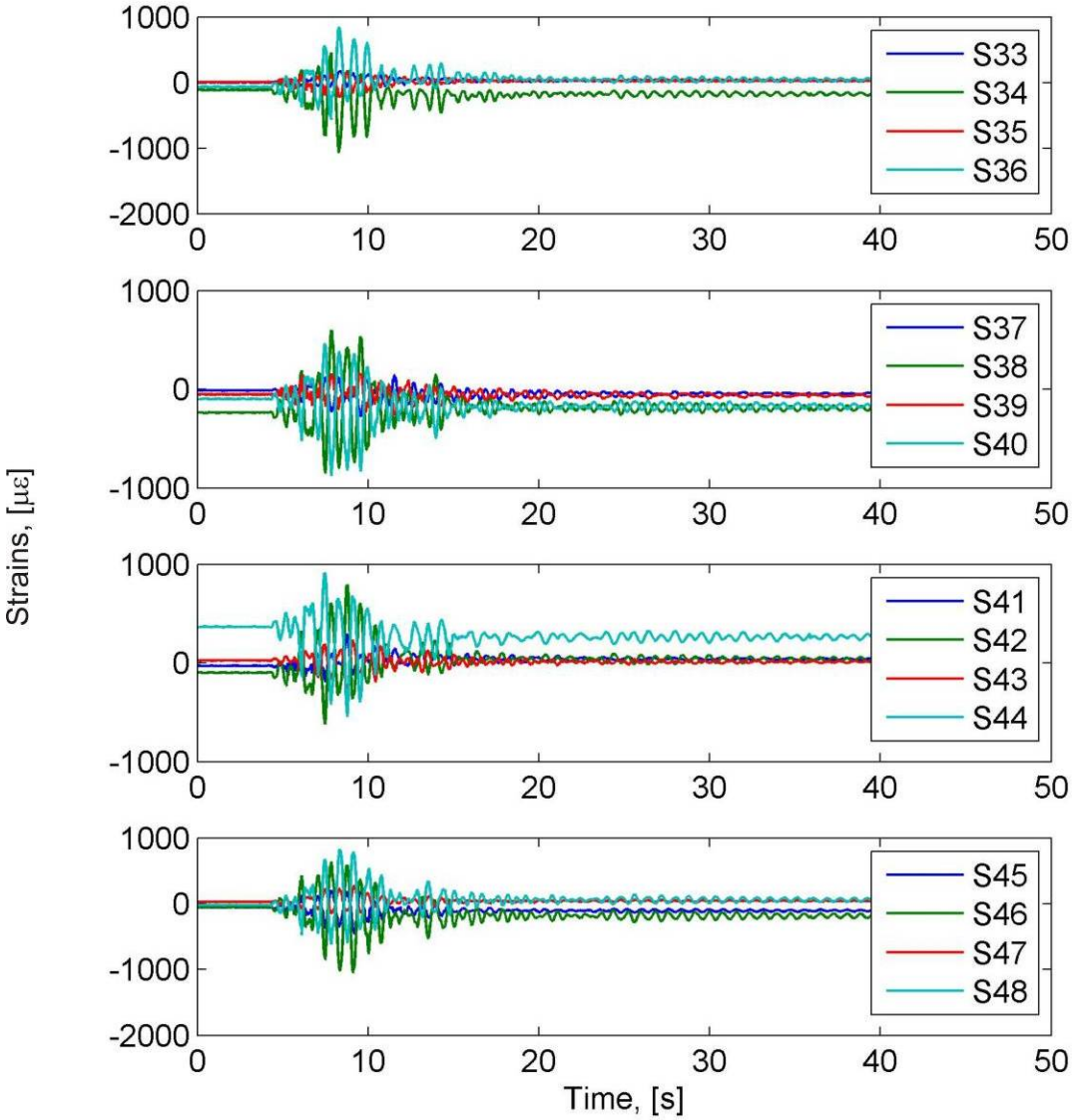

Figure C.40: Strain time histories at the top of the portal frame legs for the 60% of CLE6 excitation

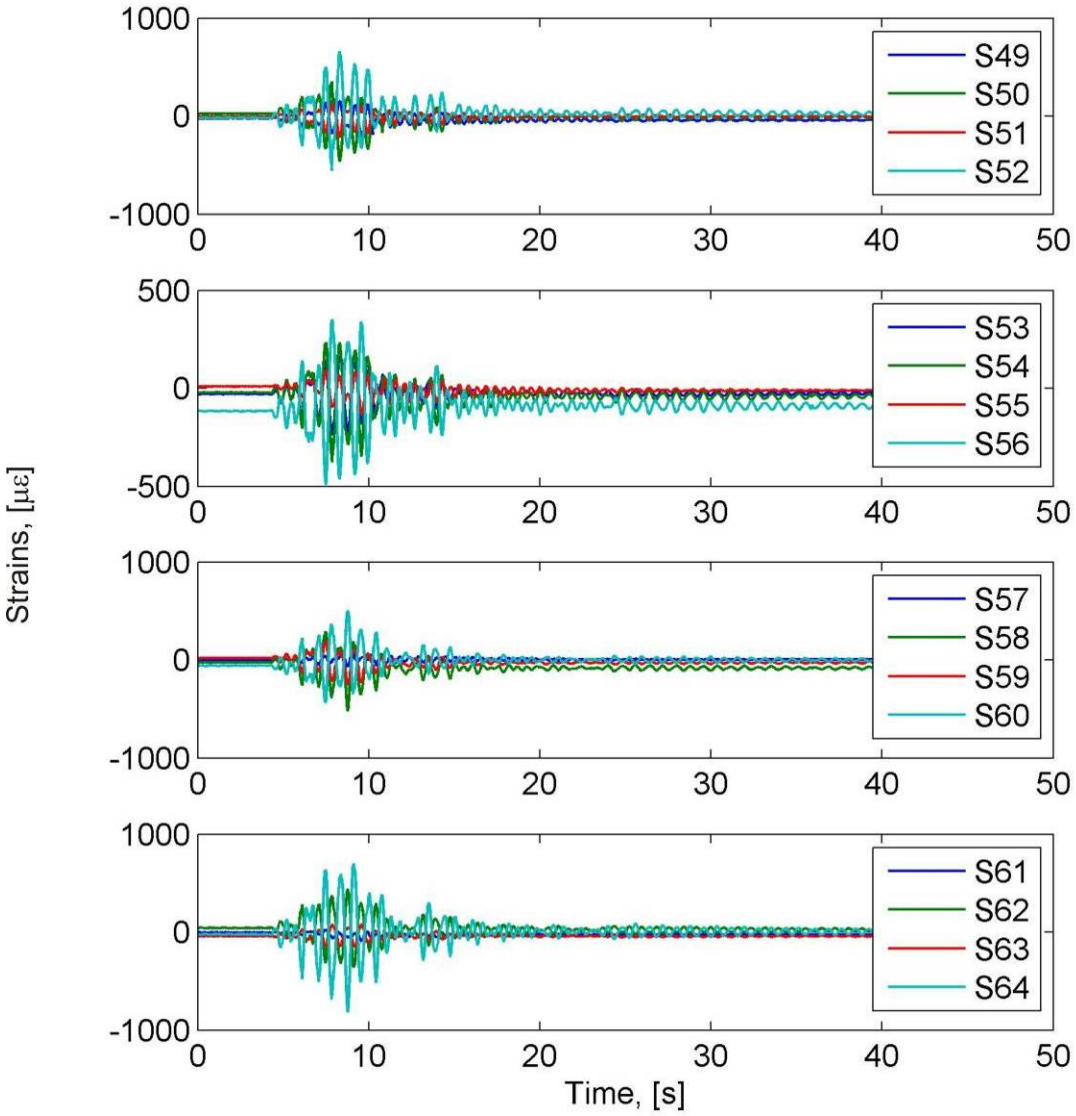

Figure C.41: Strain time histories in the portal beam for the 60% of CLE6 excitation

C.3.6 20% NJM Excitation

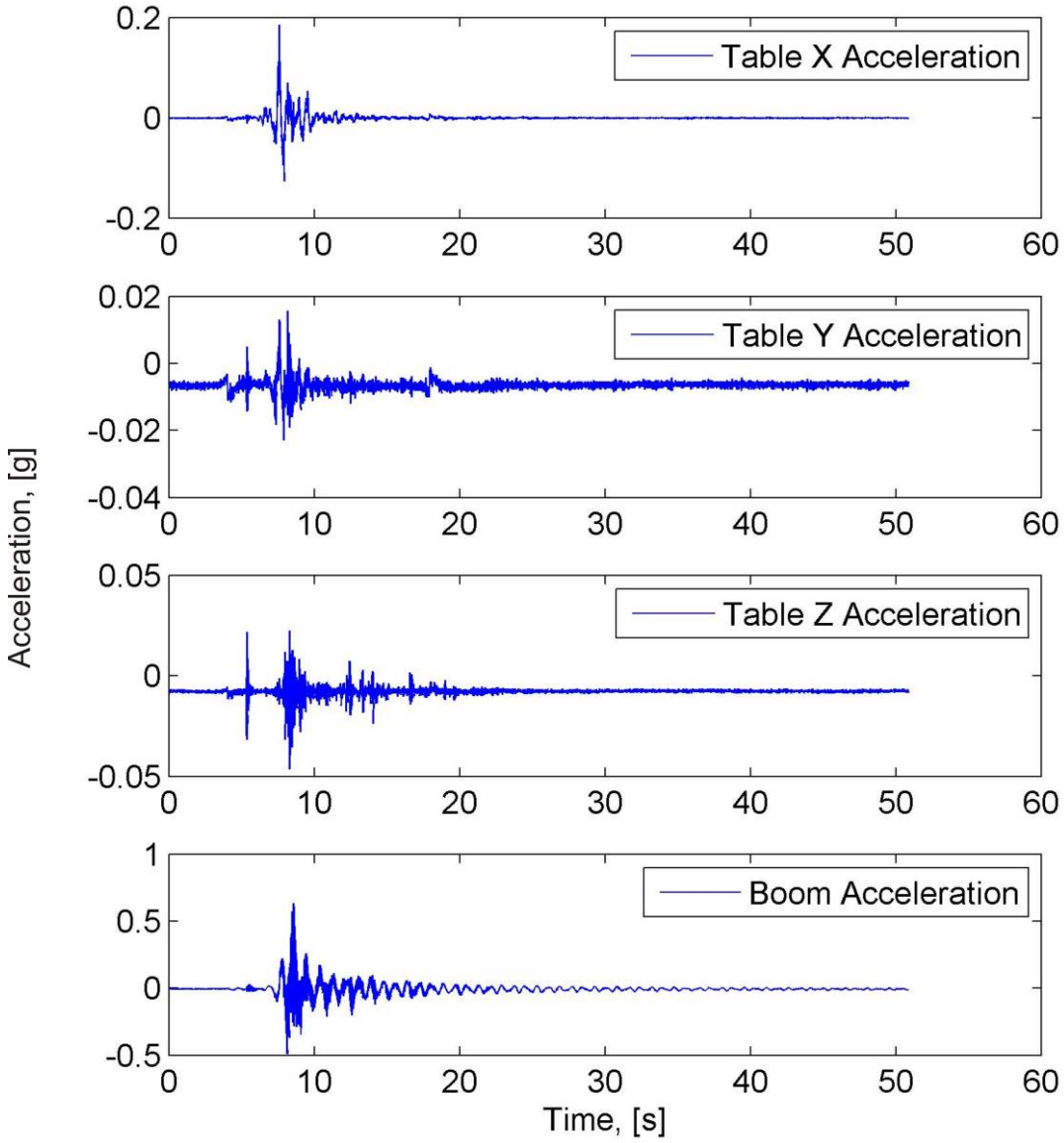

Figure C.42: Acceleration time histories for the 20% NJM excitation

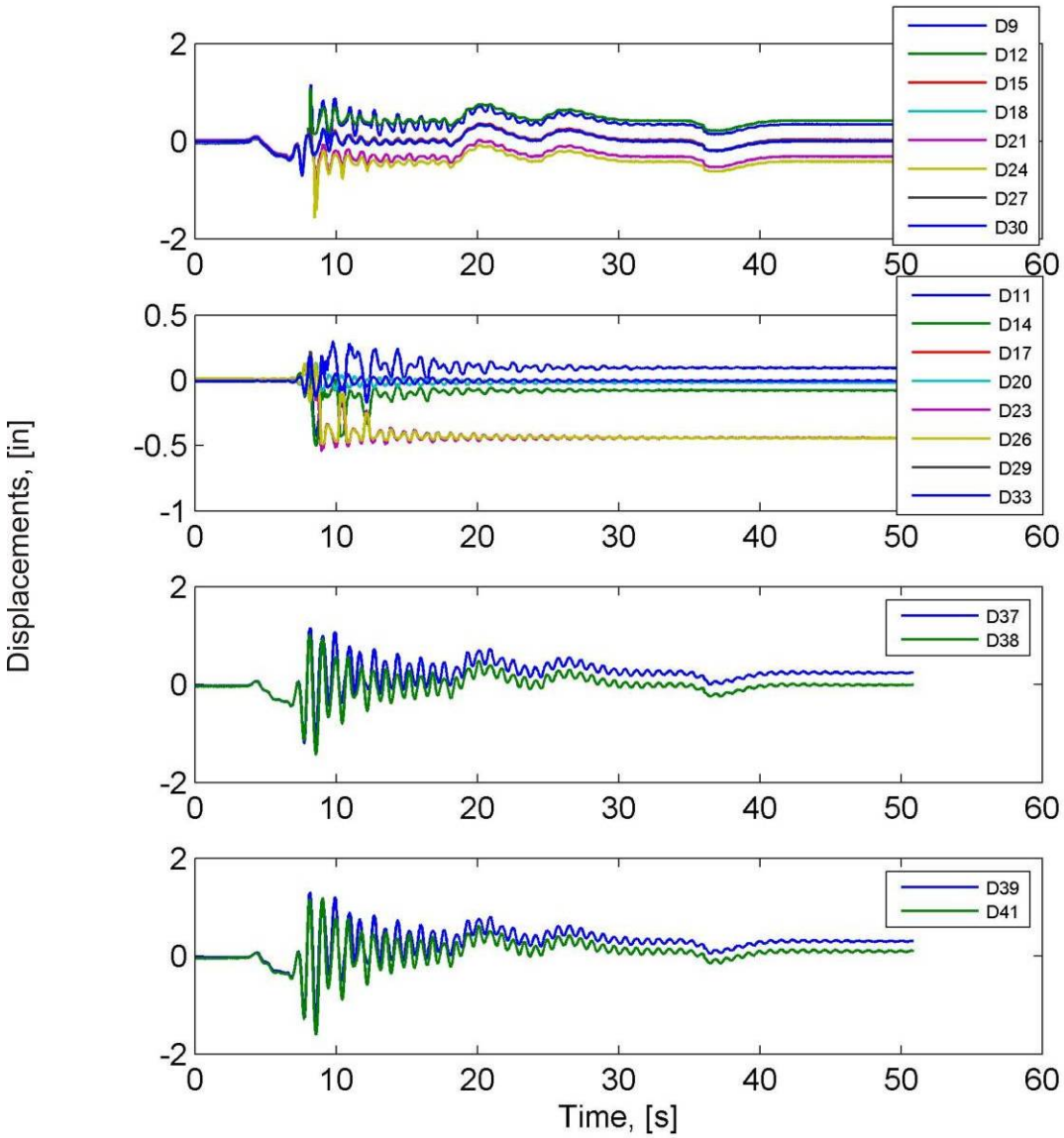

Figure C.43: Displacement time histories for the 20% NJM excitation

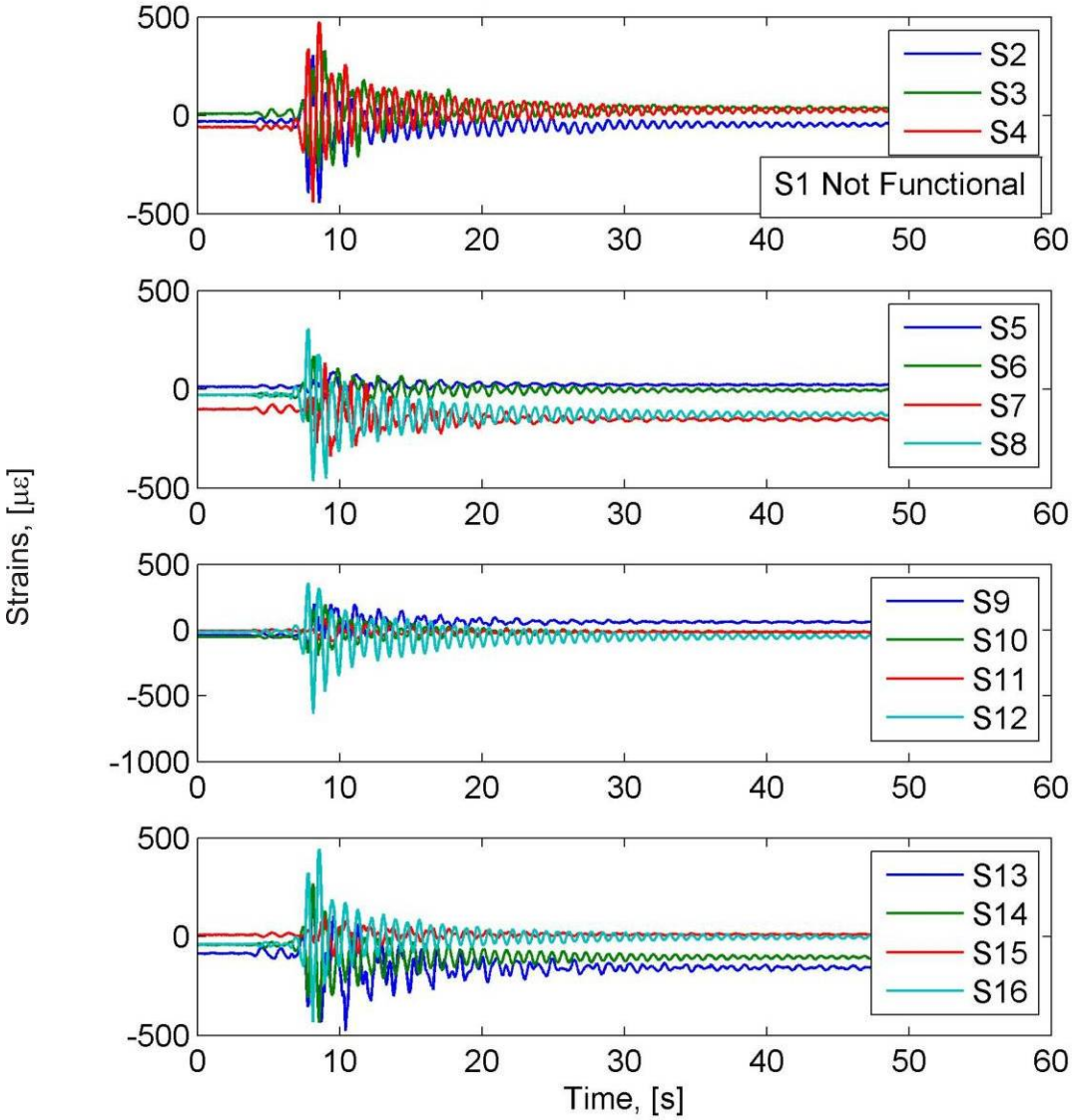

Figure C.44: Strain time histories at the bottom of the portal frame legs for the 20% of NJM excitation

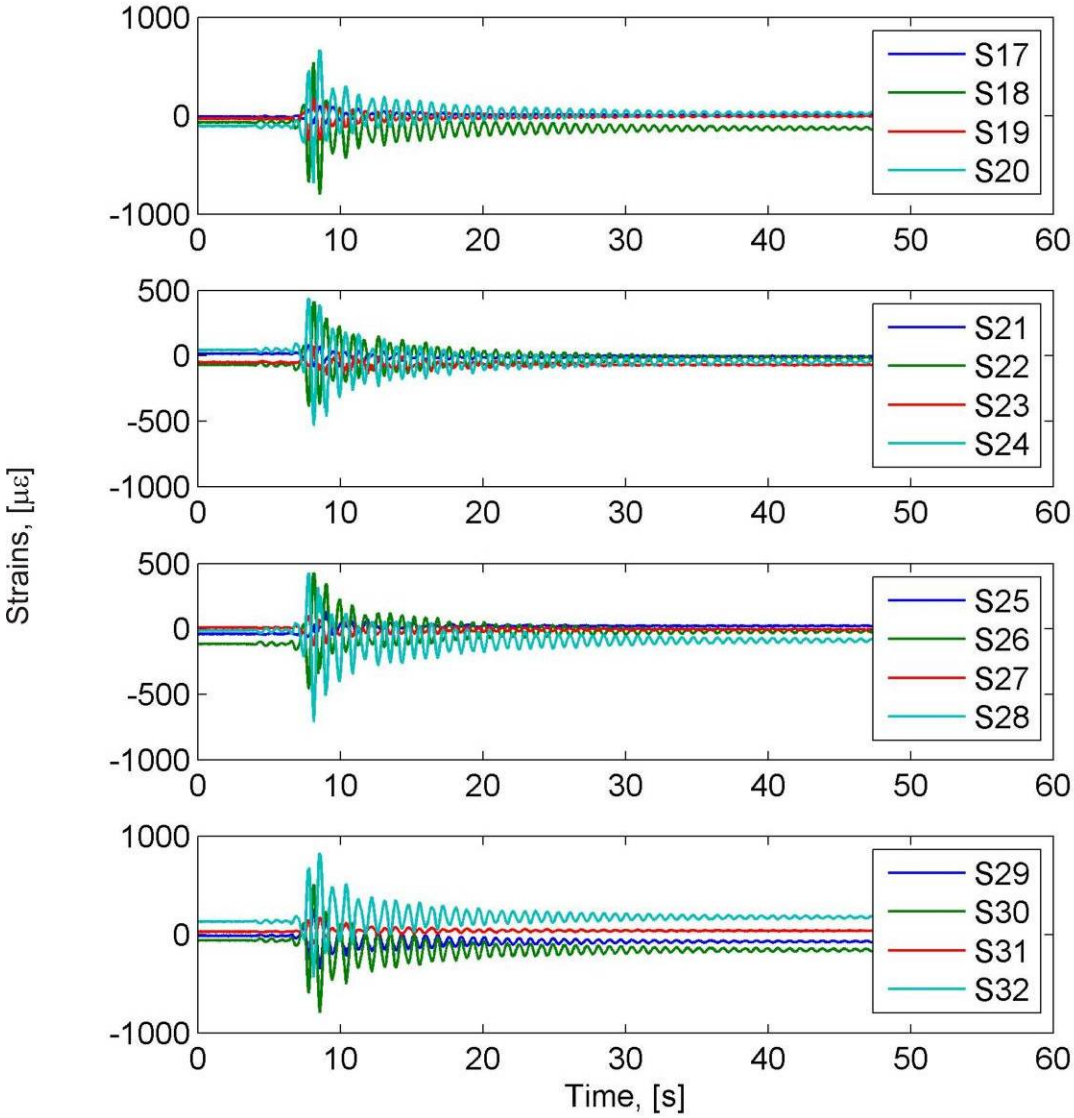

Figure C.45: Strain time histories at the middle of the portal frame legs for the 20% of NJM excitation

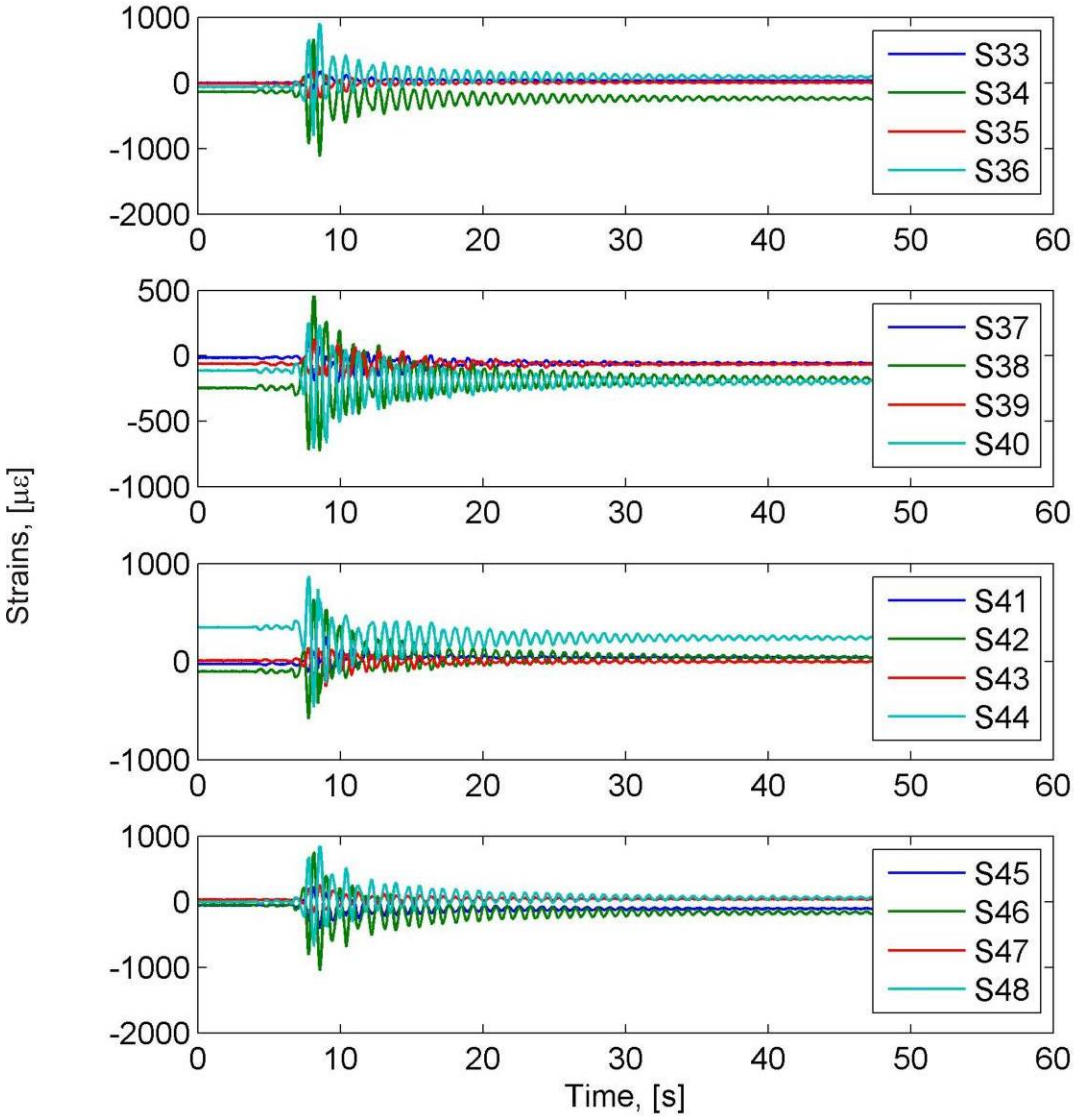

Figure C.46: Strain time histories at the top of the portal frame legs for the 20% of NJM excitation

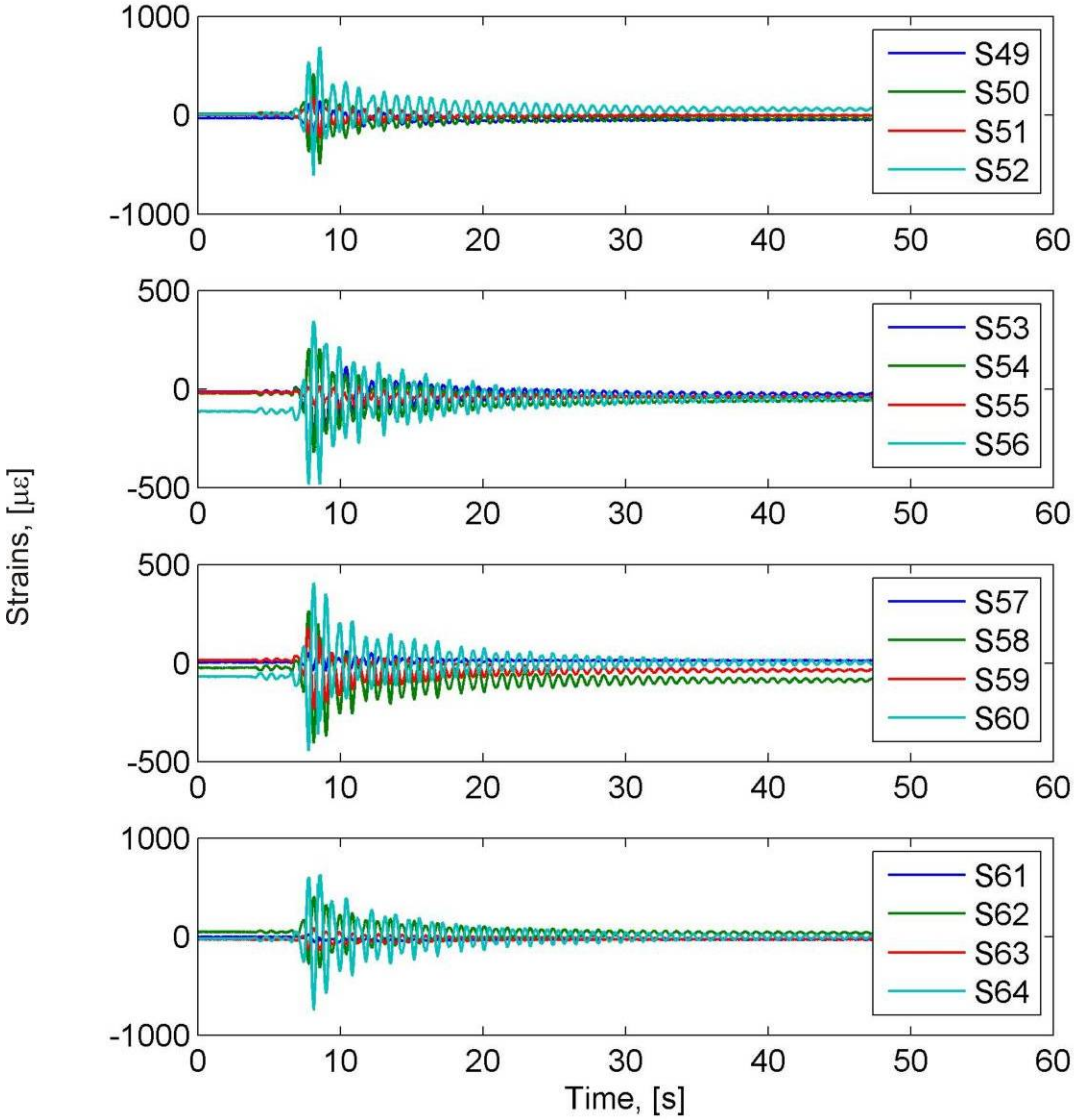

Figure C.47: Strain time histories at the portal beam for the 20% of NJM excitation

REFERENCES

American Institute of Steel Construction (AISC). (2005). Steel Construction Manual, 13th Edition. American Institute of Steel Construction, Chicago, IL.

American Society of Civil Engineers (ASCE), (1998). "Seismic Guidelines for Ports", *Technical Council on Lifeline Earthquake Engineering Monograph No. 12*, S. Werner (editor), Reston, VA.

American Society of Civil Engineers (ASCE), (2000) ."Prestandard and Commentary for the Seismic Rehabilitation of Buildings," Federal Emergency Management Agency, *FEMA-356*, Washington DC.

Ang, A.H.S., Tang W.H., *Probability Concepts in Engineering Planning and Design*, *vol. 1-Basic Principles*. New York: Wiley, 1975.

Applied Technology Council, (1985) "Earthquake damage evaluation for California," *ATC-13*, Redwood City, CA.

Arulmoli, A. K., Lam, I. P., Schell, B.A., Abrahamson, N.S., Ana, J.S., Yin, P., (2006). "Port-Wide Ground Motion Study, Port of Long Beach (POLB), California," *EMI No. 01-143* Earth Mechanics, Inc., Fountain Valley, CA.

Arulmoli, A.K., Lam, I.P., Schell, B.A., Abrahamson, N.S., Ana, J.S., Yin, P. (2007). "Port of Los Angeles and Long Beach Port-Wide Ground Motion Study." *In W. Watson (ed.), ASCE Ports 2007*, *Proc. of the 11th Triennial Intl. Conf.*, San Diego, California, USA.

Bazös, N., Kiremidjian, A., King, S.A., Law, K.H., (1999). "Statistical Analysis of Bridge Damage Data from the 1994 Northridge, CA, Earthquake." *Earthquake Spectra*, **15**(1),

Bureau of Transportation Statistics. (2004). *America's Freight Transportation Gateways: Connecting our Nation to Places and Markets Abroad*, U.S. Department of Transportation, Washington, DC.

CalTrade, (2008). "ILWU Calls for May 1 Dock Walkout." March 14, 2008. www.caltradereport.com. Accessed July 22, 2009.

Chang, S.E. (2000). "Disasters and transport systems: loss recovery, and competition at the Port of Kobe after the 1995 earthquake." *J. Transport Geography*, **8**(1), 53-65.

Choi, B., Kang, Y., and Yoo, C. (2006). "Stiffness requirements for transverse stiffeners of compression panels." *Engineering Structures* **29**, 2087-2096.

Clough, R.W., Hucklebridge, A.A. (1977). "Preliminary study of seismic uplift of a steel frame." *Report No. UBC/EERC-77/22,* EERC, University of California, Berkeley, CA.

Cornell, C. A., Jalayer, F., Hamburger, R. O., Foutch, D. A. (2002). "Probabilistic Basis for 2000 SAC Federal Emergency Management Agency Steel Moment Frame Guidelines," *Journal of Structural Engineering*, **128**,526-533.

Dinevski, D., Oblack, M. (1996). "Structural Vibrations Calculation and Testing of the Heavy Lifting Appliance." *The 1996 1st International Conference on Computational Methods and Testing for Engineering Integrity*, Kuala Lampur, Malaysia, 237-246.

Dinevski, D., Oblak, M., Novak, A. (1997). "Experimental Verification of the Container Crane Natural Frequencies." *The 1997 8th International Conference on Computational Methods and Experimental Measurements*, Rhodes, Greece, 245-254.

Ellingwood, B. R. (2001). "Earthquake risk assessment of building structures," *Reliability Engineering and System Safety*, **74**, 251-262.

Ellingwood, B. R., Celik, O. C., Kinali, K., (2007) "Fragility assessment of building structural systems in Mid-America," *Earthquake Engineering and Structural Dynamics*, **36**, 1935-1952.

Federal Emergency Management Agency (FEMA), (2003). "Multi-hazard loss estimation methodology, Earthquake model," *HAZUS-MH MR4 Technical Manual*, Washington DC .

Ge, H., Gao, S., and Usami, T. (2000). "Stiffened steel box columns. Part 1: Cyclic behavior." *Earthquake Engineering and Structural Dynamics*. **29**, 1691-1706.

Giovenale, P., Cornell, C. A., Esteva, L. (2004). "Comparing the adequacy of alternative ground motion intensity measures for the estimation of structural responses," *Earthquake Engineering and Structural Dynamics*, **33**, 951- 979.

Harris, H.G., and Sabnis, G., (1999). *Structural Modeling and Experimental Techniques*, 2nd edition, CRC Press, Boca Raton, FL.

Hucklebridge, A.A. (1977). "Earthquake simulation tests of a nine story steel frame with columns allowed to uplift." *Report No. UBC/EERC-77/23*, EERC, University of California, Berkeley, CA.

International Navigation Association (PIANC), (2001). *Seismic Design Guidelines for Port Structures*, Taylor and Francis Group, London UK, 474 pp.

Japan Society of Mechanical Engineers (JSME), (1996). "The Special Investigation Committee on Great Hanshin Awaji Earthquake Damage." *The Machines and*

Industrial Equipments Damage due to the South Hyogo-Prefecture Earthquake, pp. 153-163.

Jordan, M., (1998). Megacranes: Holdying Sway. *Port Development International*, CC10-11.

Kanayama, T., and Kashiwazaki, A., (1998). A Study on the Dynamic Behavior of Container Cranes Under Strong Earthquakes. *Proc. ASME PVP, Seismic Engineering*, **364**, 279-284.

Kanayama, T., Kashiwazaki, A., Shimizu, N., Nakamura, I., and Kobayashi, N., (1998). "Large Shaking Table Test of a Container Crane by Strong Ground Excitation." *Proc. ASME PVP, Seismic Engineering*, **364**, 243-248.

Kinali, K., Ellingwood, B. R. (2007). "Seismic fragility assessment of steel frames for consequence-based engineering: A case study for Memphis, TN," *Engineering Structures*, **29**, 1115-1127.

Kitada, T., Nakai, H., Kunihiro, M.,(1989). "Ultimate Strength of Box Stub Columns under Combined Actions of Compression, Bending and Torsion." Journal of Constructional Steel Research, **13**, 153-168.

Kobayashi, N., Kuribara, H., Honda, T., Watanabe, M. (2004). "Nonlinear Seismic Responses of Container Cranes Including the Contact Problem between Wheels and Rails." *Journal of Pressure Vessel Technology*, **126**, 59-65.

Kosbab, B.D., (2010). *Seismic performance evaluation of port container cranes allowed to uplift.* Georgia Institute of Technology, Atlanta, GA. AAT 341447

Krawinkler, H., Medina, R., Alavi, B. (2003). "Seismic drift and ductility demands and their dependence on ground motions." *Engineering Structures*, **25**, 637-653.

Lee, S., Yoo, C., and Yoon, D., (2003). "New Design Rule for Intermediate Transverse Stiffeners Attached on Web Panels." *Journal of Structural Engineering* **129**(12), 1607-1614.

Liu, J., Sabelli, R., Brockenbrough, R. L., Fraser, T. P. (2007). "Expected yield stress and tensile strength ratios for determination of expected member capacity in the 2005 AISC seismic provisions," *Engineering Journal*, **44**, 15-25.

Mazzoni, S., McKenna, F., Scott, M. H., Fenves, G.L. et al., 2009. *OpenSees Manual*, PEER Center, http://opensees.berkeley.edu/OpenSees [03/22/2010].

MacRae, G. A., Kawashima, K. (2001). "Seismic Behavior of Hollow Stiffened Steel Bridge Columns," *Journal of Bridge Engineering*, **6**, 110-119.

Midorikawa, M., Azuhata, T., Ishihara, T., Wada, A. (2006). "Shaking table tests on seismic response of steel braced frames with column uplift." *Earthquake Engineering and Structural Dynamic*s, **35**, 1767-1785.

Mills, R.S., Krawinkler, H., Gere, J.M. (1979) "Model Tests on Earthquake Simulators – Development and Implementation of Experimental Procedures." *Report No. 39 from The John A. Blume Earthquake Engineering Cente*r, Stanford University, Stanford, CA.

Moncarz, P.D., Krawinkler, H. (1981). "Theory and Application of Experimental Model Analysis in Earthquake Engineering." *Report No. 50 from The John A. Blume Earthquake Engineering Center*, Stanford University, Stanford, CA.

Murano, K. and Yoshida, K., (2002) "Analysis of Real Size Container Crane with the Rocking Type of Vibration Isolation System." *Proceedings of The 6th International Conference on Motion and Vibration Control*, Saitama, pp76-81.

Muthukumar, S., DesRoches, R. (2006)."A Hertz contact model with non-linear damping for pounding simulation," *Earthquake Engineering & Structural Dynamics*, **35**, 811-828.

Nasser, M.A. "Dynamic Analysis of Cranes." *Proceedings of IMAC XIX: A Conference on Structural Dynamics*, Kissimmee, FL, 1592-1599.

Neuenhofer, A., and Filippou, F.C., 1998. "Geometrically nonlinear flexibility-based frame finite element." *Journal of Structural Engineering* **124**, 704-711.

Port of Los Angeles. (2007). "The Port of Los Angeles Seismic Code for Port Structures (POLA Code 07)," POLA, Los Angeles, CA.

Ruge, A.C., (1934). "The Determination of Earthquake Stresses in Elastic Structures by Means of Models." *Bulletin of the Seismological Society of America* **24**,169-230.

Porter, K. A., Beck, J. L., Shaikhutdinov, R. V. (2002). "Sensitivity of building loss estimates to major uncertain variables," *Earthquake Spectra*, **18**, 719-743.

Schlechter, S.M., McCullough, N.J., Dickenson, S.E., Kutter, B.L., Wilson, D.W., (2000). "Pile-Supported Wharf Centrifuge Model (NJM02)." *Report: GEG02-2000*, Oregon State University. Corvallis, OR.

Schleiffarth, L. (2008). "Survey of Global Container Crane Sizes," Georgia Institute of Technology.

Shakal, A., Huang, M., Reichle, M., Ventura, C., Cao, T., Sherburne, R., Savage, M., Darragh, R., and Petersen, C. (1989). "CSMIP Strong-Motion Records from the Santa Cruz Mountains (Loma Prieta), California Earthquake of 17 October 1989." *Report*

No. OSMS 89-06, California Strong Motion Instrumentation Program, November 17, 1989.

Shinozuka, M., Feng, M. Q., Lee, J., Naganuma, T. (2003). "Statistical Analysis of Fragility Curves," *Journal of Engineering Mechanics*, **126**, 1224-1231.

Shinozuka, M., Feng, M.Q., Kim, H., Uzawa, T., Ueda, T. (2000). "Damage Assessment of a Highway Network Under Scenario Earthquakes for Emergency Response and Decision Support." *Proceedings of SPIE – The International Society for Optical Engineering*, vol. 3988, Newport Beach, CA, USA. Society of Photo-Optical Instrumentation Engineers, 264-275.

Soderberg, E., Hsieh, J., and Dix, A., (2009). "Seismic Guidelines for Container Cranes." in *Proc., Seventh International Conference on Lifeline Earthquake Engineering*, ASCE TCLEE, Oakland, June 28 – July 1 2009.

Soderberg, E., and Jordan, M., (2007). "Seismic Response of Jumbo Container Cranes and Design Recommendations to Limit Damage and Prevent Collapse." in *ASCE Ports 2007, Proc. of the 11th Triennial Intl. Conf.*, W. Watson (ed.), San Diego, California, 25-28 March 2007.

Soderberg, E., (2003). "Megacranes: Holding Sway – Boom Motions." *Port Technology International* **20**, 103-106.

Sugano, T., Shibakusa, T., Fukiwara,, K., Tokunaga, K., Makimoto, Y., Fujiki, T. (2003). "Study on the Seismic Performance of Container Crane; Development of the Container Crane Isolation System." *Report of the Port and Airport Research Institute*, **42**, 221-250.

Sugano, T., Takenbo, M., Suzuki, T., Shiozaki, Y. (2008). "Design Proceedures of seismic-isolated container crane at port." *Proc. of 14th World Conference on Earthquake Engineering*. Beijing, China.

Sustantha, K.A.S, Aoiki, T., Kumano, T., (2006). "Strength and ductility evaluation of steel bridge piers with linearly tapered plates." *Journal of Constructional Steel Research*. **62**, 906-916.

Tanabe, T., Etou, T., Yamamoto, S., Sugano, T., Miyata, M., Kashiwazaki, A. (2000). "Experiment on Behavior of Container Cranes during Strong Earthquakes," *Transcations of the Japan Society of Mechanical Engineers, Part C*, **66**, 205-212.

Wallace, B.J., Krawinkler, H. (1985). "Small-Scale Model Experimentation on Steel Assemblies, U.S.-Japan Research Program." *Report No. 75 from The John A. Blume Earthquake Engineering Center*, Stanford University, Stanford, CA..

Wen, Y.K., Ellingwood B.R., Bracci, J. M. (2004). "Vulnerability Function Framework

for Consequence-based Engineering," *Technical Rep. DS-4,* Mid-America Earthquake Center, Champaign, IL.

Wen, Y. K., Ellingwood, B. R., Veneziano, D., Bracci, J. M. (2003). "Uncertainty Modeling in Earthquake Engineering (white paper)," *MAE Center Project FD-2 Report*, University of Illinois at Urbana-Champaign, Urbana,IL,

Werner, S. D. (1998). *Seismic Guidelines for Ports*. Reston, VA: American Society of Civil Engineers.

Usami, T., Gao, S., Ge, H. (2000). "Stiffened steel box columns. Part 2: Ductility evaluation." *Earthquake Engineering and Structural Dynamics*. **29**, 1707-1722.

Yamamoto, S., Sugano, T., Tanabe, T., Nakashima, S., Mityata, M., Etoh, T., Tanaka, T., Tatsumi, Y. (2000). "A Study of the Interaction Between the Pier Type Wharf and Container Crane During Earthquakes*." Proceedings of the 12 World Conference on Earthquake Engineering.* Auckland, New Zealand.

Yamamoto, S., Sugano, T., Tanabe, T. (2002). "The shaking table test of the interaction between the pier type wharf and the container crane during earthquakes," *Nippon Kikai Gakkai Ronbunshu, C Hen/Transactions of the Japan Society of Mechanical Engineers, Part C*, **68**, 3209-3216.

Yamazaki, F., Hamada, T., Motoyama, H., Yamauchi, H. (1999). "Earthquake Damage Assessment of Expressway Bridges in Japan." *Technical Council on Lifeline Earthquake Engineering Monograph*, **16**, 361-370.

Yoo, C., Choi, B., and Ford, E. (2001). "Ductility Evaluation Procedure for Thin-Walled Steel Structures." *Journal of Structural Engineering*, **127**(6), 705-711.

Yuksel, Y., Cevik, E., Celikoglu, Y., Bostan, T., Ozmen, H.I., Ozguven, O., (200)1."Damages Due to Eastern Marmara Earthquake (EME) at Port Structures." *Proceedings of the Eleventh International Offshore and Polar Engineering Conference*, Stavanger, Norway, 447-451.

Zrnic, N., (2004). Development of Design of Ship-to-Shore Container Cranes: 1959-2004, in *International Symposium on History of Machines and Mechanisms, Proceedings HMM2004*, M. Ceccarelli (editor), Kluwer Academic Publishers, Dordrecht, The Netherlands, pp.229-242.

Zheng, Y., Usami, T., and Ge, H. (2000). "Ductility Evaluation Procedure for Thin-Walled Steel Structures." *Journal of Structural Engineering*, **126**(11), 1312-1319.

Zheng, Y., Usami, T., and Ge, H. (2000). "Ductility of Thin-Walled Steel Box Stub Columns." *Journal of Structural Engineering*, **126**(11), 1304-1311.